

This file is part of the following work:

Zaracho, Juan Ignacio (2025) *Wind loading and aeroelastic response of flat plates: application to solar trackers*. PhD Thesis, James Cook University.

Access to this file is available from:

<https://doi.org/10.25903/f3zg%2Dvn53>

Copyright © 2025 Juan Ignacio Zaracho

The author has certified to JCU that they have made a reasonable effort to gain permission and acknowledge the owners of any third party copyright material included in this document. If you believe that this is not the case, please email

researchonline@jcu.edu.au

JAMES COOK UNIVERSITY

COLLEGE OF SCIENCE AND ENGINEERING



**Wind loading and aeroelastic response of flat plates:
Application to Solar Trackers**

Juan Ignacio Zaracho

DOCTORAL THESIS

Thesis submitted to the College of Science and Engineering for the degree of
Doctor of Philosophy

August 2025

Ad maiorem Dei gloriam

DECLARATION

I declare that this thesis is my work and has not been submitted for another degree or diploma at any university or other institution of tertiary education. Information derived from published or unpublished work of others has been acknowledged in the text and a list of reference given.

Signed: _____

Date: _____

Juan Ignacio Zaracho

STATEMENT OF ACCESS

I, the author of this thesis, understand that James Cook University will make it available for use within the University Library and via the Australian Digital Theses network for use elsewhere.

I understand that as an unpublished work a thesis has significant protection under the Copyright act and I do not wish to place restrictions on access to this work.

Signed: _____

Date: _____

Juan Ignacio Zaracho

STATEMENT ON THE CONTRIBUTION OF OTHERS

Supervision: Prof. John Ginger was the primary advisor of this work; Dr. David Henderson and Dr. Korah Parackal were the secondary advisors of this work.

Mentoring: Dr. John Holmes provided guidance and mentorship in the conceptualization of this study.

Editorial Assistance: Principal editorial assistance was provided by Prof. John Ginger. Additional assistance was provided by Dr. John Holmes, Adjunct Prof. George Walker and Dr. Korah Parackal.

Experimental Resources: The aeroelastic models used in this study were manufactured by Mr. Troy Poole. Additional support was provided by Mr. John De Valter and Mr. Joesf Kunta. Assistance in setting up the apparatus was provided by Mr. Simon Ingham. Assistance in wind tunnel testing was provided by Prof. John Ginger.

Funding: The Cyclone Testing Station has provided the funding for the Author's PhD Candidature.

ACKNOWLEDGEMENTS

I thank God for being the source of all knowledge, especially when diving into the unknown. Thank you for blessing me with the people that helped me in this process.

I must foremost show gratitude to my Advisory Panel for their support, experience and guidance since this journey started. I specially thank Prof. John Ginger, for his time, patience and guidance through all these years. It has certainly been a pleasure. Thanks to Dr. David Henderson and Dr. Korah Parackal, for supporting me, guiding me and thinking about me not just as a PhD candidate: David, thanks for the guitar and Korah, thanks for the camping gear.

I acknowledge Dr. John Holmes and Prof. George Walker for their mentorship. Your experience, vision and guidance have enormously inspired me and influenced this work completely. Thank you for your time and generosity.

I want to express my profound gratitude to the Cyclone Testing Station staff for providing a collaborative and supportive environment for me these past years. I am very proud and happy to work alongside with you all. Big thanks to Mr. Troy Poole and the technicians at the College of Science and Engineering for bringing my conceptual ideas to life.

I want to thank my parents who have always supported me and encouraged me to follow my dreams. Thanks for always being example of giving and generosity even from far away. With them, I thank the rest of my family for their support. I want to thank Julito. Your support, care and love have made this adventure successful. Nothing would have been the same without you. The support of my friends here and back home has been fundamental to my well-being during this process. Your love has sustained me constantly. My happiness is due in part to your presence in my life.

ABSTRACT

Solar tracker systems, consisting of flexible solar panel modules mounted on frames attached to a rotating torque tube, are susceptible to structural failure from wind action, initiated by aeroelastic instabilities such as torsional galloping and divergence. This thesis studied the wind loads on axially supported flat plates to understand and predict this behaviour in solar tracker arrays. Aeroelastic models, of typical full-scale systems, were tested in simulated terrain conditions with turbulent wind flows. Configurations included variations in model length and torque tube cross-sections. The response of three adjacent solar tracker rows was also investigated.

The study obtained fluctuating wind loads for a range of approach wind directions, revealing distinct differences in the moment response of the trackers depending on whether the wind was approaching from directions close to perpendicular to the array or from oblique angles. The relationship between wind loading and tracker tilt angle was also explored, showing that low to medium tilt angles are more prone to torsional flutter than higher tilt angles.

Oblique approach winds triggered instabilities similar to perpendicular winds. The shielding effect of the leading upwind row in multi-row setups was demonstrated, but this effect diminished for rows further downwind. Instability in multi-row setups was found to be independent of array position, with critical wind speed triggering torsional flutter simultaneously across rows.

Results indicate that a stow position with the highest possible tilt angle is desirable. A preliminary assessment criterion for solar tracker stability is proposed, incorporating site-specific wind speed, natural frequency, and breadth, and facilitating design optimization for mitigating instability risks.

CONTENTS

1 INTRODUCTION	1
1.1 STRUCTURAL FAILURE OF SOLAR TRACKERS	4
1.2 STUDIES ON SOLAR TRACKERS.....	6
1.3 AIMS AND OBJECTIVES	9
1.4 CHAPTER CONTENT	10
2 LITERATURE REVIEW	13
2.1 WIND LOADS ON A PLATE	13
2.2 DYNAMIC RESPONSE.....	15
2.3 TORSIONAL GALLOPING AND DIVERGENCE	17
2.4 FLUTTER.....	20
2.5 AERODYNAMIC DERIVATIVES	22
2.6 WIND LOADS OF GROUND-MOUNTED SOLAR PANELS	35
2.7 AEROELASTIC MODEL TESTS.....	39
2.8 COMPUTATIONAL MODELLING.....	43
2.9 CODES AND STANDARDS.....	46
2.10 CHAPTER SUMMARY	51
3 METHODOLOGY	53
3.1 ATMOSPHERIC BOUNDARY LAYER IN THE WIND TUNNEL	53
3.2 FIXED FRAME RIGID MODEL	56
3.3 PROTOTYPE SOLAR TRACKER ARRAY.....	59
3.4 MODEL SCALING	62
3.5 AEROELASTIC SOLAR TRACKER MODELS	65
3.6 WIND TUNNEL TESTING	71
3.6.1 <i>Wind loading test</i>	72
3.6.2 <i>Critical wind speed test</i>	75
4 RESPONSE OF SOLAR TRACKERS – RESULTS	77
4.1 WIND LOADING.....	78
4.1.1 <i>Loads on rigid model</i>	78
4.1.2 <i>Wind loads on aeroelastic models</i>	81
4.2 AEROELASTIC INSTABILITIES	91
4.2.1 <i>Critical wind speeds for oblique approach wind directions</i>	95
4.2.2 <i>Onset of torsional galloping</i>	97

4.2.3 Onset of divergence.....	102
4.3 EFFECTIVE DAMPING AND EFFECTIVE STIFFNESS	105
4.4 QUASI-STEADY AERODYNAMIC DERIVATIVES.....	109
4.5 AERODYNAMIC DERIVATIVE A_2 * USING AUTOCORRELATION	116
4.6 APPLICATIONS TO DESIGN: PRELIMINARY ASSESSMENT OF STABILITY	126
4.7 CHAPTER SUMMARY	128
5 RESPONSE OF SOLAR TRACKERS IN A MULTI-ROW SETUP – RESULTS	
131	
5.1 MULTI-ROW TEST	131
5.2 WIND LOADING	133
5.3 AEROELASTIC INSTABILITY	138
5.4 SPECTRAL ANALYSIS	142
5.5 CHAPTER SUMMARY	147
6 CONCLUSIONS	149
6.1 APPLICABILITY OF QUASI-STEADY APPROACH	152
6.2 CONCLUDING STATEMENT	153
REFERENCES.....	155
APPENDIX A: SOLAR ARRAY MODEL	161
A.1 AEROELASTIC MODELLING CALCULATIONS	161
APPENDIX B: MEASURING INSTRUMENTS.....	171
APPENDIX C: SUPPLEMENTARY DATA FOR CHAPTER 4	178
C.1 MOMENT COEFFICIENTS.....	178
C.2 CALCULATION OF THE CRITICAL WIND SPEED	190
C.3 MOMENT AND WIND SPECTRA BEFORE AND AFTER TORSIONAL GALLOPING.....	194
C.4 EFFECTIVE DAMPING AND STIFFNESS (MODEL I-B AND MODEL II-B).....	195
C.5 AERODYNAMIC DERIVATIVES (MODEL I-B AND MODEL II-B).....	197

LIST OF TABLES

TABLE 2.1. SOLAR PANEL CONFIGURATION FOR DIFFERENT SOLAR TRACKERS SYSTEMS. EXTRACTED FROM MARTÍNEZ-GARCÍA ET AL. (2021)	40
TABLE 2.2. NET PRESSURE COEFFICIENTS FOR GROUND-MOUNTED SOLAR PANELS, SEVERAL TILT ANGLES (α) AND WIND DIRECTION $\theta = 0^\circ$. EXTRACTED FROM AS/NZS 1170.2 (2021).....	48
TABLE 2.3. NET PRESSURE COEFFICIENTS FOR GROUND-MOUNTED SOLAR PANELS, SEVERAL TILT ANGLES (α) AND WIND DIRECTION $\theta = 180^\circ$. EXTRACTED FROM AS/NZS 1170.2 (2021).....	48
TABLE 3.1. PARAMETERS OF THE PROTOTYPE AND AEROELASTIC MODELS	66
TABLE 3.2. MECHANICAL PROPERTIES IN TORSION OF AEROELASTIC MODELS	71
TABLE 3.3. LIST OF WIND TUNNEL EXPERIMENTS	74
TABLE 4.1 MEAN MOMENT COEFFICIENT FOR $\theta = 0^\circ$	88
TABLE 4.2. THEORETICAL AND EXPERIMENTAL CRITICAL WIND SPEEDS FOR TORSIONAL GALLOPING.....	92

LIST OF FIGURES

FIGURE 1.1. GROUND-MOUNTED FIXED-TILT SOLAR PANEL SYSTEM	2
FIGURE 1.2. SINGLE AXIS SOLAR TRACKER ARRAYS	2
FIGURE 1.3. SOLAR TRACKER COMPONENTS	3
FIGURE 1.4. SCHEMATIC DIAGRAM OF AN AXIALLY SUPPORTED SOLAR TRACKER	4
FIGURE 1.5. SOLAR TRACKER AFTER FAILURE. OAKEY 2 SOLAR FARM. OAKEY, QUEENSLAND, AUSTRALIA (EXTRACTED FROM GIFFORD (2019))	5
FIGURE 1.6. SOLAR TRACKER FAILURE. CASE STUDY. (EXTRACTED FROM VALENTÍN ET AL., (2022))	6
FIGURE 2.1. LOADS ON AN AXIALLY SUPPORTED FLAT PLATE EXPOSED TO WIND FLOW ...	14
FIGURE 2.2. NORMAL FORCE COEFFICIENT FOR AN INCLINED PLATE	15
FIGURE 2.3. RESPONSE OF AN AXIALLY SUPPORTED PLATE	17
FIGURE 2.4. THEODORSEN CIRCULATORY FUNCTION FOR DIFFERENT VALUES OF DAMPING RATIO. EXTRACTED FROM SCANLAN AND TOMKO (1971)	23
FIGURE 2.5. SIGN CONVENTION FOR WIND AND STRUCTURE AXIS FORCES (TOP) AND EFFECTIVE WIND ANGLE OF ATTACK (BOTTOM). EXTRACTED FROM TAYLOR AND BROWNE (2020)	26
FIGURE 2.6. MEASURED STATIC FORCE AND MOMENT COEFFICIENTS VS α . (A) DRAG AND HORIZONTAL FORCES. (B) LIFT AND VERTICAL FORCES. (C) MOMENT COEFFICIENTS. EXTRACTED FROM TAYLOR AND BROWNE (2020)	27
FIGURE 2.7. AERODYNAMIC DERIVATIVES $A2^*$ AND $A3^*$ VS REDUCED WIND SPEED U_{red} , FOR $\alpha = 0^\circ$ AND $\alpha = 20^\circ$. EXTRACTED FROM TAYLOR AND BROWNE (2020)	28
FIGURE 2.8. REFERENCE SYSTEM SHOWING APPROACH WIND DIRECTION (U_∞), MEAN EFFECTIVE TILT ANGLE (α_{meanff}), NOMINAL TILT ANGLE (α_n), STATIC VARIATION OF TILT ANGLE ($\Delta\alpha_s$), STRUCTURAL STIFFNESS K_{mech} , ELEVATION OF THE PLATE H , AND CHORD LENGTH B . EXTRACTED FROM CÁRDENAS-RONDÓN ET AL. (2023)	30
FIGURE 2.9. AERODYNAMIC DERIVATIVE $A2^*$ VS REDUCED WIND SPEED U_{red} FOR TRACKER CHORD-HEIGHT $H/B = 2$ AND DIFFERENT TILT ANGLES. EXTRACTED FROM CÁRDENAS-RONDÓN ET AL., (2023)	31

FIGURE 2.10. AERODYNAMIC DERIVATIVE A_3^* VS REDUCED WIND SPEED U_{red} , FOR TRACKER CHORD-HEIGHT $H/B = 2$ AND DIFFERENT TILT ANGLES. EXTRACTED FROM CÁRDENAS-RONDÓN ET AL., (2023)	32
FIGURE 2.11. (A) DIAGRAM SHOWING FULL SCALE DIMENSIONS OF ARRAY (IN M); (B) SIGN CONVENTION OF NORMAL FORCE AND OVERTURNING MOMENT. EXTRACTED FROM WARSIDO ET AL., (2014)	35
FIGURE 2.12. PHOTOGRAPH OF GROUND MOUNTED PANELS CONFIGURATION. 13 ROWS \times 3 COLUMNS. EXTRACTED FROM WARSIDO ET AL. (2014).....	36
FIGURE 2.13. VARIATION OF PEAK (A) NORMAL FORCE AND (B) OVERTURNING MOMENT COEFFICIENTS WITH WIND DIRECTION. SPACING BETWEEN ROWS, $s = 1.22$ m (FULL SCALE). EXTRACTED FROM WARSIDO ET AL. (2014).....	37
FIGURE 2.14. STABILITY DIAGRAM. (A) CONCEPTUAL DIAGRAM. (B) MODELS WITH DIFFERENT INERTIA. (C) MODELS WITH DIFFERENT ASPECT RATIO	41
FIGURE 2.15. SOLAR PANEL ARRAYS. GEOMETRY CHARACTERISTICS AND PRESSURE ZONES FOR THE APPLICATION OF AS/NZS 1170.2 (2021). EXTRACTED FROM AS/NZS 1170.2 (2021).....	47
FIGURE 2.16. PARAMETERS FOR APPLICATION OF GROUND-MOUNTED FIXED-TILT SOLAR PANEL SYSTEMS REQUIREMENTS. EXTRACTED FROM ASCE 7-22 (2022)	50
FIGURE 3.1. ATMOSPHERIC BOUNDARY LAYER WIND TUNNEL: (A) TURNTABLE AND DOWNSTREAM END. (B) TURNTABLE AND UPSTREAM FETCH. (C) SCHEMATIC DIAGRAM OF THE WIND TUNNEL.....	54
FIGURE 3.2. (A) MEAN VELOCITY AND (B) TURBULENCE INTENSITY PROFILES OF THE ATMOSPHERIC BOUNDARY LAYER SIMULATED AT A LENGTH SCALE OF $1/20$ IN THE WIND TUNNEL. (C) POWER SPECTRAL DENSITY AT THE HEIGHT OF THE TORQUE TUBE h , 2 M (100 MM MODEL SCALE)	55
FIGURE 3.3. RIGID MODEL ATTACHED TO TURNTABLE IN THE WIND TUNNEL ($\alpha = 20^\circ$, $\theta = 60^\circ$).....	57
FIGURE 3.4. DIAGRAM OF A TYPICAL MODULE CONSISTING OF SIXTEEN PANELS.....	58
FIGURE 3.5. PROTOTYPE SOLAR TRACKER ARRAY. A) SIDE VIEW AND B) TOP VIEW	61
FIGURE 3.6. PROTOTYPE COMPONENTS: A) SOLAR PANEL, AND B) OMEGA SECTION RAIL (CROSS-SECTION VIEW)	62

FIGURE 3.7. GENERAL VIEW OF THE MODEL AND ADAPTER	68
FIGURE 3.8. MOMENT RESPONSE VS TIME. MODELS I-A, I-B AND I-C	69
FIGURE 3.9. MOMENT RESPONSE VS TIME. MODELS II-A AND II-B	70
FIGURE 3.10. SCHEMATIC DIAGRAM OF THE AEROELASTIC MODEL IN THE WIND TUNNEL, REPRESENTING ALL FIVE MODELS.....	72
FIGURE 3.11. SET UP IN THE WIND TUNNEL. A) MODEL I-C AT $A = 0^\circ$, AND $\Theta = 0^\circ$; B) MODEL I-B AT TILT ANGLE $A = 50^\circ$, AND $\Theta = 70^\circ$	73
FIGURE 3.12. MOMENT AND WIND SPEED TIME-HISTORY OF MODEL I-C, AT $A = 10^\circ$, AND Θ $= 0^\circ$	76
FIGURE 4.1. MEAN PRESSURE DISTRIBUTION ON TOP AND BOTTOM SURFACES OF INCLINED PANELS AND MOMENT ABOUT THE AXIS	79
FIGURE 4.2. MEAN, MAXIMUM AND MINIMUM MOMENT COEFFICIENTS OBTAINED USING THE 1/20 SCALE RIGID MODEL FOR (A) $A = 0^\circ$, (B) $A = 20^\circ$, AND (C) $A = 30^\circ$	80
FIGURE 4.3. MEAN, MAXIMUM AND MINIMUM MOMENT COEFFICIENTS VS WIND DIRECTION (Θ), AT $A = 0^\circ$ AND, MODEL SCALE MEAN WIND SPEED $U_h = 7.5$ M/S. (A) MODEL II-A ($l/b = 4$), AND (B) MODEL I-C ($l/b = 8$)	82
FIGURE 4.4. MEAN, MAXIMUM AND MINIMUM MOMENT COEFFICIENTS VS WIND DIRECTION (Θ), AT $A = 10^\circ$ AND, MODEL SCALE MEAN WIND SPEED $U_h = 7.5$ M/S. (A) MODEL II-A ($l/b = 4$), AND (B) MODEL I-C ($l/b = 8$)	83
FIGURE 4.5. MEAN, MAXIMUM AND MINIMUM MOMENT COEFFICIENTS VS WIND DIRECTION (Θ), AT $A = 20^\circ$ AND, MODEL SCALE MEAN WIND SPEED $U_h = 7.5$ M/S. (A) MODEL II-A ($l/b = 4$), AND (B) MODEL I-C ($l/b = 8$)	84
FIGURE 4.6. MEAN, MAXIMUM AND MINIMUM MOMENT COEFFICIENTS VS WIND DIRECTION (Θ), AT $A = 30^\circ$ AND, MODEL SCALE MEAN WIND SPEED $U_h = 7.5$ M/S (MODEL SCALE). (A) MODEL II-A ($l/b = 4$), AND (B) MODEL I-C ($l/b = 8$).....	85
FIGURE 4.7. MEAN, MAXIMUM AND MINIMUM MOMENT COEFFICIENTS VS WIND DIRECTION (Θ), AT $A = 40^\circ$ AND, MODEL SCALE MEAN WIND SPEED $U_h = 7.5$ M/S (MODEL SCALE). (A) MODEL II-A ($l/b = 4$), AND (B) MODEL I-C ($l/b = 8$)	86
FIGURE 4.8. MEAN, MAXIMUM AND MINIMUM MOMENT COEFFICIENTS VS WIND DIRECTION (Θ), AT $A = 50^\circ$ AND, MODEL SCALE MEAN WIND SPEED $U_h = 7.5$ M/S. (A) MODEL II-A ($l/b = 4$), AND (B) MODEL I-C ($l/b = 8$).....	87

FIGURE 4.9. MEAN MOMENT COEFFICIENT CM VS TILT ANGLE A , FOR (A) $0^\circ < \theta < 40^\circ$, (B) $50^\circ < \theta < 130^\circ$, AND (C) $140^\circ < \theta < 180^\circ$. THE STANDARD DEVIATION IS SHOWN AS A GREY SHADE. MODEL I-C	90
FIGURE 4.10. REDUCED CRITICAL WIND SPEED U_{red} VS TILT ANGLE (A) MEASURED ON (A) MODEL I-B, (B) MODEL I-C, AND (C) MODEL II-B. APPROXIMATE CURVE SHOWN AS A LINE. EXPECTED TREND SHOWN WITH DASHED LINE.....	94
FIGURE 4.11. CRITICAL WIND SPEED FOR OBLIQUE WINDS. (A) MODEL I-B ($L/B = 6$) AND (B) MODEL I-C ($L/B = 8$).....	96
FIGURE 4.12. MEAN MOMENT COEFFICIENTS AND MEAN WIND SPEED IN 10-SECOND TIME STEPS LEADING UP TO INSTABILITY. MODEL I-C, $A = 20^\circ$	98
FIGURE 4.13. (A) MOMENT VS TIME BEFORE THE ONSET OF TORSIONAL GALLOPING. (B) MOMENT VS TIME DURING TORSIONAL GALLOPING, MODEL I-C, $A = 20^\circ$, AND $\theta = 10^\circ$	99
FIGURE 4.14. POWER SPECTRAL DENSITY OF THE WIND SPEED AND MOMENT (A) BEFORE TORSIONAL GALLOPING, AND (B) DURING TORSIONAL GALLOPING. MODEL I-C, $A = 20^\circ$, AND $\theta = 10^\circ$	101
FIGURE 4.15. MEAN MOMENT COEFFICIENTS AND MEAN WIND SPEED VS TIME, LEADING UP TO DIVERGENCE. MODEL I-C AT $A = 0^\circ$	102
FIGURE 4.16. MOMENT AND WIND SPEED TIME-HISTORY DURING CRITICAL WIND SPEED TEST. MODEL I-C AT $A = 0^\circ$ AND $\theta = 0^\circ$	104
FIGURE 4.17. (A) EFFECTIVE DAMPING VS REDUCED WIND SPEED AND, (B) EFFECTIVE STIFFNESS VS REDUCED WIND SPEED, FOR $\theta = 0^\circ$. MODEL I-C	107
FIGURE 4.18. (A) EFFECTIVE DAMPING VS REDUCED WIND SPEED AND, (B) EFFECTIVE STIFFNESS VS REDUCED WIND SPEED, FOR $\theta = 180^\circ$. MODEL I-C	108
FIGURE 4.19. VARIATION OF AERODYNAMIC DERIVATIVE $A2^*$ WITH WIND SPEED	110
FIGURE 4.20. AERODYNAMIC DERIVATIVE $A2^*$ VS REDUCED WIND SPEED U_{red} , FOR $\theta = 0^\circ$ AND (A) $A = 5^\circ, 10^\circ$ AND (B) $A = 15^\circ, 20^\circ$. MODEL I-C.....	112
FIGURE 4.21. AERODYNAMIC DERIVATIVE $A2^*$ VS REDUCED WIND SPEED U_{red} , FOR $\theta = 180^\circ$ AND (A) $A = 0^\circ, 5^\circ, 10^\circ$ AND (B) $A = 15^\circ, 20^\circ, 25^\circ$. MODEL I-C.....	113
FIGURE 4.22. AERODYNAMIC DERIVATIVE $A3^*$ VS REDUCED WIND SPEED U_{red} , FOR (A) $\theta = 0^\circ$ AND (B) $\theta = 180^\circ$. MODEL I-C	115

FIGURE 4.23. (A) MOMENT RESPONSE AND (B) AUTOCORRELATION, BEFORE INSTABILITY. MODEL I-C, $\alpha = 20^\circ$ AND $\theta = 0^\circ$	119
FIGURE 4.24. (A) MOMENT RESPONSE AND (B) AUTOCORRELATION, APPROACHING INSTABILITY. MODEL I-C, $\alpha = 20^\circ$ AND $\theta = 0^\circ$	120
FIGURE 4.25. (A) MOMENT RESPONSE AND (B) AUTOCORRELATION, DURING INSTABILITY. MODEL I-C, $\alpha = 20^\circ$ AND $\theta = 0^\circ$	121
FIGURE 4.26. AERODYNAMIC DERIVATIVE $A2^*$ VS REDUCED WIND SPEED U_{red} . COMPARISON BETWEEN AUTOCORRELATION (AC) AND QUASI-STEADY APPROXIMATION (QS). MODEL I-C, $\alpha = 0^\circ$ AND $\theta = 0^\circ$	124
FIGURE 4.27. AERODYNAMIC DERIVATIVE $A2^*$ VS REDUCED WIND SPEED U_{red} . COMPARISON BETWEEN AUTOCORRELATION (AC) AND QUASI-STEADY APPROXIMATION (QS). MODEL I-C, $\alpha = 5^\circ$ AND $\theta = 0^\circ$	124
FIGURE 4.28. AERODYNAMIC DERIVATIVE $A2^*$ VS REDUCED WIND SPEED U_{red} . COMPARISON BETWEEN AUTOCORRELATION (AC) AND QUASI-STEADY APPROXIMATION (QS). MODEL I-C, $\alpha = 15^\circ$ AND $\theta = 0^\circ$	125
FIGURE 4.29. AERODYNAMIC DERIVATIVE $A2^*$ VS REDUCED WIND SPEED U_{red} . COMPARISON BETWEEN AUTOCORRELATION (AC) AND QUASI-STEADY APPROXIMATION (QS). MODEL I-C, $\alpha = 20^\circ$ AND $\theta = 0^\circ$	125
FIGURE 5.1. MULTI-row CONFIGURATION, COMPRISING TWO ROWS WITH INSTRUMENTED AEROELASTIC MODELS AND A THIRD ROW WITH AN UNINSTRUMENTED AEROELASTIC MODEL	132
FIGURE 5.2. CONFIGURATIONS C1 AND C2 OF MULTIPLE ARRAYS TESTED IN THE WIND TUNNEL.....	133
FIGURE 5.3. MEAN MOMENT COEFFICIENT CM VS WIND DIRECTION θ . UNCERTAINTY IS PLOTTED AS A GREY SHADE. ROW 1 AND ROW 2 (C1), $\alpha = 10^\circ$	134
FIGURE 5.4. MEAN MOMENT COEFFICIENT CM VS WIND DIRECTION (θ). UNCERTAINTY IS PLOTTED AS A GREY SHADE. ROW 1 AND ROW 2 (C1), $\alpha = 20^\circ$	135
FIGURE 5.5. MEAN MOMENT COEFFICIENT CM VS WIND DIRECTION (θ). UNCERTAINTY IS PLOTTED AS A GREY SHADE. ROW 2 AND ROW 3 (C2), $\alpha = 10^\circ$	136
FIGURE 5.6. MEAN MOMENT COEFFICIENT CM VS WIND DIRECTION θ . UNCERTAINTY IS PLOTTED AS A GREY SHADE. ROW 2 AND ROW 3 (C2), $\alpha = 20^\circ$	137

FIGURE 5.7. FLUCTUATING MOMENT VS TIME OF (A) ROW 1, AND (B) ROW 2 (C1). MODEL I-B, $A = 10^\circ$ AND $\Theta = 0^\circ$. $U_{cr} = 11.4 \text{ m/s}$ (WIND SPEED IN MODEL SCALE)	138
FIGURE 5.8. FLUCTUATING MOMENT VS TIME OF (A) ROW 1, AND (B) ROW 2. CONFIGURATION 1. MODEL I-B, $A = 10^\circ$ AND $\Theta = 20^\circ$. $U_{cr} =$ 13.1 m/s (WIND SPEED IN MODEL SCALE).....	139
FIGURE 5.9. FLUCTUATING MOMENT VS TIME OF (A) ROW 1, AND (B) ROW 2 (C1). MODEL I-B, $A = 10^\circ$ AND $\Theta = 160^\circ$. $U_{cr} = 11.2 \text{ m/s}$ (MODEL SCALE).....	140
FIGURE 5.10. FLUCTUATING MOMENT VS TIME OF (A) ROW 1, AND (B) ROW 2 (C1). MODEL I-B, $A = 10^\circ$ AND $\Theta = 180^\circ$. $U_{cr} = 9.0 \text{ m/s}$ (MODEL SCALE).....	140
FIGURE 5.11. FLUCTUATING MOMENT VS TIME OF (A) ROW 2, AND (B) ROW 3 (C2). MODEL I-B, $A = 10^\circ$ AND $\Theta = 0^\circ$. $U_{cr} = 11.6 \text{ m/s}$ (WIND SPEED IN MODEL SCALE).....	141
FIGURE 5.12. FLUCTUATING MOMENT VS TIME OF (A) ROW 2, AND (B) ROW 3 (C2). MODEL I-B, $A = 10^\circ$ AND $\Theta = 180^\circ$. $U_{cr} = 11.3 \text{ m/s}$ (WIND SPEED IN MODEL SCALE).....	142
FIGURE 5.13. POWER SPECTRAL DENSITY OF THE MOMENT, $A = 10^\circ$, $\Theta = 0^\circ$. ROW 1 AND ROW 2 (C1), DURING GALLOPING.....	143
FIGURE 5.14. POWER SPECTRAL DENSITY OF THE MOMENT, $A = 10^\circ$, $\Theta = 20^\circ$. ROW 1 AND ROW 2 (C1), STABLE CONDITION	144
FIGURE 5.15. POWER SPECTRAL DENSITY OF THE MOMENT, $A = 10^\circ$, $\Theta = 40^\circ$. ROW 1 AND ROW 2 (C1), STABLE CONDITION	145
FIGURE 5.16. POWER SPECTRAL DENSITY OF THE MOMENT, $A = 10^\circ$, $\Theta = 160^\circ$. ROW 1 AND ROW 2 (C1), DURING INSTABILITY	146
FIGURE 5.17. POWER SPECTRAL DENSITY OF THE MOMENT, $A = 10^\circ$, $\Theta = 180^\circ$. ROW 1 AND ROW 2 (C1), DURING INSTABILITY	146

LIST OF SYMBOLS

Roman Symbols

A	Area of the panel / plate	[m ²]
A_2^*	Aerodynamic derivative associated to aerodynamic damping	[-]
A_3^*	Aerodynamic derivative associated to aerodynamic stiffness	[-]
b	Panel breadth/ plate chord length	[m]
b_p	Breadth of the prototype panels	[m]
$C_{(\tau)}$	Autocorrelation of the moment response	[-]
c_0	Structural damping	[Nm/s]
c_{eff}	Effective damping	[Nm/s]
C_{p_n}	Net pressure coefficient	[-]
C_F	Net force coefficient	[-]
C_{FX}	Net horizontal force coefficient	[-]
C_{FZ}	Net vertical force coefficient	[-]
C_M	Moment coefficient	[-]
C_{shp}	Aerodynamic shape factor	[-]
D_{0p}	External diameter of the prototype torque tube	[m]
D_{ip}	Internal diameter of the prototype torque tube	[m]
d	Thickness of the flat plate	[m]
d_p	Thickness of the prototype panels	[m]
E	Young's modulus	[Pa]
$(EI)_r$	Bending stiffness ratio	[-]
F_N	Wind-induced net force acting on the plate	[N]
F_Z	Wind-induced vertical force	[N]

F_x	Wind-induced horizontal force	[N]
f	Wind speed frequency	[Hz]
f_0	Torsional natural frequency	[Hz]
f_{0eff}	Effective torsional natural frequency	[Hz]
f_v	Vortex shedding frequency	[Hz]
G	Shear modulus	[Pa]
$(GJ)_r$	Shear stiffness ratio	[-]
I_u	Longitudinal turbulence intensity	[%]
I_0	Polar mass moment of inertia	[kgm ²]
J_0	Polar second moment of area	[m ⁴]
k_0	Structural (torsional) stiffness	[Nm]
k_{eff}	Effective stiffness	[Nm]
K	Reduced frequency	[-]
L_r	Length ratio	[-]
l	Span of the solar tracker / Length of the torque tube	[m]
M	Aerodynamic moment	[Nm]
m_r	Mass ratio	[-]
p_n	Net wind pressure	[Pa]
p_t	Pressure acting on top surface of the panel/ plate	[Pa]
p_b	Pressure acting on bottom surface of the panel/ plate	[Pa]
S_u	Spectral density of the longitudinal wind speed	[m ² /s]
St	Strouhal number	[-]
t	Time	[s]
T_r	Time ratio	[-]
U	Horizontal component of wind speed	[m/s]
U_{cr}	Critical wind speed	[m/s]

U_{red}	Reduced wind speed	[-]
U_r	Wind speed ratio	[-]
\bar{U}_z	Mean wind speed at height z	[m/s]
\bar{U}_h	Wind speed at the model torque tube middle height	[m/s]

Greek Symbols

α	Tilt angle	[°]
γ	Angle of twist	[°]
ζ_0	Damping ratio	[-]
θ	Wind direction	[°]
ρ	Air density	[kg/m ³]
σ_u	Standard deviation of the wind speed	[m/s]
τ	Time lag	[s]



1 INTRODUCTION

Solar trackers are used extensively in the industry for large solar power generation plants. Their efficiency to produce solar energy is given by its capacity to track the sun during the day, thus increasing energy output up to 30% when compared to fixed-frame solar panels.

Increasing popularity of solar energy generation has prompted research on wind loading of ground mounted solar panel systems, requiring structural design methods for large solar energy projects. Originally, ground-mounted systems consisted of solar panels supported by a fixed-tilt angle frame, as shown in Figure 1.1.



Figure 1.1. Ground-mounted fixed-tilt solar panel system

However, in recent years solar trackers have become an option that increases the power generation efficiency. In these systems, solar panels are attached to rails that are fixed on to a horizontal axis, commonly defined as the torque tube, as shown in Figure 1.2, allowing the system to rotate and seek sunlight, thus increasing energy output.



Figure 1.2. Single axis solar tracker arrays

The tracking ranges from a tilt angle $\alpha = 0^\circ$, traditionally described as the stow position, up to 60° . The torque tube is supported by posts along the span, as shown in Figure 1.3. The cross-section of the tube is typically hollow circular, rectangular, or hexagonal. It is supported at the posts by bearings. The posts are fixed to the ground acting as driven piles, or with ground screws or concrete strips.

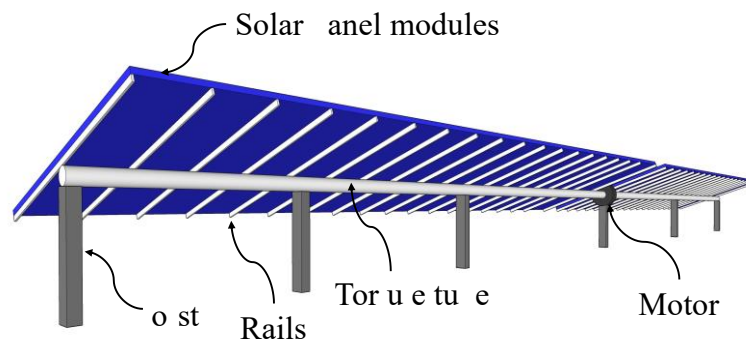


Figure 1.3. Solar tracker components

Solar trackers are active systems that use motors and gear trains to direct the tracker as commanded by a control unit that responds to the position of the sun. The gear or torque motor is commonly placed in the middle of the span, although there are systems which use a torque motor located in one of the endpoints of the torque tube.

Given their structural configuration, these systems can be structurally analysed as axially supported flat plates. In such structures the axis is constrained, allowed to rotate

but fixed at one end. The parameters of interest for this study are the length of the array l , breadth of the plate b , aspect ratio l/b , thickness of the plate d , tilt angle α (measured from the horizontal to the surface of the plate), and the height from the ground to the centre of the torque tube, h . A group of arrays are separated a distance, s from each other. Additionally, wind direction is indicated by the angle θ , as shown in Figure 1.4.

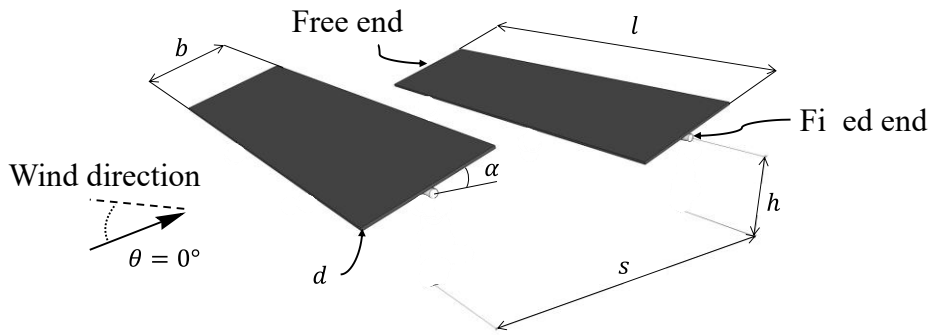


Figure 1.4. Schematic diagram of an axially supported solar tracker

1.1 Structural failure of solar trackers

Solar trackers consist of lightweight and slender components which may experience dynamic excitation due to wind action. These effects can influence their structural stability eventually causing structural failure. An example of structural failure is shown in the photo of Figure 1.5. Being a flexible structure, that is allowed to rotate about the torque tube, solar trackers are subjected to dynamic torsional effects such as vortex-induced vibrations, and aeroelastic instabilities such as torsional flutter. These effects are further explained in Chapter 2.



Figure 1.5. Solar tracker after failure. Oakey 2 Solar Farm. Oakey, Queensland, Australia (extracted from Gifford (2019))

An investigation by Valentín et al. (2022) analysed the catastrophic failure of a single-axis solar tracker due to wind-induced torsional flutter, which can be seen in Figure 1.6. The authors combined on-site damage observations with numerical modelling to identify the failure mechanisms and critical factors involved. Their study highlighted the detrimental effects of galloping instability, particularly the plastic deformation of the torque tube and the separation of solar panels. The numerical model confirmed the torsional vibrations as the primary contributor to the failure, emphasizing the importance of considering dynamic wind effects in the design and operation of solar trackers. They recommended increasing torsional stiffness, optimizing tilt angle control strategies,

and implementing real-time monitoring systems to mitigate the risk of torsional galloping-induced failures.



Figure 1.6. Solar tracker failure. Case study. (Extracted from Valentín et al., (2022))

1.2 Studies on solar trackers

The study of aeroelastic instabilities in solar trackers has gained significant attention in recent years, driven by the need to ensure the structural integrity and performance of these systems under varying environmental conditions. A key focus has been on understanding torsional flutter. Rohr et al. (2015) initiated early efforts by combining Computational Fluid Dynamics (CFD) with experimental validation to model the fluid-structure interaction of single-axis solar trackers. Their work established a theoretical framework for predicting the critical wind speed, U_{cr} at which torsional

galloping is initiated. The study provided practical design recommendations, such as increasing torsional stiffness or incorporating damping systems, to mitigate torsional galloping.

Taylor and Browne (2020) explored wind loads on multi-row solar tracker arrays using wind tunnel tests and sectional models. Their research revealed that traditional methods for estimating wind loads, based on dynamic amplification factors, often fail to capture the complex aeroelastic behaviour of solar trackers. Specifically, they demonstrated that self-excited forces at high wind speeds can produce peak moments far exceeding those predicted by conventional approaches.

The influence of tilt angle (α) on torsional flutter was further investigated by Martínez-García et al. (2021). Through aeroelastic model tests, they developed a Stability Diagram that maps the critical wind speed U_{cr} for different tilt angles and normal wind directions ($\theta = 0^\circ$ and 180°).

The influence of turbulence intensity on solar trackers were investigated by Zhang et al. (2023), who conducted wind tunnel experiments under varying turbulence levels. Their findings highlighted that higher turbulence significantly amplifies the oscillations associated with torsional flutter, emphasizing the importance of considering realistic wind conditions in stability analyses.

Enshaei et al. (2023) focused on low-tilt scenarios ($\alpha = 0^\circ$). Using analytical models, they demonstrated that structural damping has minimal impact on U_{cr} at small tilt angles, suggesting that other factors, such as aerodynamic stiffness, dominate in these conditions.

Cárdenas-Rondón et al. (2023) contributed to the field by studying the aerodynamic stability of a flat-plate solar tracker and analysing aerodynamic derivatives to assess stability. Their work introduced a method for calculating the effective damping coefficient as a function of wind speed, revealing that U_{cr} varies with the tracker's height h .

More recently, Taylor et al. (2024) provided a comprehensive analysis of aeroelastic instability mechanisms, differentiating between stiffness-driven (torsional divergence) and damping-driven (torsional galloping) instabilities. By introducing the concept of "structurally averaged gust speed," they highlighted the sensitivity of solar trackers to turbulent gusts, offering valuable validation for numerical models and deeper insights into the factors influencing stability.

Rodríguez-Casado et al. (2024) addressed the need for standardized experimental methodologies by proposing a benchmark model for wind tunnel testing. Their work emphasized the influence of tilt angle on U_{cr} and highlighted discrepancies in existing stability diagrams, underscoring the importance of consistent testing protocols. While their benchmark represents a significant step forward, they acknowledged the need to extend it to multi-row configurations and more realistic turbulence conditions.

Collectively, these studies have advanced our understanding of solar tracker instabilities, yet critical gaps remain. The influence of terrain characteristics, approach wind direction and multi-row interactions, among other factors, warrant further investigation. This thesis seeks to build on these foundations by addressing these gaps and contributing to the development of more robust and reliable solar tracking systems.

1.3 Aims and objectives

This thesis studied the behaviour of solar trackers in their usual environment. To achieve this, several aeroelastic models were tested in the wind tunnel, simulating terrain conditions typical of the sites where they are usually located: approach turbulent flows and oblique wind directions.

The models were designed based on typical components used by industry, simulating the variables of interests such as the structural stiffness, the damping ratio, the natural frequency, and the inertia. This was achieved by varying the length of the models (i.e. increasing the aspect ratio) and using different cross sections to model the torque tube. Additionally, a series of arrays were tested together to evaluate the effects of spacing and shielding.

Currently, there is a lack of widely available scientific literature regarding the causes of failure in solar trackers due to confidentiality and commercial sensitivities. This scarcity has also been noted by Cárdenas-Rondón (2023). Therefore, this thesis aims to contribute to the understanding of solar tracker behaviour under on-site conditions.

Hence, based on the research gaps identified for the response of solar trackers, the objectives of this thesis are to:

- Obtain the fluctuating wind loads on typical solar trackers within a range of tilt angle (α), for different approach wind directions (θ).
- Define the properties of the solar tracker (i.e. tilt angle, damping, stiffness) and wind characteristics (speed, direction) that instigate instabilities.
- Describe the aerodynamic loading on solar trackers before and during the onset of aeroelastic instabilities and define the mechanism causing them.

- Study the effects of oblique approach winds on solar tracker stability.
- Study the effect of adjacent rows of solar tracker arrays on their response.

The hypothesis of this thesis is that increased aspect ratios and reduced stiffness and damping in solar trackers will increase the susceptibility to aeroelastic instabilities for a range of tilt angles. These instabilities take place for a range of oblique approach wind directions in turbulence intensities commonly found in their operating environments.

1.4 Chapter content

Chapter 2 presents a review of the literature about wind loading on flat plates and solar panels, their dynamic response, and the theory of their aeroelastic instabilities (i.e. torsional flutter). In addition, computational modelling applications on solar trackers and the current scope of standards for designing solar panel structures are also presented.

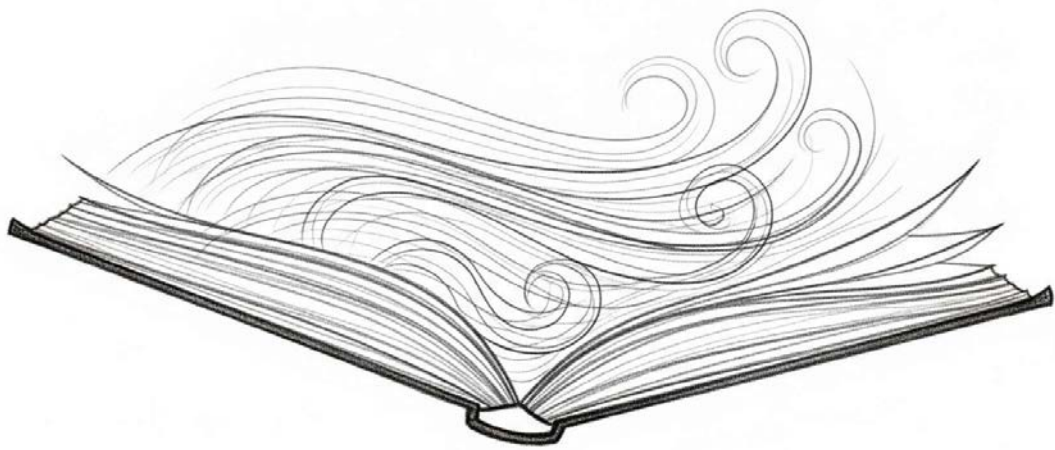
Chapter 3 details the methodology used in this study, including the wind tunnel and the simulated wind flow characteristics; the characteristics of prototypes of solar trackers used in this study; the design, construction, and structural parameters of the aeroelastic models (stiffness, damping, natural frequency, etc) used in this study; and the wind tunnel test procedures.

Chapter 4 presents the results obtained and the wind loading analysis (i.e. moment coefficients) for different tilt angles, wind speeds and wind directions. Wind loading induced by torsional flutter is characterised. The variation of the effective damping and effective stiffness against the wind speed is presented and the aerodynamic derivatives A_2^* and A_3^* are calculated and analysed for several wind directions and tilt angles. The results are also compared with other studies.

Chapter 5 presents the results of wind loading (i.e. moment coefficients) and aeroelastic instability on multiple arrays, considering several wind directions and tilt angles.

Chapter 6 presents the conclusions and relates them to the outcomes of the study. It also provides recommendations from this thesis.

Appendices provide supplementary information for Chapters 3 and 4.



2 LITERATURE REVIEW

This Chapter reviews the background theory related to flat plates subjected to wind loading. This includes the characteristics of wind flow, the characteristics of forces generated on the plates and the dynamic response associated with wind loading. Aeroelastic instabilities are described and the theory to evaluate them is presented. This is followed by a review of research on wind loading on ground-mounted solar panels. Additionally, the scope of wind loading standards are analysed to determine their applicability for the design of solar trackers. Gaps in the literature are identified and related to the objectives of this thesis.

2.1 Wind loads on a plate

A flat plate of length, l , breadth b (i.e. area, $A = l \cdot b$, and aspect ratio, l/b), tilt angle, α subjected to an approach velocity, U_h that varies with time, t is shown in Figure 2.1. The top and bottom surfaces of the plate will experience time-varying pressures $p_t(t)$, $p_b(t)$ respectively resulting in a net pressure $p_n(t) = p_t(t) - p_b(t)$. This pressure will produce a net load $F_N(t) = [p_t(t) - p_b(t)] \cdot A$, as well as the moment $M(t) = F_N(t) \cdot d'$ acting about the horizontal axis.

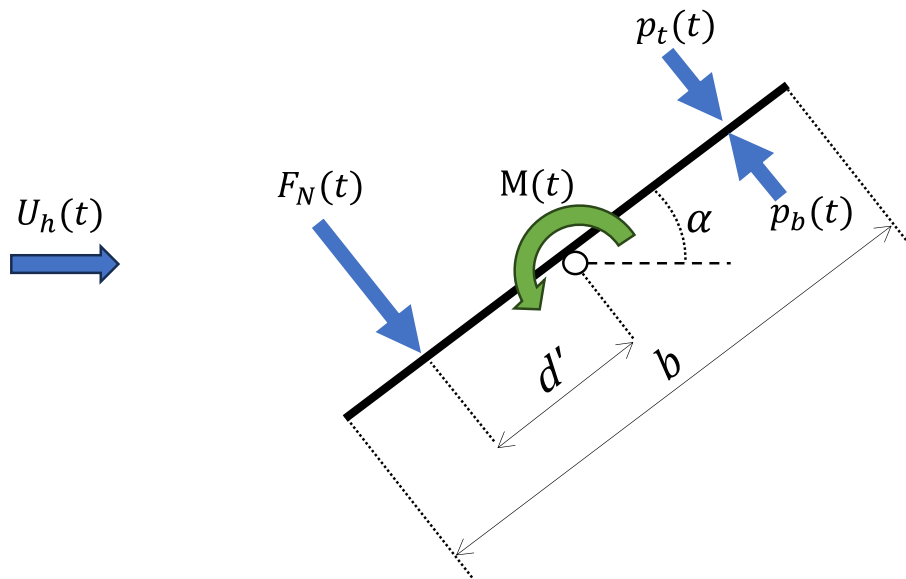


Figure 2.1. Loads on an axially supported flat plate exposed to wind flow

For $\alpha < 10^\circ$, ESDU (1970) specifies the normal force coefficient $C_{F_N} \cong 2\pi\alpha$, and the centre pressure near, one-quarter of the breadth b from the leading edge as shown in Figure 2.2. As the tilt angle, α increases, the normal force coefficient, C_{F_N} , progressively increases towards the normal plate case ($\alpha = 90^\circ$), with the centre of pressure at $0.5b$. According to Holmes and Bekele (2021), for $\alpha = 30^\circ$, the value of C_{F_N} and position of the line of action are about 1.2 and $0.38b$ respectively.

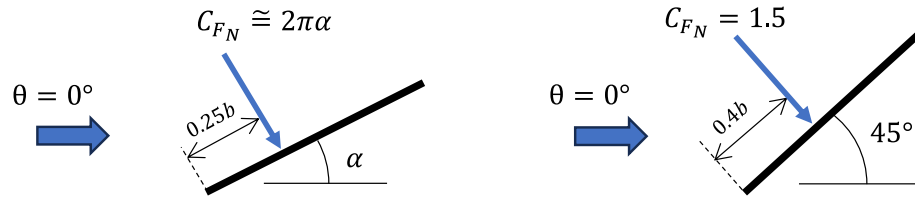


Figure 2.2. Normal force coefficient for an inclined plate

2.2 Dynamic response

The response of a plate to fluctuating wind pressures will depend on the structural properties and dimensions of the plate and support system. Fage and Johansen, (1927) examined the flow behind a plate inclined in an air stream and found that vortices generated at each edge pass downstream with a frequency f_v , which can be evaluated with the Strouhal number, $St = f_v b / \bar{U}_h$.

Chen and Fang, (1996) measured the frequencies of vortex shedding from flat plates at tilt angles ($0^\circ < \alpha < 90^\circ$). They found that for $\alpha = 0^\circ$ to 5° , St is sensitive to the Reynolds number, Re , due to flow reattachment. However, St was kept nearly constant at 0.160 ± 0.003 for $5^\circ < \alpha < 90^\circ$. Then, vortex-induced vibrations of the structure can occur if its natural frequency, f_0 matches the frequency of the vortex shedding, f_v .

In structures with shallow cross-sections, the thickness d is significantly smaller than the breadth b . Long-span bridges and solar trackers are examples of such structures. There are several cases of suspended bridges collapsing due to extreme torsional motion,

with the Tacoma Narrows Bridge failure being one of the most iconic. Farquharson et al., (1954) demonstrated that the collapse was due to severe torsional instability. Since then, torsional flutter has been studied extensively for bridge decks.

With regards of solar trackers, the case study presented by Valentín et al., (2022) is possibly the only scientific publication available addressing the failure of such structures due to dynamic instabilities, although anecdotal evidence also suggests that aeroelastic instabilities cause most typical failures.

The rotational motion of a plate supported axially by a tube (or rod), fixed at one end and free at the other end is shown in Figure 2.3. Here, γ is the angle of twist. I_0 is the polar mass moment of inertia about the centre of the axis, and is given by $I_0 = (I_{t_0} + I_{p_0} + m_p d_0^2)$; where I_{t_0} is the polar moment of inertia of the tube, I_{p_0} the polar moment of inertia of the plate and m_p the mass of the plate. The distance d_0 is measured from the centre of mass of the plate, C to the centre of the tube O. $c_0 = 2I_0\zeta_0(2\pi f_0)$, is the structural damping, where ζ_0 is the structural damping ratio and f_0 the torsional natural frequency. k_0 is the torsional stiffness of the tube.

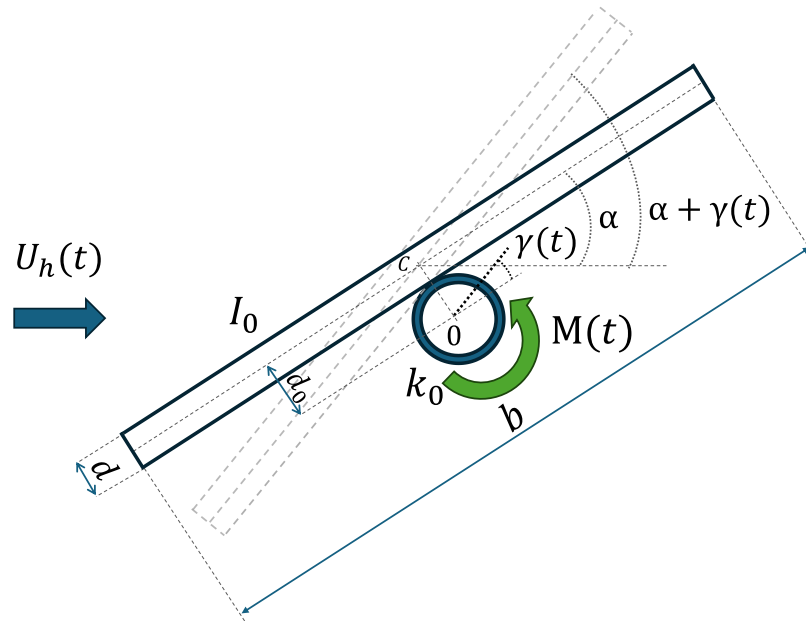


Figure 2.3. Response of an axially supported plate

The dynamic response can be described using the general equation of motion in torsion shown in Equation 2.1.

$$I_0 \frac{d^2\gamma}{dt^2} + c_0 \frac{d\gamma}{dt} + k_0\gamma = M(t) \quad 2.1$$

2.3 Torsional galloping and divergence

Torsional galloping is a form of single degree of freedom structural aerodynamic instability, which can occur in structures with a long-span. The use of lighter, more flexible components cause more frequent failures due to torsional galloping as reported by Slater (1969).

In torsional galloping, the tilt angle changes with the angle of twist, $\gamma(t)$ and with the angular velocity ($d\gamma/dt$). According to Blevins (1990, Chapter 4, p. 111) the vertical velocity component associated with the angular velocity ($d\gamma/dt$), modifies the effective angle of attack $[\alpha + \gamma(t)]$. Then $[\alpha + \gamma(t)] \simeq - (d\gamma/dt)b/4\bar{U}_h$, where the vertical velocity of the plate under rotational motion has been calculated at the quarter-chord point.

Therefore, the moment is, $M(t) \simeq -(\partial C_M/\partial\alpha)\frac{1}{2}\rho\bar{U}_h^2 b^2[\alpha + \gamma(t)]l$. So, replacing $[\alpha + \gamma(t)]$ in the expression gives, $M(t) = -(\partial C_M/\partial\alpha)\frac{1}{8}\rho\bar{U}_h b^3(d\gamma/dt)l$.

Then, applying this to Equation 2.1, gives:

$$I_0 \frac{d^2\gamma}{dt^2} + c_0 \frac{d\gamma}{dt} + k_0\gamma = -\left(\frac{\partial C_M}{\partial\alpha}\right)\frac{1}{8}\rho\bar{U}_h b^3 \frac{d\gamma}{dt} l \quad 2.2$$

This equation can be rearranged as shown by Blevins (1990),

$$I_0 \frac{d^2\gamma}{dt^2} + \left[c_0 + \left(\frac{\partial C_M}{\partial\alpha}\right)\frac{1}{8}\rho\bar{U}_h b^3 l \right] \frac{d\gamma}{dt} + \left[\left(k_0 - \left(\frac{\partial C_M}{\partial\alpha}\right)\frac{1}{2}\rho\bar{U}_h^2 b^2 l \right) \right] \gamma = 0 \quad 2.3$$

Here $\left[c_0 + \left(\frac{\partial C_M}{\partial\alpha}\right)\frac{1}{8}\rho\bar{U}_h b^3 l \right]$ is the *effective damping* c_{eff} , comprising structural damping, c_0 and the aerodynamic damping, $\left(\frac{\partial C_M}{\partial\alpha}\right)\frac{1}{8}\rho\bar{U}_h b^3 l$. The onset of torsional galloping happens when the effective damping is negative, which defines the critical velocity U_{cr} given in Equation 2.4, in a similar way to that obtained by Blevins (1990). From the effective damping expression, this is only possible if $(\partial C_M/\partial\alpha) < 0$.

$$U_{cr} \cong \frac{8c_0}{\left| \left(\frac{\partial C_M}{\partial \alpha} \right) \right| \rho b^3 l} \quad 2.4$$

Another term of interest in Equation 2.3 is $\left[\left(k_0 - \left(\frac{\partial C_M}{\partial \alpha} \right) \frac{1}{2} \rho \bar{U}_h^2 b^2 l \right) \right]$. This is the *effective stiffness* k_{eff} , comprising structural stiffness k_0 and the aerodynamic stiffness. A form of instability that can be derived from that term, is called torsional divergence. Bisplinghoff et al. (1996) describe it as a static instability of a lifting surface, where elasticity plays an essential role in the stability. This occurs if the effective stiffness falls to zero and is associated with tilt angles $\alpha \approx 0^\circ$.

Similar to U_{cr} , Blevins (1990) proposes an expression of the wind speed, U_d at which divergence can happen. This is derived from the steady equation of motion (i.e., neglecting the time derivative terms): $U_d = \sqrt{2k_0 / (\pi \rho b^2 / 4)}$.

Then, from the effective stiffness term in Equation 2.3, a similar expression can be obtained:

$$U_d \cong \sqrt{\frac{2k_0}{\rho b^2 l \left| \left(\frac{\partial C_M}{\partial \alpha} \right) \right|}} \quad 2.5$$

According to Taylor et al. (2024), it is unclear to which averaging period the critical wind speed corresponds. In the case of bridges, the critical wind speed is considered as the 10-min mean wind speeds due to the observed build-up period of aerodynamic instabilities. This is also related to bridges in low turbulence wind tunnel conditions. However, solar trackers are significantly smaller and lighter than bridges and they are installed in the most turbulent part of the atmospheric boundary layer. Therefore, Taylor et al., (2024)

analysed the concept of *structurally averaged peak gust speed* to define the critical wind speed. The build-up time of the instability is of fundamental importance. The number of cycles required for the development of aerodynamic instabilities has not received much attention and the experiments required are challenging to define in terms of the use of steady flow versus turbulent flow conditions as well as steady versus accelerating flows. However, for the across-wind galloping instability, Parkinson and Smith (1964) estimated the number of cycles for development of the instability to be approximately 300. The studies of Pigolotti et al., (2017) and Taylor et al., (2010) on the flutter of rectangular cylinders suggests the required number of cycles to be on the order of 50 to 200. A steady flow examination of the build-up of cycles for vortex-induced oscillations of a circular cylinder showed the number can be more than 1000 cycles (Dallaire, 2010). Taylor et al., (2024) experience with single-axis solar trackers demonstrated that dynamic oscillations could result due to the stiffness-driven instability. In this case it has been observed that only a few cycles are necessary. They have assumed that 10 cycles were reasonable for a range of tilt angles. However, Taylor et al., (2024) acknowledged the number of cycles for instability could vary depending on the torque tube elevation, structural damping, aspect ratio, etc.

2.4 Flutter

Bisplinghoff et al., (1983) describe flutter as the dynamic instability of an elastic body in an airstream. It is mostly encountered on bodies such as aircraft wings that are subjected to large lateral aerodynamic loads. Blevins (1990) analyses galloping and flutter together and states that differences in usage of the terms is largely based on the industry. Flutter is aerospace terminology for coupled torsion-plunge instability of airfoils, whereas galloping is the term favoured by civil engineers for one-degree-of-freedom instability of bluff structures in winds and currents.

Wardlaw (1994) noted that the term flutter derives from aeronautical practices, where it is used to describe an aeroelastic instability in coupled torsion and vertical bending of aircraft wings. However, when referring to road decks of long span bridges, a difference is stated in terms of a related (to flutter) oscillatory response of the structure and a single-degree-of-freedom torsional instability.

Holmes and Bekele (2001) describe flutter as a dynamic response involving a structure that is able to move, with elastic restraint, in both vertical translation and rotation. They defined galloping as a form of single degree of freedom aerodynamic instability, such as the seen in single axis solar trackers studied in this thesis.

Dowell (2015) describes flutter as a motion that involves heaving or (bending) vertical displacement as well as a rotational/torsional motion. Furthermore, the phenomenon of “stall flutter” occurs with a partial or complete separation periodically of the flow from the airfoil during its oscillation. This requires large incidence angles (i.e. tilt) to induce separation of the flow. Additionally, the essential feature of stall flutter is the nonlinear aerodynamic response to the motion of the airfoil or structure.

The industry and some design engineers use the term “torsional instabilities” to describe aeroelastic instabilities on solar trackers. Additionally, terms such as “torsional galloping” and “torsional divergence” describe the characteristic failure mode of solar trackers, although the latter is less cited (Enshaei et al., (2023)).

The term “flutter” is used in the analysis of airfoils and ridges, that are subjected vertical and rotational displacements. Single axis solar trackers are a different type of structure, as described as described in Chapter 1 and Section 2.2, where the structural response is analysed by the moment acting on the torque tube and its twist. Further differences between the aerodynamic and structural conditions on solar trackers and bridges are discussed in Section 2.5.

The term “stall flutter” is sometimes used by researchers and academics to describe aeroelastic instabilities observed in solar trackers. This terminology appears in publications such as Martínez-García et al, (2021), Cárdenas-Rondón et al, (2023), Cárdenas-Rondón et al, (2024) and Rodríguez-Casado et al. (2024).

In this Thesis when referring generally to the aeroelastic instabilities on solar tracker, the term “torsional flutter” may be used as per Nakamura and Miota (1975), and Nakamura (1979) definition. However, in order to facilitate the description of the mechanisms involved in the onset of aeroelastic instabilities, the terms “torsional galloping” and “torsional divergence” will be applied, as per Blevins (1990) definitions.

2.5 Aerodynamic derivatives

Theodorsen (1935) developed a rigorous theoretical framework for calculating unsteady lift and moment on a thin airfoil undergoing harmonic oscillations (i.e. $\zeta_0 = 0$) within a fluid flow at very small tilt angle ($\alpha \approx 0^\circ$). The Theodorsen function is instrumental for analysing aeroelastic instabilities in structures like airfoils.

In the wind loading of bridges, the self-excited terms are generally represented by *aerodynamic derivatives* defined by Scanlan and Tomko (1971). They compared the Theodorsen function, related to a theoretical totally undamped system, with the aerodynamics of a system oscillating with exponential decay, typical of bridges. They obtained the so-called *modified Theodorsen functions* which can be applied to structures with damping ratio $\zeta_0 > 0$. The Theodorsen circulatory function and its variation for different values of ζ_0 are shown in Figure 2.4.

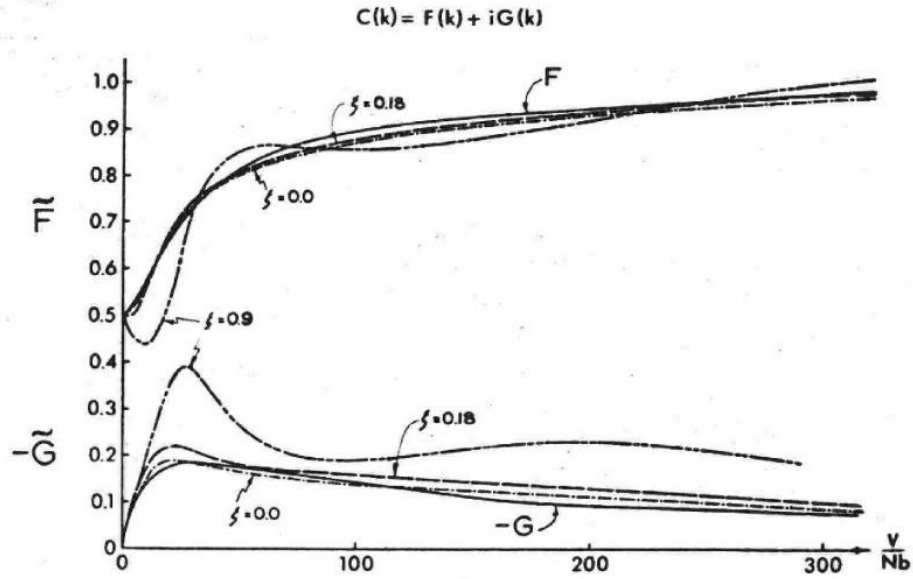


Figure 2.4. Theodorsen circulatory function for different values of damping ratio.

Extracted from Scanlan and Tomko (1971)

The aerodynamic moment acting on a solar tracker can be described in terms of the aerodynamic derivatives, using Scanlan and Tomko (1971) formulation, as shown in Equation 2.6.

$$M(t) = \frac{1}{2} \rho \bar{U}_h^2 b^2 \left[\frac{KA_2^* b}{\bar{U}_h} \left(\frac{d\gamma}{dt} \right) + K^2 A_3^* \gamma \right] l \quad 2.6$$

Where $K = f_0 b / \bar{U}_h$ is the reduced frequency of the structure.

Analysing the terms in brackets in Equation 2.6, the term $\frac{KA_2^* b}{\bar{U}_h} \left(\frac{d\gamma}{dt} \right)$ relates to the aerodynamic damping, and the term $K^2 A_3^* \gamma$ to the aerodynamic stiffness. An

expression for A_2^* can be obtained by comparing the equivalent terms in Equations 2.3 and 2.6. Therefore, $\frac{1}{2}\rho\bar{U}_h b^3 K A_2^* = -\left(\frac{\partial C_M}{\partial \alpha}\right)\frac{\rho\bar{U}_h b^3}{8}$. This gives a quasi-steady definition for A_2^* , as shown in Equation 2.7.

$$A_2^* \approx -\frac{U_{red}}{4\pi} \left(\frac{\partial C_M}{\partial \alpha}\right) \quad 2.7$$

Where, $U_{red} = \bar{U}_h / f_0 b$, is the reduced wind speed.

The value of A_2^* can be calculated to determine if the system will undergo torsional galloping. In fact, positive values of A_2^* [i.e., negative values of $(\partial C_M / \partial \alpha)$] imply torsional instability.

Similarly, an expression of A_3^* can also be derived using the same approach. This is shown in Equation 2.8, and has been previously used by Taylor and Browne (2020).

$$A_3^* \approx \frac{1}{K^2} \left(\left| \frac{\partial C_M}{\partial \alpha} \right| \right) \quad 2.8$$

In this case, the quasi-steady model suggests that A_3^* always increases as the wind speed increases.

Nakamura and Mizota (1975) studied torsional flutter on rectangular prisms. The study examined the stability criterion for torsional flutter based on the sign of the static aerodynamic torsional moment derivative, which is the theory used by Blevins, described at the beginning of this Section. They found that this criterion is not universally applicable, and that the time history of the moment needs to be considered as well. They determined that the damping derivative (i.e. the aerodynamic derivative A_2^*) of the

unsteady aerodynamic torsional moment acting on a structure has two components: one arising from the fluid memory effect (time history of the moment) and the other from the quasi-steady flow effect. A key outcome of the research was the identification of fluid memory effects as a dominant factor in the onset of torsional flutter. The study showed that the unsteady aerodynamic torsional moment consisted of two distinct components: a quasi-steady flow component, which could be estimated based on the instantaneous aerodynamic forces, and a fluid memory component, which depended on the past motion of the structure. The presence of fluid memory introduced a phase lag between the structural oscillations and the aerodynamic forces, leading to conditions where flutter could develop even if $\left(\frac{\partial C_M}{\partial \alpha}\right)$ remained positive. This finding challenged the traditional assumption that torsional stability could be determined solely from steady-state aerodynamic derivatives, reinforcing the need to account for unsteady effects in flutter predictions.

Taylor and Browne (2020) presented a methodology to evaluate the wind-induced loads on solar trackers. Their study introduced a hybrid approach that combined wind tunnel pressure measurements with a sectional model study to determine the aerodynamic forces acting on these flexible structures. The findings contributed to understanding the aeroelastic response of solar tracker arrays, particularly focusing on aerodynamic stiffness, damping, and buffeting response.

Taylor and Browne (2020) highlighted that single-axis trackers are flexible structures, exhibiting more deflections than conventional aeroelastic structures such as long-span bridges or aircraft wings. The study then employed a buffeting response analysis to simulate the interaction between turbulent wind fluctuations and the structural response of the trackers. The sign convention adopted in [their](#) study is shown in Figure

2.5. The force and moment coefficients extracted from this analysis are shown in Figure

2.6.

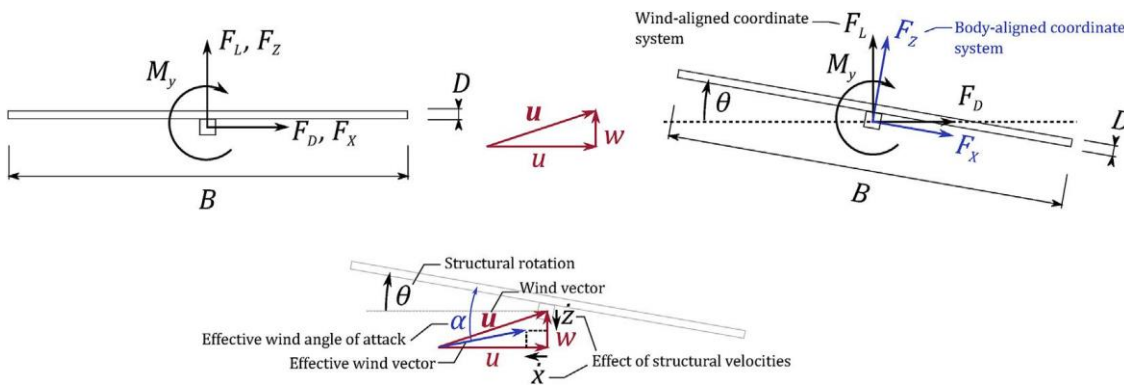


Figure 2.5. Sign convention for wind and structure axis forces (top) and effective wind angle of attack (bottom). Extracted from Taylor and Browne (2020)

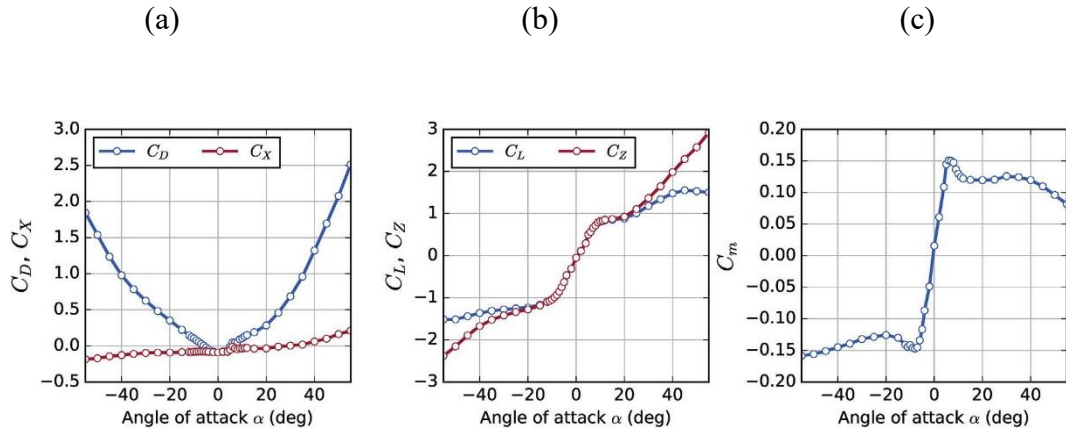


Figure 2.6. Measured static force and moment coefficients vs α . (a) Drag and Horizontal forces. (b) Lift and vertical forces. (c) Moment coefficients. Extracted from Taylor and Browne (2020)

One of the key insights from their research was that at high wind speeds, the contribution of self-excited forces becomes significant, increasing the peak design moments compared to static pressure-based predictions. It was emphasized that self-excited forces modified the effective stiffness k_{eff} and damping c_{eff} of the system, potentially influencing its stability. To investigate these effects, the study used a sectional wind tunnel model to measure the dynamic characteristics of a typical tracker section. By varying the wind speed, they extracted the aerodynamic derivatives A_2^* and A_3^* and plotted them against the reduced wind speed $U_{red} = U/f_0b$. These are shown in Figure 2.7. The derivatives were measured from free vibration tests in a smooth wind tunnel flow (turbulence intensity $< 1\%$). The study confirmed that the quasi-steady assumption did not fully capture the observed variations in aerodynamic stiffness and damping. For instance, using static moment coefficients [Figure 2.6 (c)] for $\alpha = 20^\circ$, and given that there is almost no variability of $(\partial C_M / \partial \alpha)$, it could lead to the assumption that 20° is the most

stable tilt angle since no changes in the aerodynamic stiffness would be expected. However, the aerodynamic derivatives reveal that the damping coefficient A_2^* in fact changes its sign at about $U_{red} \approx 3$, implying the potential for torsional galloping. This result demonstrated that stability assessments relying solely on static coefficients may be misleading, and dynamic effects must be considered.

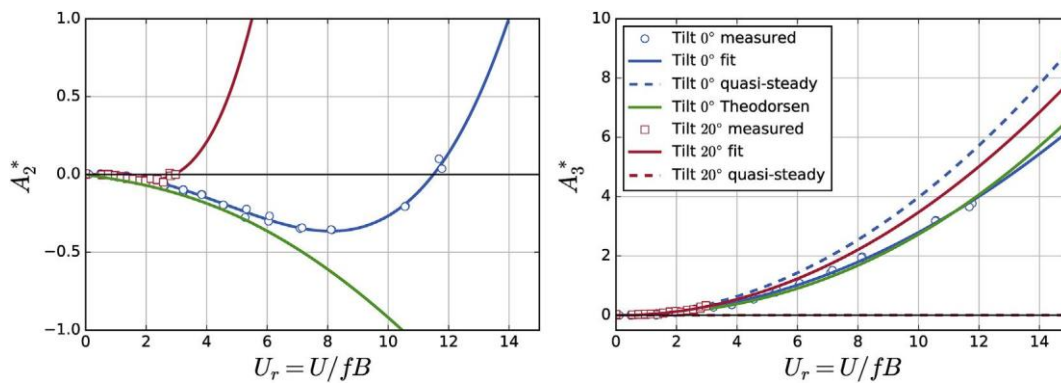


Figure 2.7. Aerodynamic derivatives A_2^* and A_3^* vs reduced wind speed U_{red} , for $\alpha = 0^\circ$ and $\alpha = 20^\circ$. Extracted from Taylor and Browne (2020)

The inclusion of aerodynamic derivatives in the buffeting response analysis provided a more realistic assessment of the loads these structures will experience in strong winds. However, while their study presented a comprehensive approach to evaluating the wind-induced loads on single-axis solar trackers, it also acknowledged several limitations that should be considered when interpreting the results and applying the methodology in practical design scenarios.

The numerical buffeting response analysis assumed that the aerodynamic forces can be decomposed into buffeting and self-excited components, and treated separately. But, in real-world conditions, the interaction between these forces may be more complex. The analysis relied on the quasi-steady assumption for the buffeting forces, which may not fully capture the unsteady flow effects that occur in highly turbulent atmospheric conditions.

The aerodynamic derivatives were extracted in a nominally steady flow (turbulence intensity $< 1\%$), which may not accurately represent real atmospheric conditions where turbulence levels are significantly higher.

The sectional model study, while effective in isolating aerodynamic derivatives, cannot fully capture end effects such as tip vortices, which can influence the self-excited forces. Additionally, the large scale required for sectional model tests makes it challenging to accurately model turbulent boundary layer effects.

The aerodynamic derivatives were extracted using free vibration tests with initial amplitudes up to approximately $\pm 5^\circ$. However, the study acknowledged that single-axis trackers can experience significantly larger oscillations in strong winds. The amplitude dependence of aerodynamic derivatives was not well understood, and their validity for large deflections remains uncertain. Beyond $\pm 20^\circ$ of dynamic rotation, discrepancies between numerical methods based on aerodynamic derivatives and direct quasi-steady simulations become noticeable, suggesting that the current framework may not fully capture extreme oscillatory behaviour.

Their study primarily examined aerodynamic forces for wind directions near normal to the tracker axis, as these directions are most critical for inducing large aerodynamic moments. However, it was noted that self-excited forces and inertial loads are likely to vary significantly for oblique wind angles. The study did not include a full

stability assessment for all possible wind directions, which could be relevant in cases where lateral effects become significant.

Cárdenas-Rondón et al. (2023) investigated the aeroelastic stability of flat-plate solar trackers subjected to wind loads. The sign convention for their study is shown in Figure 2.8.

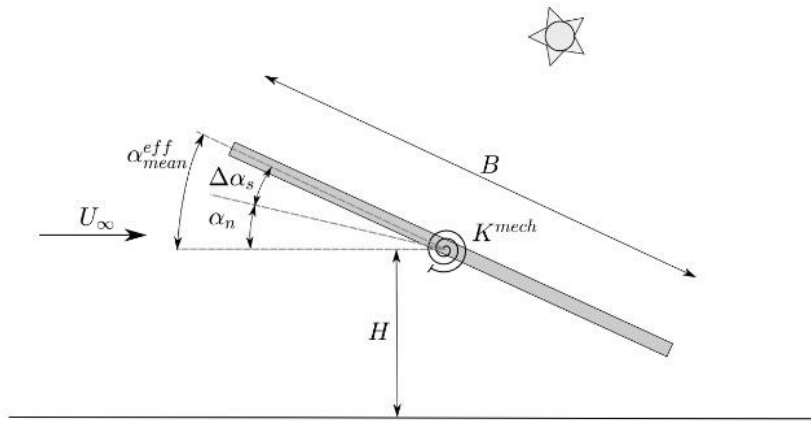


Figure 2.8. Reference system showing approach wind direction (U_{∞}), mean effective tilt angle (α_{mean}^{eff}), nominal tilt angle (α_n), static variation of tilt angle ($\Delta\alpha_s$), structural stiffness K^{mech} , elevation of the plate H , and chord length B . Extracted from Cárdenas-Rondón et al. (2023)

The study focused on the aerodynamic derivatives A_2^* and A_3^* to determine the critical wind speed U_{cr} , at which instability occurred. Their analysis considered different height-

to-chord ratios ($H/B = 0.3, 0.4, 0.5, 0.6, 1.0, 2.0$) and a range of nominal angles of attack (tilt angles) $\alpha_n = \pm 40^\circ$, to evaluate how ground proximity affected the aerodynamic response of solar trackers. Some of the results obtained in this study are shown in Figure 2.9 and Figure 2.10.

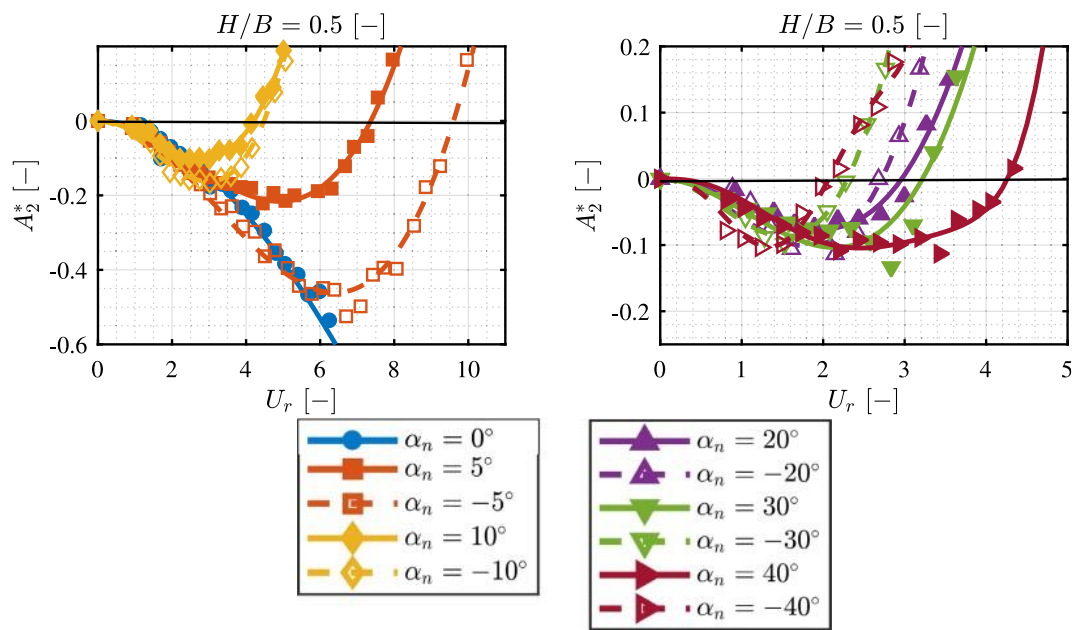


Figure 2.9. Aerodynamic derivative A_2^* vs reduced wind speed U_{red} for tracker chord-height $H/B = 2$ and different tilt angles. Extracted from Cárdenas-Rondón et al.,

(2023)

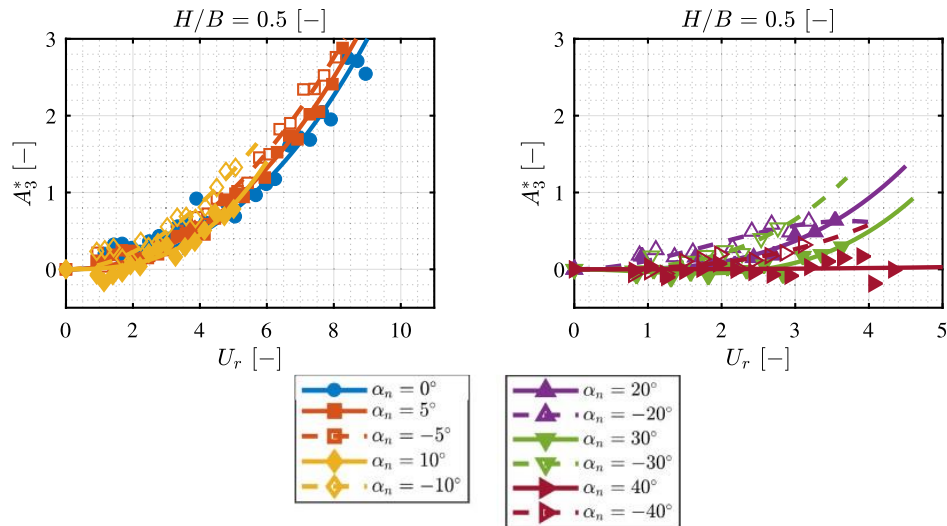


Figure 2.10. Aerodynamic derivative A_3^* vs reduced wind speed U_{red} , for tracker chord-height $H/B = 2$ and different tilt angles. Extracted from Cárdenas-Rondón et al., (2023)

The aerodynamic derivative A_2^* was associated with energy dissipation due to aerodynamic forces. A negative A_2^* indicated that the aerodynamic forces amplified oscillations rather than dampening them, suggesting a risk of instability. At the same time, A_3^* influenced the effective torsional rigidity of the system. If the aerodynamic stiffness decreased significantly with wind speed, the tracker was more likely to experience torsional flutter.

At small tilt angles ($|\alpha_n| < 10^\circ$), the aerodynamic damping remained positive (negative values of A_2^*), suggesting stable behaviour at low wind speeds. At larger tilt angles ($|\alpha_n| > 20^\circ$), A_2^* became positive at specific reduced speeds, indicating the onset

of torsional galloping. Higher H/B ratios increased stability, as ground proximity enhanced damping effects by modifying the wake structure and reducing vortex shedding intensity.

To predict instability, Cárdenas-Rondón et al., (2023) introduced an iterative method to compute the effective damping coefficient (ζ_{eff}), which accounted for both structural and aerodynamic contributions. The critical speed was identified as the point where $\zeta_{eff} = 0$.

The limitation of their study is the assumption that aerodynamic derivatives remained constant regardless of oscillation amplitude. However, torsional flutter is a nonlinear phenomenon, and the actual aerodynamic forces could depend on oscillation amplitude. The approach was valid only for small perturbations around equilibrium and did not capture post-torsional galloping behaviour. The study considered a sectional model, which neglected three-dimensional effects such as spanwise variations in flow and structural response. While modal decomposition could extend the results to full-scale trackers, a fully three-dimensional analysis would be required for more accurate predictions.

Their wind tunnel experiments were conducted in smooth flow conditions with a turbulence intensity of approximately 3%. However, real atmospheric flows are highly turbulent, which could affect vortex shedding and modify the aerodynamic damping characteristics. The study primarily considered normal wind incidence, which may be the most critical scenario for torsional flutter. However, real conditions include wind approaching from oblique angles, which could influence the aerodynamic derivatives and modify the onset of instability.

Cárdenas-Rondón (2023) considers that there are three fundamental differences between the instability encountered for airfoils and bridges, and the aeroelastic instabilities of solar trackers. Firstly, solar trackers are usually placed very close to the ground, which significantly impacts the aerodynamic forces. Secondly, the deflections experienced by solar trackers which change the nominal tilt angle α as the oscillations occur, makes the aerodynamic derivatives dependant of the structural characteristics of the trackers. Finally, the large oscillations that occur during aeroelastic instabilities, explained in the literature by Gifford, (2019); Valentín et al. (2022), Taylor and Browne, (2020), Zang et al., (2023) generate non-linear aerodynamic behaviours, hence implying non-linear aerodynamic derivatives.

Despite acknowledging non-linear phenomena, existing research on solar tracker aerodynamics primarily employs linear formulations. In fact, Cárdenas-Rondón (2023) states that linear approximations provide a simple tool to analyse the trends of experimental results. This is used by Blevins (1990) to enunciate the aeroelastic response of a flat plate, that was shown in Section 2.3.

Enshaei et al., (2023) described that torsional instability on solar trackers at small tilt angles (i.e., $\approx 0^\circ$) is first initiated by static torsional divergence, where the interaction between elastic and aerodynamic forces is dominant. Then, as explained by Bisplinghoff et al. (2013), as the tilt increases, torsional galloping occurs. At this stage, the interaction is given by elastic, inertial and aerodynamic forces.

2.6 Wind loads of ground-mounted solar panels

Warsido et al. (2014) conducted wind tunnel tests to investigate the effect of lateral and longitudinal spacing between panels on a 1/30 scale rigid model of ground-mounted solar panel systems. The array dimensions and the group configuration are shown in Figure 2.11 and Figure 2.12, respectively.

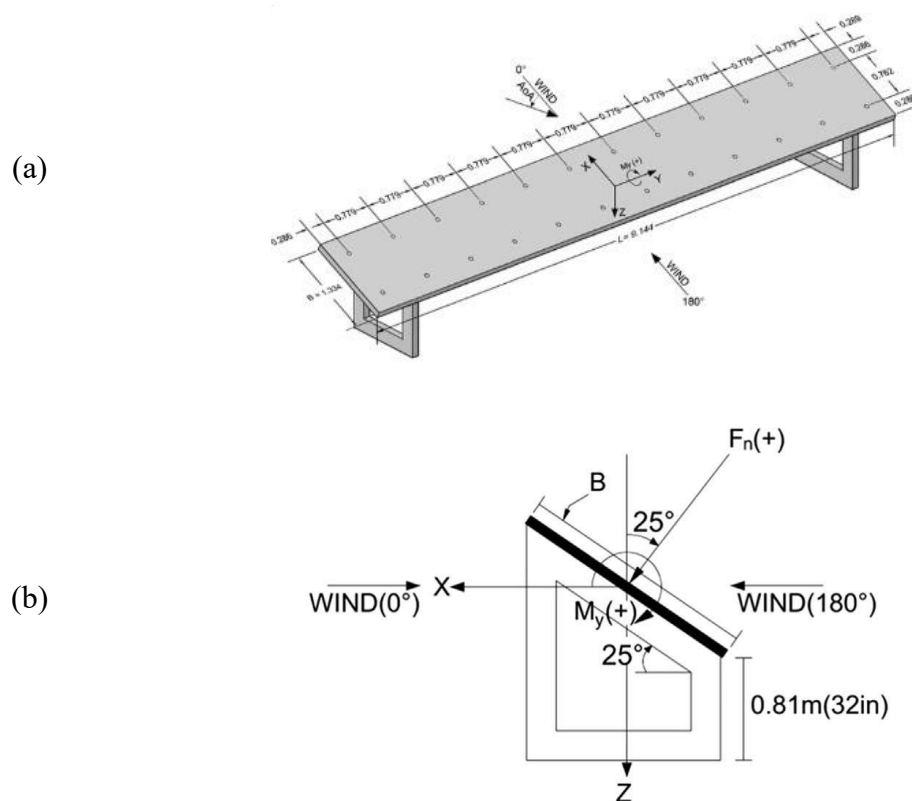


Figure 2.11. (a) Diagram showing full scale dimensions of array (in m); (b) sign convention of normal force and overturning moment. Extracted from Warsido et al.,

(2014)

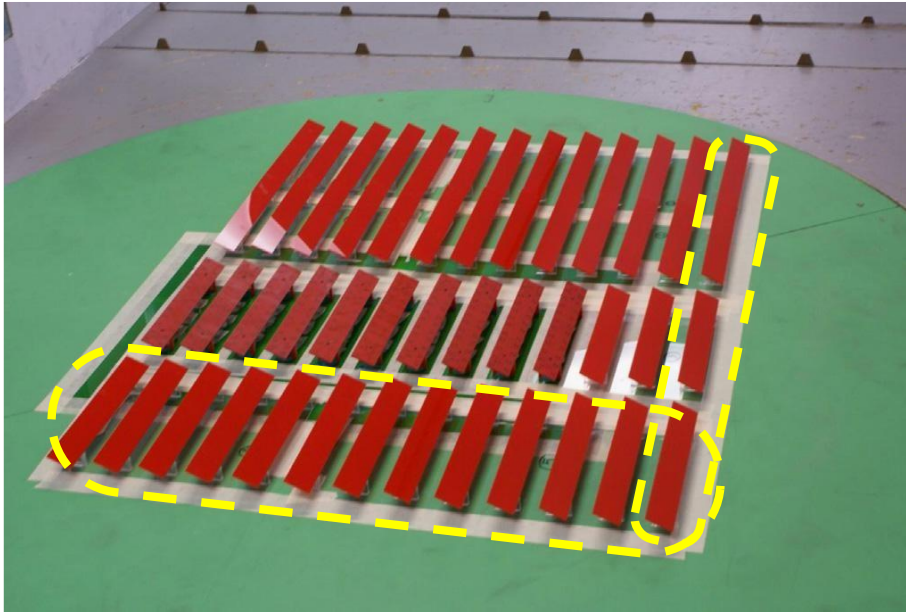


Figure 2.12. Photograph of ground mounted panels configuration. 13 rows \times 3 columns. Extracted from Warsido et al. (2014)

The variation of force and moment coefficients vs wind direction are shown in Figure 2.13. Results showed shielding effects, as wind load coefficients on the second-row panels were reduced by as much as 50% compared to the first row. This reduction decreased for further back rows, becoming minimal after the fourth row. Increasing lateral spacing between columns from 1.5 times the panel width to 3 times the panel width had a minimal effect on the force and moment coefficients. Increasing the distance between rows from 2 times the panel height to 4 times the panel height increased the wind load coefficients by up to 10%. Panels in the outer array columns experienced wind loads that were approximately 10% higher than those in the inner column.

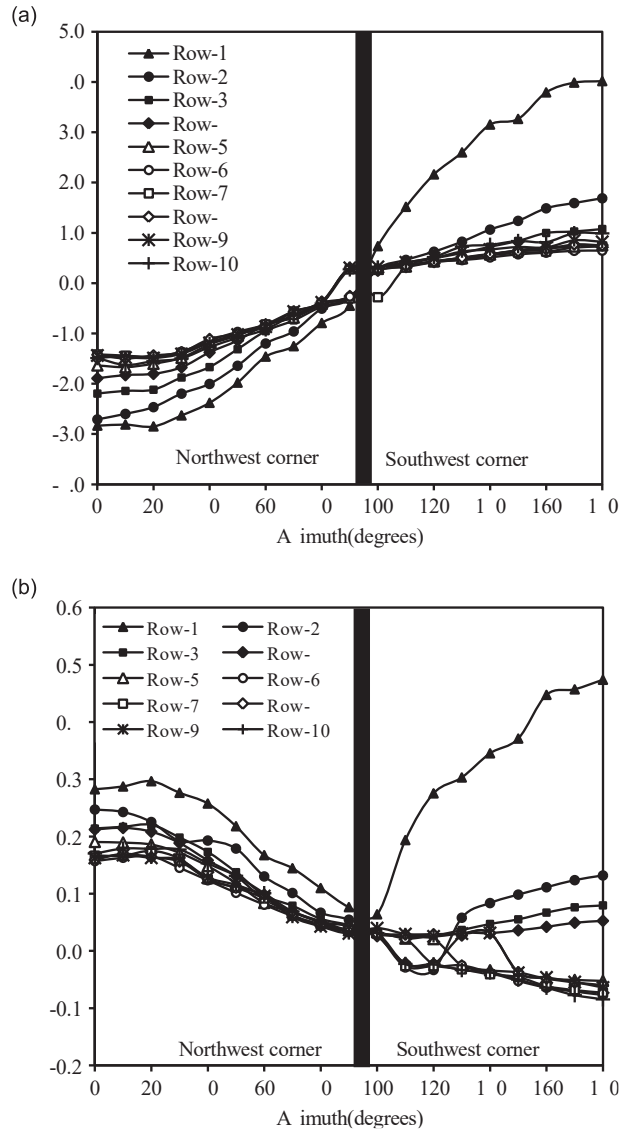


Figure 2.13. Variation of peak (a) normal force and (b) overturning moment coefficients with wind direction. Spacing between rows, $s = 1.22 \text{ m}$ (full scale).

Extracted from Warsido et al. (2014)

Ginger et al., (2019) studied wind loading on a set of four solar panel arrays. Net wind pressures acting across solar panels were obtained by testing 1/20 scale rigid models covering a range of typical array configurations at the commonly used tilt angle of 20° ,

as well as for other inclinations. Large net negative (upward) pressures were measured on the panels at the leading edges for wind blowing towards the bottom surface of the sloping panels. Large net positive (downward) pressures were measured on the panels at the bottom leading edge for wind blowing towards the top surface of the sloping panels. Aerodynamic shape factors C_{shp} on panels and arrays were given in a form adopted by the Australian/New Zealand wind loading standard AS/NZS 1170.2 (2021).

Koekemoer et al., (2024) investigated the effects of wind loading on single-axis trackers. The study involved the design and implementation of a measurement system attached to an existing single axis tracker structure. This system was used to conduct full-scale measurements of wind load effects on the structure. The array, used for testing various module technologies, consists of six rows, each approximately 32 m long and spaced 5 m apart. A binning procedure was used to classify wind conditions and tracker positions during specific time intervals. Data was sorted into 10-minute intervals, characterized by mean wind direction, average module tilt angle, mean near-field wind speed, mean far-field wind speed, maximum 3-second gust far-field wind speed, and maximum 3-second gust near-field wind speed. The results of the study showed that wind-induced loads on the mounting rails were significantly influenced by wind direction and speed.

2.7 Aeroelastic model tests

Martínez-García et al. (2021) carried out aeroelastic model tests on seven solar tracker models, with different inertias and aspect ratios based on full-scale data shown in Table 2.1. The models used different materials to correctly reproduce their structural characteristics. Typical test speeds ranged from 6 m/s to 15 m/s, and turbulence intensities from 0.5% to 5%. The critical wind speed U_{cr} for instability was found by increasing the velocity until the onset of torsional flutter; then the velocity was gradually lowered until the oscillation disappeared.

The study found that U_{cr} at which torsional flutter initiates, changes depending on the tilt angle (α) of the solar tracker. The critical wind speed for torsional flutter (among the models tested) was found to be independent of the inertia of the system, the aspect ratio of the structure, and the torsional stiffness of the torque tube. Based on their findings, the authors developed a Stability Diagram, shown in Figure 2.14. This diagram indicates the potential reduced wind speed (U_{red}) at which the solar tracker becomes unstable for different α , and for wind directions $\theta = 0^\circ$ ($-\alpha$) and $\theta = 10^\circ$ ($+\alpha$). The proximity to the ground was accounted for, but the effects of higher turbulence intensity levels were not studied.

Table 2.1. Solar panel configuration for different solar trackers systems. Extracted from
Martínez-García et al. (2021)

Id	Type of Panel	Number of modules	b (m)	l (m)	Inertia I (kg.m ²)
1	1F ¹	60	3.0	20.0	704
2	2F ²	90	4.0	22.5	2127
3	Tf ³	90	4.0	22.5	1495
4	1F	90	4.3	23.5	2274
5	1F	270	3.6	27.0	2072
6	1F	90	4.0	27.5	2458
7	2F	120	4.0	30.0	2836
8	Tf	120	4.0	30.0	1994
9	1F	120	4.3	31.5	3033
10	2F	90	2.0	45.0	570
11	Tf	90	2.0	45.0	401
12	1F	90	2.1	47.0	604
13	1F	240	1.8	48.0	501
14	1F	78	2.0	48.0	570
15	2F	100	2.0	50.0	633
16	Tf	100	2.0	50.0	446
17	1F	100	2.1	53.5	651
18	2F	180	2.0	90.0	1140
19	Tf	180	2.0	90.0	802
20	1F	180	2.1	94.5	1209

1 Monofacial solar panel; 2 Bifacial solar panel; 3 Thin film solar panel

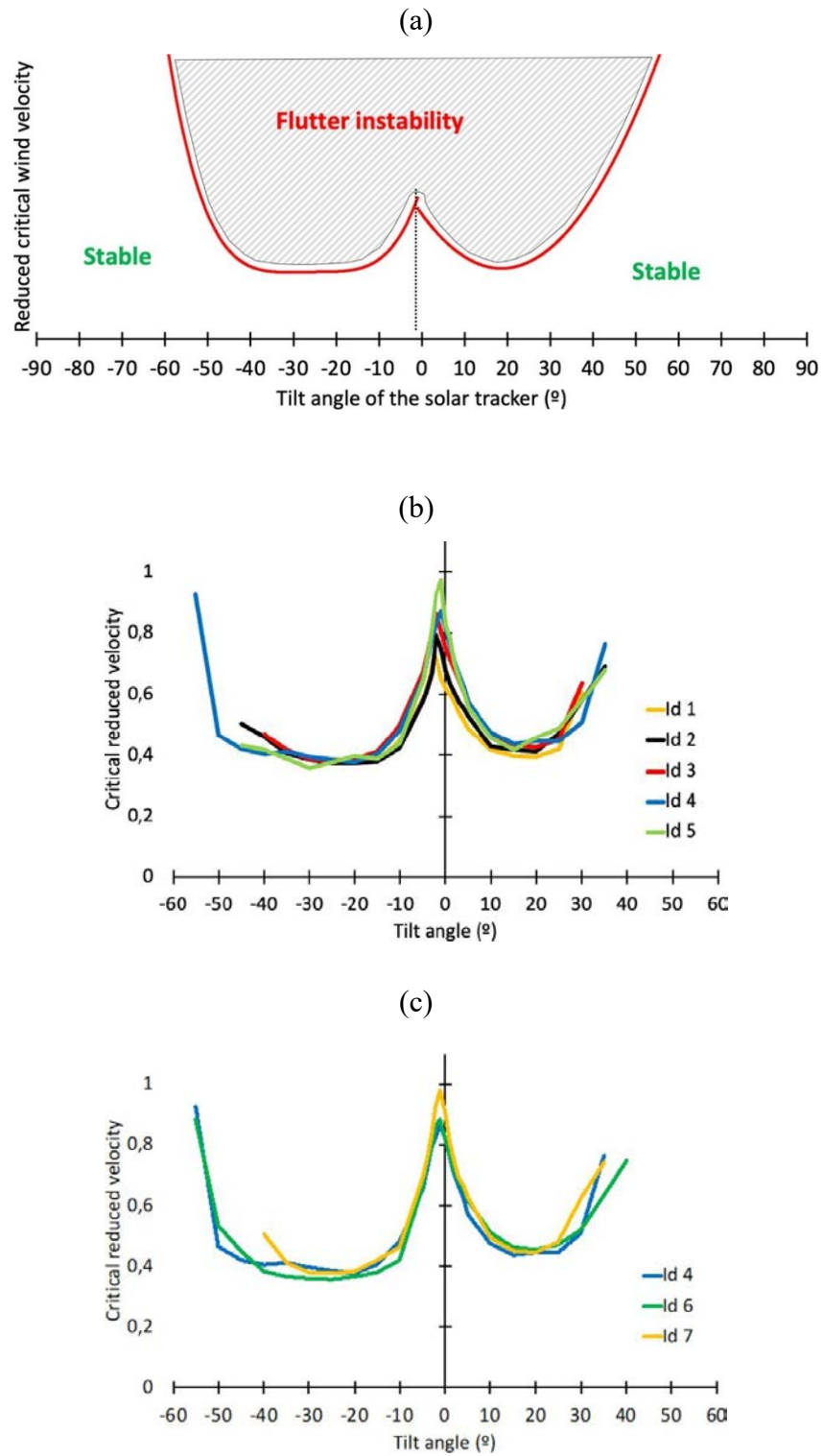


Figure 2.14. Stability diagram. (a) Conceptual diagram. (b) Models with different inertia. (c) Models with different aspect ratio

Their experiments were conducted in a low-turbulence wind tunnel with an uniform flow profile, which did not replicate real atmospheric boundary layer conditions. The study acknowledged that the critical velocity might be higher in real conditions due to lower wind speed near the ground in a boundary layer, but it did not explicitly model these effects.

Zhang et al. (2023) conducted their study using a combination of wind tunnel experiments and theoretical analysis to investigate the torsional aeroelastic instability of solar trackers under low levels of turbulence (0.4 %) and higher levels of turbulence (19% to 21%). A sectional model of a solar tracker was mounted in a wind tunnel capable of generating different turbulence intensities. The study revealed that turbulence intensity significantly influences the torsional aeroelastic instability of single-axis solar trackers. The oscillations produced during torsional galloping are larger at high levels of turbulence intensity than at lower levels.

Enshaei et al. (2023) investigated the torsional instability phenomenon in solar trackers focusing on the low-tilt scenario, (i.e. traditional stow position). They used an analytical approach to predict the critical wind speed at $\alpha = 0^\circ$ and validated this against measured data from various solar tracker designs. The study concluded that structural parameters that are related to torsional galloping (i.e. damping) have minimal impact on the critical wind speed at small tilt angles. This is because the stiffness is a critical parameter at small tilt angles and influences more the structural behaviour.

In an effort to standardize experimental investigations of aeroelastic instabilities in single-axis solar trackers, Rodríguez-Casado et al. (2024) proposed a benchmark model and methodology for wind tunnel testing. They defined a detailed three-dimensional aeroelastic model, including geometry, materials, and construction specifications, to facilitate replication and comparison of results across different research groups. They

conducted experiments in two separate wind tunnels, validating the repeatability and reliability of the proposed benchmark. Their study focused on the influence of tilt angle on the critical wind speed for instability onset, highlighting the varying aerodynamic mechanisms at play. By comparing their results with existing stability diagrams from the literature, they emphasized the need for a standardized benchmark to address discrepancies and improve comparability. However, the study also acknowledges that further research is needed to extend the benchmark to multi-row configurations, explore the influence of other parameters, such as wind directions, and incorporate more realistic turbulent flow conditions.

2.8 Computational modelling

The complexity of wind flow is a challenge for carrying out computational analysis on fluid dynamics because of the high levels of turbulence that can be encountered, from large eddy structures of the atmospheric turbulence to turbulence induced by bluff-body shapes of buildings and other structures. The most common Computational Fluid Dynamic (CFD) techniques may predict the mean pressures on buildings with reasonable accuracy but are not sufficiently accurate for the fluctuating and peak pressures. This is because of the oversimplifications of the turbulence needed to be made in the fluid flow equations. On the other hand, CFD is currently an accessible and very flexible methodology that allows variations to an experiment, which compared to physical modelling/testing is a more time-efficient tool. Compared with aeroelastic modelling, it is also more cost effective.

There are various examples of application of CFD on flat plates and solar panels. Brydges (2019) examined the behaviour of steady, incompressible flow around normal and inclined flat plates using three different turbulence models. The drag and lift

coefficients, the mean recirculation lengths behind the plate and the streamwise velocities and turbulence kinetic energy readings along the centrelines of the plates were collected. Nonetheless, Brydges recognized that a number of turbulence relationships must be modelled, or else the results were inaccurate.

The study by Young et al. (2020) investigated the phenomenon of torsional galloping in solar-tracking photovoltaic panel arrays, focusing on the role of fluid-structure interactions in driving this instability. They developed a computational solver to model the aerodynamic forces and structural response of the panel arrays, with the goal of identifying the conditions that lead to galloping and informing design choices to mitigate this risk.

Their computational model was based on a mass-spring representation of the panel array, where each panel was treated as a rigid body connected to its neighbours via torsional springs. This simplification allowed the study to focus on the dominant mode of instability, which was the twisting motion of the panels around the torque tube. The aerodynamic forces were computed using a moving mesh numerical solver that captured the unsteady flow field around the panels. These simulations revealed that the instability was primarily driven by cyclic vortex shedding along the top surface of the panels. As wind flowed past the panel edges, it created alternating regions of high and low pressure that reinforced the torsional oscillations rather than damping them. Over time, this vortex-induced pressure variation amplified the rotational motion, pushing the system into an unstable galloping mode.

A key finding of their study was the significant influence of nominal tilt angle on the stability of the panels. Their study demonstrated that certain nominal tilt angles were more prone to galloping than others. Panels stowed at positive angles (when $\theta = 180^\circ$), particularly in the range of 22.5° to 30° , were found to be the most unstable, with

galloping occurring at full scale wind speeds as low as 22.5 m/s. In contrast, panels positioned at negative angles, where the leading edge was positioned closer to the ground, exhibited greater aerodynamic stability. They attributed this to ground-blocking effects, where proximity to the ground altered the flow patterns and suppressed the formation of unstable vortices. Among the angles tested, the most stable configurations were found at 0° and -37.5° (when $\theta = 0^\circ$), where galloping only developed at significantly higher wind speeds.

The study also explored the implications of these findings for practical solar tracker design and operational guidelines. By identifying stable and unstable stow angles, the results provided a basis for optimizing tracker stow strategies during extreme wind events. They suggested that modifying the geometry of the panel edges or increasing the stiffness of the torque tube could further enhance stability, though these aspects were left for future investigations.

Despite its valuable insights, the study acknowledged several limitations. The simulations were conducted for a single array solar tracker, meaning that the results were directly applicable only to the leading row in a larger multi row setup. In real-world installations, multi-row interactions may significantly influence aerodynamic forces, and the presence of upstream rows could alter the onset and development of galloping in downstream panels. Additionally, the study employed a quasi-two-dimensional approach, which did not fully account for three-dimensional flow effects, such as spanwise vortex interactions and structural mode coupling. The structural model was also simplified, treating the panels as rigid bodies and neglecting bending deformations, which might play a role in full-scale solar tracker dynamics. Moreover, the wind conditions in the simulations were based on a statistically generated turbulent profile rather than a fully

resolved atmospheric boundary layer model, meaning that the effects of transient wind events and localized turbulence were not explicitly considered.

2.9 Codes and standards

Wind loading codes and standards are often based on research outcomes, but they necessarily provide simplified models of wind loading. They are usually related to a certain region or country, so they incorporate the knowledge of the structure of windstorms for those places.

The quasi-steady assumption is the basis of many wind-loading codes and standards. The quasi-steady pressure coefficient, $C_{\bar{p}}$, is approximately equal to the mean pressure coefficient, $C_{\bar{p}}$. Then, it is possible to establish a quasi-steady relationship between mean-square pressure fluctuations and mean-square longitudinal velocity fluctuations. Thus, according to the quasi-steady assumption, peak pressures (maxima \hat{p} , and minima \check{p}) can be predicted by using quasi-steady pressure coefficients and peak gust wind speed, as shown in Equation 2.9. Its main disadvantage is that pressure fluctuations may not be adequately accounted for.

$$\hat{p}, \check{p} = C_{\bar{p}} \frac{1}{2} \rho (\hat{U}^2) \cong C_{\bar{p}} \frac{1}{2} \rho (\hat{U}^2) \quad 2.9$$

Two standards are reviewed to analyse the information available for designing solar panel systems.

- AS-NZS 1170.2 (2021)

The Australian and New Zealand Standard AS/NZS 1170.2 (2021), titled "Structural Design Actions, Part 2: Wind Actions" provides a comprehensive framework for calculating wind loads, focusing on static, quasi-static and some dynamic wind effects. AS/NZS 1170.2 outlines procedures for determining design wind pressures based on various factors, including regional wind speeds, terrain categories, and structural geometry.

With regards to solar panels design, Appendix B, clause "B.6 Solar panels", provides net pressure coefficients to calculate wind loading on ground-mounted solar panels. Figure 2.15 shows the geometrical characteristics and pressure zoning to obtain pressure coefficients for several tilt angles (α) and approaching wind directions $\theta = 0^\circ$ and 180° for ground-mounted solar panels. The pressure coefficients are summarized for these conditions and shown in Table 2.2 and Table 2.3.

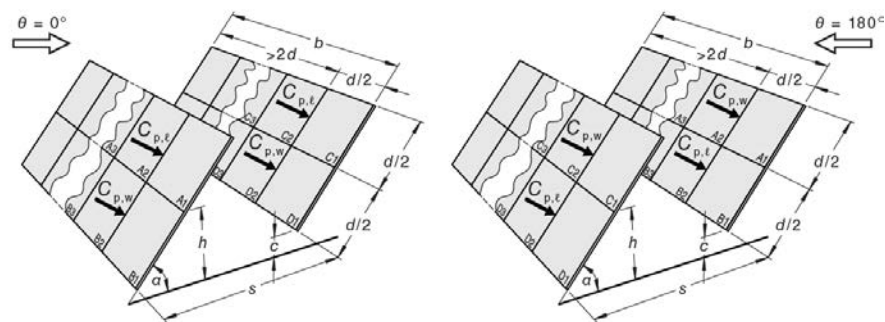


Figure 2.15. Solar panel arrays. Geometry characteristics and pressure zones for the application of AS/NZS 1170.2 (2021). Extracted from AS/NZS 1170.2 (2021)

Table 2.2. Net pressure coefficients for ground-mounted solar panels, several tilt angles (α) and wind direction $\theta = 0^\circ$. Extracted from AS/NZS 1170.2 (2021)

Panel pitch (α) degrees	$\theta = 0$ degrees							
	$C_{p,w}$		$C_{p,l}$		$C_{p,w}$		$C_{p,l}$	
	B1	B2, B3	A1	A2, A3	D1	D2, D3	C1	C2, C3
0	0.45	0.45	0.25	0.10	0.40	0.25	0.25	0.10
15	1.20	1.20	0.80	0.45	1.40	0.80	0.90	0.40
20	1.30	1.20	0.80	0.45	1.50	0.75	0.90	0.45
25	1.45	1.35	0.95	0.60	1.60	0.85	1.00	0.55
30	1.50	1.25	0.95	0.70	1.70	0.85	1.10	0.65

Table 2.3. Net pressure coefficients for ground-mounted solar panels, several tilt angles (α) and wind direction $\theta = 180^\circ$. Extracted from AS/NZS 1170.2 (2021)

Panel pitch (α) degrees	$\theta = 180$ degrees							
	$C_{p,w}$		$C_{p,l}$		$C_{p,w}$		$C_{p,l}$	
	A1	A2, A3	B1	B2, B3	C1	C2, C3	D1	D2, D3
0	-0.50	-0.55	-0.35	-0.20	-0.50	-0.35	-0.35	-0.15
15	-1.20	-1.40	-0.60	-0.85	-1.40	-1.45	-0.70	-0.65
20	-1.40	-1.45	-0.75	-0.90	-1.40	-1.40	-0.70	-0.70
25	-1.50	-1.45	-0.75	-0.95	-1.50	-1.35	-0.75	-0.80
30	-1.60	-1.50	-0.80	-0.95	-1.55	-1.30	-0.90	-0.85

Once the coefficients are determined based on wind direction and geometrical properties of the solar panel installations, peak pressures acting on the panels can be obtained from

$$\hat{p}, \check{p} = C_{pn} K_a K_l \frac{1}{2} \rho (V_{des, \theta})^2 \quad 2.10$$

Where, C_{pn} is the net pressure coefficient, K_a is the area reduction factor, K_l is the local-pressure effects factor, $V_{des,\theta}$ is the 0.2 s duration peak gust design wind speed at the reference mid-height of panels.

The standard is explicit in stating that its provisions for aeroelastic phenomena are limited. It recommends that for flexible solar trackers that are highly sensitive to dynamic wind effects, specialist advice should be sought.

- ASCE 7-22 (2022)

The American Standard ASCE 7-22 (2022), titled "Minimum Design Loads and Associated Criteria for Buildings and Other Structures," provides data for calculating environmental loads on structures, including wind, seismic, and snow loads. The wind load provisions are detailed for most conventional buildings and structures. These guidelines allow engineers to estimate wind-induced forces based on factors like location, terrain, building shape, and height, which are essential for designing buildings and structures to withstand expected wind pressures.

For ground-mounted solar panels, the application requires accounting for some typical geometrical parameters. This standard provides indications to obtain the wind loading for the solar panels depending on their location within a solar farm, as shown in Figure 2.16.

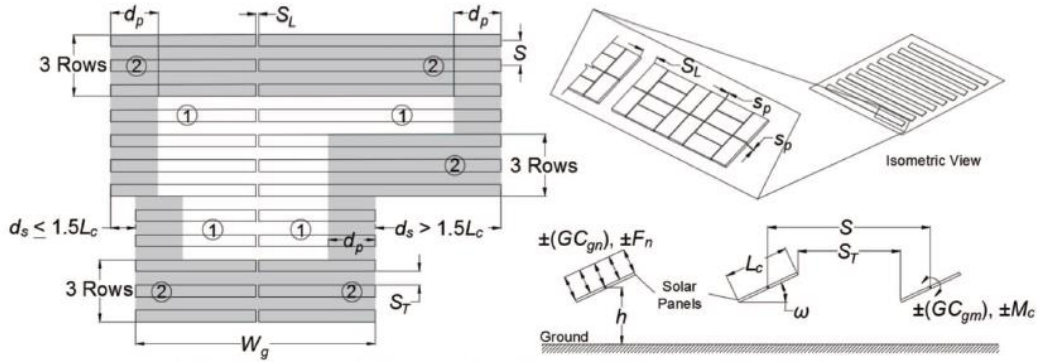


Figure 2.16. Parameters for Application of Ground-Mounted Fixed-Tilt Solar Panel Systems Requirements. Extracted from ASCE 7-22 (2022)

Users of the Standard can determine static and dynamic pressure and moment coefficients. Dynamic coefficients are obtained by determining the reduced frequency of the structure and considering the relative position of the array within the solar farm (Figure 2.16). The static and dynamic moment coefficients can be found from Figures 29.4-10 and 29.4-11 of ASCE 7-2022 (pp. 312–313). Once the coefficients are determined, the design force and moment acting about the central axis of panels can be calculated using Equations 2.11 and 2.12.

$$F_n = q_h K_d [\pm(GC_{gn})] A \quad 2.11$$

$$M_c = q_h K_d [\pm(GC_{gm})] A L_c \quad 2.12$$

Here, F_n is the design force, M_c is the design moment about the central axis of the panels, q_h is the pressure evaluated at the mid-height of the panel, K_d is a directionality factor, L_c is the panel chord length, and $GC_{gi} = \pm(GC_{gi_{static}}) \pm(GC_{gi_{dynamic}})$, is the resultant force or moment coefficient, combining static and dynamic coefficients.

In its section C29. .5 “Ground-Mounted Fixed-Tilt Solar Panel Systems”, it is stated that the design forces and moments derived using the combined static and dynamic wind load coefficients are appropriate for fixed-tilt ground-mounted systems, assuming the wind-induced deflections are small. It also indicates that, flexible structures, such as unrestrained single-axis trackers, are prone to aeroelastic effects and torsional instabilities, which must be considered in the design of such systems. The approach of ASCE 7-22 to aeroelastic phenomena such as complex interactions between wind forces and structural motion, such as torsional galloping, is relatively limited.

2.10 Chapter summary

Previous research has shown that:

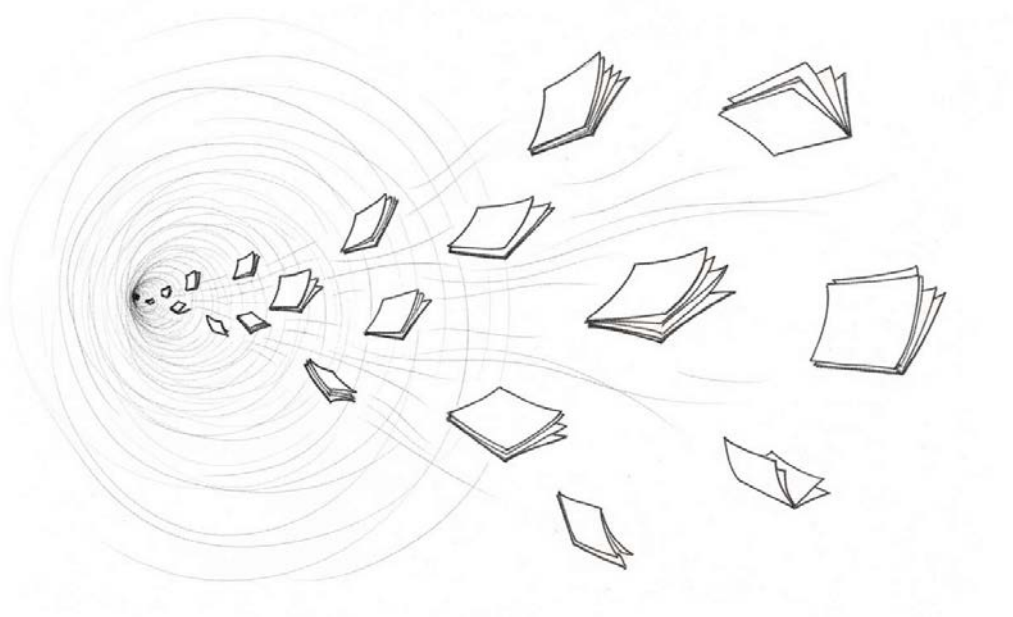
- The centre of pressure on a plate changes as the tilt angle (α) varies, implying a variation of the magnitude of the moment with the tilt angle.
- Effective damping (c_{eff}) and effective stiffness (k_{eff}) are influenced by the variation of the moment coefficient C_M in terms of α , which for increasing wind speeds, can result in c_{eff} or k_{eff} falling to zero, indicating the onset of torsional galloping or divergence respectively.
- The aerodynamic derivatives A_2^* and A_3^* can be used to assess the aeroelastic behaviour of the structure.

- High pressures are expected for leading solar panel arrays within a solar farm, and shielding may occur for downstream arrays depending on the spacing between arrays and the wind direction.
- Standards do not currently provide adequate data for designing solar trackers to avoid instabilities such as torsional flutter.

From the literature review on solar trackers, it was found that these structures can fail due to torsional flutter instabilities such as torsional galloping and torsional divergence. It is possible to determine a critical wind speed at which the solar trackers will become unstable. This wind speed changes with the tilt angle. Wind loading obtained with pressure data could underestimate the peak moments generated by aeroelastic instabilities. Furthermore, turbulence intensity also influences oscillations during instability onset.

Current gaps in the understanding of instabilities in solar trackers include:

- The critical parameters that define the onset of torsional instability.
- The effect of oblique wind approach directions, including wind loading and aeroelastic response of solar trackers.
- The influence of turbulence intensity on the onset of instabilities of solar trackers.
- Characterization of torsional galloping and divergence considering their potential onset at the same time or during the same event.
- The behaviour of multiple arrays of solar trackers under atmospheric flow.



3 METHODOLOGY

This Chapter describes the experimental procedure carried out to obtain the wind loads and response of flat plates (solar panel arrays) in atmospheric wind flow. The four distinct 1/20 aeroelastic models that were used in this study are described, as well as scaling and measurement techniques used. Tests were carried out in the Boundary Layer Wind Tunnel at the Cyclone Testing Station (CTS), James Cook University, in Townsville, Australia.

3.1 Atmospheric boundary layer in the wind tunnel

Tests were conducted in a 22 m long \times 2.1 m high \times 2.5 m wide open-circuit wind tunnel, shown in Figure 3.1. The approach Atmospheric Boundary Layer (ABL) was simulated at a length scale of 1/20. The fluctuating velocity $U(t)$ was measured at a range of heights, z above the floor using a TFI Cobra Probe (Turbulent flow instrumentation, Series 100).

The mean velocity \bar{U}_z , turbulence intensity $I_u = \sigma_u / \bar{U}_z$, and the power spectral density at the height $h = 100$ mm (full scale of 2 m, height of the torque tube), were determined as shown in Figure 3.2. To achieve an open terrain profile as defined in

AS/NZ 1170.2 (2021), a 250 mm high trip board was placed at the upstream end, followed by a combination of carpet and an array of blocks on the tunnel floor. The von Karman spectrum is plotted with a full-scale turbulence length scale $L_u = 56$ m. The wind tunnel spectrum (Figure 3.2 (c)) is shifted to a higher frequency by a factor of about five. This distortion is acceptable in wind tunnel testing to allow large models to be used (Surry, 1982).

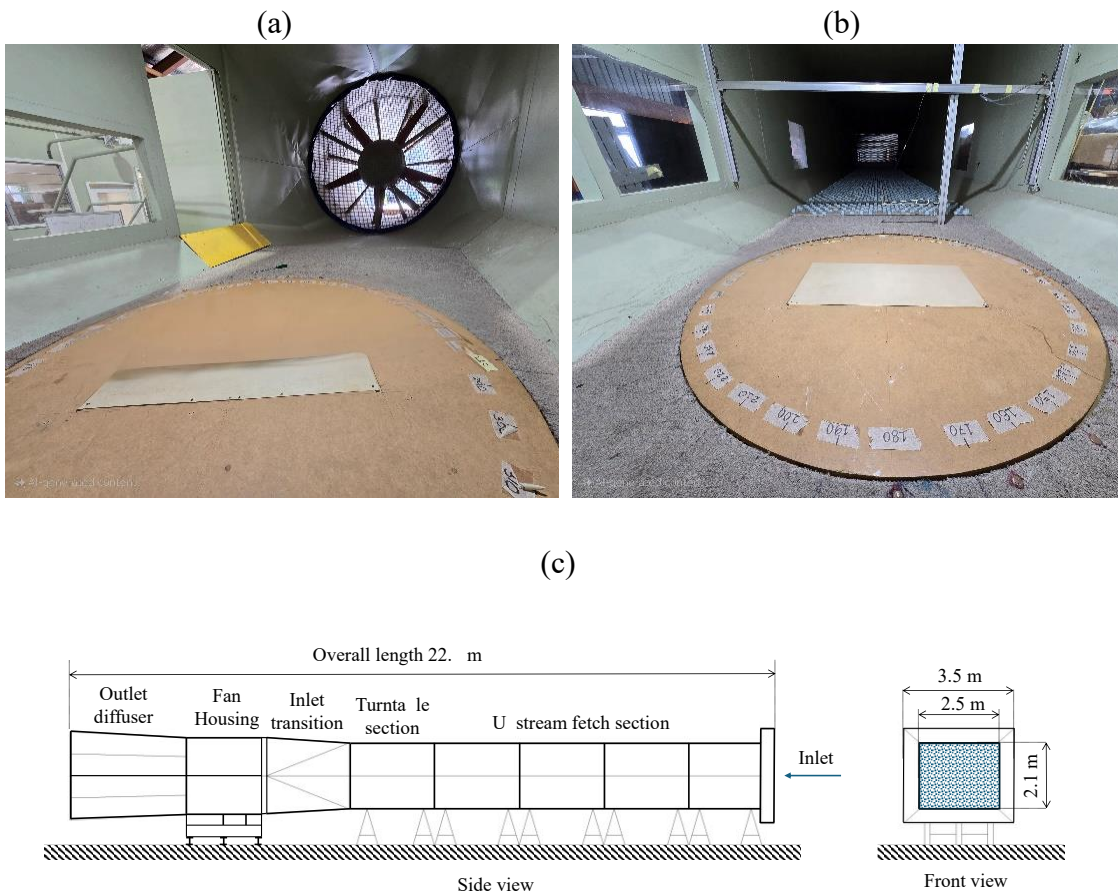


Figure 3.1. Atmospheric boundary layer wind tunnel: (a) Turntable and downstream end. (b) Turntable and upstream fetch. (c) Schematic diagram of the wind tunnel

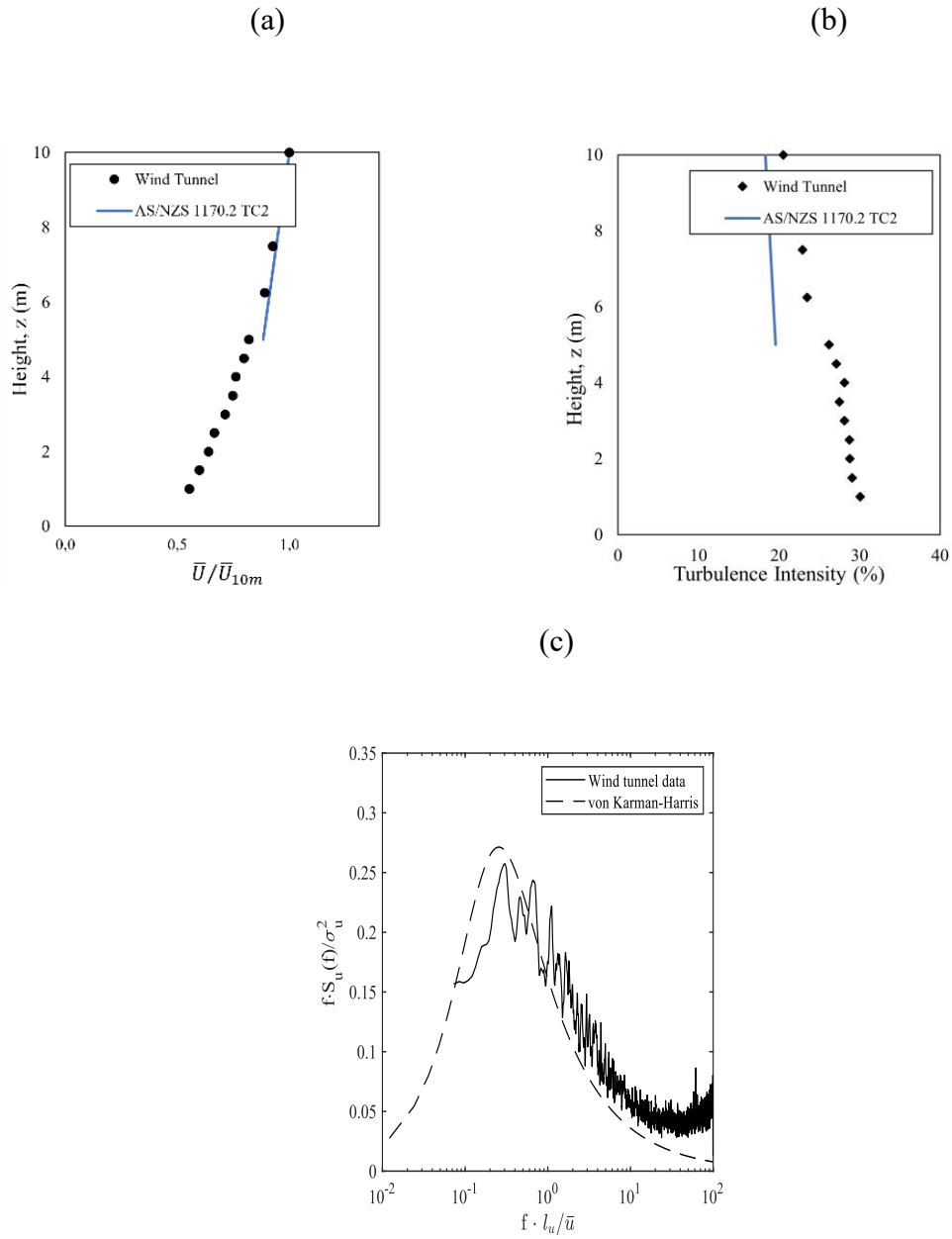


Figure 3.2. (a) Mean velocity and (b) turbulence intensity profiles of the atmospheric boundary layer simulated at a length scale of 1/20 in the wind tunnel. (c) Power spectral density at the height of the torque tube h , 2 m (100 mm model scale)

An experimental approach called Partial Turbulence Simulation (PTS), described in ASCE 49-21 (ASCE, 2022) is able to match the scale of velocity fluctuations for obtaining the aerodynamic coefficients in large scale models, as shown by Acosta et al. (2024). Kopp (2023) described approaches for improving Partial Turbulence Simulation (PTS) in ASCE 49-21 for wind tunnel testing, which may be able accommodate turbulence scaling for larger bridge section model testing such as those by Irwin, (1998) Macdonald et al. (2002).

However, the simulation of the mean velocity and turbulence intensity profiles and the magnitude of the turbulence intensity are more important for studying the response of solar trackers in this study. Therefore, the simulated mean velocity and turbulence intensity profiles satisfactorily replicate the atmospheric flow conditions to study the response of solar trackers notwithstanding the mismatch in the velocity spectrum.

3.2 Fixed frame rigid model

A six-module single array $14.40 \text{ m } (l) \times 5 \text{ m } (b)$ of a fixed-frame solar panel system was modelled at $L_r = 1/20$, as shown in Figure 3.3. The rigid model was subjected to the atmospheric boundary layer wind flow and tested for tilt angles $\alpha = 0^\circ, 15^\circ, 20^\circ, 25^\circ, 30^\circ$, at a fixed mid-height $h = 94\text{mm}$ (1.88 m full-scale). The aspect ratio of the model was $l/b \approx 3$. Tests were carried out for wind direction (θ) from 0° to 180° , at intervals of 10° , for 3 repeat runs.

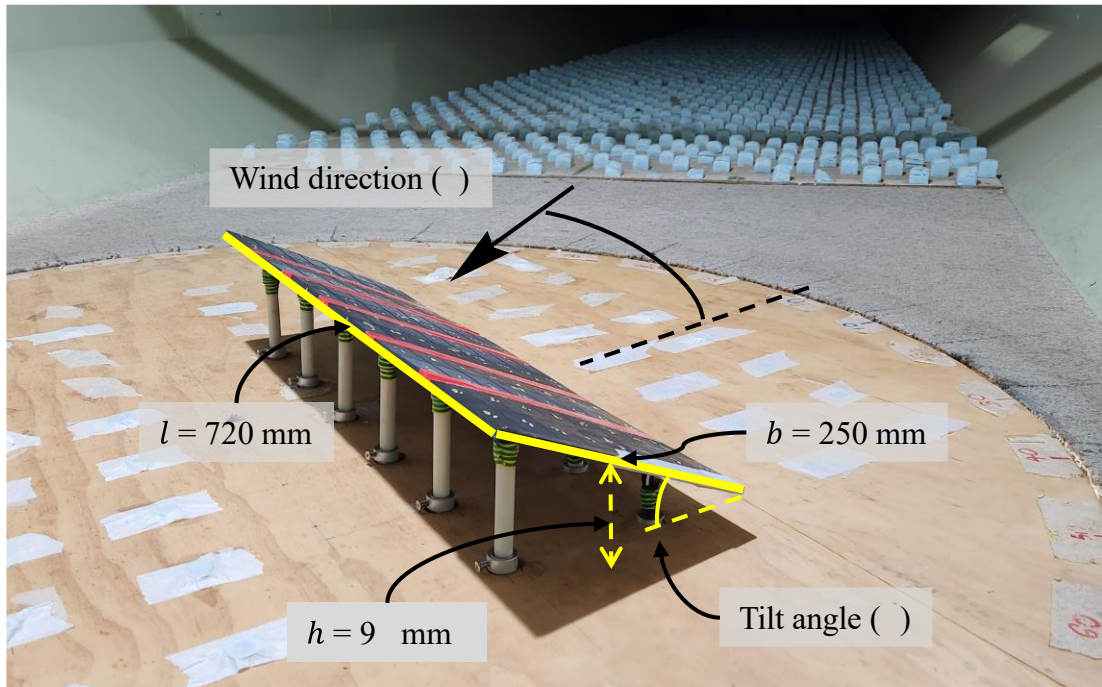


Figure 3.3. Rigid model attached to turntable in the wind tunnel ($\alpha = 20^\circ$, $\theta = 60^\circ$)

Top and bottom surface pressures, at 32 taps on each module (250 mm x 120 mm), were measured simultaneously to give net (i.e. (top-bottom)) pressure fluctuations. These fluctuating pressures were low-passed filtered at 250 Hz and sampled at 500 Hz, for 60 sec (i.e. corresponding to about 10 mins in full scale), and the net pressure coefficients $C_{pn}(t) = p_n(t) / \left(\frac{1}{2} \rho \bar{U}_h^2 \right)$, recorded. Figure 3.4 shows the sixteen top pressure taps on each module.

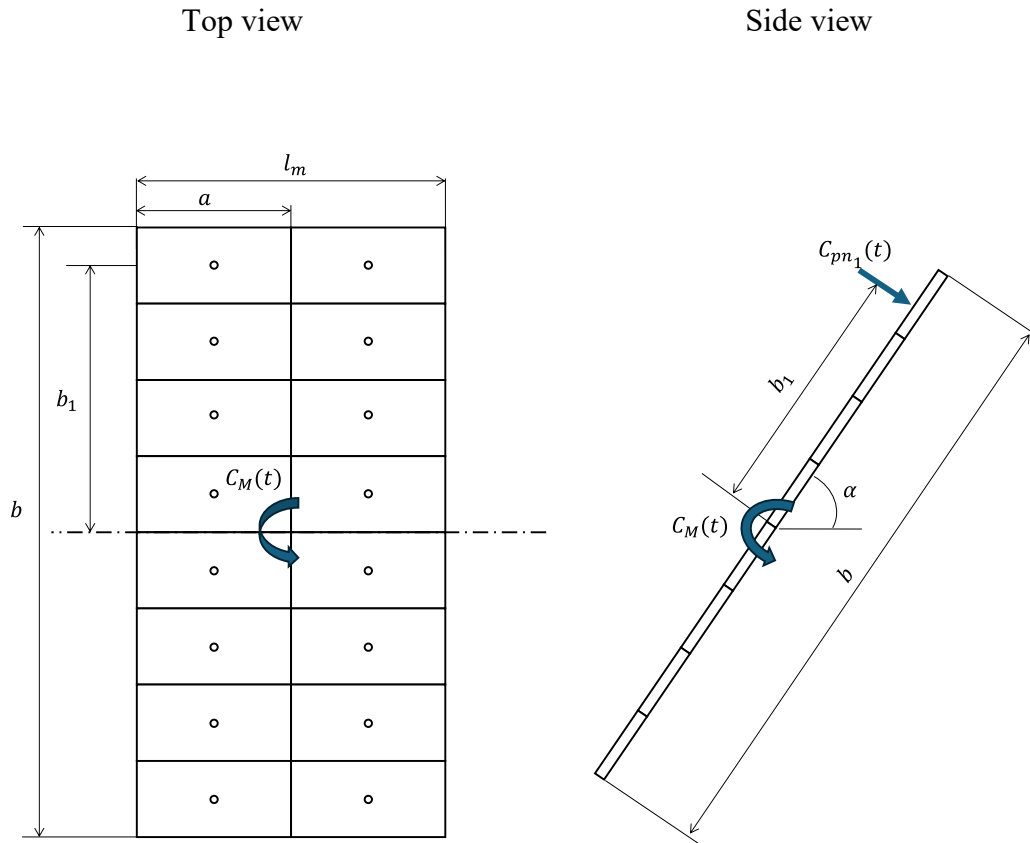


Figure 3.4. Diagram of a typical module consisting of sixteen panels

The pressure at each position b_i was utilized to calculate the moment coefficients $C_M(t)$ on each module using Equation 3.1.

$$C_M(t) = \frac{\sum_{i=1}^{16} C_{pn_i}(t) a \cdot b_i}{Ab} \quad 3.1$$

Where, $C_{pn_i}(t)$ is the time-varying net pressure coefficient at the location b_i (top and bottom tap location), a is the length of each panel, l_m is the length of the module, and $A = l_m \cdot b$, is the area of the module. The mean moment coefficients for each 90-second-

run were also obtained using: $C_{\bar{M}} = \frac{\sum_{i=1}^{16} C_{\bar{p}n_i} a \cdot b_i}{Ab}$.

3.3 Prototype solar tracker array

The prototype solar tracker used in this study represents standard commercial components readily available in the market and widely installed in the field. The prototype is shown in Figure 3.5.

The solar panels are a composite structure comprising an aluminium frame, protective glass, and silicon/cellulose solar cells. Each panel has a breadth $b = 1952$ mm, a length $l = 992$ mm and thickness $d = 40$ mm, and an average mass of 20 kg/panel. The rails are 2-m-long aluminium omega sections. These components are shown in Figure 3.6.

The torque tube properties were determined from a summary of information for tubes used by the industry. Two distinct circular cross-sections for the torque tube were selected from a commercial catalogue for the prototypes. The first cross-section has an external diameter $D_0 = 210$ mm and an internal diameter $D_i = 160$ mm. The second cross-section had an external diameter $D_0 = 84.4$ mm and an internal diameter $D_i = 71.8$ mm. Details of the calculations of the prototype's mechanical properties are shown in Appendix A.

The prototype's posts were not assigned a specific structural component, as they were assumed to act solely as supports for the solar trackers, with only their elevation

influencing the structure's wind loads but not structural response (i.e. torque). In practice, posts are typically steel I-beams driven into the ground, with bearings attached at the top to facilitate the placing and rotation of the torque tube.

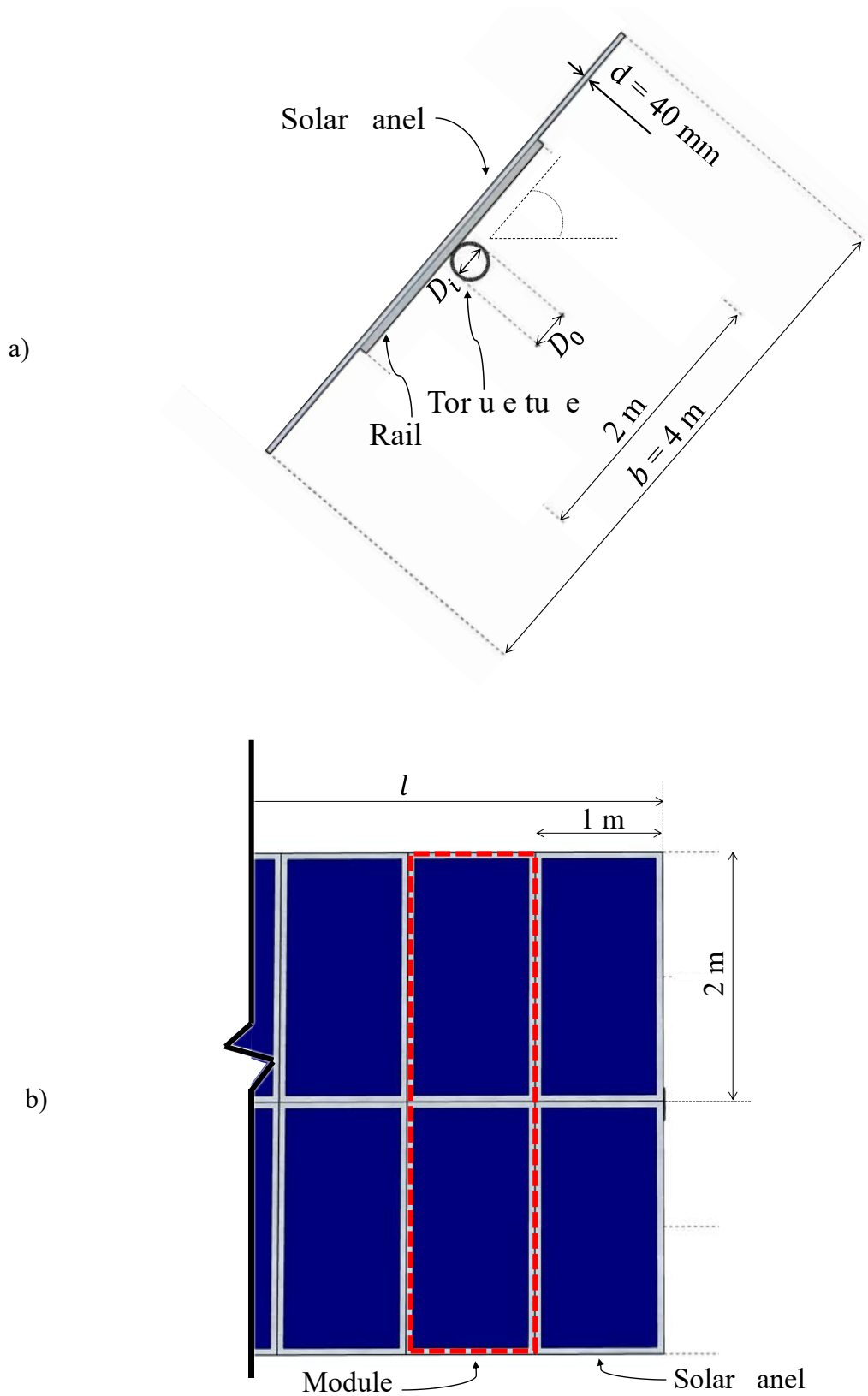


Figure 3.5. Prototype solar tracker array. a) Side view and b) Top view

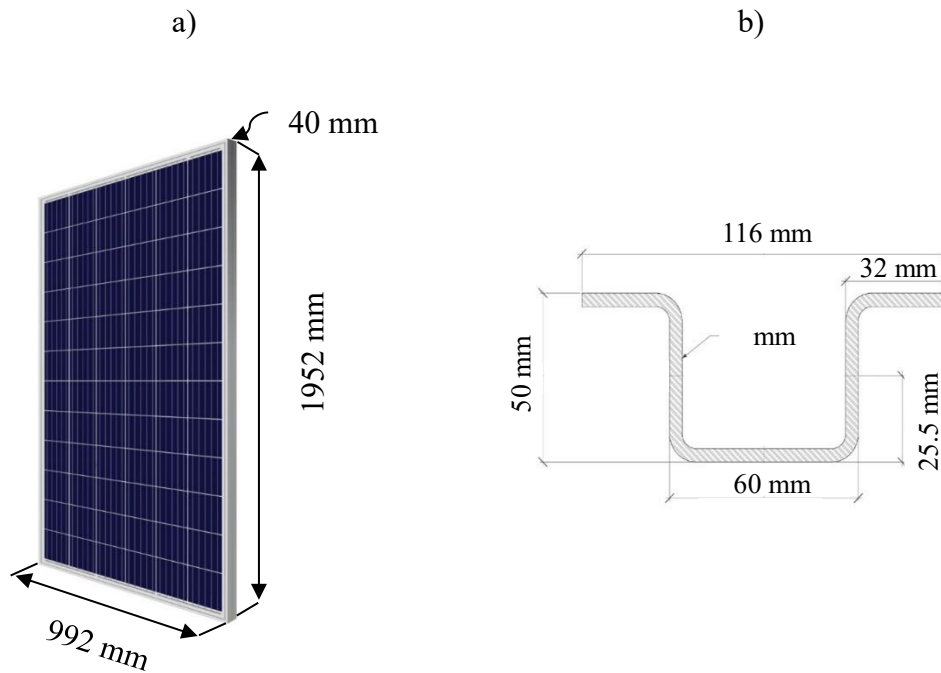


Figure 3.6. Prototype components: a) solar panel, and b) omega section rail (cross-section view)

3.4 Model scaling

Modelling of a structure to assess wind effects in boundary-layer winds, requires the approach of dimensional analysis. A series of prototype variables need to be identified and modelled, so that the response of the structure (e.g. dynamic response) can be accurately simulated at model scale.

The following parameters were considered:

\bar{U}_z : the mean wind speed at elevation z ;

σ_u : Standard deviation of the wind speed;

$I_u = \sigma_u / \bar{U}_z$: Turbulence intensity of the wind speed at elevation z ;

L_u : Integral length scale of turbulence;

z_0 : Roughness length defining the approaching terrain and velocity profile;

f : Frequency of velocity fluctuations;

ρ : Density of air;

μ : Viscosity of air;

p : Pressure acting on the structure;

L_s : Length associated with the structure;

ρ_s : Density of the structure;

E : Young's modulus of the structure (Solar panel array);

G : Shear modulus of the structure (Torque tube);

I_s : Second moment of area of the structure (Solar panel array);

J_s : Polar moment of inertia of the structure (Torque tube);

f_0 : Natural (torsional) frequency of the structure;

ζ_0 : Damping ratio of the structure;

Dynamic similarity with respect to these parameters can be achieved by combining them into non-dimensional parameters, as follows:

\bar{U}_z / \bar{U}_h : Velocity profile;

$f S_u(f) / \sigma_u^2$: Normalised spectral density for the wind speed;

$f L_s / \bar{U}_h$: Strouhal number (St);

$\rho \bar{U}_h L_s / \mu$: Reynolds number (Re);

$p / (\frac{1}{2} \rho \bar{U}_h^2)$: Pressure coefficient;

ρ_s / ρ : Density ratio;

$\rho \bar{U}_h^2 / E$: Cauchy number for relationship between bending stiffness of panels and inertial forces (air);

$\rho \bar{U}_h^2 / G$: Cauchy number for internal shear forces in torque tube and inertial forces (air).

Aeroelastic modelling requires achieving similarity between the model (subscript m) and prototype (subscript p) parameters to ensure the dynamic response of the model accurately represents the prototype behaviour. This means that the non-dimensional parameters of the model and the prototype, should be numerically equal. The prototype to model ratio is indicated with the subscript “ r ”.

In this study, the Cauchy number relating inertial forces to elastic forces was matched between the model and prototype to achieve similarity with bending of the panels and torsion of the tube, as $\left(\frac{\rho \bar{U}^2}{EI/L^4}\right)_m = \left(\frac{\rho \bar{U}^2}{EI/L^4}\right)_p$ and $\left(\frac{\rho \bar{U}^2}{GJ/L^4}\right)_m = \left(\frac{\rho \bar{U}^2}{GJ/L^4}\right)_p$. Here, EI and GJ are the flexural rigidity of the panels and the torsional rigidity of the torque tube respectively. Then, given the density of the air is the same for the model and the prototype, the ratio is $\rho_r = 1$. The Cauchy number condition is given by Equations 3.2 and 3.3.

$$(EI)_r = L_r^4 U_r^2 \quad 3.2$$

$$(GJ)_r = L_r^4 U_r^2 \quad 3.3$$

The requirement to maintain a constant ratio of inertia forces is that the density ratio of the model and the prototype must be the same: $\rho_{sr} = 1$. This is satisfied by the mass per unit length ratio, given by Equation 3.4.

$$m_r = L_r^2 \quad 3.4$$

Therefore, the required stiffness of the panels and tube, and the mass distribution of the model can be determined by defining the length ratio L_r , and wind speed ratio U_r . These scaling rules are crucial for replicating the aeroelastic behaviour in a model as described by Simiu and Yeo (2019), Martínez-García et al., (2021) and Rodríguez-Casado et al., (2024).

3.5 Aeroelastic solar tracker models

Five distinct models, listed in Table 3.1, were constructed for wind tunnel testing at a length scale $L_r = 1/20$ for a velocity ratio $U_r = 1/2$, based on the prototype described in Section 3.3. The length of the models was varied to achieve different aspect ratios. The materials selected to manufacture the models were PLA plastic, for the panels and rails, and brass for the torque tube.

Table 3.1. Parameters of the prototype and aeroelastic models

Model		Prototype				Aeroelastic model			
ID	Number of modules	Total length (m)	Torque tube			Total length (mm)	Torque tube		
			Cross section	External diameter D_0 (mm)	Internal diameter D_i (mm)		Cross section	External diameter D_0 (mm)	Internal diameter D_i (mm)
I-a	16	16	Circular hollow	84.4	71.8	800	Circular hollow	7.94	7.23
I-b	24	24				1200			
I-c	32	32				1600			
II-a	16	16	Circular rod	210	160	800	Circular rod	8	-
II-b	32	32				1600			-

Model I-a and II-a have the same length, accommodating 16 solar panel modules each, while Model I-b and Model I-c and II-b have longer lengths, of 24 and 32 modules respectively. Model II-a and II-b utilized a solid brass rod as the torque tube, while models I-a, I-b and I-c employed a hollow brass tube. These variations in length and torque tube cross-section produced different mechanical properties such as damping, stiffness, and inertia, which were determined for each model.

Given the flexural rigidity of the prototype solar panel $(EI)_p$, the Young's modulus of PLA ($E_m = 4 \text{ GPa}$), and considering a rectangular cross section, using

Equation 3.2 gives model thickness, $d_m = \sqrt[3]{12L_r^4 U_r^2 (EI)_p / bE_m} = 0.47 \text{ mm}$.

Given, the mass per unit length of the prototype solar panel (20 kg/m) and density of PLA (1200 kg/m³), using Equation 3.4 results in a model mass per unit length, $m_m = 0.05 \text{ kg/m}$. Mass was added to the model as ribs on the panels, in intervals of 50

mm, (i.e., at the edges of each individual panel). The same solar panel-rail system was utilized for all models.

Given the torsional rigidity of the prototype torque tube $(GJ_o)_p$, the shear modulus of brass, $G_m = 36 \text{ GPa}$, the diameter of the brass rod used as the torque tube was determined from Equation 3.3. Then, the diameter of the torque tube for Model II-a

can be expressed $D_m = \sqrt[4]{32L_r^4 U_r^2 (GJ_o)_p / \pi G_m} = 8 \text{ mm}$; and for the rest of the models,

$$D_{0m} = \sqrt[4]{32L_r^4 U_r^2 (GJ_o)_p 0.02 / (\pi G_m)} = 8 \text{ mm (resulting in } D_{im} = 7.8 \text{ mm)}.$$

The mass per unit length of model torque tube was 0.5 kg/m, obtained with Equation 3.4 and adopting the density of brass (8800 kg/m³). The additional mass required was added to the rod as brass screws. Further details of the calculations of the dimensions of the models can be found in Appendix A.

The panels were attached to the torque tube with brass screws. 100 mm tall PLA legs (equivalent to 2 m prototype posts) were used to support the torque tube. A cylindrical adapter, which allowed the panels to be inclined at different tilt angles α , was attached to the fixed end. Figure 3.7 shows a sketch of the models. Details of the models can be found in Appendix A.

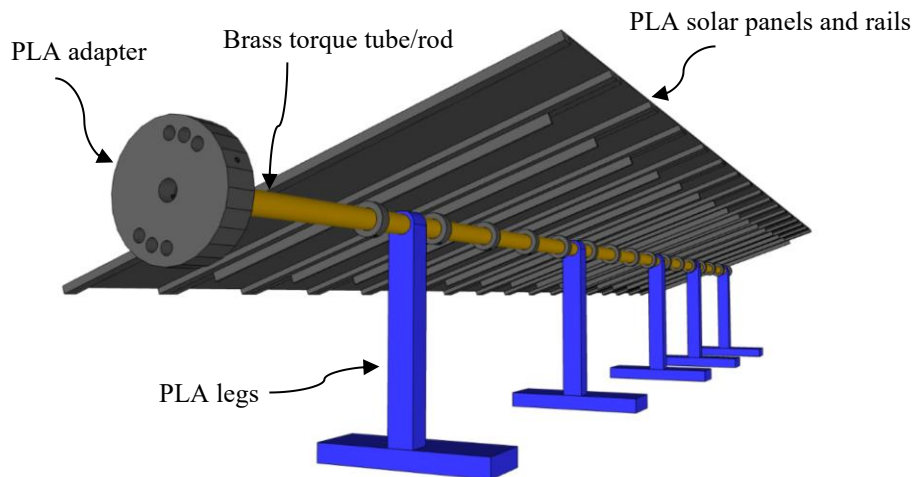
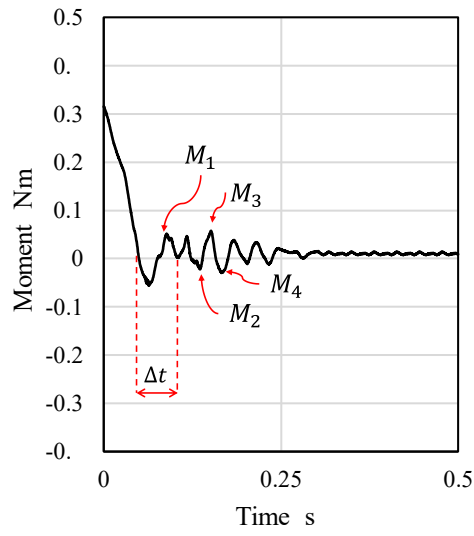


Figure 3.7. General view of the model and adapter

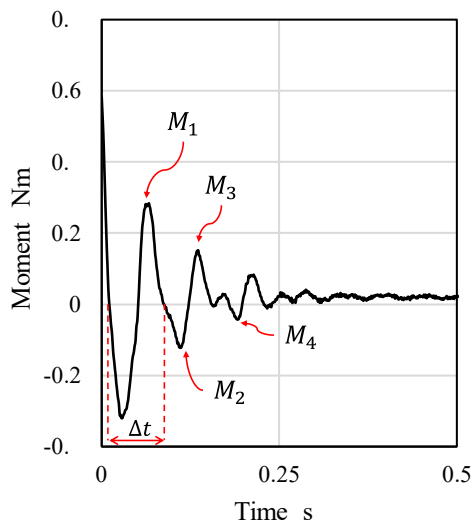
The natural frequency in torsion was measured experimentally by twisting the model, with no wind acting and measuring its response using the moment transducer at the fixed end.

Figure 3.8 and Figure 3.9 show the torsional response of each model measured after an initial twist and release from equilibrium. This test was repeated several times to obtain the average natural frequency in torsion $f_0 = 1/\Delta t$, where Δt is the period to complete one cycle. The torsional stiffness of each model is $k_0 = GJ/l$.

Model I-a



Model I-b



Model I-c

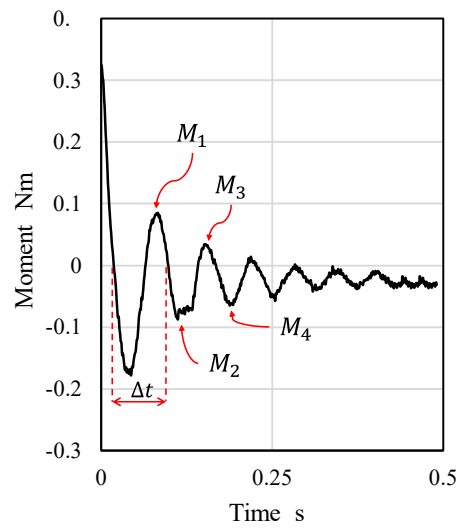


Figure 3.8. Moment response vs time. Models I-a, I-b and I-c

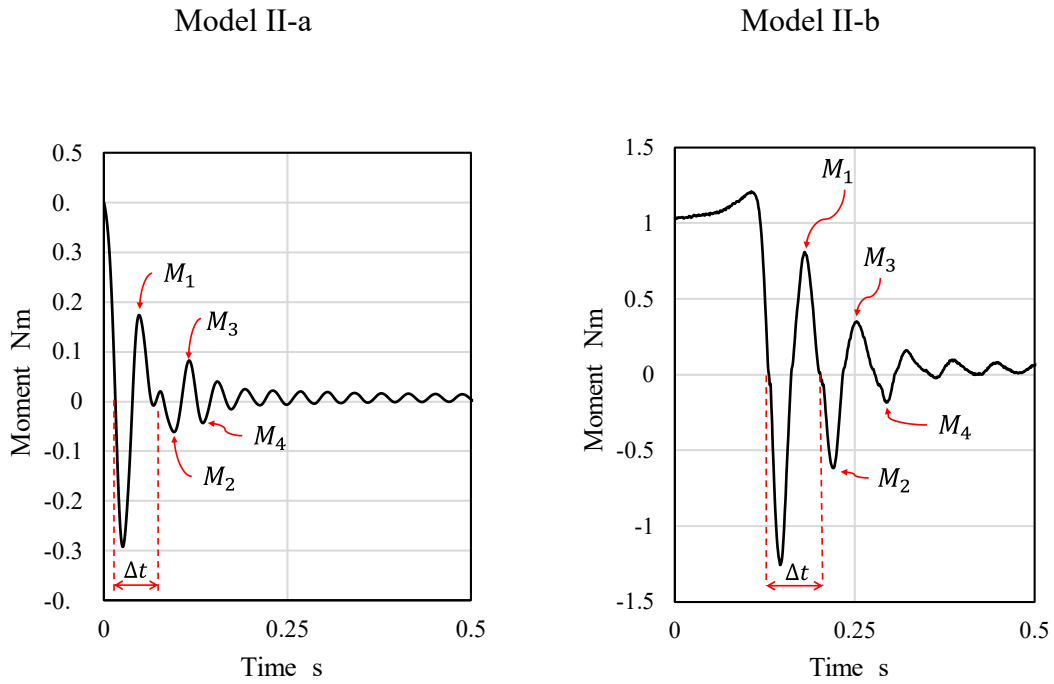


Figure 3.9. Moment response vs time. Models II-a and II-b

The Hilbert transform was applied to the measured moment decaying function of the torsional oscillations. The logarithmic decrement was obtained as $\delta = \ln[(M_1 - M_2)/(M_3 - M_4)]$; where M_1 and M_3 are amplitudes of two successive positive peaks and M_2 and M_4 are amplitudes of two successive negative peaks. The damping ratio ζ_0 was calculated as $\zeta_0 = \delta/2\pi$. The structural damping $c_0 = 2I_0\zeta_0(2\pi f_0)l$ was then determined. The mechanical properties of the models are summarized in Table 3.2.

Table 3.2. Mechanical properties in torsion of aeroelastic models

Model	Aspect ratio [l/b]	Natural frequency f_0 [Hz]	Structural Stiffness k_0 [Nm]	Damping ratio ζ_0	Structural Damping c_0 [Nm/s]
I-a	4	20.9	11.6	0.12	0.02
I-b	6	14.8	7.9	0.15	0.04
I-c	8	7.6	6.0	0.28	0.06
II-a	4	22.0	17.0	0.22	0.04
II-b	8	14.6	8.8	0.22	0.09

3.6 Wind tunnel testing

Testing of the aeroelastic models were performed in two parts. The first part was aimed at determining the wind loads acting on the models (i.e. Moment coefficients C_M) and the second part, to determine the wind speed at which the models became unstable (i.e. Critical wind speed U_{cr}). Figure 3.10 shows a schematic diagram of the model in the wind tunnel.

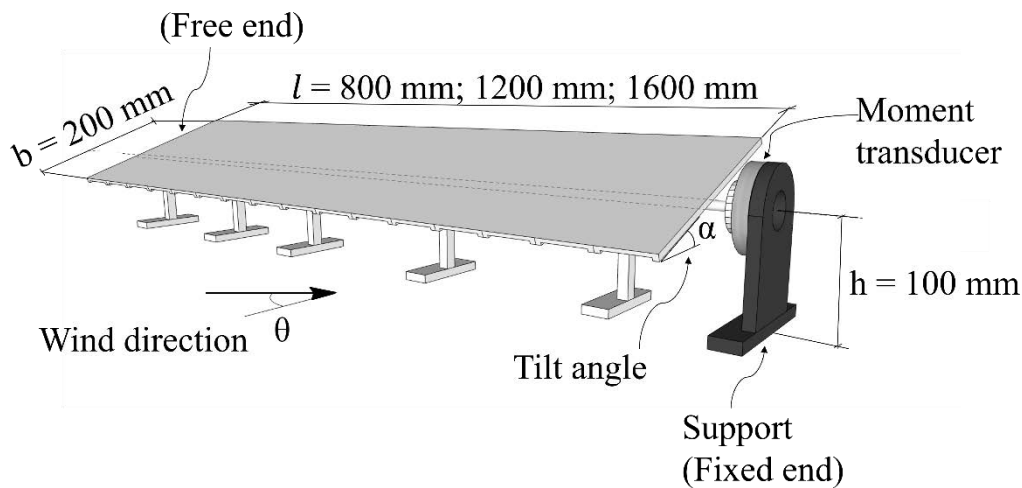


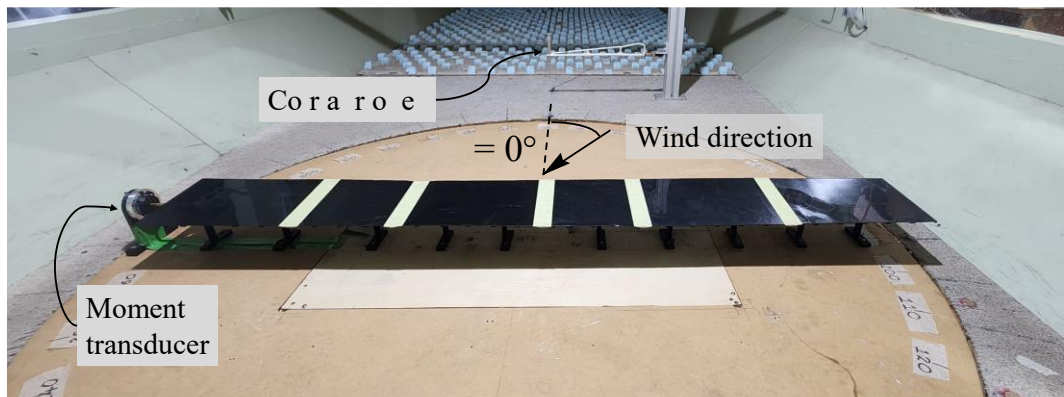
Figure 3.10. Schematic diagram of the aeroelastic model in the wind tunnel, representing all five models

3.6.1 Wind loading test

The models were setup on the turntable as shown in Figure 3.11. Tests were carried out for tilt angles (α) listed in Table 3.3; for a range of wind directions (θ) from 0° to 180° , in steps of 10° . The range of wind speeds at which the tests were carried out are shown in Table 3.3. The time varying moment $M(t)$ was measured at 1000 Hz, and low pass filtered at 500 Hz, using a moment transducer. Further details of the equipment are provided in Appendix B.

The length and velocity ratios gave a time ratio, $T_r = L_r/U_r = 10$. Therefore, the fluctuating moments were recorded for 60 seconds in model scale for each run, corresponding to 10 minutes in full scale. Five runs were performed for each approach wind direction. The time-varying approach wind speeds were measured with the TFI Cobra Probe positioned upstream at the same height as the tube height (100 mm).

a)



b)



Figure 3.11. Set up in the wind tunnel. a) Model I-c at $\alpha = 0^\circ$, and $\theta = 0^\circ$; b) Model I-b at tilt angle $\alpha = 50^\circ$, and $\theta = 70^\circ$

Table 3.3. List of wind tunnel experiments

Model	Tilt angle (α) [°]	Wind direction (θ) [°]	Mean wind speed \bar{U}_h [m/s]
I-a	0, 5, 10, 20, 25, 30, 40, 50	0, 45, 90, 135, 180	6.5, 7.5, 8.5
I-b	0, 5, 10, 15, 20, 25, 30, 40, 50	0 to 180 (10° intervals)	6.5, 7.5
I-c	0, 5, 10, 15, 20, 25, 30, 40, 50	0 to 180 (10° intervals)	6.5, 7.5, 8.5
II-a	0, 5, 10, 20, 25, 30, 40, 50	0 to 180 (10° intervals)	6.5, 7.5, 8.5
II-b	0, 5, 10, 20, 25, 30, 40, 50	0, 40, 90, 140, 180	7.5

The moments measured are represented as moment coefficients $C_M(t) = \frac{M(t)}{\frac{1}{2}\rho\bar{U}_h^2 Ab}$

referenced to the mean dynamic pressure at the tube height $h = 100$ mm, (2 m full-scale).

Here, $M(t)$ is the time-varying moment at the fixed end and $A = l \cdot b$, the area of the array. The mean, maximum, minimum, and standard deviation moment coefficients for

each 60-second-run were obtained using: $C_{\bar{M}} = \frac{\bar{M}}{\frac{1}{2}\rho\bar{U}_h^2 Ab}$, $C_{\hat{M}} = \frac{\hat{M}}{\frac{1}{2}\rho\bar{U}_h^2 Ab}$,

$C_{\check{M}} = \frac{\check{M}}{\frac{1}{2}\rho\bar{U}_h^2 Ab}$, $C_{\sigma_M} = \frac{\sigma_M}{\frac{1}{2}\rho\bar{U}_h^2 Ab}$. Where \bar{M} , \hat{M} , \check{M} , σ_M are the mean, maximum,

minimum and standard deviation moments measured at the fixed end of the model.

The maximum and minimum moments were obtained as the average of the peaks of the five runs. \bar{U}_h is the equivalent 10-min mean wind speed at the tube height h .

3.6.2 Critical wind speed test

The Models were then subjected to wind tunnel testing to determine the critical wind speed at the onset of instability. Tilt angles (α) of 0° , 5° , 10° , 15° , 20° , 25° , and 30° were evaluated, along with approach wind directions (θ) of 0° , 10° , 20° , 30° , 110° , 160° , 170° , and 180° , as these were determined to be the cases where instability occurs with the speeds achievable in the wind tunnel. Time-varying moment and wind speed data were recorded simultaneously at progressively increasing wind speeds until the instability was visible. The test was then immediately stopped to prevent damaging the model and fixings.

The critical wind speed U_{cr} was determined by analysing the time-history data of the moment and wind speed. The onset of instability was identified as the point where the moment began to oscillate between positive and negative. The 10-second mean wind speed immediately preceding this point was calculated and averaged to determine the critical wind speed \bar{U}_{cr} . Figure 3.12 depicts a typical test measurement.

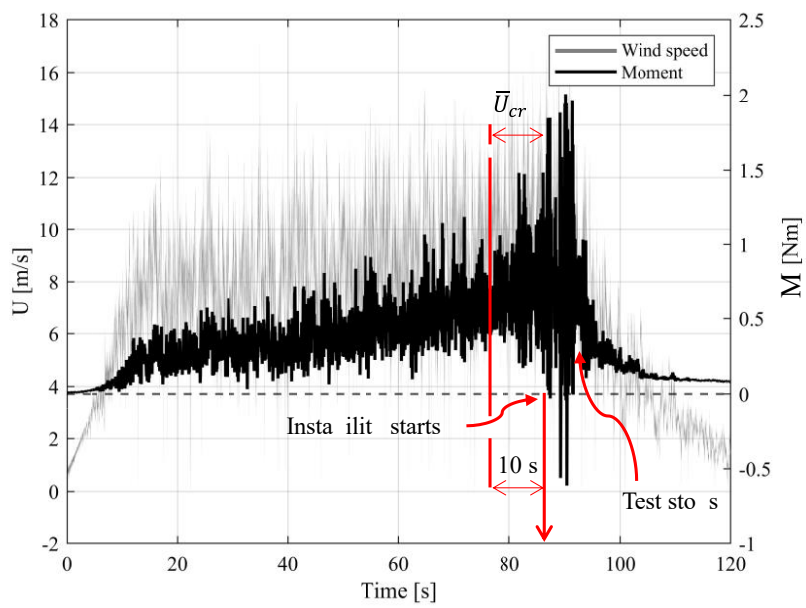
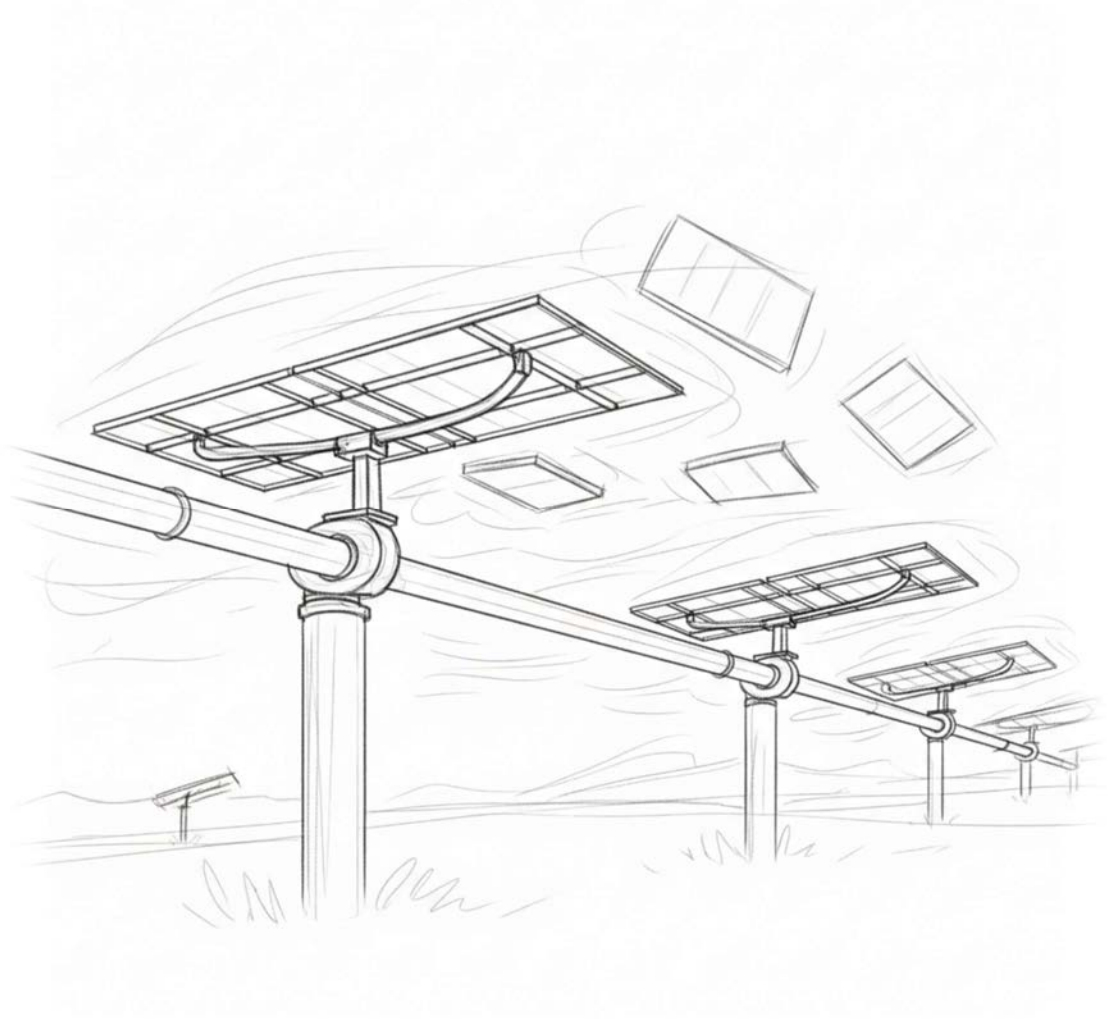


Figure 3.12. Moment and wind speed time-history of Model I-c, at $\alpha = 10^\circ$, and $\theta = 0^\circ$.



4 RESPONSE OF SOLAR TRACKERS – RESULTS

This Chapter presents the results from the wind tunnel tests described in Chapter 3. The analysis focuses on the wind loads (moment coefficients) and the aeroelastic response of the models.

Firstly, data collected using the rigid 1/20 scale model to derive mean and peak moment coefficients are presented. These are compared with moment coefficients obtained from the aeroelastic Models I-a and I-c, for a range of wind speeds highlighting similarities and differences.

A description of the aeroelastic behaviour of the models is presented, based on the response of the structure for different wind speeds and directions. Torsional galloping and divergence are identified by analysing the wind loading and response for each case, as well as the variation of the effective damping and stiffness.

Finally, the aerodynamic derivatives, A_2^* and A_3^* , are presented and discussed. These are plotted as a function of the reduced wind speed, U_{red} following the representation used by Taylor and Browne (2020) and Cárdenas-Rondón et al., (2023).

4.1 Wind Loading

This section analyses the mean and peak moment coefficients obtained using two sets of data. Firstly, the mean and peak moment coefficients derived from the rigid 1/20 scale model (described in Section 3.2) are presented. Then, the wind loading obtained using the aeroelastic models (described in Section 3.5) are presented and compared for the range of wind directions (θ). Finally, the variation of the wind loading vs tilt angle (α) is analysed and related to the aeroelastic instabilities.

4.1.1 Loads on rigid model

The analysis of the data collected revealed the pressure distribution across the panels. The results show that wind approaching from $\theta = 0^\circ$ generates net positive pressures on the panels, and that winds approaching from $\theta = 10^\circ$ generate net negative pressures. Winds approaching from $\theta = 90^\circ$ generally produce small net pressures, as noted by Ginger et al., (2019).

Figure 4.1 schematically illustrates the pressure distribution on the solar panels, showing that the combination of negative and positive net pressures produces a counterclockwise moment independent of wind direction.

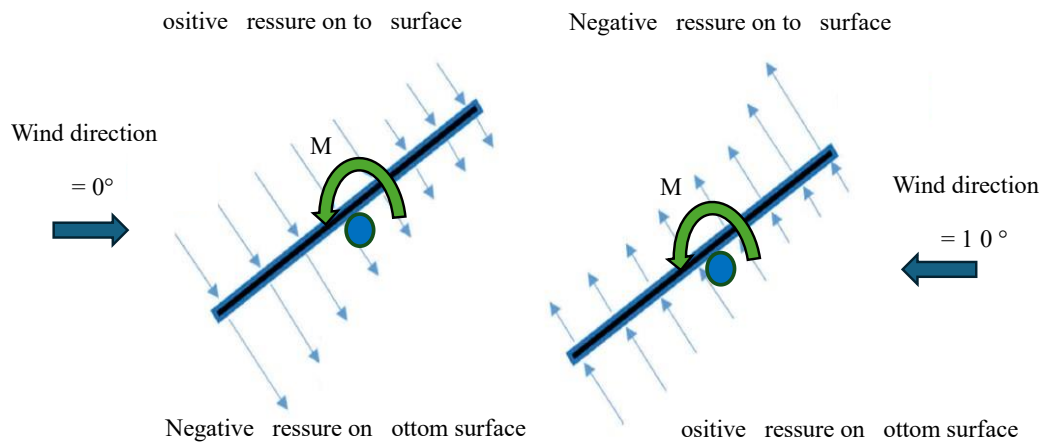


Figure 4.1. Mean pressure distribution on top and bottom surfaces of inclined panels and moment about the axis

The mean, maximum and minimum moment coefficients obtained from the rigid model tests for $\alpha = 0^\circ, 20^\circ$ and 30° are shown in Figure 4.2. The moment acting about the central axis of the modules for $\theta = 0^\circ$ and 10° , is similar in magnitude and direction. This is attributed to the pressure distribution on the array, which is higher near the leading edges of the panels for both wind directions as shown in Figure 4.1. At $\theta = 90^\circ$, the moment decreases because the pressures on the top and bottom surfaces balance each other, resulting in a low net pressure.

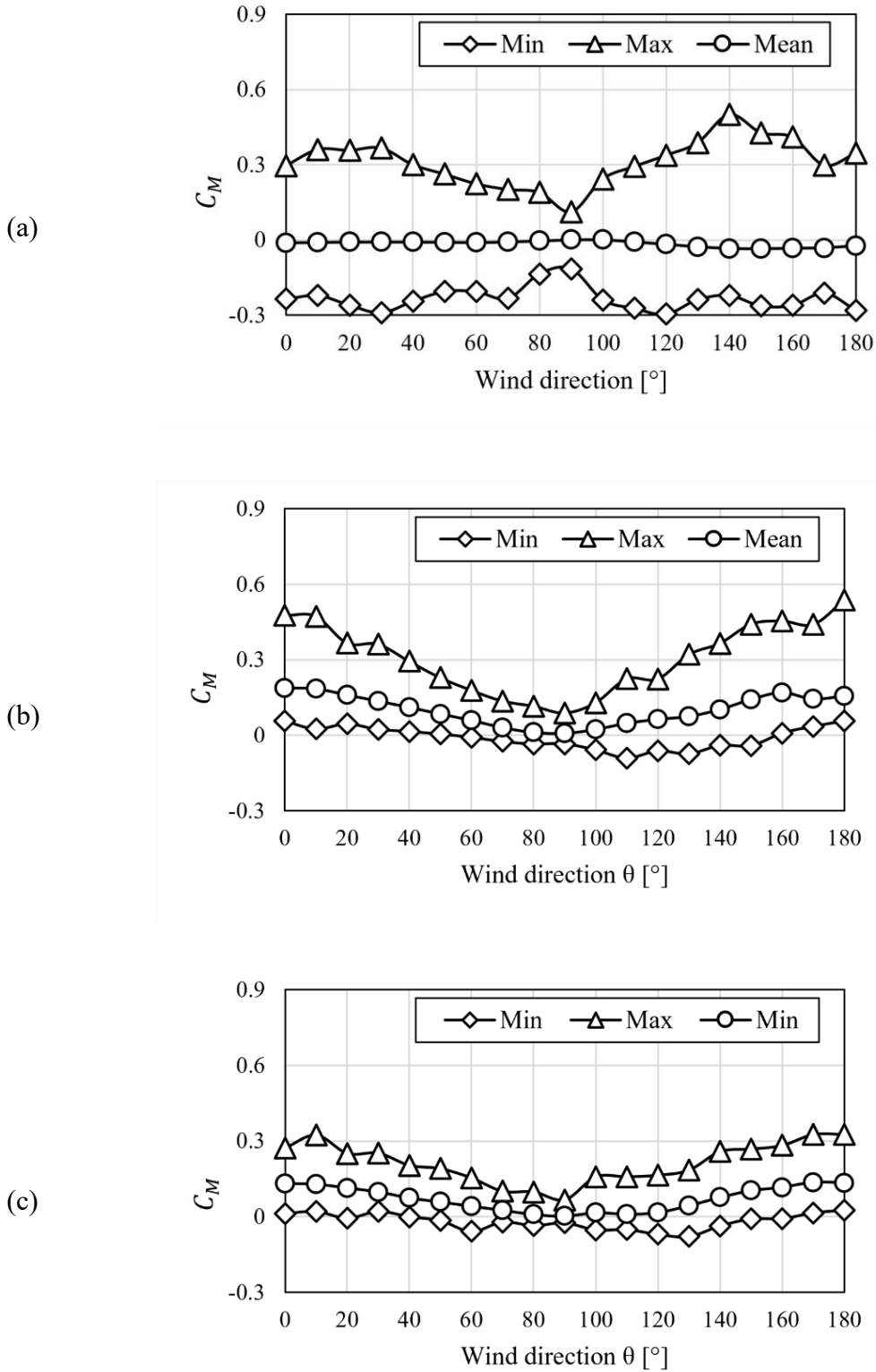


Figure 4.2. Mean, maximum and minimum moment coefficients obtained using the 1/20 scale rigid model for (a) $\alpha = 0^\circ$, (b) $\alpha = 20^\circ$, and (c) $\alpha = 30^\circ$

4.1.2 Wind loads on aeroelastic models

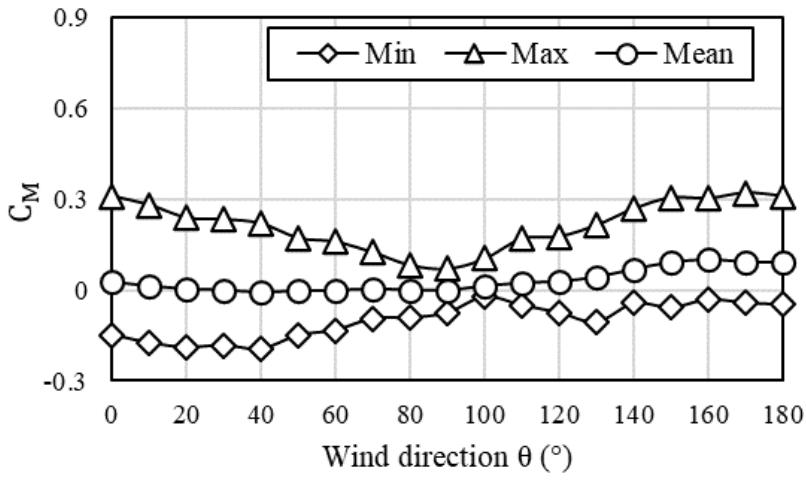
The variation of the mean and peak C_M with wind direction on Models I-c and II-a for tilt angles (α) of 0° , 10° , 20° , 30° , 40° and 50° , for $\bar{U}_h = 7.5$ m/s (model scale) are shown in Figure 4.3 to Figure 4.8. Further results and statistical data for all models can be found in Appendix C.

Results for $\alpha = 0^\circ$, in Figure 4.3, show that the mean moment coefficient is ≈ 0 for all wind directions (θ) and the peaks show the largest values at $\theta = 0^\circ$ and $\theta = 180^\circ$. The peaks drop progressively towards $\theta = 90^\circ$, similar to Figure 4.2 (a) where they reach their smallest values.

Figure 4.4 and Figure 4.5 show results for tilt angles $\alpha = 10^\circ$, and $\alpha = 20^\circ$. There is an increase in the mean moment coefficient, with the largest values for $\theta = 0^\circ$ and $\theta = 180^\circ$, and smallest at $\theta = 90^\circ$. The minimum moment coefficients are close to zero, for all wind directions. The mean and maximum moment coefficients increase in magnitude as the tilt angle increases and are always positive. These results in Figure 4.4 are similar to those obtained for the rigid model in Figure 4.2 (b).

Figure 4.6, Figure 4.7 and Figure 4.8 show results for tilt angles $\alpha = 30^\circ$, $\alpha = 40^\circ$, and $\alpha = 50^\circ$ respectively. Moment coefficients (mean and maximum) drop in magnitude as the tilt angle increases, but they are always positive. Minimum moment coefficients are close to zero for all tilt angles and wind directions. As explained in Section 2.1, increasing the tilt angle shifts the centre of pressure toward the plate centre (torque tube), thereby reducing the moment coefficient. The results in Figure 4.6 are similar to the results obtained for the rigid model in Figure 4.2 (c).

(a)



(b)

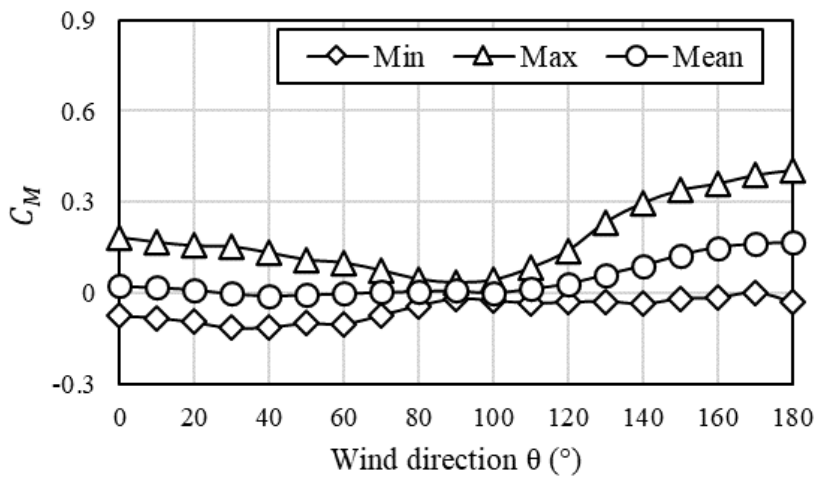
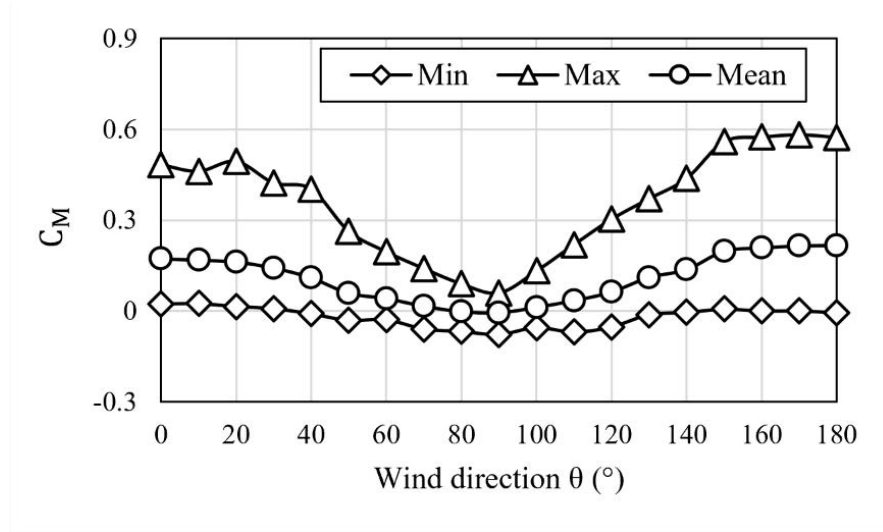


Figure 4.3. Mean, maximum and minimum moment coefficients vs wind direction (θ), at $\alpha = 0^\circ$ and, model scale mean wind speed $\bar{U}_h = 7.5$ m/s. (a) Model II-a ($l/b = 4$), and (b) Model I-c ($l/b = 8$)

(a)



(b)

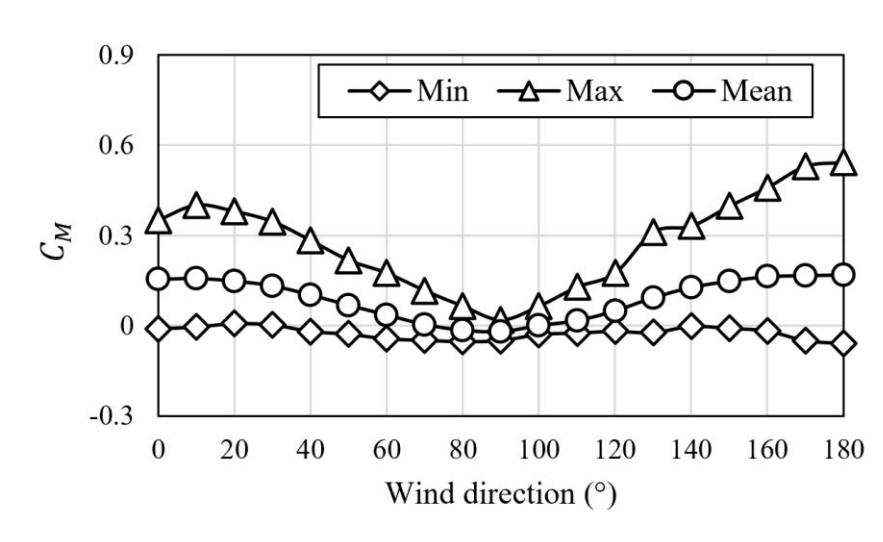
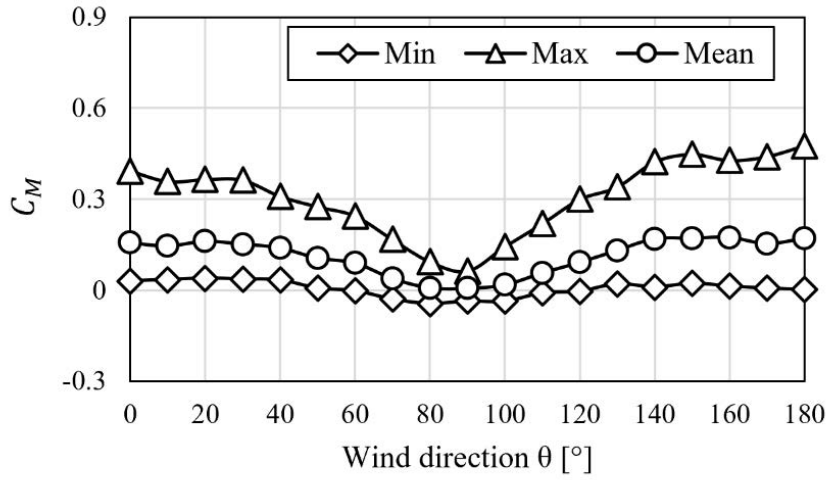


Figure 4.4. Mean, maximum and minimum moment coefficients vs wind direction (θ), at $\alpha = 10^\circ$ and, model scale mean wind speed $\bar{U}_h = 7.5$ m/s. (a) Model II-a ($l/b = 4$), and (b) Model I-c ($l/b = 8$)

(a)



(b)

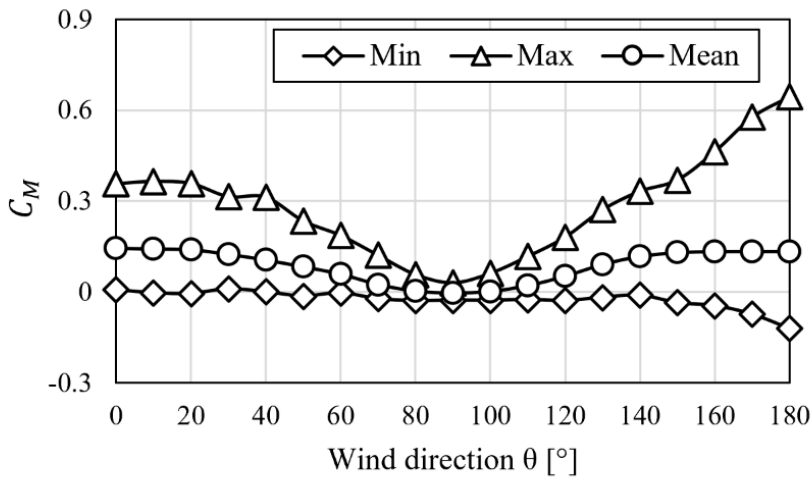


Figure 4.5. Mean, maximum and minimum moment coefficients vs wind direction (θ), at $\alpha = 20^\circ$ and, model scale mean wind speed $\bar{U}_h = 7.5$ m/s. (a) Model II-a ($l/b = 4$), and (b) Model I-c ($l/b = 8$)

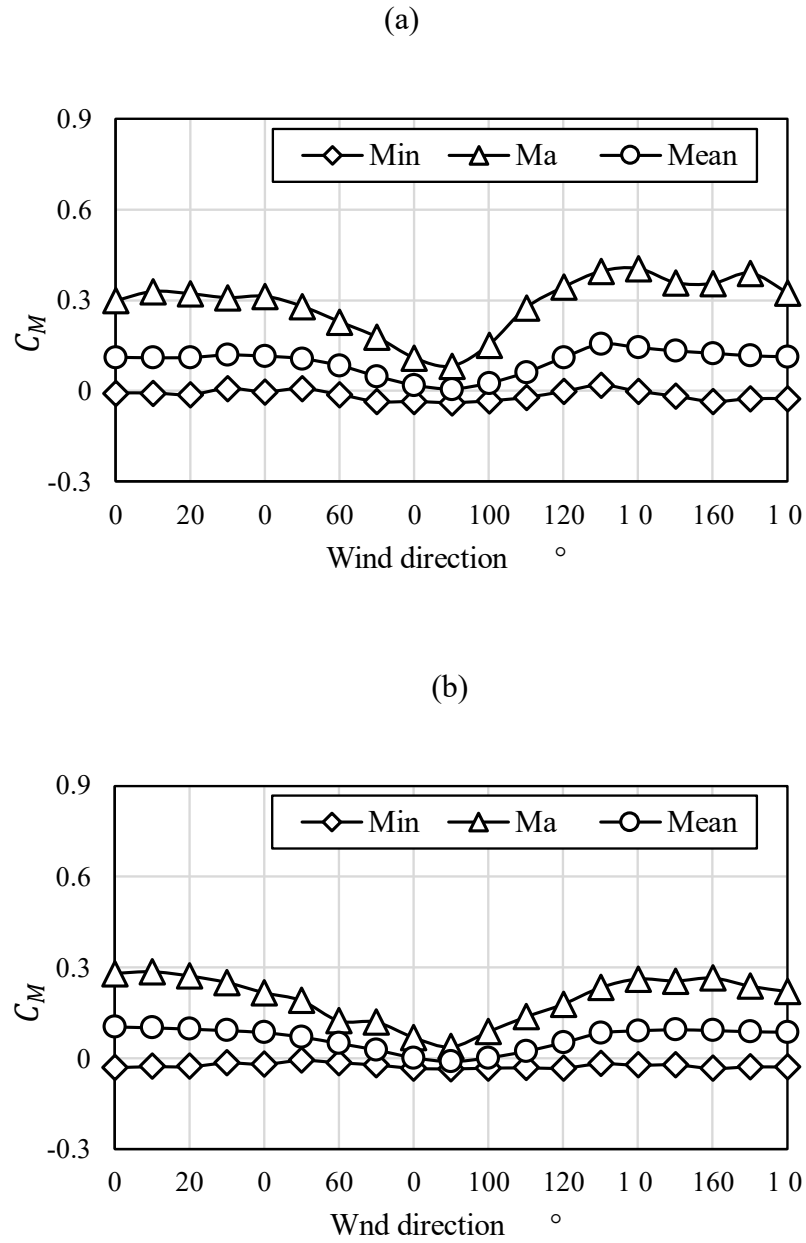
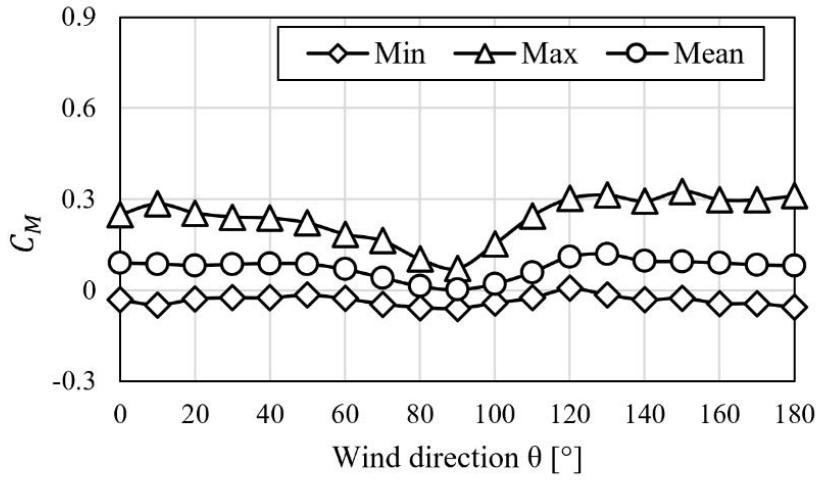


Figure 4.6. Mean, maximum and minimum moment coefficients vs wind direction (θ), at $\alpha = 30^\circ$ and, model scale mean wind speed $\bar{U}_h = 7.5$ m/s (model scale). (a) Model II-a ($l/b = 4$), and (b) Model I-c ($l/b = 8$)

(a)



(b)

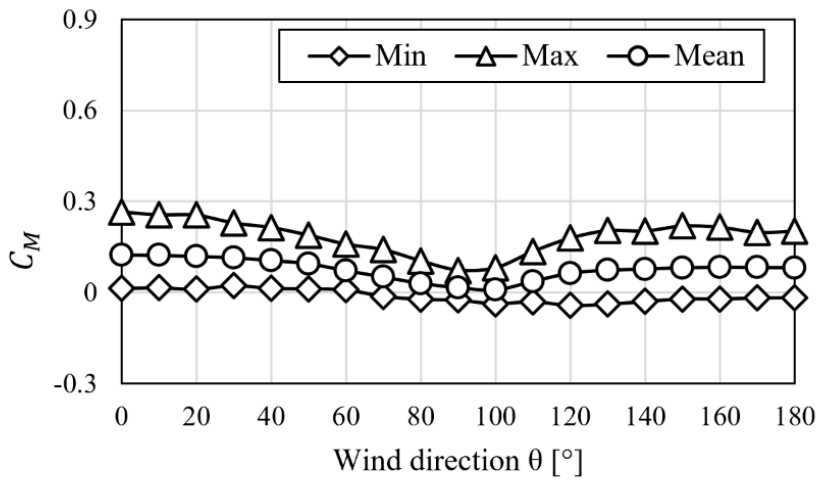
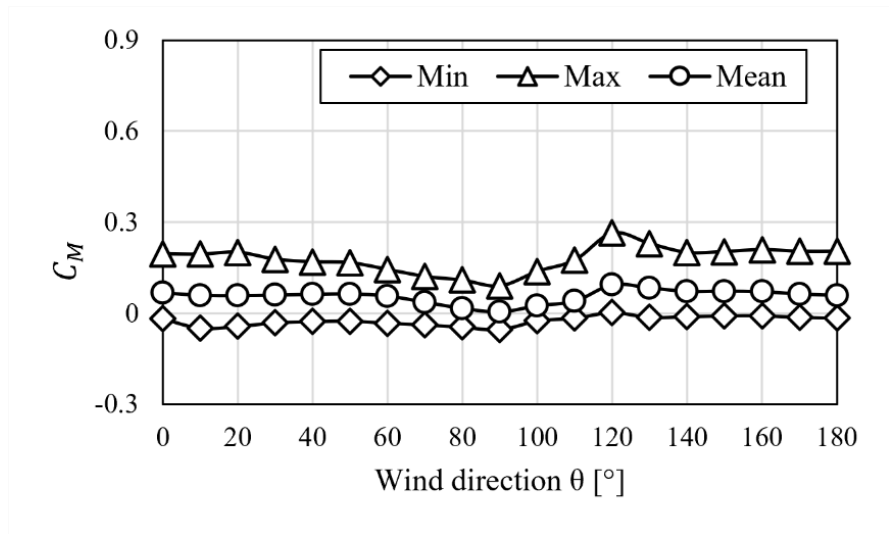


Figure 4.7. Mean, maximum and minimum moment coefficients vs wind direction (θ), at $\alpha = 0^\circ$ and, model scale mean wind speed $\bar{U}_h = 7.5$ m/s (model scale).

(a) Model II-a ($l/b = 4$), and (b) Model I-c ($l/b = 8$)

(a)



(b)

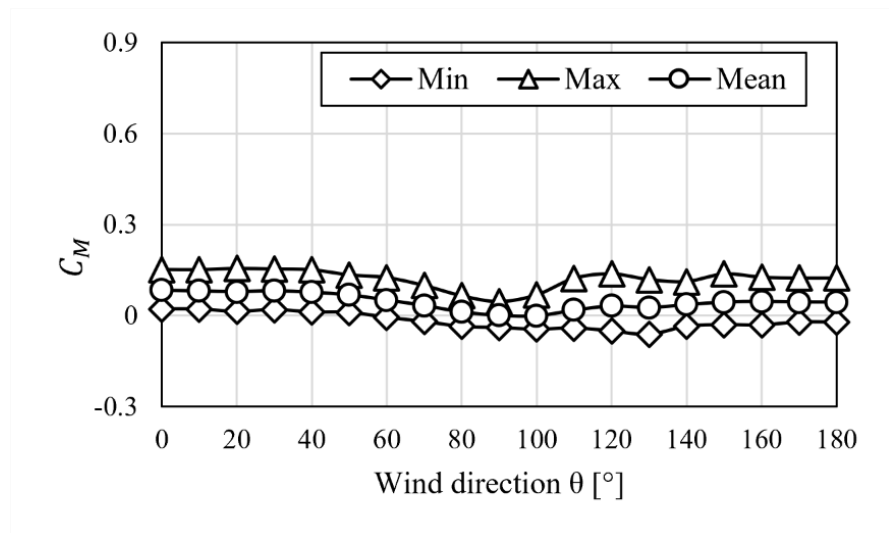


Figure 4.8. Mean, maximum and minimum moment coefficients vs wind direction (θ), at $\alpha = 50^\circ$ and, model scale mean wind speed $\bar{U}_h = 7.5$ m/s. (a) Model II-a ($l/b = 4$), and (b) Model I-c ($l/b = 8$)

The mean moment coefficients obtained with the aeroelastic models are within the range of other studies. Examples for different tilt angles (α) are shown in Table 4.1.

Table 4.1 Mean moment coefficient for $\theta = 0^\circ$

Tilt angle α ($^\circ$)	Taylor and Browne (2020)	Zang et al. (2023)	Cárdenas-Rondón et al. (2023)	Average $C_{\bar{M}}$ rigid model	Average $C_{\bar{M}}$ aeroelastic models
0	0.05	0.09	0.085	0.01	0.01
20	0.11	0.10	0.12	0.15	0.13
40	0.14	0.06	0.11	-	0.13

Figure 4.9 shows the mean moment coefficients $C_{\bar{M}}$ for Model I-c with tilt angles (α) and wind directions (θ). Two distinctive patterns can be identified: 1) for θ varying between 0° and 40° (Figure 4.9 (a)), and 140° and 180° (Figure 4.9 (c)); and 2) for θ between 50° and 130° (Figure 4.9 (b)).

In the first pattern, it can be seen that $C_{\bar{M}}$ increases for α between 0° and 15° , reaching its peak at about 15° , for θ varying between 0° and 40° (Figure 4.9 (a)). When θ varies between 140° and 180° , $C_{\bar{M}}$ reaches its maximum at $\alpha = 10^\circ$ (Figure 4.9 (c)). In the second pattern, (Figure 4.9 (b)), mean moments remain relatively unchanged for all θ and α . For $\theta = 0^\circ$ and 10° , a range of small tilt angles (i.e. $0^\circ < \alpha < 10^\circ$ to 15°), the increasing mean moment coefficient implies that $(\partial C_M / \partial \alpha) > 0$, which indicates susceptibility to divergence (Equation 2.3), when the effective stiffness reaches zero. Then, in a range of medium to large tilt angles (i.e. 10° to $15^\circ < \alpha < 50^\circ$), the decrease of moment implies $(\partial C_M / \partial \alpha) < 0$, which indicates susceptibility to torsional galloping, when the effective damping reaches zero (Equation 2.3). On the other hand, lateral wind directions θ , (from 50° to 130°) show little variation of the mean moment coefficient, suggesting that aeroelastic

instability is unlikely. Therefore, the wind direction θ and the tilt angle α are key parameters to consider in the analysis of the structural stability of solar trackers. Therefore, understanding the relationship between the moment coefficient variation and the tilt angle is essential to characterise the aeroelastic response of the structure. In this case, it allows to define the configurations (i.e. tilt angles) where the structure is prone to undergo divergence or torsional galloping. As presented in Section 2.3, divergence is related to variations of the moment coefficient in terms of the tilt angle where $(\partial C_M / \partial \alpha) > 0$. From Figure 4.9, occurs for tilt angle (α) between 0° and 10° , where there is an increase of the moment coefficient as the tilt angle increases.

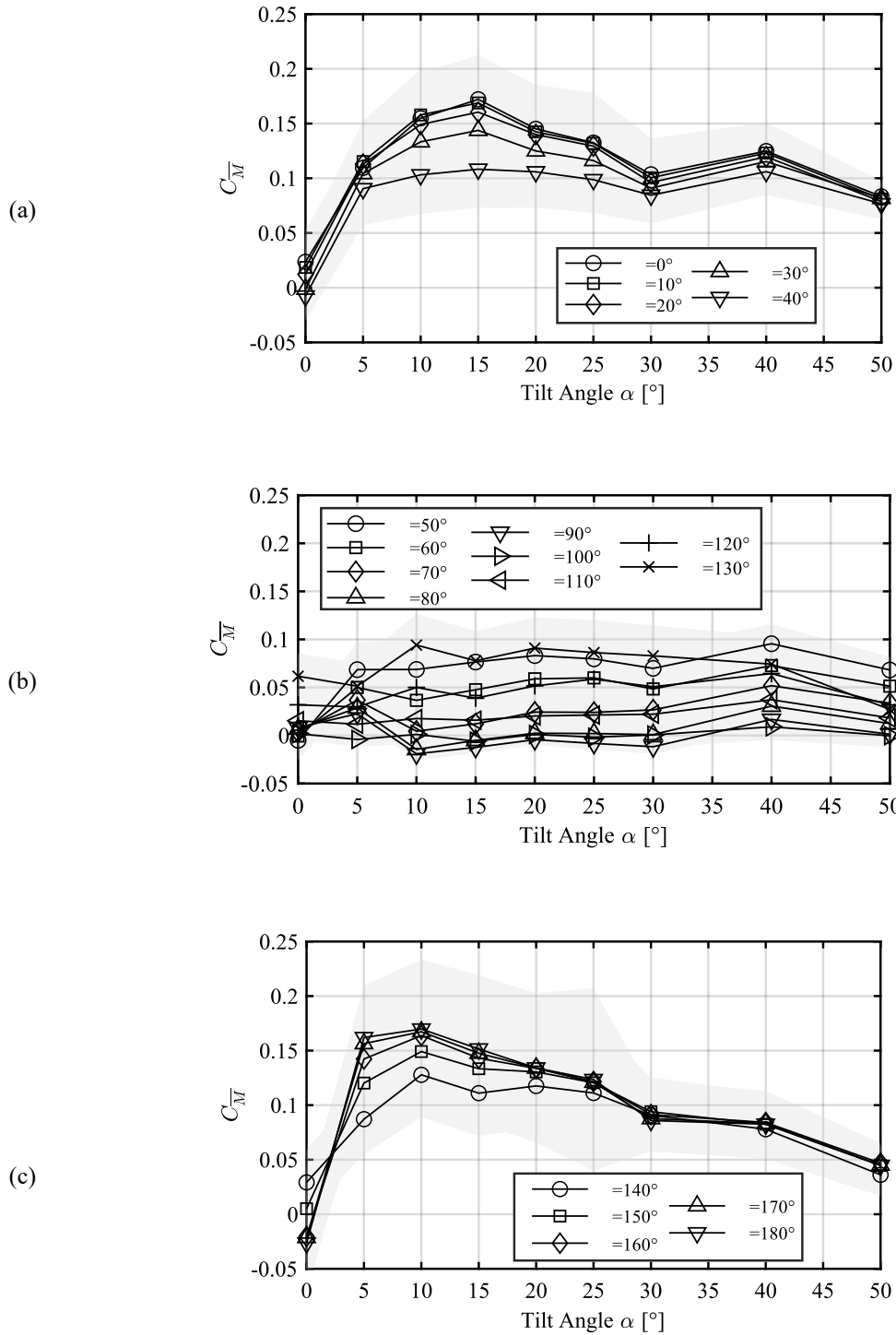


Figure 4.9. Mean moment coefficient $C_{\bar{M}}$ vs tilt angle α , for (a) $0^\circ < \theta < 50^\circ$, (b) $50^\circ < \theta < 130^\circ$, and (c) $130^\circ < \theta < 180^\circ$. The standard deviation is shown as a grey shade.

Model I-c

The relationship between the variation of $(\partial C_M / \partial \alpha)$ and the aeroelastic response of the structure is further studied in Section 4.2. The variation of $(\partial C_M / \partial \alpha)$ for Model I-c is calculated using the results shown in Figure 4.9. This is then applied in the linear formulation for determining the effective damping c_{eff} , the effective stiffness k_{eff} , and the aerodynamic derivatives A_2^* and A_3^* . These are discussed in Sections 4.3 and 4.4, respectively. Further results for all models can be found in Appendix C.

4.2 Aeroelastic instabilities

Theoretical values of the critical wind speed, U_{cr} for torsional galloping were determined using Equation 2.4. The calculations are shown in Appendix C. Experimental results were determined as per Section 3.6.2. These are shown in Appendix C.

Both theoretical and experimental results are shown in Table 4.2. Theoretical critical wind speeds for Model I-a, which has an aspect ratio of 4, are high. Such wind speeds cannot be achieved in the wind tunnel used for this study. Models I-b and I-c which have aspect ratios of 6 and 8, respectively, show lower critical wind speeds. The change in aspect ratio implies a variation of the stiffness (k_0) and natural frequency (f_0), as shown in Table 3.2. Here, the stiffness and the natural frequency decrease with increasing length of the model. This is because increasing length (i.e. increasing aspect ratio l/b), indicates decreasing natural frequency as $f_0 \propto (1/l)$. Then, the lower the natural frequency, the lower the critical wind speed.

Table 4.2. Theoretical and experimental critical wind speeds for torsional galloping

Model	Tilt angle α [°]	U_{cr} (Blevins) [m/s]	U_{cr} (Experimental) [m/s]
I-a	5	98.0	-
	10	72.6	-
	20	31.1	-
I-b	5	17.8	11.3
	10	31.7	10.7
	20	127.0	9.3
I-c	5	12.6	9.9
	10	12.6	10.2
	20	43.9	9.0

The wind speeds at the onset of torsional galloping were determined experimentally as described in Section 3.6.2. The instability curves presented in this section show the critical wind speeds U_{cr} at which the aeroelastic models transition from stable behaviour to unstable, torsional galloping oscillations. To normalise and compare the results, the reduced critical wind speed, $U_{red} = U_{cr}/(b \times f_0)$, is plotted against the tilt angle. Figure 4.10 shows the reduced critical wind speeds U_{red} for Models I-b, I-c and II-b for the range of tilt angles (α), and wind directions $\theta = 0^\circ$ and $\theta = 180^\circ$. These two wind directions have been indicated as the most critical by Taylor and Browne (2020), Martínez-García et al. (2021) and Cárdenas-Rondón et al. (2023).

The tilt angle (α) significantly influences the critical wind speed for instability. It can be seen that tilt angles (α) between 5° and 20° have a lower critical wind speed than small tilt angles ($\alpha < 5^\circ$) or large tilt angles ($\alpha > 25^\circ$). The traditional stow position ($\alpha = 0^\circ$), while becoming unstable at higher wind speeds, is not exempt from torsional

galling. For $\alpha > 25^\circ$, the wind speeds achieved in the wind tunnel did not enable any of the models to become unstable. Nonetheless, it is important to note that critical wind speeds were observed at higher tilts ($\alpha > 25$) by Martínez-García et al. (2021), Cárdenas-Rondón et al. (2023) and Zhang et al. (2023).

Figure 4.10 also shows that for $\theta = 10^\circ$, the critical wind speed is slightly lower than for $\theta = 0^\circ$. This behaviour can be essentially attributed to the aerodynamic impact of the support system (i.e. the torque tube and rails). Their irregular surface and structural complexity disrupt the incoming flow (i.e. $\theta = 10^\circ$) more significantly than the relatively smooth panel surfaces (i.e. $\theta = 0^\circ$), thereby enhancing local aerodynamic loading and promoting flow separation. Then, the enhanced flow disruption when the support system is exposed to the wind lowers the critical wind speed.

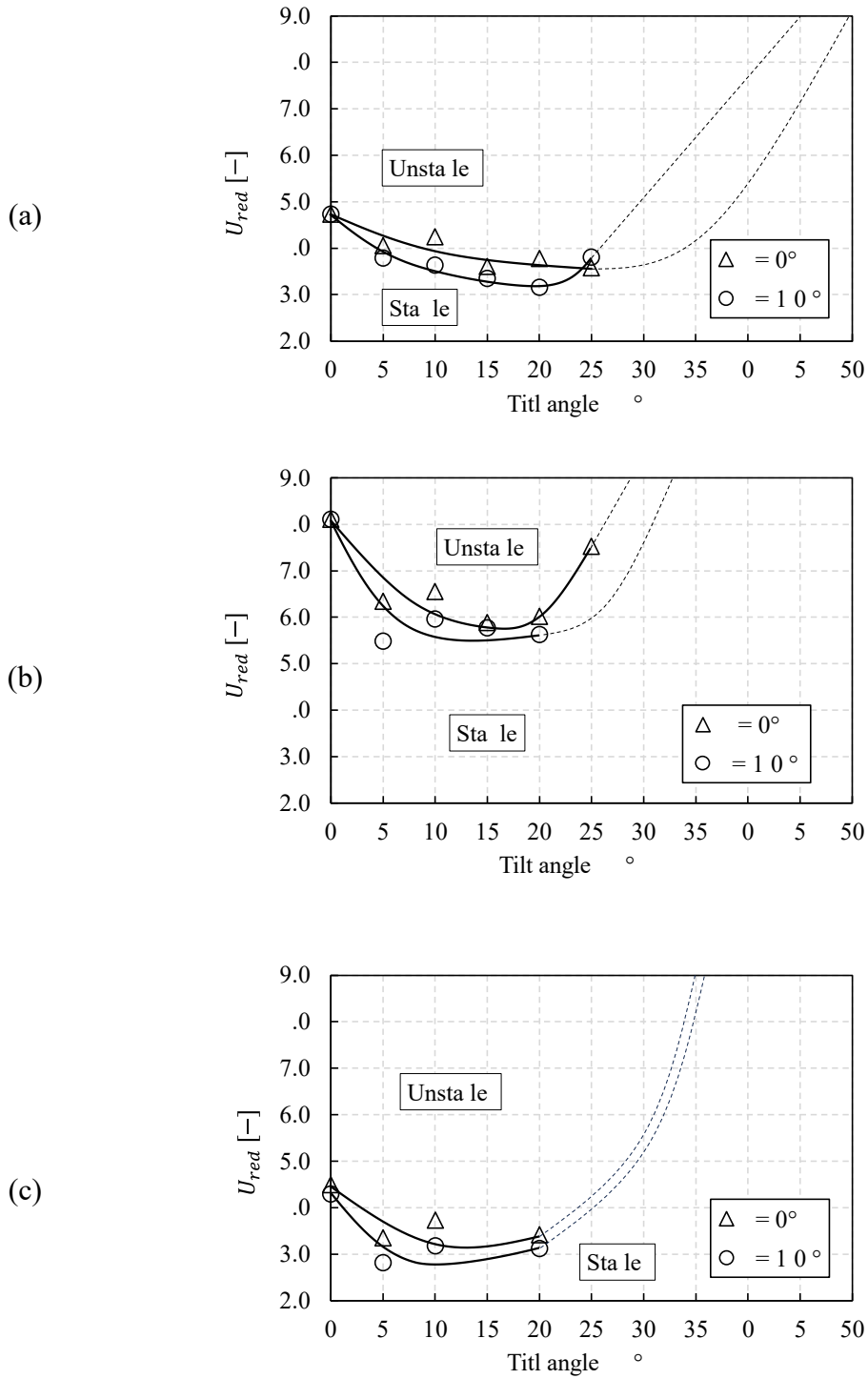


Figure 4.10. Reduced critical wind speed U_{red} vs tilt angle (α) measured on (a) Model I-b, (b) Model I-c, and (c) Model II-b. Approximate curve shown as a line. Expected trend shown with dashed line

4.2.1 Critical wind speeds for oblique approach wind directions

The results of the critical wind speed tests for other wind directions (θ) are shown in Figure 4.11. The models experienced torsional galloping within a range of directions (θ) from $0^\circ \pm 40^\circ$, and $180^\circ \pm 20^\circ$ for Model I-b ($l/b = 6$), also $0^\circ \pm 40^\circ$, and $180^\circ \pm 40^\circ$ for Model I-c ($l/b = 8$). This is associated with the wind load patterns described in Section 4.1.2, for the tilt angles, where $(\partial C_M / \partial \alpha) < 0$. The critical reduced wind speed U_{red} is generally lower for θ ranging from $180^\circ \pm 40^\circ$, than for θ from 0° to 40° . For the same tilt angle (α), U_{red} generally remains around the same magnitude, when the wind direction ranges from $\theta = 0^\circ \pm 20^\circ$, and from $\theta = 180^\circ \pm 20^\circ$. For tilts $\alpha > 25^\circ$, the models remained stable for all wind directions, for the achievable wind speeds in the wind tunnel.

It is notable when comparing results between the models in Figure 4.11, that when the aspect ratio decreases, the model is less sensitive to wind directionality for wind directions ranging from $180^\circ \pm 40^\circ$. However, the critical wind speed for these directions is still relatively lower than for θ ranging from $0^\circ \pm 40^\circ$. It is also pertinent, that for tilt angles $\alpha \geq 5^\circ$, the reduced wind speed is almost the same for θ ranging from $0^\circ \pm 20^\circ$, and $180^\circ \pm 20^\circ$. This is consistent with the fact that the moment coefficient, C_M is about the same for that range of wind directions (Figure 4.3 to Figure 4.8), therefore implying that the critical wind speed should also be the same for the onset of torsional galloping.

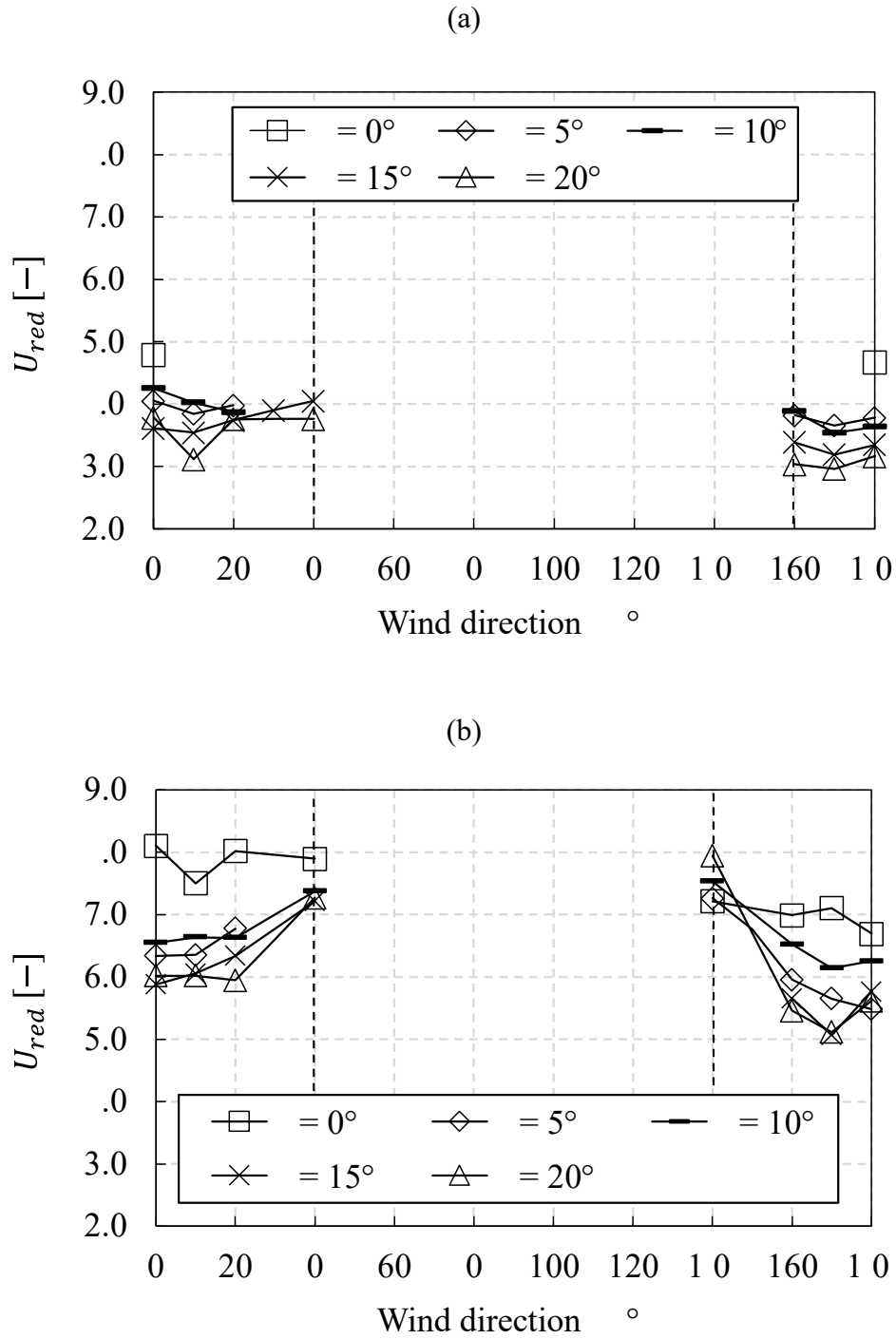


Figure 4.11. Critical wind speed for oblique winds. (a) Model I-b ($l/b = 6$) and (b)

Model I-c ($l/b = 8$)

The traditional stow position ($\alpha = 0^\circ$) represents a distinct behaviour. Figure 4.11 (b) shows that the critical wind speed (U_{red}) is the same amongst the range $\theta = 0^\circ \pm 40^\circ$. This repeats for $180^\circ \pm 40^\circ$.

Figure 4.11 (a) shows that for Model I-b ($l/b = 6$), the traditional stow position is only unstable when $\theta = 0^\circ$ and $\theta = 180^\circ$. Model I-b has a higher structural stiffness (k_0) than Model I-c (see Table 3.2) and is the cause for the difference in the response. This confirms the fluid-structure interaction at small tilt angles presented in Sections 2.3 and 4.1.2.

4.2.2 Onset of torsional galloping

Torsional galloping is governed by the interaction between wind-induced aerodynamic forces and the inertial response of the structure. A key characteristic of this interaction is the resulting oscillatory behaviour, which also depends on the mechanical characteristics of the system. In this section, the torsional frequencies of the structure are analysed.

The critical wind speed tests measured the variation of the wind loading including the moments at onset of instability. Figure 4.12 shows the variation of 10-second time step mean moment coefficient, of Model I-c at $\alpha = 20^\circ$, for several wind directions (θ), leading up to the onset of instability. The mean wind speed \bar{U}_h during each 10-second time step and wind direction (θ) is shown as a grey scatter plot in the background. It can be observed that regardless of the wind direction, the mean moment coefficient $C_{\bar{M}}$ is relatively unchanged in all time intervals, even just before torsional galloping initiates.

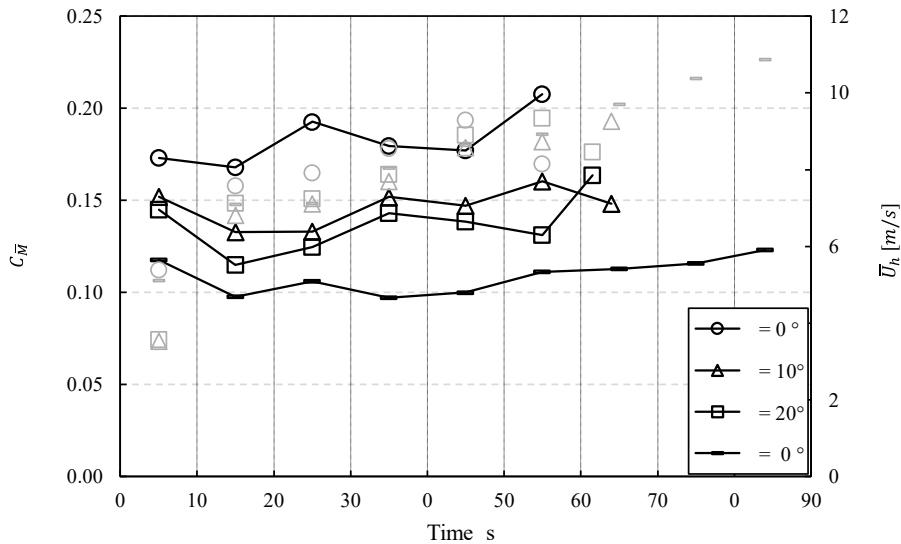


Figure 4.12. Mean moment coefficients and mean wind speed in 10-second time steps leading up to instability. Model I-c, $\alpha = 20^\circ$

Figure 4.13 shows the time varying moment within a time interval (a) before the onset of instability, and (b) during torsional galloping, for wind direction $\theta = 10^\circ$. Figure 4.13 (a) shows that the moment is positive and exhibits oscillations around the mean value. At this stage, the structural damping is still dissipating the energy generated by the aerodynamic moment.

Figure 4.13 (b) shows the time varying moment when the model is undergoing torsional galloping. It is observed that the moment increases significantly and also changes sign, causing instability. The moment, although increased, oscillates around a positive mean value, which is almost the same as before instability shown in Figure 4.13 (a). The observed increase and fluctuation in amplitude implies that the aerodynamic damping has exceeded the structural damping, impeding the dissipation of energy from the flow. This negative effective damping signifies instability. This effect is further discussed in Section 4.3.

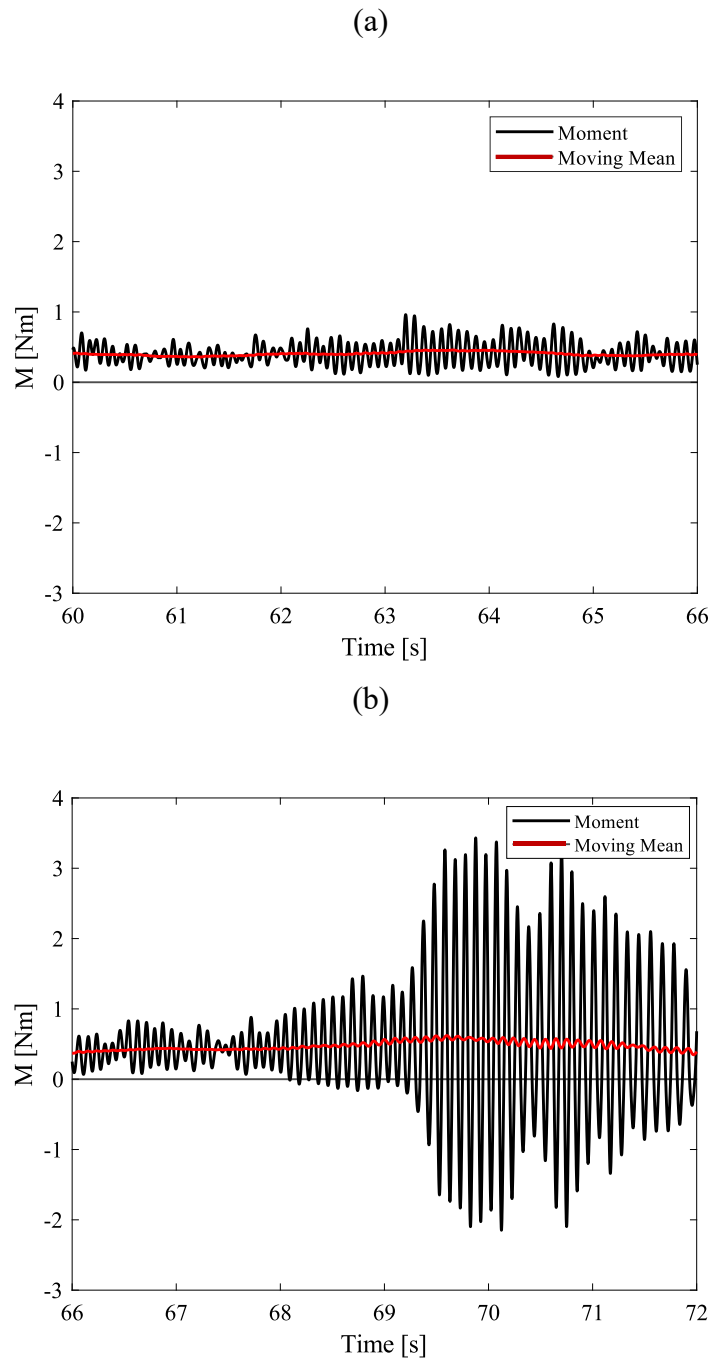


Figure 4.13. (a) Moment vs time before the onset of torsional galloping. (b) Moment vs time during torsional galloping, Model I-c, $\alpha = 20^\circ$, and $\theta = 10^\circ$

The spectra of the approach velocity $U_h(t)$ and the moment $M(t)$ before and during torsional galloping, for Model I-c, $\alpha = 20^\circ$ and $\theta = 10^\circ$, are shown in Figure 4.14.

It is observed in Figure 4.14 (a) that the frequency dominating the moment response before torsional galloping is the natural frequency (i.e. 7.6 Hz) of the model (see Table 3.2). Figure 4.14 (b) shows that there is a change in the dominant frequency to 9.64 Hz during torsional galloping, which is higher than the natural frequency. This change in the frequency is driven by the interaction between the aerodynamic and structural damping. The torsional galloping oscillations alter the aerodynamic forces, producing a frequency shift, that can be taken then as a characteristic of the self-excitation process. In this case, a higher frequency indicates an increase in the structural stiffness.

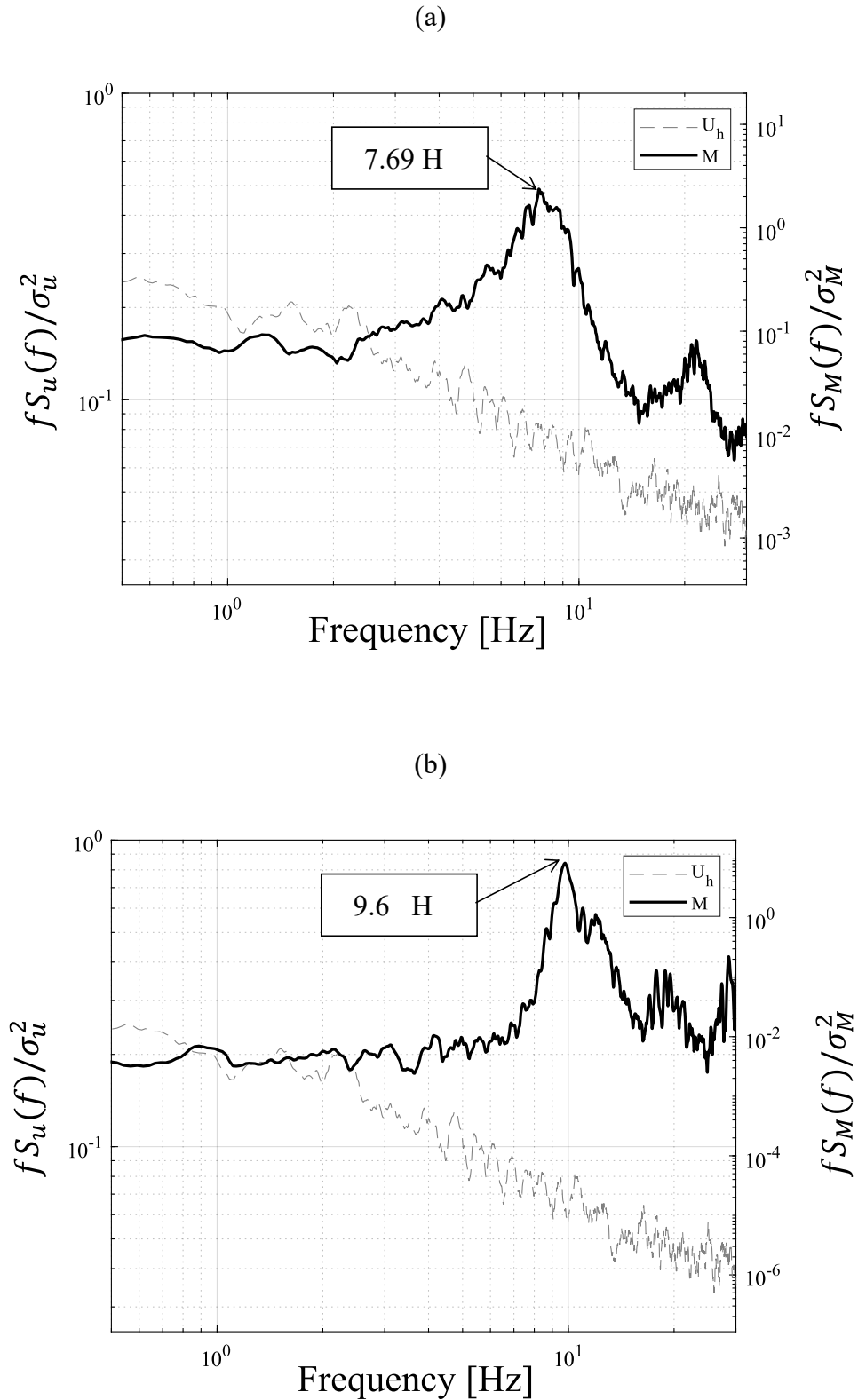


Figure 4.14. Power spectral density of the wind speed and moment (a) before torsional galloping, and (b) during torsional galloping. Model I-c, $\alpha = 20^\circ$, and $\theta = 10^\circ$

4.2.3 Onset of divergence

During torsional divergence, the aerodynamic forces cause the structure to twist increasingly in a predominant direction (i.e. positive moment). As the twist increases, the moment also increases further twisting the tube. This leads to a feedback loop, causing the structure to diverge. The critical condition occurs when the aerodynamic stiffness exceeds the structural stiffness, as discussed in Section 4.3.

The analysis of the variation of the mean moment coefficient was also performed for the traditional stow position ($\alpha = 0^\circ$), typically susceptible to divergence. Figure 4.15 shows the mean moment coefficient at 10-second time steps for Model I-c, at tilt angle $\alpha = 0^\circ$ leading to divergence. The mean wind speed \bar{U}_h for each wind direction and time interval is shown as a grey scatter plot in the background.

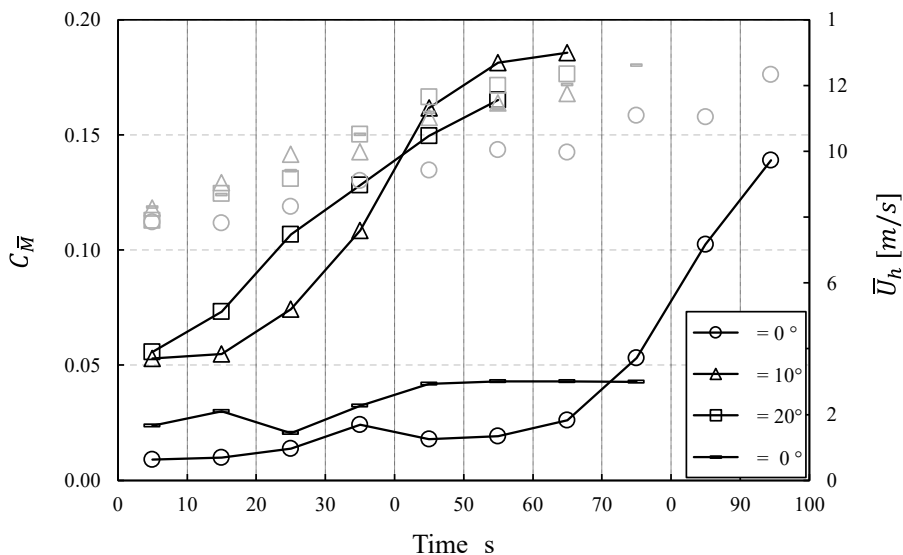


Figure 4.15. Mean moment coefficients and mean wind speed vs time, leading up to divergence. Model I-c at $\alpha = 0^\circ$

Figure 4.15 shows that the mean moment coefficient increases for each 10-second time interval, leading up to divergence. The rate of increase of the moment coefficient is greater than that of the mean wind speed. This is a typical characteristic of divergence and is different to what was observed for torsional galloping shown in Figure 4.12.

The case $\theta = 0^\circ$ shown in Figure 4.15, corresponds to a configuration that did not experience instability. This is also evident as the mean moment coefficient, $C_{\bar{M}}$ remains low and almost unchanged. For other wind directions in Figure 4.15, the (positive) moment increment implies that the moment increases in the same direction of twist, leading up to divergence. This means that as the moment increases, the structure is subjected to a sustained increment of twist in the same direction. It is also noticeable that more oblique wind directions have lower rate of moment increment.

Depending on the structural conditions, divergence can induce a “static failure” due to structural stiffness being exceeded by the aerodynamic stiffness. Alternatively, the system could change the tilt angle α progressively as the effective stiffness k_{eff} decreases, which leads to the occurrence of torsional galloping.

Figure 4.16 shows the time varying moment with increasing wind speed for Model I-c at $\alpha = 0^\circ$, for $\theta = 0^\circ$. From the start ($t = 0$) and until approximately $t = 75$ s, where the moment oscillates about 0 Nm. This is typical for $\alpha = 0^\circ$, where the moment fluctuates between positive and negative values. Then, from time $t = 75$ s and until $t = 95$ s approximately, the moment increases progressively, and despite some negative peaks, the moment oscillates within a positive range. This indicates the moment acting in one direction, causing an increase of the twist in that direction. This characterizes divergence instability in the model. Finally, when the model acquires a new tilt due to the

increased twist, at about $t = 100$ s, the oscillation increases sharply with little change in wind speed U , showing onset of torsional galloping.

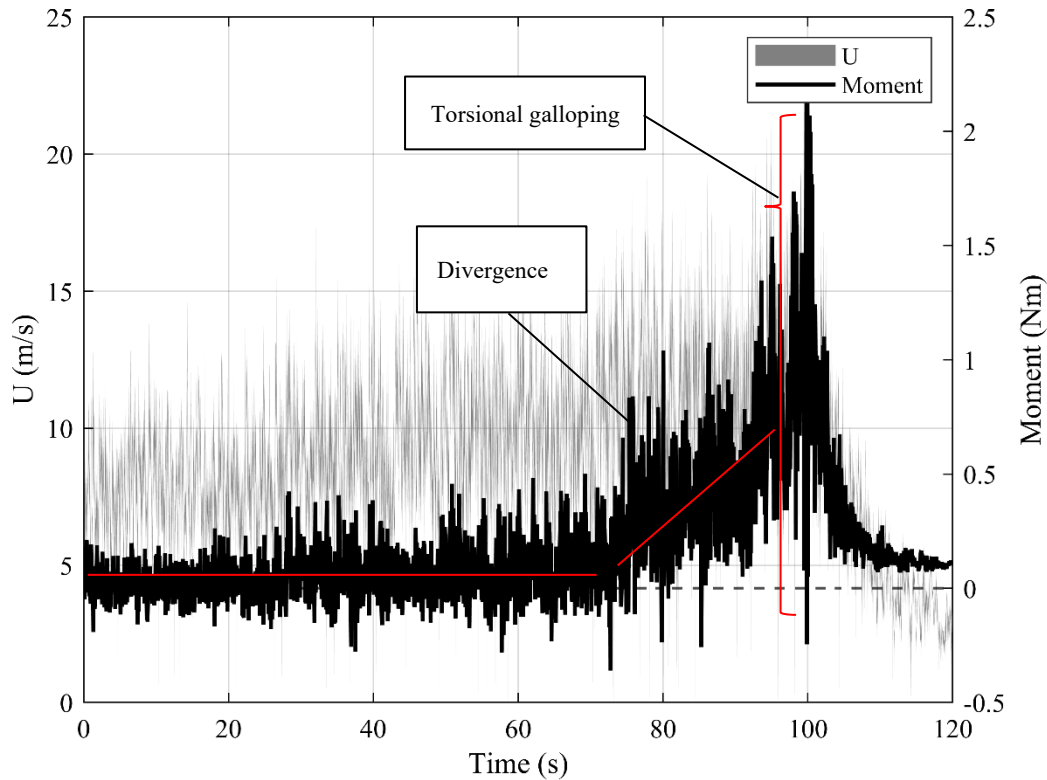


Figure 4.16. Moment and wind speed time-history during critical wind speed test.

Model I-c at $\alpha = 0^\circ$ and $\theta = 0^\circ$

Figure 4.16 shows an example of “chained instabilities”, when the system firstly has its structural stiffness exceeded by the aerodynamic stiffness, to the point when an increased tilt α occurs. The higher tilt causes an increase of aerodynamic damping that interacts with the structural damping (c_0), to give effective damping $c_{eff} = 0$, and the onset of torsional galloping.

4.3 Effective dam in g and effective stiffness

The effective damping, c_{eff} , and the effective stiffness, k_{eff} , were calculated using Equation 2.3. The variation ($\partial C_M/\partial\alpha$) was determined for each tested wind speed, \bar{U}_h , using the data presented in Section 4.1.2. Mechanical properties such as the structural stiffness, k_0 , structural damping, c_0 , natural frequency, f_0 , and damping ratio, ζ_0 were adopted from Table 3.2. Figure 4.17 and Figure 4.18 show the variation of c_{eff} and k_{eff} for Model I-c as a function of the reduced wind speed U_{red} , for wind directions $\theta = 0^\circ$ and $\theta = 10^\circ$, respectively. Data for Models I-b and II-b are provided in Appendix C.

At a reduced wind speed $U_{red} = 0$, where aerodynamic forces are absent, c_{eff} and k_{eff} are taken as the inherent structural damping, c_0 and the structural stiffness k_0 , respectively. Figure 4.17 (a) and Figure 4.18 (a) show that for tilt angles $\alpha = 10^\circ, 15^\circ$, and 20° , the effective damping transitions rapidly from positive values to zero over a short reduced wind speed interval. This behaviour is in agreement with the rate of change of C_M observed in Figure 4.9 and aligns with the description of the time-varying moment presented in Section 4.2.2. In particular, the abrupt change in both the magnitude and direction of the moment indicates an enhanced aerodynamic damping effect, as reflected by a negative ($\partial C_M/\partial\alpha$). For tilt angles $\alpha \geq 30^\circ$, c_{eff} deviates only slightly from its initial structural value, and as U_{red} increases further, a slight decline in c_{eff} is observed. Note 1, for $\alpha = 5^\circ$ and 10° (and to a lesser extent at 0°), a small increase in U_{red} precedes its drop to zero at approximately $U_{red} \approx 6.5$.

Figure 4.17 (b) and Figure 4.18 (b) show the effective stiffness, k_{eff} , as a function of the reduced wind speed. For wind directions $\theta = 0^\circ$ and $\theta = 10^\circ$, and for all tilt angles exceeding 5° , k_{eff} experiences a slight increase. This increase is attributed to the negative ($\partial C_M/\partial\alpha$) typical of the wind loading conditions observed in Figure 4.9. In

contrast, for $\alpha = 0^\circ$ and $\alpha = 5^\circ$, k_{eff} progressively decreases, ultimately reaching zero. Specifically, for $\alpha = 0^\circ$, c_{eff} falls to zero at approximately $U_{red} \approx 10$, while k_{eff} approaches zero near $U_{red} \approx 9$. This is in line with the chained instabilities described in Section 4.2.2, wherein the increasing moment increases the tilt angle, causing a progressive reduction in k_{eff} that eventually produces torsional galloping (marked by $c_{eff} = 0$).

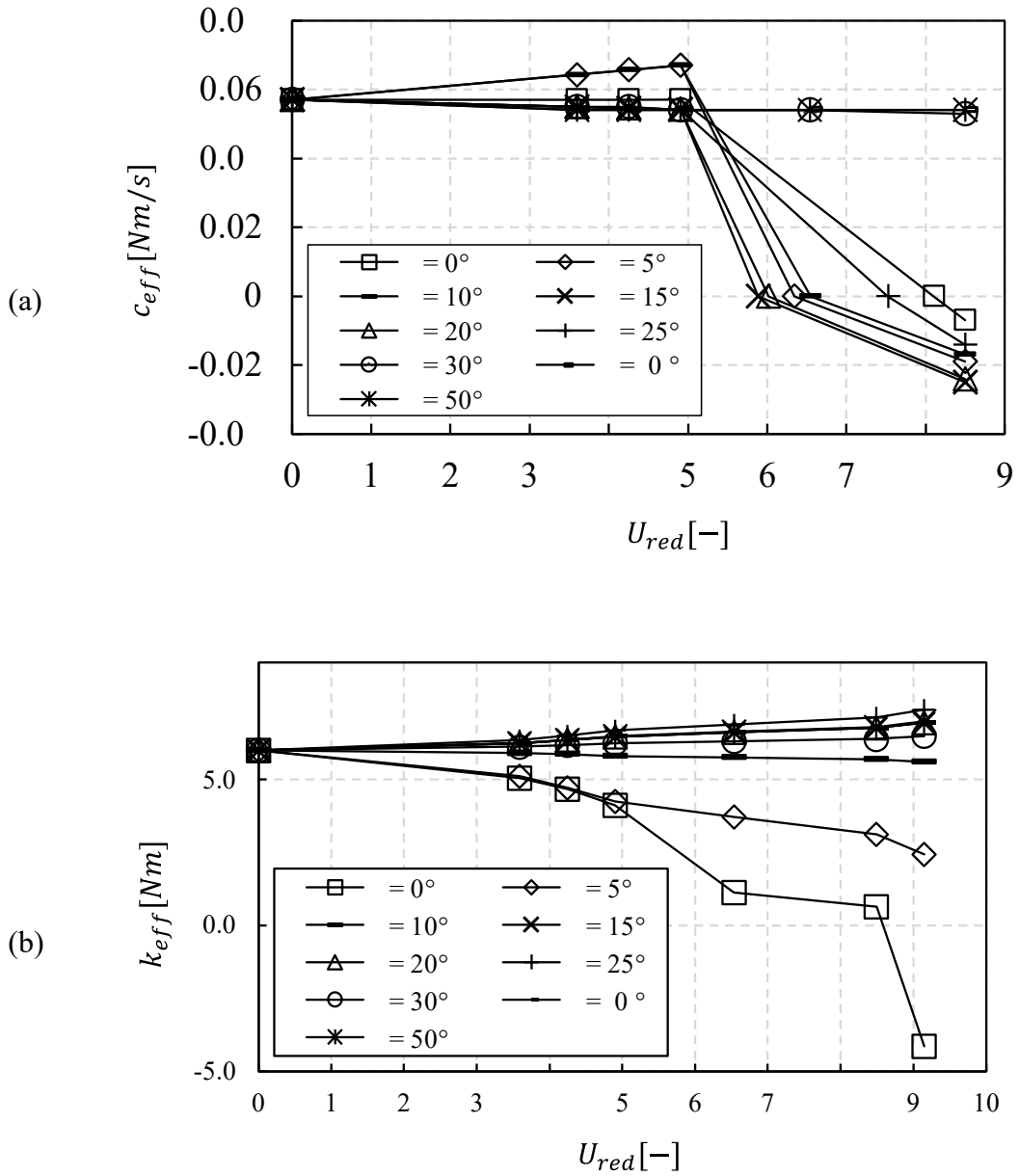


Figure 4.17. (a) Effective damping vs reduced wind speed and, (b) effective stiffness vs reduced wind speed, for $\theta = 0^\circ$. Model I-c

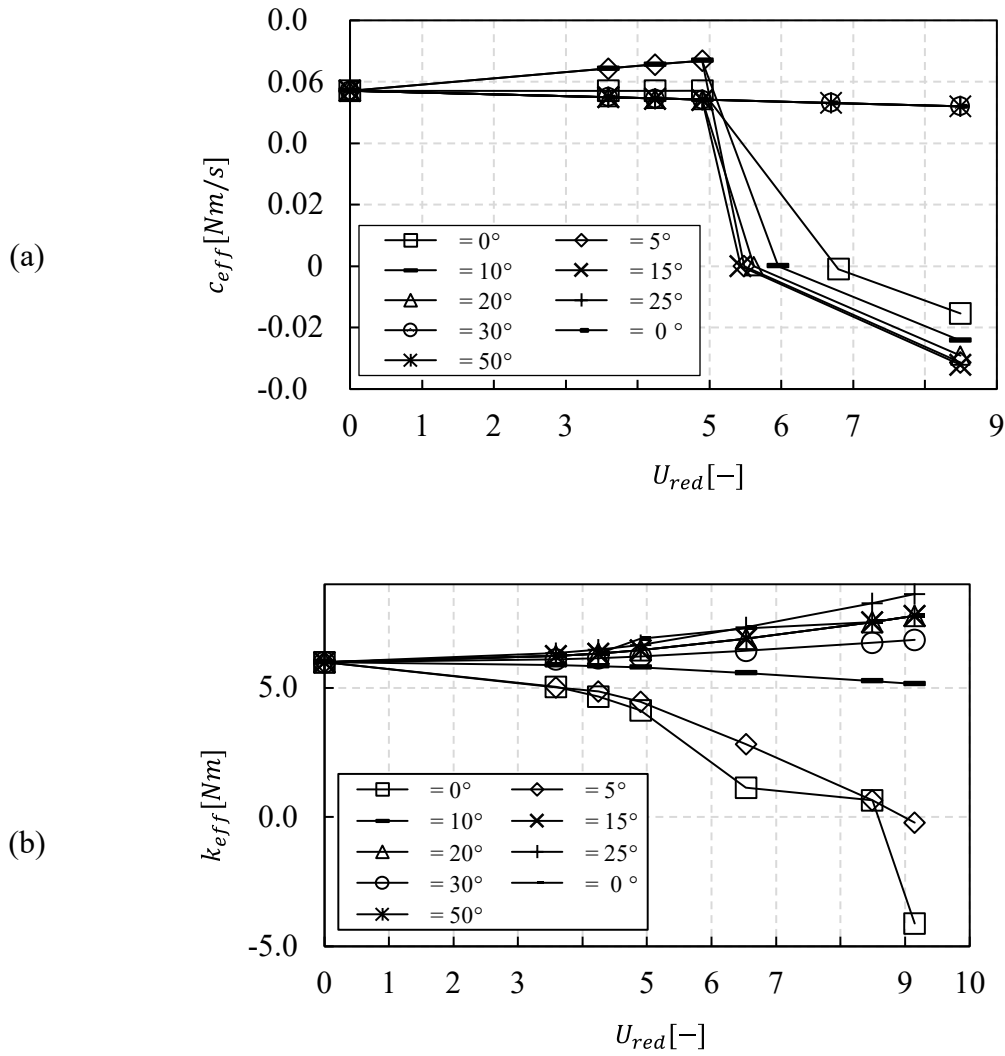


Figure 4.18. (a) Effective damping vs reduced wind speed and, (b) effective stiffness vs reduced wind speed, for $\theta = 10^\circ$. Model I-c

The variations in c_{eff} and k_{eff} offer valuable insight into the nature of the instabilities. The sharp change in c_{eff} with a small increment of U_{red} explains the rapid increase of oscillation amplitudes during torsional galloping. Conversely, the gradual decrease of k_{eff} with increasing U_{red} indicates that the moment gradually increases in

magnitude, twisting the structure progressively and eventually causing structural failure or triggering a shift in the tilt angle α , that results in torsional galloping.

4.4 Quasi-steady aerodynamic derivatives

The quasi-steady aerodynamic derivatives A_2^* and A_3^* were calculated using Equation 2.7 and Equation 2.8. The variations of $(\partial C_M / \partial \alpha)$ were calculated from the mean moment coefficients presented in Figure 4.9 (Model I-c). Equations 2.4 and 2.5 were rearranged to solve for $(\partial C_M / \partial \alpha)$ using the critical wind speeds (U_{cr}) determined experimentally. Consequently, the aerodynamic derivatives presented are applicable only to the configurations that became unstable during the critical wind speed test. The discrete points obtained were fitted to a polynomial of 3rd order using the methodology proposed by Cárdenas-Rondón et al. (2023).

A diagram explaining the variation of the aerodynamic derivative A_2^* with U_{red} is shown in Figure 4.19. From $U_{red} = 0$ (point P_0), the aerodynamic damping contributes to the stability of the structure with increasing U_{red} . This contribution always reaches a minimum. Cárdenas-Rondón et al. (2023) refer to this point as P_1 . This minimum point represents the most stable state for the fluid-structure interaction, where the structural damping c_0 and the aerodynamic damping contribute to the (total) effective damping c_{eff} .

Beyond this point, A_2^* increases, reaching zero at the critical wind speed U_{cr} (point P_2), where instability begins. With increasing wind speed, from P_1 onwards, the aerodynamic damping works against the structural damping, making the structure aerodynamically less stable. A_2^* then increases sharply.

After point P_2 , the effective damping c_{eff} is negative, causing increasing instability. For tilt $\alpha = 0^\circ$, shown as a dash line in Figure 4.19, the aerodynamic derivative

A_2^* only decreases as U_{red} increases. Therefore, the aerodynamic damping only contributes to the effective damping. With sufficient structural stiffness k_0 , this could be the most stable configuration for a solar tracker. However, as indicated by Enshaei et al., (2023) and demonstrated by the results of this study, at small tilt angles (i.e. $\alpha = 0^\circ$), the nominal tilt angle α can change, onsetting torsional galloping once the effective damping, $c_{eff} = 0$.

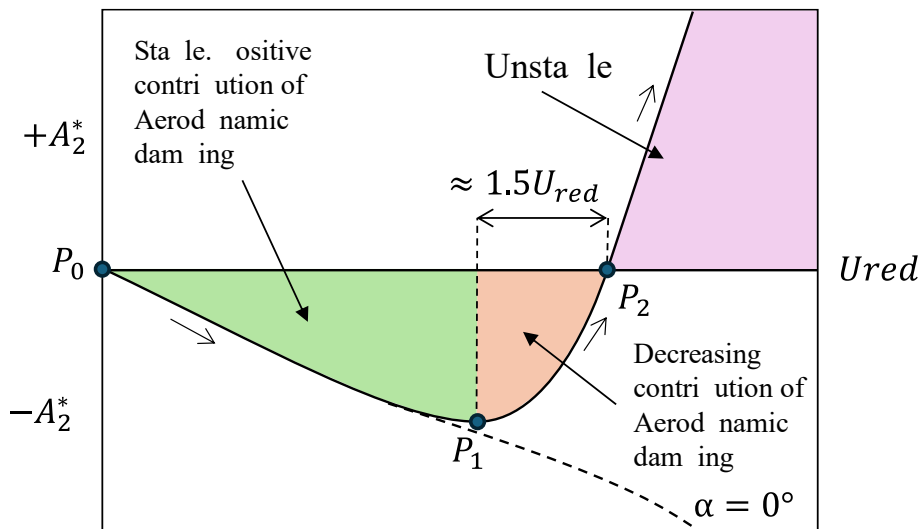


Figure 4.19. Variation of aerodynamic derivative A_2^* with wind speed

Figure 4.20 and Figure 4.21 show the quasi-steady aerodynamic derivative A_2^* as function of U_{red} , for Model I-c, for $\theta = 0^\circ$ and $\theta = 10^\circ$, respectively. The fitted curves of A_2^* for each tilt angle (α) are similar to those obtained by Taylor and Browne (2020) and Cárdenas-Rondón et al. (2023) and shown in Figure 2.7 and Figure 2.9. Results for Model I-b and Model II-b are provided in Appendix C.

Lower tilt angles (such as $\alpha = 5^\circ$) (Figure 4.20 (a) and Figure 4.21 (a)) exhibit lower minimum values of A_2^* (point P_1) when $\theta = 0^\circ$, suggesting increased aerodynamic stability over a wider range of wind speeds. Intermediate tilt angles (i.e. $\alpha = 15^\circ$ and 20°) (Figure 4.20 (b)) present negative values (i.e. minimum) P_1 that are closer to 0. This is even more accentuated when $\theta = 10^\circ$ (Figure 4.21 (b)), indicating that intermediate tilt angles present less aerodynamic stable behaviour. In those cases, point P_2 occurs when $U_{red} \approx 4$ (i.e. $\alpha = 15^\circ$ and 20°). Furthermore, analysing the results in this study, as well previous research such as Taylor and Browne (2019), Cárdenas-Rondón et al., (2023) and Cárdenas-Rondón et al., (2024), P_1 (i.e. minimum A_2^*) and P_2 (i.e. $A_2^* = 0$), are separated by $1.5U_{red}$. This suggest that torsional galloping happens when wind speed increases by about 50% from when the fluid-structure interaction is most stable.

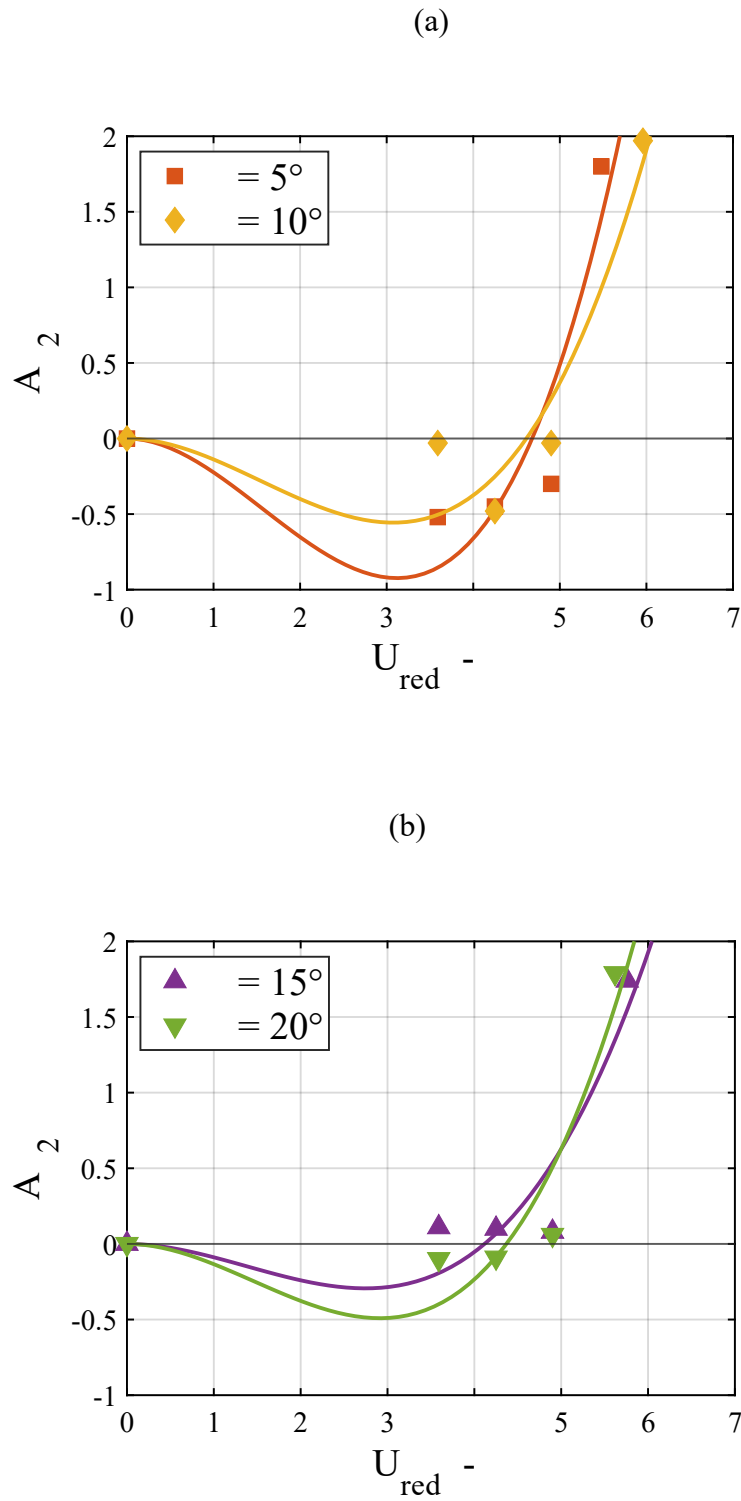


Figure 4.20. Aerodynamic derivative A_2^* vs reduced wind speed U_{red} , for $\theta = 0^\circ$ and
 (a) $\alpha = 5^\circ, 10^\circ$ and (b) $\alpha = 15^\circ, 20^\circ$. Model I-c

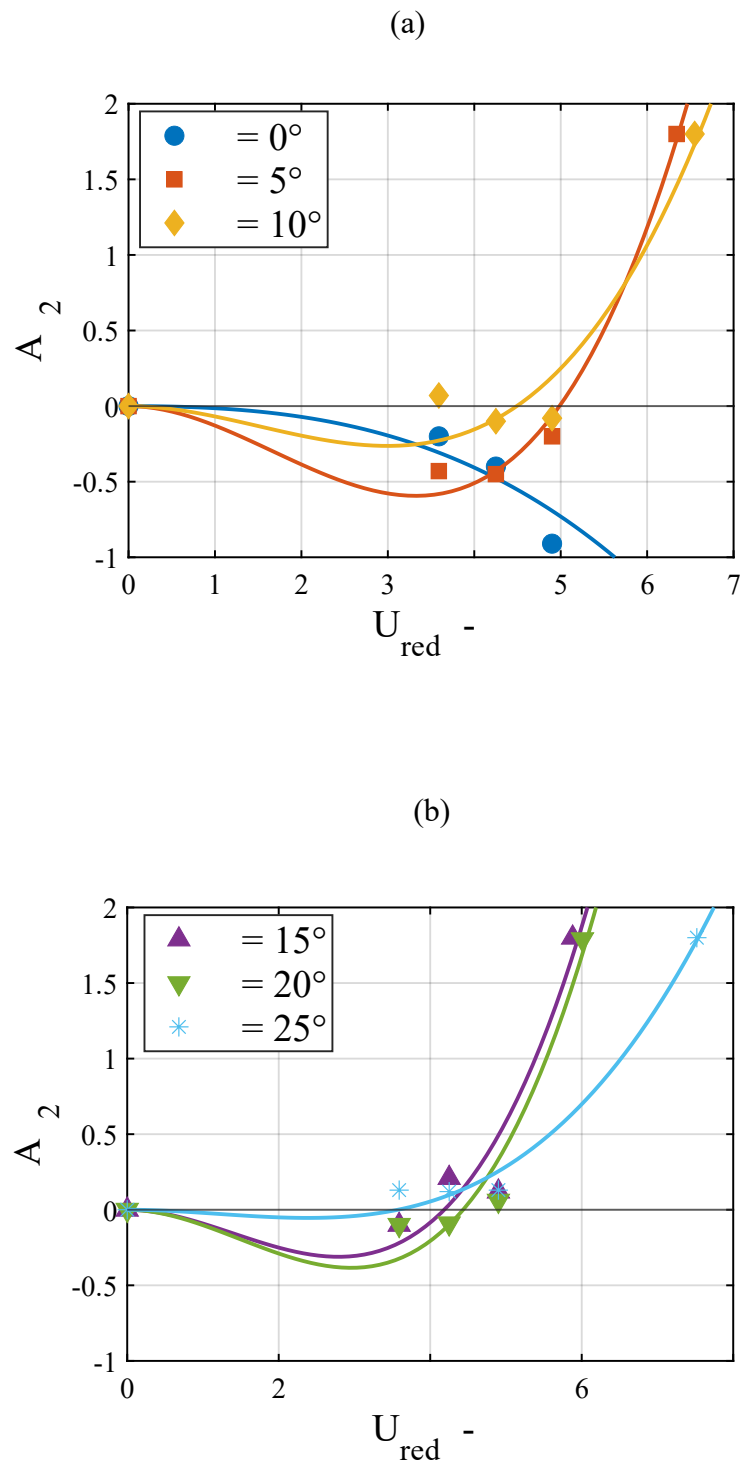


Figure 4.21. Aerodynamic derivative A_2^* vs reduced wind speed U_{red} , for $\theta = 10^\circ$ and (a) $\alpha = 0^\circ, 5^\circ, 10^\circ$ and (b) $\alpha = 15^\circ, 20^\circ, 25^\circ$. Model I-c

Figure 4.22 shows the variation of aerodynamic derivative, A_3^* , for Model I-c with the reduced wind speed, U_{red} . The fitted A_3^* curve shows similarity with the data presented by Taylor and Browne (2020) and Cárdenas-Rondón et al., (2023) (and given in Figure 2.7 and Figure 2.10). Figure 4.22 shows that the aerodynamic derivative A_3^* increases as the wind speed increases for all tilt angles. Small tilt angles (α), such as 0° and 5° , exhibit larger values of A_3^* and a steeper slope compared to higher tilt angles ($\alpha = 10^\circ, 15^\circ, 20^\circ$, and 25°). These larger values of A_3^* along with $(\partial C_M / \partial \alpha) > 0$ (as analysed in Sections 4.1.2 and 4.3), suggest that aerodynamic stiffness increases with wind speed for small tilt angles. Then, if the structural stiffness (k_0) is low, the susceptibility to divergence increases significantly at small tilt angles (i.e. $\alpha = 0^\circ$ or 5°).

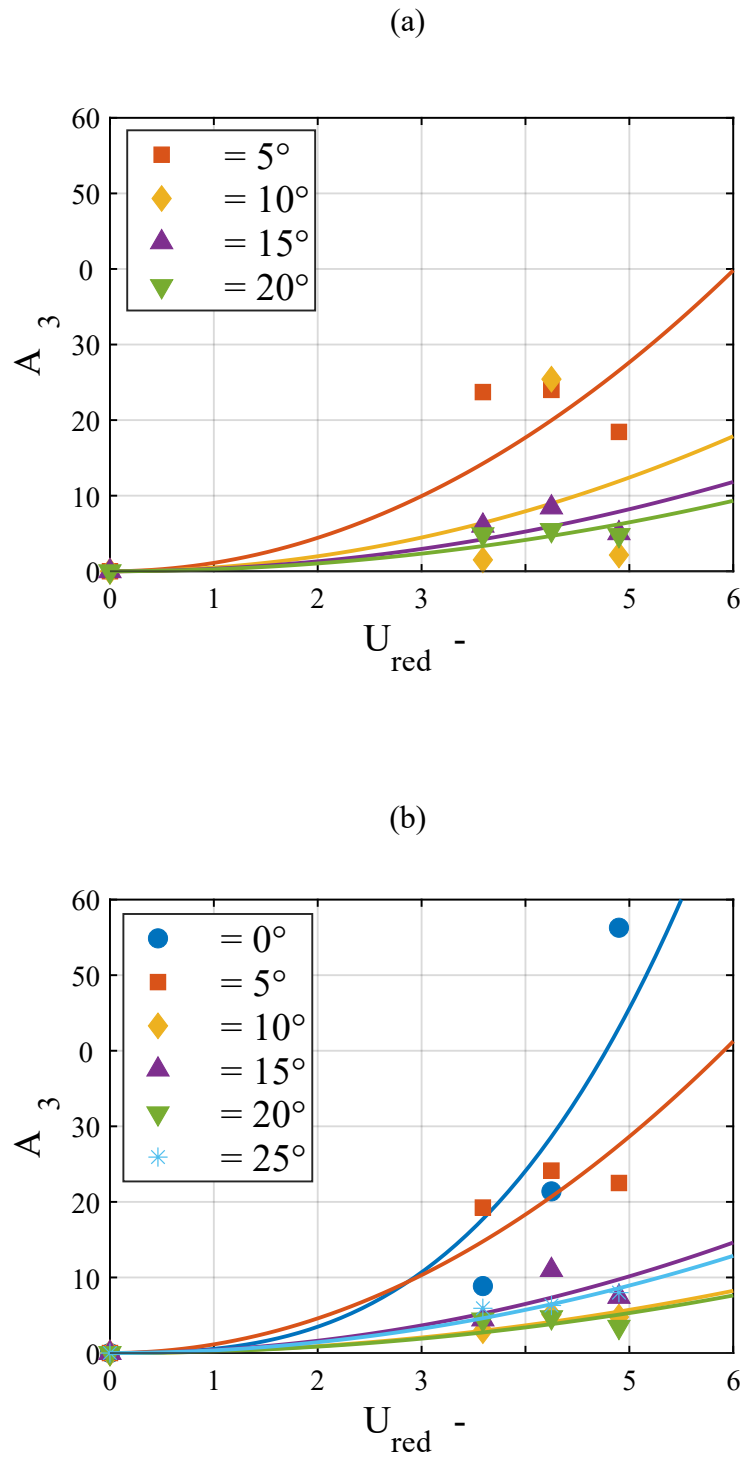


Figure 4.22. Aerodynamic derivative A_3^* vs reduced wind speed U_{red} , for (a) $\theta = 0^\circ$ and (b) $\theta = 10^\circ$. Model I-c

The linear quasi-steady approximation described in Section 2.5 and used in this Section to calculate the aerodynamic derivatives gives a simple way to estimate the aeroelastic behaviour of the structure. By calculating the mechanical characteristics of the structure, presented in Section 3.5 and the wind loading described in Section 4.1.2, it is possible to estimate a critical wind speed U_{cr} for the onset of torsional galloping by means of the Aerodynamic derivative A_2^* . Similarly, the onset of divergence can be evaluated using the same approach to calculate the Aerodynamic derivative A_3^* .

4.5 Aerodynamic derivative A_2^* using Autocorrelation

Nakamura and Mizota (1975) utilised a free oscillation technique to measure the unsteady aerodynamic torsional moment of a prismatic bar model exposed to a smooth flow. They determined the damping derivative (i.e. aerodynamic derivative A_2^*) using the effective (total) logarithmic decrement of the oscillation δ , under influence of wind. This effective decrement accounts for both the structural decrement δ_0 , and the aerodynamic decrement δ_a , such that $\delta = \delta_0 + \delta_a$. Conversely, the very turbulent flow near the ground, as it is the case of this study, requires a different method (i.e. autocorrelation) to estimate the effective total and aerodynamic damping. The accurate determination of aerodynamic damping is critical in predicting aeroelastic instability. As highlighted by Nakamura (1979) and Yoshimura and Nakamura (1980), unsteady aerodynamic forces, and consequently aerodynamic damping, depend not only on the instantaneous motion of the structure but also on the history of that motion, a phenomenon they called "fluid memory". While the term "fluid memory" is not widely used, the concept emphasizes the limitations of quasi-steady theories, which neglect these history effects.

The autocorrelation of the moment response captures the combined effects of structural and aerodynamic damping, and the “fluid memor” effects because it quantifies how well the moment at one instant in time predicts the moment at a later instant. Then, if the moment response is random over time, the autocorrelation will decay quickly. This is because the moment at one time becomes less and less related to the moment at later times. But if the moment response oscillates within a particular frequency, the autocorrelation will decay slowly, showing that the moment is correlated with its future values.

Therefore, determining the structural decrement as per Section 3.5, and analysing the autocorrelation of the moment response of the models when exposed to wind flow, allows to obtain the aerodynamic decrement δ_a , and therefore the derivative A_2^* .

The autocorrelation coefficient of the moment response $M(t)$ is defined by Equation 4.1.

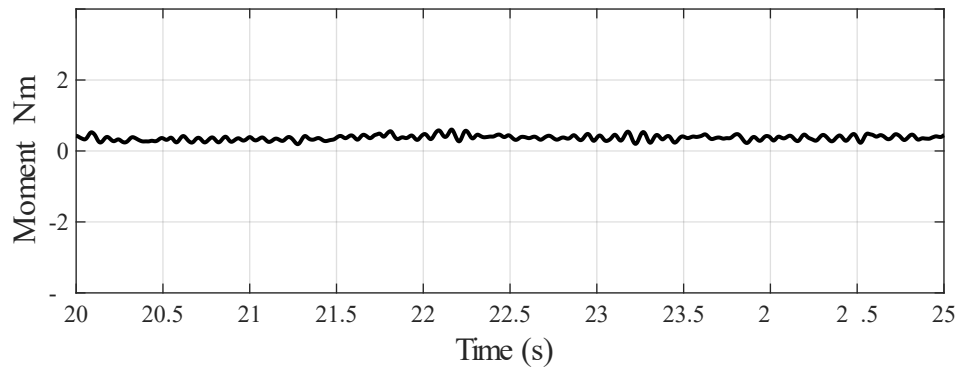
$$C(\tau) = \frac{\frac{1}{T} \int_0^T [M(t) - \bar{M}] \cdot [M(t + \tau) - \bar{M}] dt}{\sigma_M^2}, \quad \text{for } \tau \geq 0 \quad 4.1$$

Where, $C(\tau)$ is the autocorrelation coefficient at time lag τ , $M(t)$ is the moment response at the time t and T is the observation time.

By subtracting the mean \bar{M} , the autocorrelation focuses solely on the fluctuations of the moment response around its average. This is essential because damping is related to how these fluctuations decay over time, not the average value of the moment.

The autocorrelation coefficient $C(\tau)$ of three different time steps (before, approaching and during instability) for Model I-c ($\alpha = 20^\circ$ and $\theta = 0^\circ$) are shown in Figure 4.23, Figure 4.24 and Figure 4.25. The autocorrelation coefficient changes according to the moment response characteristics before, approaching and during instability. In the first case, during the stable response, shown in Figure 4.23, $C(\tau)$ decays randomly to oscillate about zero for large τ . Figure 4.24 shows the moment response and the autocorrelation coefficient five seconds before instability. The autocorrelation coefficient shows an initial oscillatory decay, to then oscillate about zero. During instability, shown in Figure 4.25, $C(\tau)$ presents an oscillatory decay that eventually becomes zero. This decay in $C(\tau)$ is directly related to the effective (total) damping c_{eff} , from which the structural damping (c_0) can be subtracted to determine the contribution of the aerodynamic damping. Additionally, the presence of "beating" in the autocorrelation plots (e.g., Figure 4.25 (b)), suggesting the influence of two dominant frequencies during the response with the changing aerodynamic stiffness.

(a)



(b)

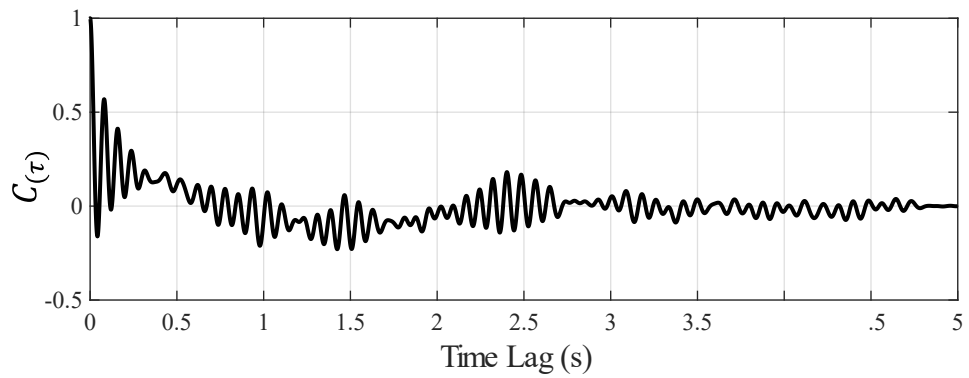
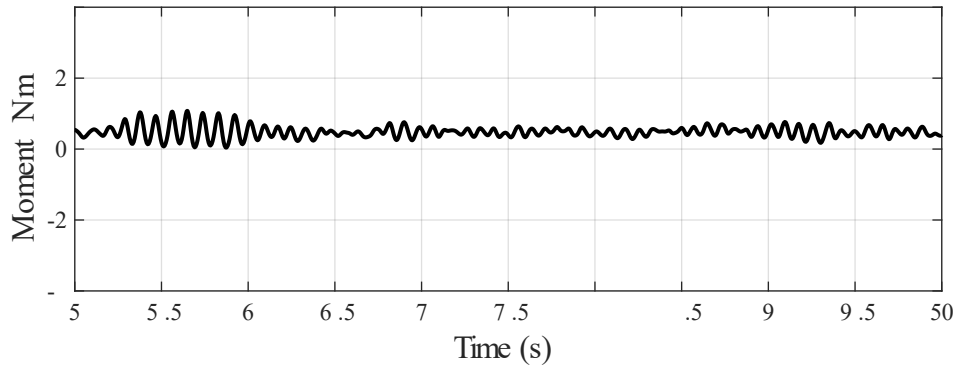


Figure 4.23. (a) Moment response and (b) autocorrelation, before instability.

Model I-c, $\alpha = 20^\circ$ and $\theta = 0^\circ$

(a)



(b)

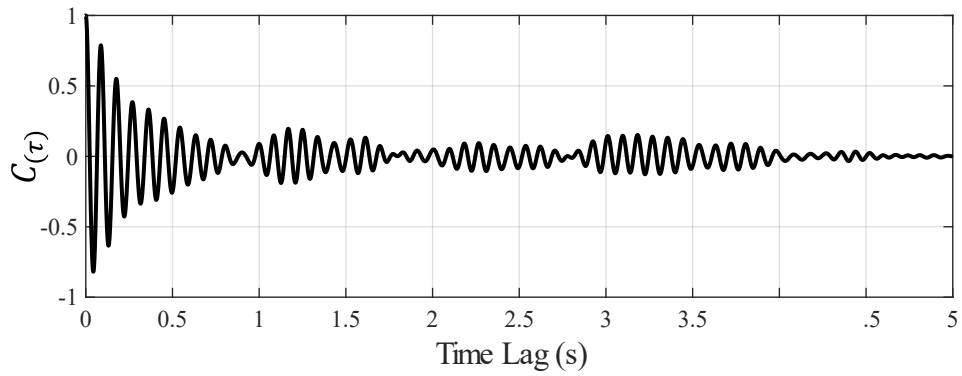


Figure 4.24. (a) Moment response and (b) autocorrelation, approaching instability.

Model I-c, $\alpha = 20^\circ$ and $\theta = 0^\circ$

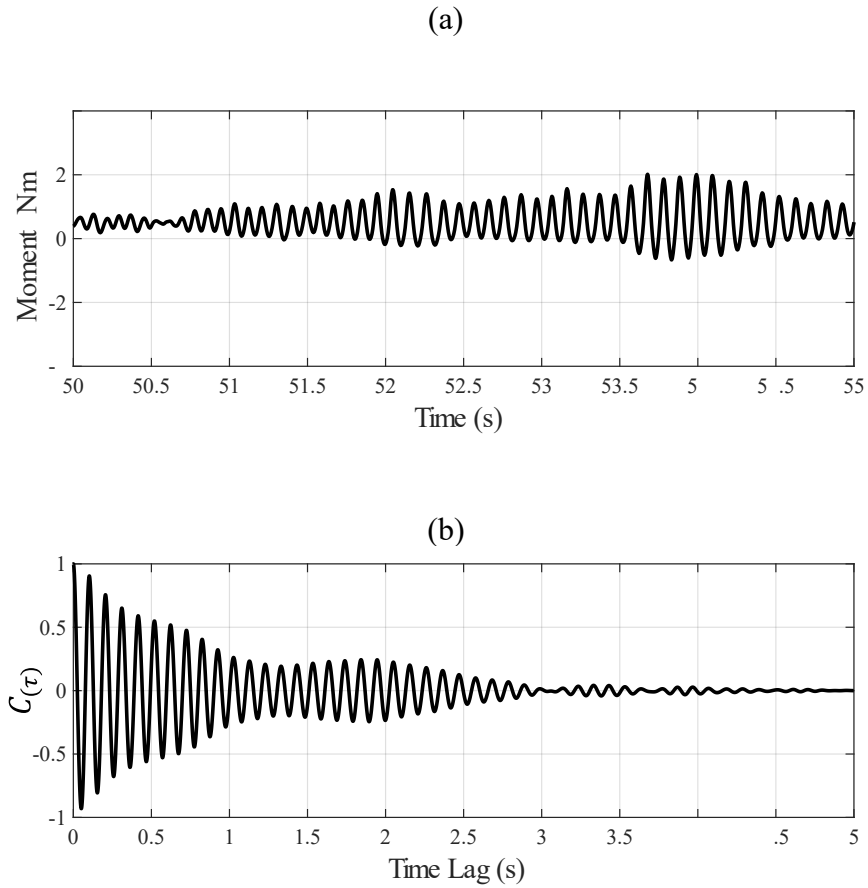


Figure 4.25. (a) Moment response and (b) autocorrelation, during instability.

Model I-c, $\alpha = 20^\circ$ and $\theta = 0^\circ$

The logarithmic decrement (δ) of the autocorrelation was calculated considering n positive peaks from the autocorrelation plot, so that $\delta = \frac{1}{n} \ln \left(\frac{p_1}{p_n} \right)$. Here p_1 is the first positive peak and p_n the n^{th} positive peak. Then, the effective (total) damping ratio was obtained as $\zeta_{eff} = \frac{\delta}{2\pi}$. The difference between ζ_{eff} and the structural damping ratio ζ_0 (see Table 3.1) gives the aerodynamic damping ratio ζ_a . Then, the aerodynamic

derivative A_2^* was calculated using an expression proposed by Bisplinghoff et al., (1996) and shown in Equation 4.2.

$$A_2^* = -\frac{2I_0 f_0 \zeta_a}{\rho \bar{U}_h b^4} \quad 4.2$$

The data were fitted using the methodology proposed by Cárdenas-Rondón et al., (2023) (and used in Section 4.4). The autocorrelation-derived (AC) aerodynamic derivatives A_2^* are plotted against the reduced wind speed, U_{red} , and compared with those obtained using the quasi-steady (QS) approximation in Section 4.4., as shown in Figure 4.26 to Figure 4.29.

The aerodynamic derivative A_2^* obtained using autocorrelation provides more detail on how the aerodynamic damping varies before, approaching and during instability comparing with the QS approximation. This is because it considers "fluid memory" effects, critical in aeroelasticity, which are missed by quasi-steady methods. Autocorrelation evidently incorporates how past motion influences the current flow around the oscillating structure, a point emphasized by Nakamura and Mizota (1975) and Yoshimura and Nakamura (1980).

For the case $\alpha = 0^\circ$, shown in Figure 4.26, the aerodynamic derivative decreases gradually with the increasing reduced wind speed U_{red} . This corresponds with Theodorsen's results on the airfoil positioned at $\alpha = 0^\circ$ (see Section 2.5), where an undamped airfoil at a very small tilt angle will remain stable with increasing wind speed. It is important to note that the QS expression for aerodynamic damping (Equation 2.7) is based on the somewhat-arbitrary assumption of the quarter chord point when calculating the apparent angle of attack, for the plate in rotational motion. If the leading edge of the

plate is taken, for instance $R = b/2$ instead of $b/4$, (see Section 2.3 and Blevins (1990, Chapter 4, p. 111)) the QS value for A_2^* doubles in magnitude. With that assumption the QS points and line in Figure 4.27 (for $\alpha = 0^\circ$) would move closer to the AC points. In both cases, however, the increase in negative value indicates that the aerodynamic damping adds to the effective damping (c_{eff}) with increasing wind speed, and therefore, to the stability of the structure (in terms of torsional galloping).

Figure 4.27, Figure 4.28 and Figure 4.29 show that, for $\alpha = 5^\circ, 15^\circ$ and 20° respectively, the critical wind speed (i.e. point P_2) given by the autocorrelation (AC) is close to the critical wind speeds given in Section 4.2. The point P_1 reaches the lowest minimum at tilt angle $\alpha = 5^\circ$, and it moves closer to zero as the tilt angle increases. This is a more accurate representation of the fluid-structure interaction with increasing U_{red} . The quasi-steady approximation does not capture this variation adequately (QS) and is a more conservative indication of the critical wind speed. However, the QS and AC predictions do seem to converge at a high reduced velocity (of about 6), but differences at lower reduced velocities is large. This difference is also noticeable when comparing results from Taylor and Browne (2020) and Cárdenas-Rondón et al., (2023) (Figure 2.7 and Figure 2.9, respectively). Nonetheless, these studies obtained the aerodynamic derivatives using free vibration techniques in a smooth flow and on two-dimensional plates, so differences could be expected.

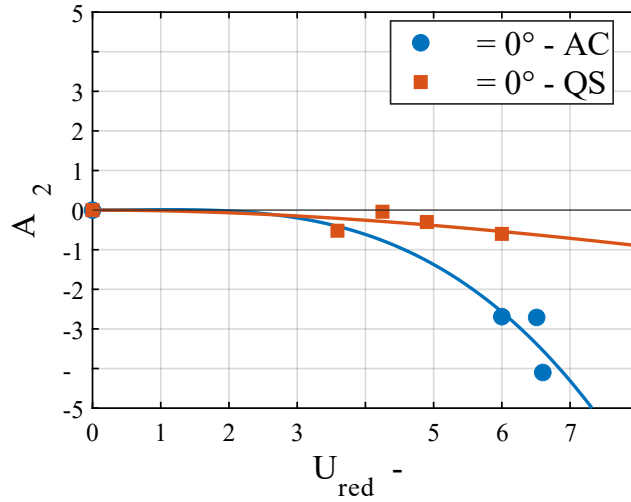


Figure 4.26. Aerodynamic derivative A_2^* vs reduced wind speed U_{red} . Comparison between autocorrelation (AC) and quasi-steady approximation (QS).

Model I-c, $\alpha = 0^\circ$ and $\theta = 0^\circ$

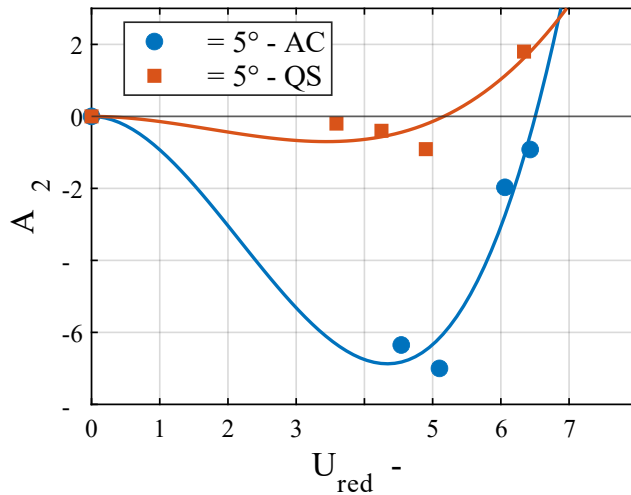


Figure 4.27. Aerodynamic derivative A_2^* vs reduced wind speed U_{red} . Comparison between autocorrelation (AC) and quasi-steady approximation (QS).

Model I-c, $\alpha = 5^\circ$ and $\theta = 0^\circ$

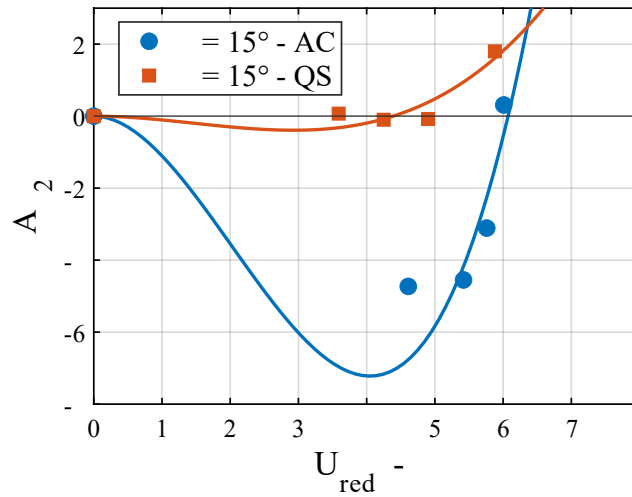


Figure 4.28. Aerodynamic derivative A_2^* vs reduced wind speed U_{red} . Comparison between autocorrelation (AC) and quasi-steady approximation (QS).

Model I-c, $\alpha = 15^\circ$ and $\theta = 0^\circ$

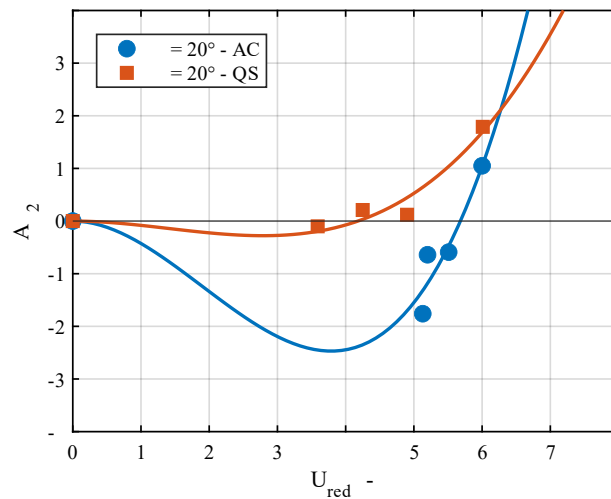


Figure 4.29. Aerodynamic derivative A_2^* vs reduced wind speed U_{red} . Comparison between autocorrelation (AC) and quasi-steady approximation (QS).

Model I-c, $\alpha = 20^\circ$ and $\theta = 0^\circ$

These results not only verify that the aerodynamic damping contributes positively with the effective damping, c_{eff} , but also that the larger the contribution, the larger the critical wind speed. For instance, when $\alpha = 5^\circ$, critical $U_{red} \cong 6.5$; when $\alpha = 15^\circ$, critical $U_{red} \cong 6$ and, when $\alpha = 20^\circ$, critical $U_{red} \cong 5.5$ (See Figure 4.27, Figure 4.28 and Figure 4.29, respectively). This is because a larger contribution of the aerodynamic damping provides a more stable fluid-structure interaction. Then, a larger wind speed is required to disrupt that stability.

4.6 Applications to design: preliminary assessment of stability

The results presented in this Chapter provide strategies to assess the stability of solar trackers.

The wind speed at the site should first be characterised. The design (i.e. Ultimate Limit State (ULS)) wind speed at the standard reference height (\hat{U}_{10m}) can then be determined using a reference Standard. For instance, the 0.2 s average gust wind speed at 10 m given by AS/NZS1170.2 (2021). Preferably, designers should perform a detailed wind climate study to determine the likelihood of wind speeds occurring from a range of wind directions. However, based on the orientation of the tracker (which is usually North-South), special attention should be given to wind directions (θ) ranging from East and West directions $\pm 40^\circ$. The design ULS wind speed \hat{U}_{10m} can then be converted into a mean wind speed \bar{U}_{10m} , using the method described by Holmes et al., (2014). Then, for known mean wind speed profile, the mean wind speed \bar{U}_h , at the height of the torque tube can be obtained. With the anecdotal evidence available for the types of trackers being installed, and the outcomes of this study, this critical gust wind speed is likely to be significantly smaller than typical values given for ultimate limit state design (usually

values based on 200-500 yrs), or even serviceability limit state design (of less than 50 yrs).

Other key parameters of interest are the natural frequency (f_0) of the tracker, and the breadth (b). Therefore, the reduced wind speed can be calculated so that $U_{red} = \bar{U}_h / (f_0 \times b)$. For reliable stability $U_{red} \leq 4$, to ensure the fluid-structure interaction is within the “stable” stage of the aerodynamic damping (i.e. around point P_1 , where A_2^* is a minimum).

Another action to minimize torsional flutter is to adopt large tilts (i.e. $\alpha = 50^\circ$). This will reduce the aerodynamic moment as per Section 4.1.2. At the same time, it could also provide reduced risks against other hazards such as snow and hail impact.

For a preliminary design, it is possible to determine an effective natural frequency $f_{0\,eff}$, using the condition $U_{red} = 4$. This criterion aims to determine the ideal natural frequency of the structure that assures that the aerodynamic damping contributes positively to the stability of the tracker. Hence, $f_{0\,eff} \geq \bar{U}_h / (4b)$.

After determining the effective natural frequency, the designer can select the appropriate parameters for the solar tracker to match the effective natural frequency. This includes the torque tube properties (i.e. shear modulus, G and polar moment of inertia, J_0), as well as the structure’s mass moment of inertia I_0 (given by the solar panels and the torque tube’s mass) and the length (l) of the solar tracker.

4.7 Chapter summary

This Chapter presented the results obtained from wind tunnel tests on rigid solar panel arrays and aeroelastic models of solar trackers. The findings provide insights into the wind loads acting on the structure, the critical wind speed causing the onset of aeroelastic instabilities, and the aerodynamic derivatives governing the response of solar trackers.

The analysis of wind loading showed that moment coefficients about the axial support are strongly dependent on wind direction and tilt angle. The largest moments occur at wind directions normal to the structure (i.e. $\theta = 0^\circ$ and 180°), whereas wind directions ($50^\circ < \theta < 130^\circ$) generate lower wind loads. Beginning from $\alpha = 30^\circ$, the moments decrease as tilt angle increases, due to the shift in the centre of pressure towards the torque tube. The variation of moment coefficients with tilt angle was found to be a key factor in determining aeroelastic stability.

Torsional flutter is the aeroelastic instability that occurs at a critical wind speed. Torsional galloping occurred for tilt angles between 5° and 25° , with a lower critical wind speed as the tilt angle increased up to 30° . Wind direction also played a key role, with instability occurring within the ranges of $0^\circ < \theta < 90^\circ$, and $180^\circ < \theta < 270^\circ$. Divergence was observed at small tilt angles ($0^\circ < \alpha < 5^\circ$), where the progressive increase in moment with wind speed led to instability. Additionally, the change in tilt angle due to divergence resulted in the onset of torsional galloping. The aspect ratio is also critical for the susceptibility to instability. Ratios $l/b = 6$ and $l/b = 8$ did show instability, indicating that increasing aspect ratio increases the chances of instability. Related to this is the natural frequency, which depends partly on the length l of the tracker. The lower the natural frequency, the higher the chances of instability. At the same time, because of the

natural frequency is related to stiffness, damping and geometrical characteristics of the structure, it can be used as a variable to assess the aeroelastic behaviour of solar trackers.

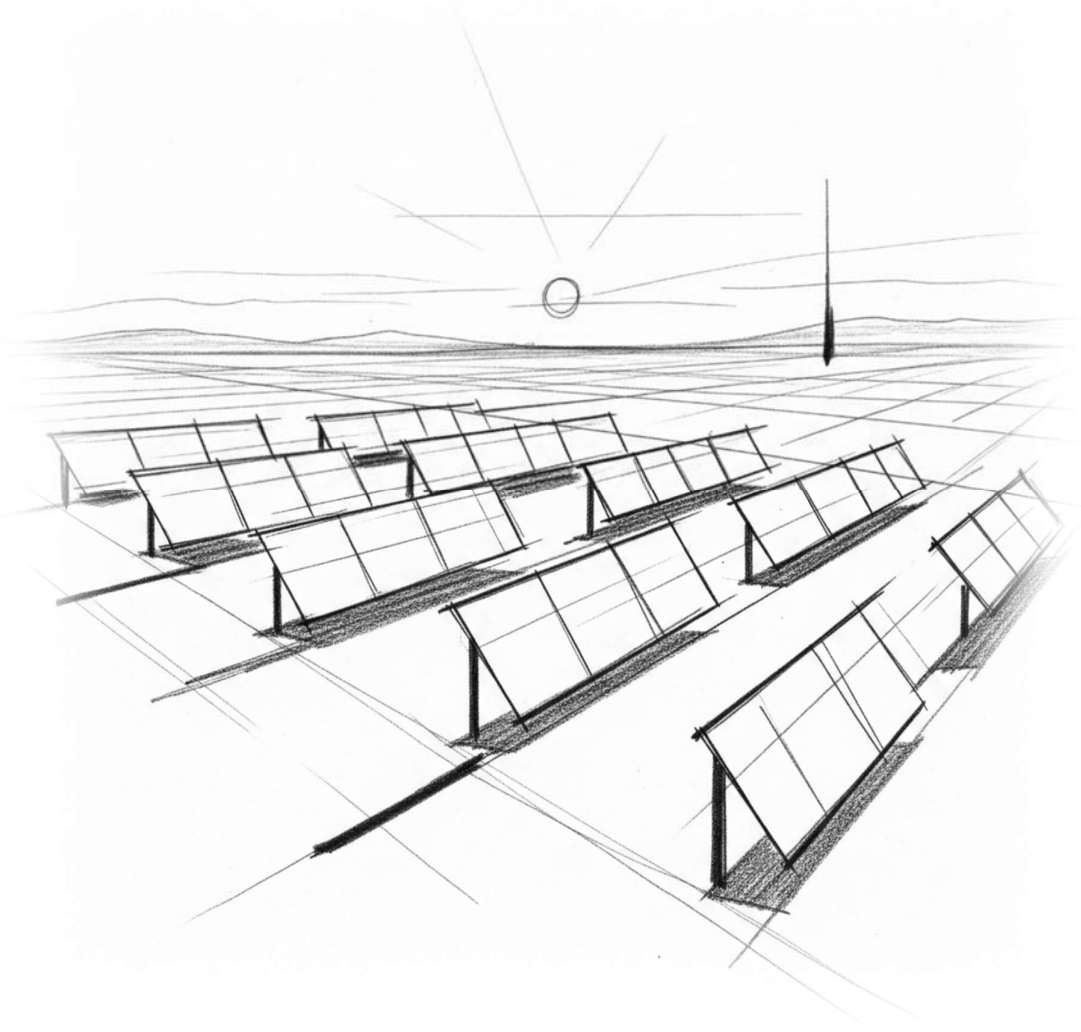
The critical wind speed varies with the tilt angle. Moderate tilt angles (i.e. $\alpha = 15^\circ$ and 20°) gave lowest critical wind speeds. The critical wind speed remains unchanged for a range of wind directions ($\theta = 0^\circ \pm 40^\circ$ and $\theta = 180^\circ \pm 40^\circ$). Furthermore, models with similar natural frequencies would become unstable at similar critical wind speeds. This implies that the critical wind speed is characteristic of the structural properties and is related to the natural frequency.

The aerodynamic derivatives A_2^* and A_3^* were used to assess the aeroelastic response. The aerodynamic derivative A_2^* initially decreased with increasing wind speed until reaching a minimum, indicating an initial contribution of the aerodynamic damping for stability. It then increased until $A_2^* = 0$, where the wind speed is critical, indicating the onset of instability. Tilt angles $\alpha = 5^\circ$ and 10° showed lower minimums of A_2^* than $\alpha = 15^\circ$ and 20° . This suggested that moderate tilt angles are less aerodynamically stable configurations. Moreover, the critical reduced wind speed U_{red} was lower for these tilt angles than for $\alpha = 5^\circ$ and 10° . Analysing results, it was found that once A_2^* reaches a minimum at a certain U_{red} , it takes $1.5U_{red}$ to reach the critical condition $A_2^* = 0$.

The quasi-steady theory and autocorrelation were used to determine the aerodynamic derivative A_2^* . The quasi-steady theory gives a conservative critical wind speed (i.e. lower) than the autocorrelation method. This is because the quasi-steady theory only relies on the change of mean moment (with increasing wind speed) which remains unchangeable even during instability. Conversely, the autocorrelation method captures better the variation of the effective damping, and reflects the fluid memory effect, which is critical for identifying the onset of instability.

The aerodynamic derivative A_3^* showed that the aerodynamic stiffness increases exponentially with increasing wind speed, particularly at small tilt angles ($\alpha = 0^\circ, 5^\circ$ and 10°). For a given wind speed, the rate of increase in aerodynamic stiffness is higher at these lower tilt angles compared to higher.

Based on these results it is possible to assess the stability of the structure by determining the wind conditions on site (U_{site}), the natural frequency (f_0) of the structure and the breadth (b). The following condition can be then applied: $[U_{site}/(f_0 \times b)] \leq 4$. $U_{red} \leq 4$ indicate that the fluid-structure interaction provides a stable structural response. Moreover, employing large tilt angles, such as $\alpha \geq 50^\circ$, during stowing reduces the aerodynamic moment around the torque tube, significantly decreasing the risk of aeroelastic instability.



5 RESPONSE OF SOLAR TRACKERS IN A MULTI-ROW SETUP – RESULTS

This Chapter presents an analysis of wind loads and aeroelastic response in multi-row configurations of single-axis solar trackers. The testing considers parameters such as row spacing (s), tilt angles (α), and wind direction (θ). Two configurations were tested within a three-row setup: Configuration 1, where Rows 1 and 2 were instrumented, and Configuration 2, where Rows 2 and 3 were instrumented. The chapter details the test setup and discusses the resulting moment coefficients and aeroelastic behaviour observed in these multi-row scenarios.

5.1 Multi-row test

A group of three rows of solar trackers spaced a distance $s = 350$ mm apart (7 m in full-scale, typically used in solar farms), was tested in the wind tunnel. The spacing parameter can be non-dimensionally described with the ratio $(s/h) = 3.5$. Tests were carried out using the procedure for wind loading described in Section 3.6.1, and for the critical wind speed, described in Section 3.6.2. Tests were conducted for a range of tilt angles (α) and wind directions (θ). Figure 5.1 shows a photograph of the set-up in the wind tunnel.

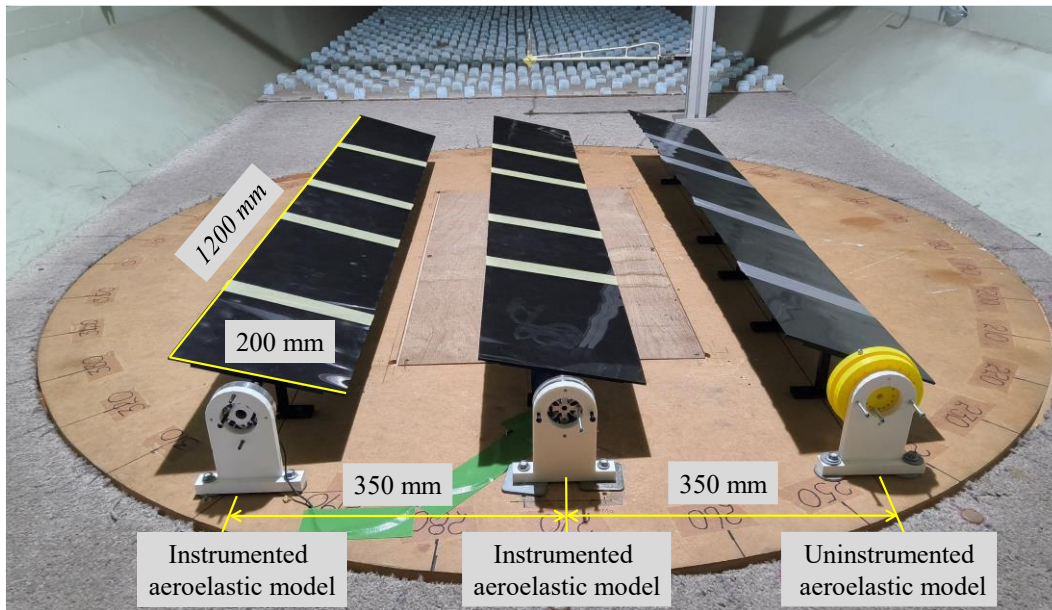


Figure 5.1. Multi-row configuration, comprising two rows with instrumented aeroelastic models and a third row with an uninstrumented aeroelastic model

The arrangement consisted of two instrumented aeroelastic model arrays (i.e. moment transducer connected at the fixed end), and an uninstrumented aeroelastic model array (i.e. without moment transducer at fixed end), all with an aspect ratio of 6 ($l = 1.2$ m, and $b = 0.2$ m). To maintain a controlled comparison between models with similar torque tube characteristics, the two models featuring hollow-tube torque tubes (i.e. Model I-b) were instrumented with the available moment transducers, leaving the rod torque tube model ($D_m = 8$ mm) as the uninstrumented row.

Wind loads were measured for tilt angles $\alpha = 10^\circ$ and 20° . Wind directions tested were $\theta = 0^\circ$ to 0° , and $\theta = 10^\circ$ to 10° , in 10° steps. The critical wind speed tests were carried out for $\alpha = 10^\circ$ and 20° , and wind directions from $\theta = 0^\circ$ to 0° , and $\theta = 10^\circ$ to 180° , in steps of 20° . Figure 5.2 shows a diagram of the configurations tested in the wind

tunnel. The arrays were defined according to their position when $\theta = 0^\circ$. In Configuration 1 (C1), Rows 1 and 2 were instrumented while Row 3 used an uninstrumented model. In Configuration 2 (C2), Rows 2 and 3 were instrumented, with Row 1 having an uninstrumented model.

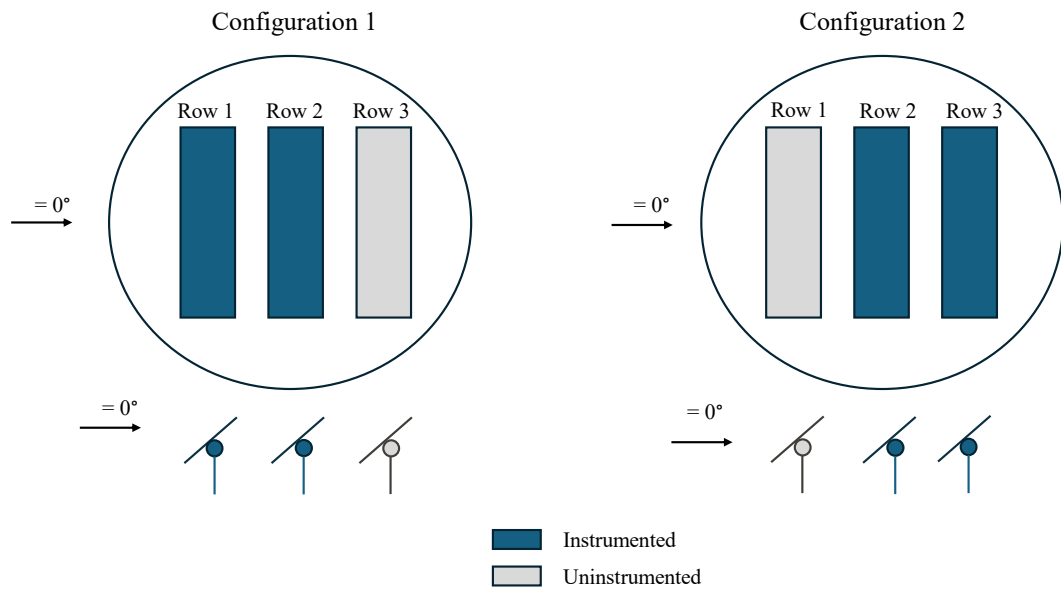


Figure 5.2. Configurations C1 and C2 of multiple arrays tested in the wind tunnel

5.2 Wind loading

The mean moment coefficients (C_M) for C1 and C2, for $\alpha = 10^\circ$ and $\alpha = 20^\circ$ are shown in Figure 5.3 to Figure 5.6. Wind directions (θ) studied were those determined to be critical for causing instability, from Section 4.1.2 (i.e. $(0^\circ < \theta < 90^\circ)$ and $(180^\circ < \theta < 270^\circ)$).

Figure 5.3 and Figure 5.4 show the mean moment coefficient ($C_{\bar{M}}$) vs. wind direction (θ) for Configuration 1 (i.e. Rows 1 and 2 are instrumented), for tilt angles (α) of 10° and 20° , respectively.

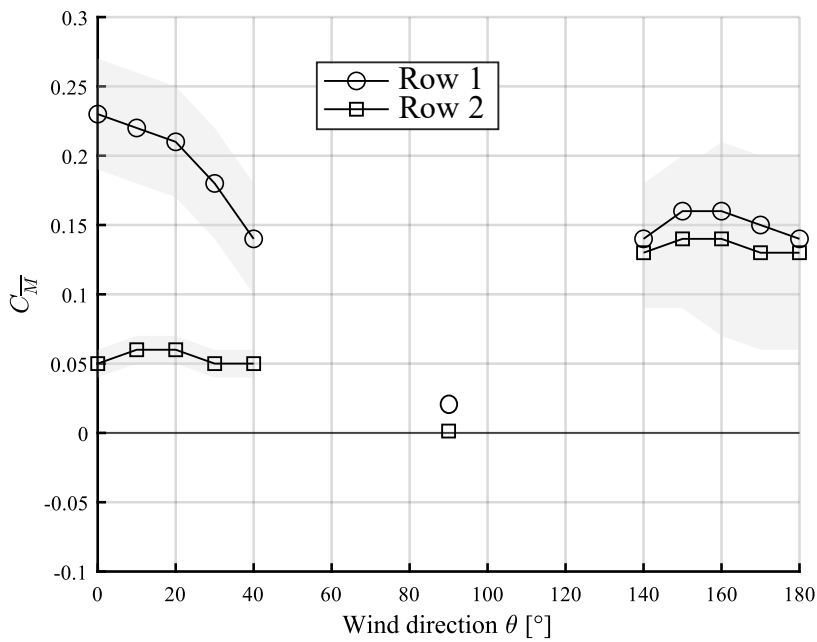


Figure 5.3. Mean moment coefficient $C_{\bar{M}}$ vs wind direction θ . Uncertainty is plotted as a grey shade. Row 1 and Row 2 (C1), $\alpha = 10^\circ$

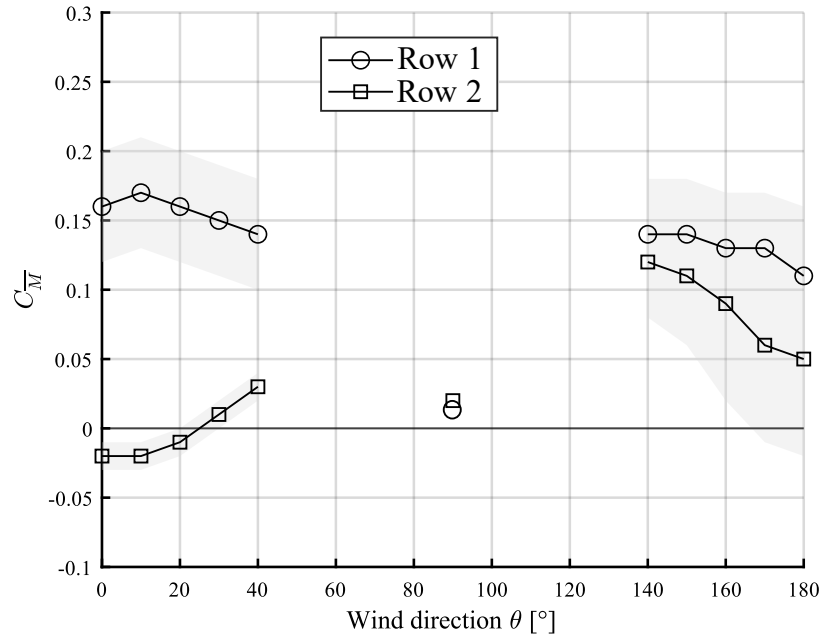


Figure 5.4. Mean moment coefficient C_M vs wind direction (θ). Uncertainty is plotted as a grey shade. Row 1 and Row 2 (C1), $\alpha = 20^\circ$

Figure 5.3 and Figure 5.4 show that for a row shielding winds $\theta \leq 40^\circ$, Row 1 (upwind) shields Row 2 (middle row). The shielding effect on Row 2 from upwind Row 1 is similar between tilt angle $\alpha = 10^\circ$ (Figure 5.3) and $\alpha = 20^\circ$ (Figure 5.4). Similar shielding from upwind row was observed for wind loading of multiple arrays of fix-tilt angle solar panels (Figure 2.13) by Warsido et al., (2014), and Ginger et al., (2019).

When the wind direction (θ) is between 10° and 170° , Row 1 (downwind) experiences slightly larger C_M than Row 2 (middle row) for both $\alpha = 10^\circ$ and $\alpha = 20^\circ$. This indicates that, for these wind directions, there is no shielding. This result differs with Warsido et al., (2014), who observed a progressive increase in the shielding effect on each row after the first on the upstream side (Figure 2.13). However, findings of this study agree with Ginger et al., (2019) who also reported a negligible shielding effect within this

wind direction range. A key difference between these studies lies in the spacing between the rows. Warsido et al., (2014) used relatively closer spacing distances ($s = 0.61$ m, 1.22 m, and 1.83 m full-scale), while both Ginger et al., (2019) and the current study utilized a larger more realistic typical spacing (Ginger et al.: $s = 7.0$ m full-scale; current study: $s = 7.0$ m full-scale). This suggests that the shielding effect reduces with increasing spacing.

Figure 5.5 and Figure 5.6 show the mean moment coefficient ($C_{\bar{M}}$) vs. wind direction (θ) for Configuration 2 (i.e. Rows 2 and 3 are instrumented), with tilt angles (α) of 10° and 20° , respectively.

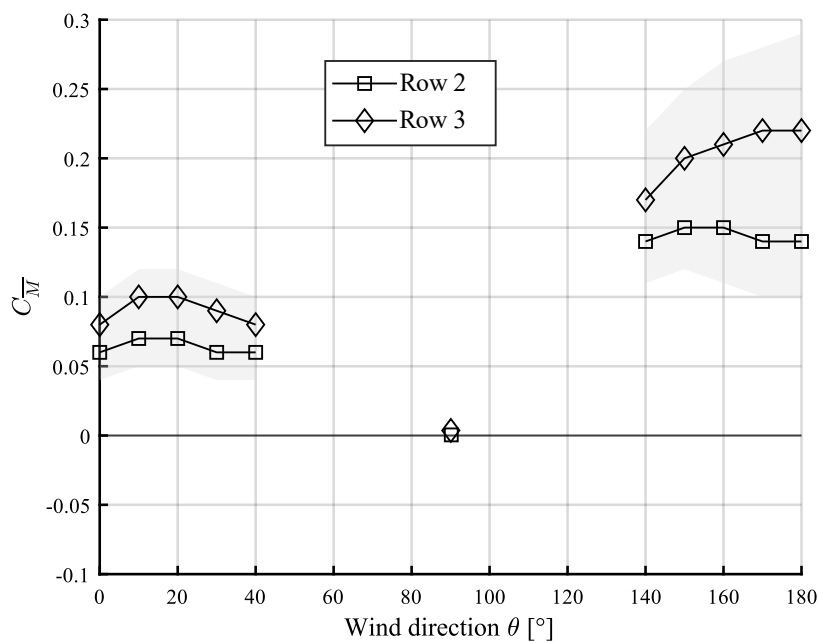


Figure 5.5. Mean moment coefficient $C_{\bar{M}}$ vs wind direction (θ). Uncertainty is plotted as a grey shade. Row 2 and Row 3 (C2), $\alpha = 10^\circ$

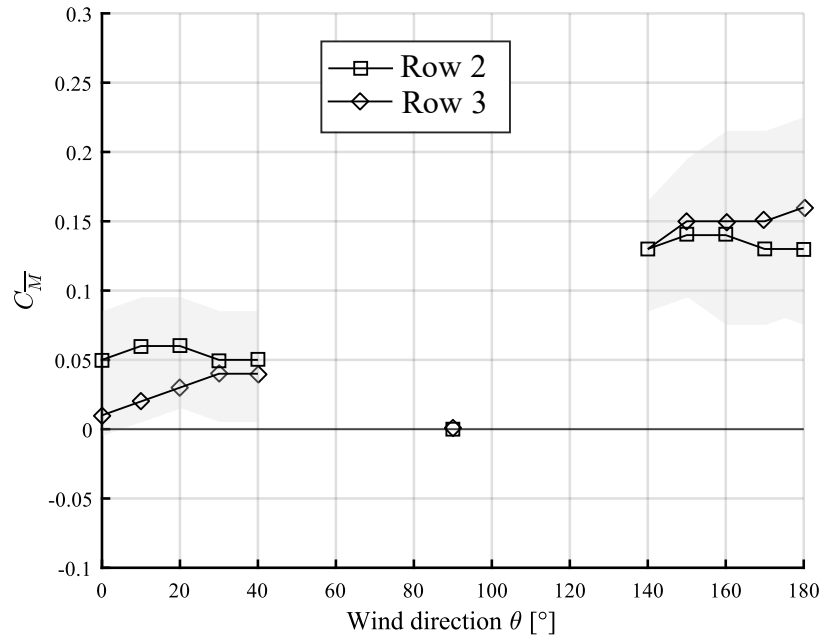


Figure 5.6. Mean moment coefficient C_M vs wind direction θ . Uncertainty is plotted as a grey shade. Row 2 and Row 3 (C2), $\alpha = 20^\circ$

Figure 5.5 shows that for $\alpha = 10^\circ$ and wind directions $\theta \leq 40^\circ$, Row 3 (downwind) shows slightly higher moment coefficients than Row 2 (middle row), indicating that Row 2 does not shield Row 3. For θ between 110° and 170° , both instrumented rows (Rows 2 and 3) show larger moment coefficients compared to $\theta \leq 40^\circ$. This is consistent with the observations in C1. Conversely, Figure 5.6 shows that for tilt angle $\alpha = 20^\circ$, when $\theta \leq 40^\circ$ Row 3 (downwind) is shielded by Row 2 (middle row). For approaching wind θ between 140° and 180° , Row 3 (upwind) shields Row 2 (middle row).

5.3 Aeroelastic instability

Figure 5.7 and Figure 5.8 show the moment response of Row 1 and Row 2 for Configuration 1 (C1), for $\alpha = 10^\circ$, and $\theta = 0^\circ$ and $\theta = 20^\circ$ respectively. Figure 5.7 shows that at about $t = 93$ s, both rows become unstable at the same time (i.e. the critical wind speed is the same, $U_{cr} = 11.4$ m/s). This demonstrates that shielding of the downstream row does not prevent the onset of instabilities. However, there is a difference in the magnitude of the moment response on each row. The response of Row 1 (upwind) shows larger amplitude than Row 2 (middle row). A similar result is shown for $\theta = 20^\circ$ at 97 s (Figure 5.8), although the critical wind speed increases slightly ($U_{cr} \cong 13$ m/s).

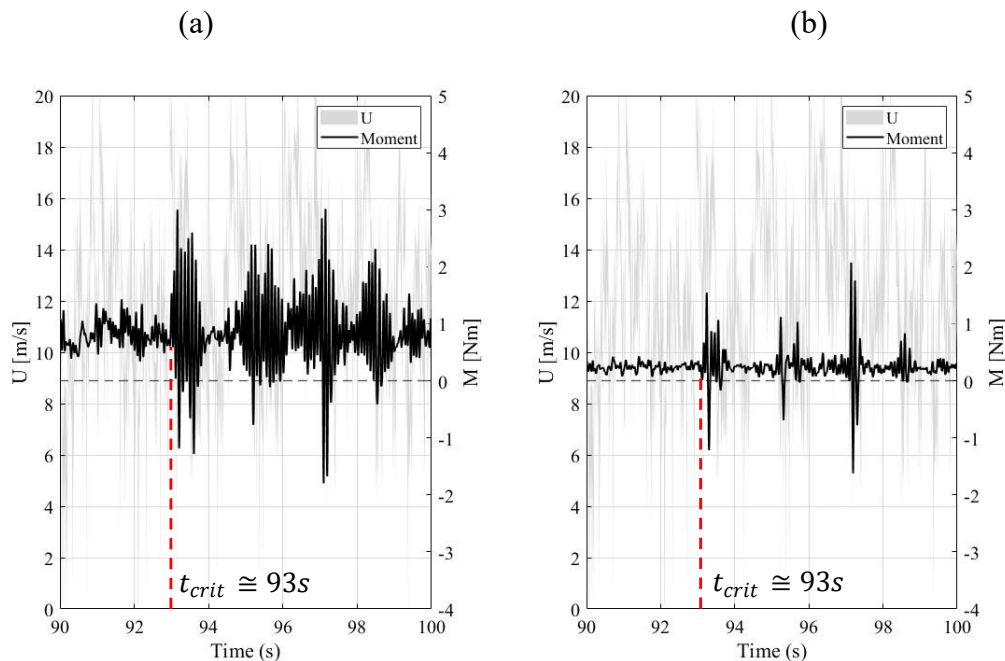


Figure 5.7. Fluctuating moment vs time of (a) Row 1, and (b) Row 2 (C1).

Model I-b, $\alpha = 10^\circ$ and $\theta = 0^\circ$. $U_{cr} = 11.4$ m/s (wind speed in model scale)

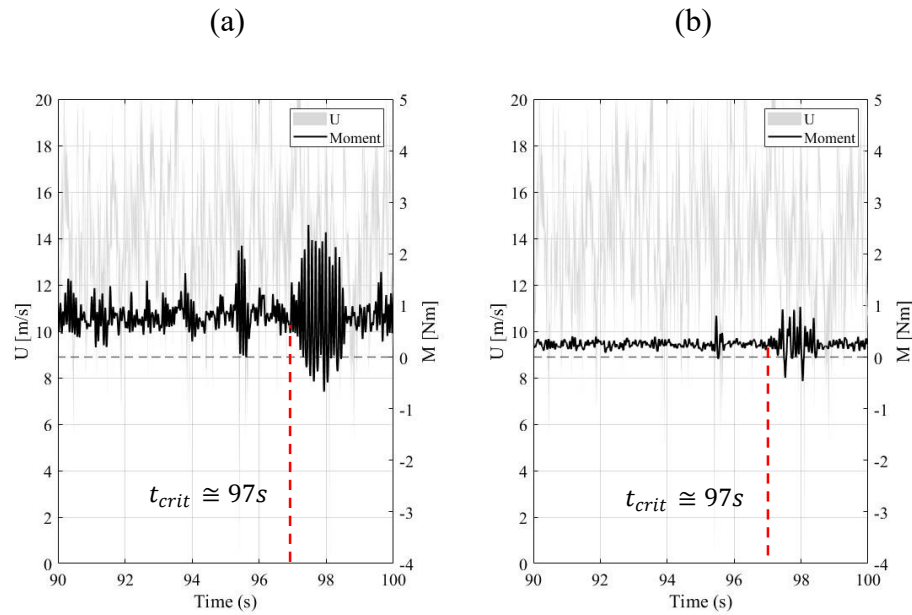


Figure 5.8. Fluctuating moment vs time of (a) Row 1, and (b) Row 2. Configuration 1.

Model I-b, $\alpha = 10^\circ$ and $\theta = 20^\circ$. $U_{cr} = 13.1 \text{ m/s}$ (wind speed in model scale)

Figure 5.9 and Figure 5.10 show the response of Row 1 and Row 2 (C1) for $\alpha = 10^\circ$, and wind approaching from $\theta = 160^\circ$ and $\theta = 180^\circ$ respectively. The aeroelastic instability occurs at the same time t and critical wind speed in both rows, but the moment response during instability of Row 2 (middle row) shows greater amplitude than that of Row 1 (downwind). It is also noticeable that the moment on both rows for $\theta = 10^\circ$, is larger than the moment (on both rows) for wind approaching from $\theta = 0^\circ$. This highlights the influence of wind direction approaching from $\theta = 10^\circ$ as the less favourable approach direction, not only for a single array, but even for a multiple array configuration. This is related to the discussion in Section 4.2.1 regarding the disruption of the flow when the supports of the structure (rails and torque tube) face the approaching wind flow.

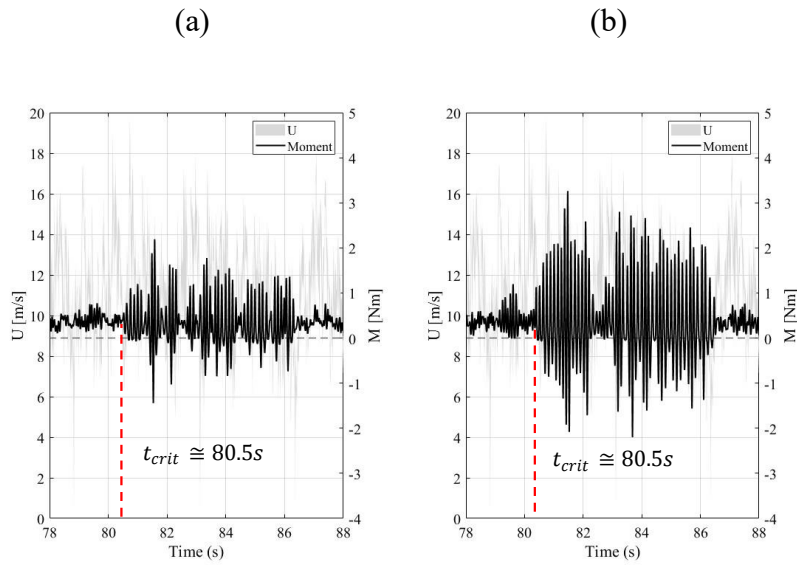


Figure 5.9. Fluctuating moment vs time of (a) Row 1, and (b) Row 2 (C1).

Model I-b, $\alpha = 10^\circ$ and $\theta = 160^\circ$. $U_{cr} = 11.2 \text{ m/s}$ (model scale)

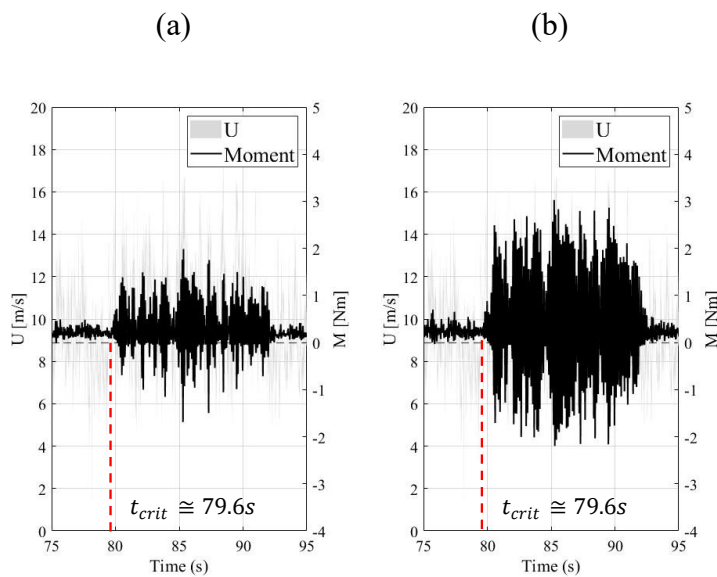


Figure 5.10. Fluctuating moment vs time of (a) Row 1, and (b) Row 2 (C1). Model I-

b, $\alpha = 10^\circ$ and $\theta = 10^\circ$. $U_{cr} = 9.0 \text{ m/s}$ (model scale)

Figure 5.11 and Figure 5.12 show the response of Row 2 and Row 3 (C2) for $\alpha = 10^\circ$; for wind approaching from $\theta = 0^\circ$ and $\theta = 180^\circ$ respectively. When $\theta = 0^\circ$, Row 2 (upwind) shows a response with larger peaks than Row 3. Evidently, the uninstrumented Row 1, which is the leading upwind row, does not shield Rows 2 and Row 3. When $\theta = 180^\circ$ (shown in Figure 5.12), Row 3 is upwind, and its response displays larger peaks than Row 2.

The greater magnitude of the response on both instrumented rows when $\theta = 180^\circ$, which has been observed in both Configurations tested (i.e. C1 and C2) is in agreement with the concept of Zhang et al., (2023) that increasing turbulence intensity increases the magnitude of the response during installation. This is because, when $\theta = 180^\circ$, the rails and torque tube disrupt the wind flow more, (thus, increasing local turbulence). Conversely, when the wind flow approaches the smooth surface of the panels (i.e. $\theta = 0^\circ$), the local increase of turbulence is less.

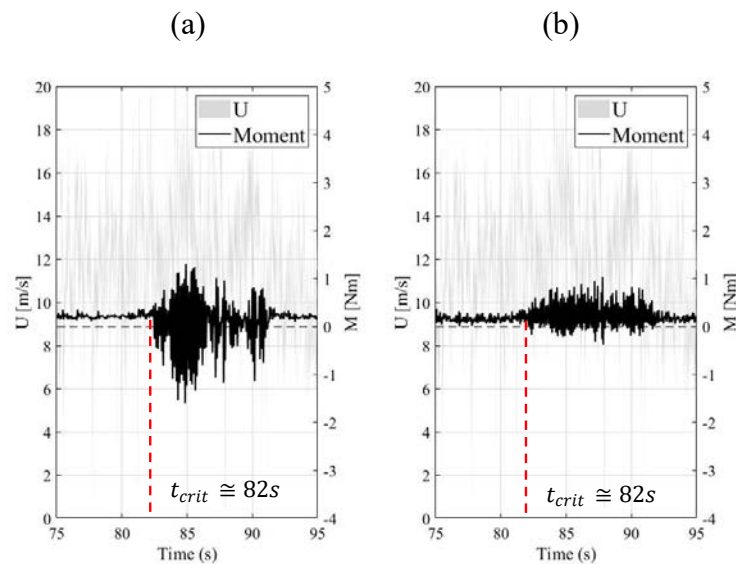


Figure 5.11. Fluctuating moment vs time of (a) Row 2, and (b) Row 3 (C2). Model I-

, $\alpha = 10^\circ$ and $\theta = 0^\circ$. $U_{cr} = 11.6 \text{ m/s}$ (wind speed in model scale)

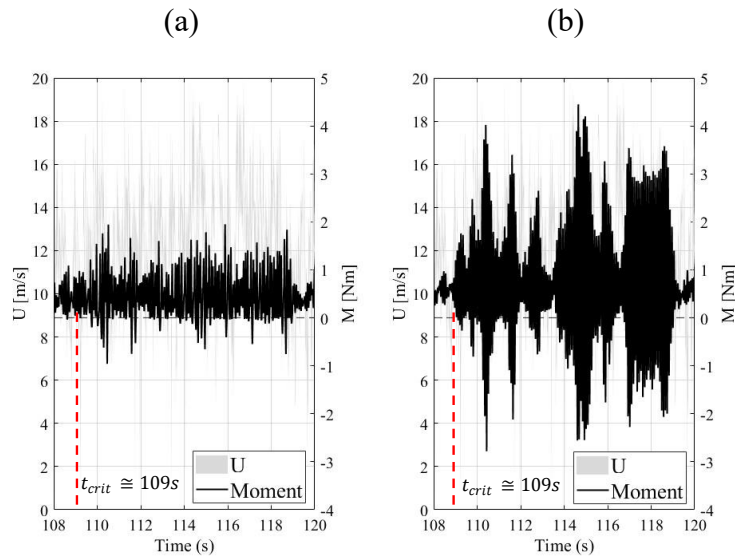


Figure 5.12. Fluctuating moment vs time of (a) Row 2, and (b) Row 3 (C2). Model I-
 $\alpha = 10^\circ$ and $\theta = 10^\circ$. $U_{cr} = 11.3 \text{ m/s}$ (wind speed in model scale)

The analysis of the behaviour observed in the multiple array configuration showed that shielding effects do not reduce the occurrence of instability. Moreover, the response to both normal (i.e. $\theta = 0^\circ$, $\theta = 10^\circ$) and oblique (i.e. $\theta = 20^\circ$, $\theta = 160^\circ$) approaching winds is the same as described for a single array in Section 4.2.1, with each row exhibiting the same critical wind speed U_{cr} . This indicates that regardless of the solar tracker array relative position, the critical wind speed can be taken as an intrinsic property of the solar tracker with typical spacing.

5.4 Spectral analysis

The dynamic response of the trackers in multiple array set-up is analysed using the spectrum of the aerodynamic moments. The power spectral densities of the moments measured on Row 1 and Row 2 (C1) for $\alpha = 10^\circ$ and for a range of wind directions are shown in Figure 5.13 to Figure 5.17.

Figure 5.13 shows the spectra for Row 1 and Row 2 (C1) for $\theta = 0^\circ$ during torsional galloping. Characteristic peaks on the spectrum of each moment response are observed around 10 Hz. However, the natural frequency f_0 of these models is 14.8 Hz (see Table 3.2). Therefore, the characteristic frequency observed is in fact the aeroelastic response frequency, which tends to be different to the natural frequency as per discussed in Section 4.2.2. Strobel and Banks (2014) showed that in a multiple array setup, the dynamic response of the arrays is caused by resonance produced by the vortex shedding from the first row. The shedding frequency f_v dominates the fluctuating load on the second row through buffeting. This effect decreases moving further downstream. The vortex shedding, however, does not cause significant excitation on the first row.

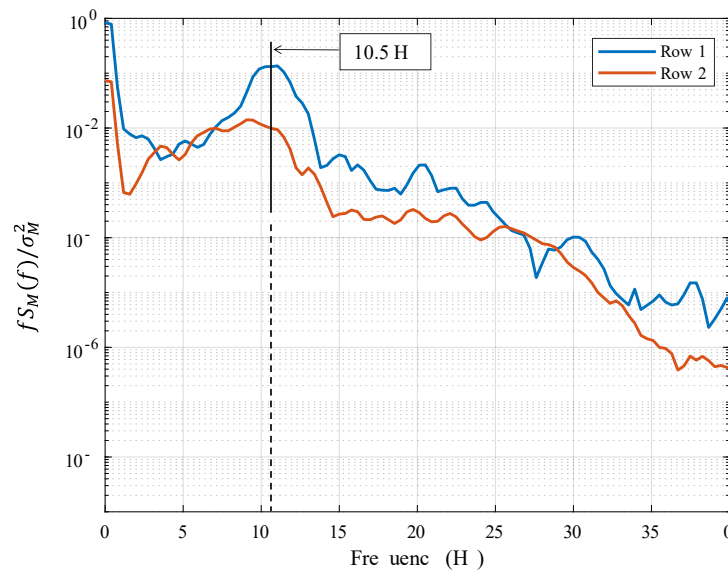


Figure 5.13. Power spectral density of the moment, $\alpha = 10^\circ$, $\theta = 0^\circ$. Row 1 and Row 2 (C1), during galloping

Figure 5.14 and Figure 5.15 show the spectra for C1, for a reaching wind $\theta = 20^\circ$ and $\theta = 0^\circ$, respectively. For wind direction $\theta = 20^\circ$, a condition that triggered instability, the frequency peak is 10 Hz. Then, at $\theta = 0^\circ$ (a condition that did not trigger instability) the characteristic frequency is closer to f_0 . In all cases, the spectrum of the upwind row shows a higher level of energy, which is in agreement with the greater amplitude of the response measured on the upwind row, which was analysed in Section 5.3.

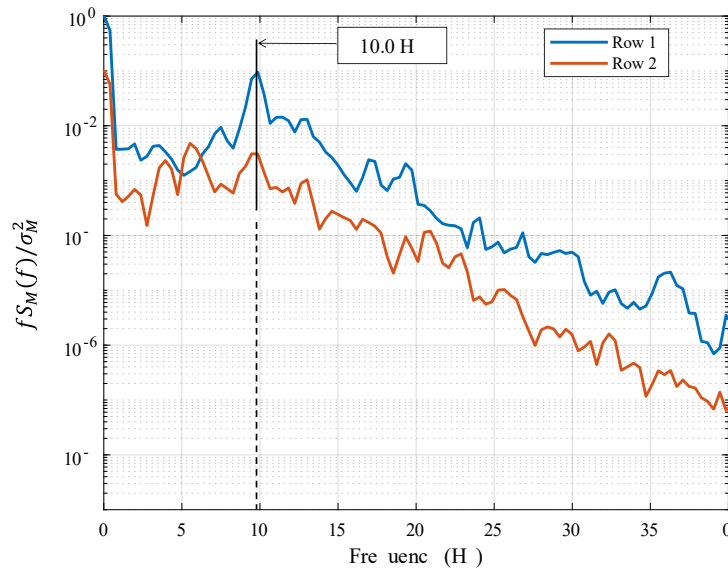


Figure 5.14. Power spectral density of the moment, $\alpha = 10^\circ$, $\theta = 20^\circ$.

Row 1 and Row 2 (C1), stable condition

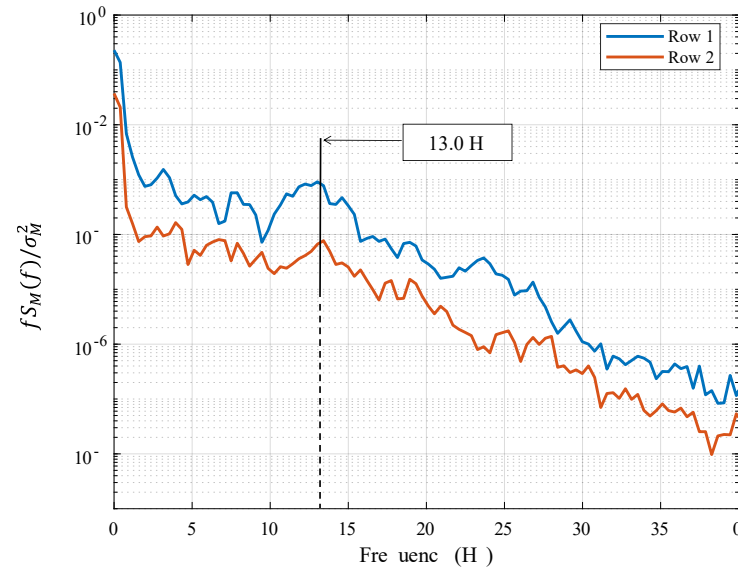


Figure 5.15. Power spectral density of the moment, $\alpha = 10^\circ$, $\theta = 0^\circ$.

Row 1 and Row 2 (C1), stable condition

The response for the cases $\theta = 160^\circ$ and $\theta = 10^\circ$ are shown in Figure 5.16 and Figure 5.17, respectively. Winds approaching from $160^\circ < \theta < 180^\circ$ tend to produce a response that has a lower characteristic frequency, compared with $\theta = 0^\circ$ or $\theta = 20^\circ$. The characteristic frequency is about 8 Hz in both rows. This can be associated with the increased amplitude of the moment response when installation occurs for $160^\circ < \theta < 10^\circ$, which was discussed in Section 5.3.

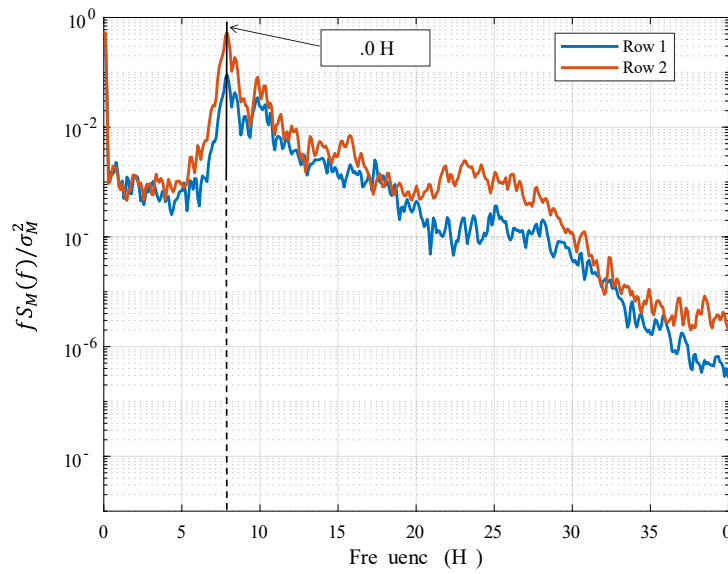


Figure 5.16. Power spectral density of the moment, $\alpha = 10^\circ$, $\theta = 160^\circ$.

Row 1 and Row 2 (C1), during instability

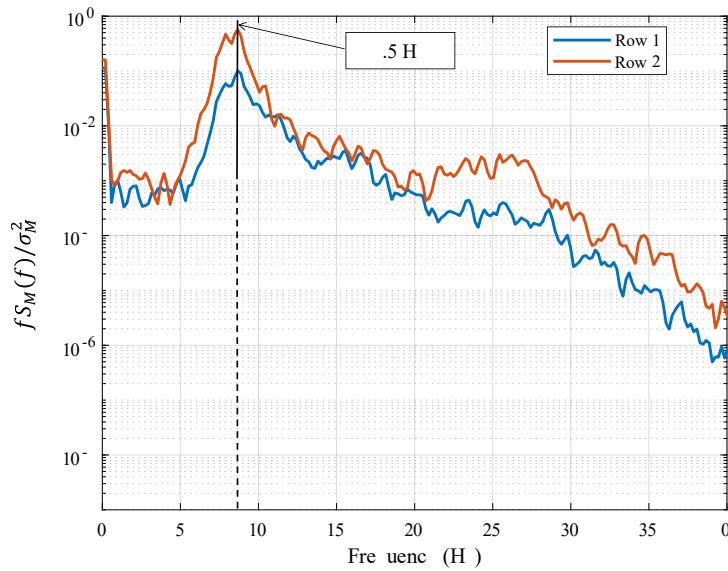


Figure 5.17. Power spectral density of the moment, $\alpha = 10^\circ$, $\theta = 10^\circ$.

Row 1 and Row 2 (C1), during instability

5.5 Chapter summary

This chapter analysed wind loads and the aeroelastic response of solar trackers in a multi-row (i.e. three row) arrangement with a row spacing, $s = 7.0$ m, and ratio $(s/h) = 3.5$. A range of tilt angles (α) and wind directions (θ) were examined.

Under stable conditions (i.e. $U < U_{cr}$) at $\theta = 0^\circ$ and $\theta = 10^\circ$, the upwind row shields the middle row. This shielding effect is negligible for the downwind rows. The shielding for $\alpha = 10^\circ$ compared to $\alpha = 20^\circ$ is similar.

Critical wind speed tests demonstrated that the onset of instability occurs simultaneously on all rows, regardless of tilt angle (α) or wind direction (θ). This suggests that the position of the tracker within a multi-row setup does not influence the initiation of instability. The models exhibited similar behaviour to a single-array configuration (Section 4.2), indicating that the critical wind speed is an intrinsic property of the structure. Therefore, if the wind speed remains constant across the multi-row, all trackers will become unstable once their critical wind speed is reached (i.e., when the effective damping $c_{eff} = 0$).

Wind directions $\theta = 10^\circ \pm 0^\circ$ triggered greater moment amplitude during instability compared to $\theta = 0^\circ \pm 0^\circ$. Furthermore, the characteristic frequency of oscillation during torsional galloping was lower at $\theta = 10^\circ \pm 0^\circ$.



Árbol Patagónico

6 CONCLUSIONS

This thesis studied the wind loads on axially supported flat plates and related them to the behaviour of solar tracker arrays in the field. A range of aeroelastic models were tested in simulated terrain conditions for approach turbulent wind flows.

The models were constructed from typical designed full-scale components used by the industry, by simulating the parameters, such as the structural stiffness and the structural damping, natural frequency, and inertia. A range of configurations were studied by varying the length of the models (i.e. increasing the aspect ratio) and using different cross sections to model the torque tube. Furthermore, three solar tracker rows were tested together to evaluate the effects of adjacent arrays on the response.

The literature review and theoretical analysis described how these structures can fail due to aeroelastic instabilities defined as torsional flutter. The effect of oblique approach wind directions and the influence of realistic atmospheric flow on the wind loading and the aeroelastic response of solar trackers were also assessed.

This study addressed the aims listed in Section 1.3 and the research gaps identified in Section 2.10. Consequently, this study,

- Obtained the fluctuating wind loads on typical solar trackers for a range of approach wind directions (θ). This showed that there are two characteristic moment responses about the axis (i.e. torque tube): i) for $\theta = 0^\circ \pm 0^\circ$, and $\theta = 180^\circ \pm 40^\circ$; and ii) for $\theta = 90^\circ \pm 40^\circ$. In the first, the structure may experience aeroelastic instabilities. In the second, the moments are significantly lower, and aeroelastic instability is unlikely.
- Determined the wind loading with changing tilt angle (α). Small tilt angles (i.e. $0^\circ < \alpha < 10^\circ$) gave a positive change of the moment coefficient with tilt angle ($\partial C_M / \partial \alpha$), and the possibility for torsional divergence. Medium tilts (i.e. $15^\circ < \alpha < 25^\circ$) showed a negative ($\partial C_M / \partial \alpha$), and the possibility of torsional galloping. Large tilts (i.e. $30^\circ < \alpha < 50^\circ$) resulted in a stable configuration for solar trackers.
- Analysed the aerodynamic loading on solar trackers before and during the onset of aeroelastic instabilities to show that the onset of torsional divergence (at small tilt angle) is preceded by a sustained increase of the mean moment coefficient. Torsional divergence occurs when the effective stiffness k_{eff} gradually decreases and approaches zero with increasing wind speed.
- Showed that the onset of torsional galloping (at medium tilt angles) occurs suddenly when the effective damping (c_{eff}) drops to zero with a small wind speed increase, as the critical wind speed is reached.
- Showed that oblique approach winds within $\pm 40^\circ$ from normal approach, can trigger torsional galloping at a similar critical wind speed, as for the normal approach winds. Tilt angle $\alpha = 15^\circ$ to 20° are the most prone to instability, at low

critical wind speeds, followed by small tilt angles (i.e. $\alpha = 0^\circ$ to 15°). Large tilt angles (i.e. $\alpha = 30^\circ$ to 50°) were unlikely to experience instability.

- Demonstrated that the leading upwind row in a multi row solar tracker setup shields the next row. The rows further downstream experience loads that are similar to that on the second row when the spacing distance $s = 7\text{ m}$.
- Demonstrated that the instability of a multirow solar tracker setup does not depend on the position of the array within the setup. The critical wind speed U_{cr} triggers instabilities on solar trackers on all rows at the same time at a similar wind speed.

The hypothesis of this thesis, that increased aspect ratios and reduced stiffness of solar trackers will increase the susceptibility to aeroelastic instability, has been proven in the study. The increased aspect ratio l/b reduces the structural stiffness k_0 and natural frequency f_0 , which then leads to a lower critical wind speed U_{cr} . Therefore, the lower the natural frequency and structural stiffness, the higher the occurrence of aeroelastic instabilities.

Based in the results of this study, the stow position should be considered as the highest tilt angle possible (i.e. $\alpha \geq 50^\circ$) for the trackers because this reduces the aerodynamic moment about the torque tube, minimizing the occurrence of aeroelastic instabilities. Moreover, the condition $U_{red} = [U_{site}/(f_0 \times b)] \leq 4$ is a criterion for both the preliminary assessment of an existing solar tracker, and for the design of new systems. By utilizing site-specific wind speeds (U_{site}), the natural frequency (f_0), and breadth (b), the stability can be determined. Furthermore, this relationship facilitates the optimization of structural properties during the design phase, ensuring that solar trackers are designed with adequate natural frequency to mitigate potential instability risks.

6.1 A Critical Evaluation of Quasi-steady Approach

The quasi-steady (Q-S) aerodynamic approach has served in this study as a foundational model for understanding certain wind-induced instabilities. Its simplicity makes it valuable for preliminary assessments. In the context of torsional flutter, the Q-S model better captures stiffness-driven instabilities, as its formulation inherently does not account for aerodynamic damping terms.

In this study, the experimental results consistently demonstrated that, for damping-driven torsional flutter (torsional galloping), the quasi-steady model tends to conservatively predict the critical wind speed. This observed conservatism derives from its inability to fully capture the effective damping variation due to the flow-structure interaction. While a conservative prediction is generally safe for design, it may lead to less efficient designs if the underlying mechanisms are not fully understood. For instance, at tilt angles where torsional galloping dominates, the autocorrelation method provides a much closer agreement with experimental observations because it better captures the variation of the effective damping.

This work concludes that while the Q-S approach is valuable for identifying and characterizing the potential of instability, its direct application for all torsional flutter phenomena, especially those where damping is critical, warrants careful consideration of its inherent simplifications.

6.2 Concluding statement

This thesis has successfully demonstrated the significant influence of various parameters on the aeroelastic stability of single-axis solar trackers. The results emphasize the necessity for a comprehensive approach to design, incorporating the relationships between wind loads, structural dynamics, and operational conditions. By providing both a means of preliminary verification and a framework for design optimization, this work offers practical tools to mitigate aeroelastic instability risks and ensure the safe and efficient design and operation of solar tracking technology.

REFERENCES

- Acosta, T. J., Guo, Y., Wang, J., Brusco, S., & Kopp, G. A. (2024). Requirements for partial turbulence simulations using nondimensional turbulence energy contributions. *Journal of Wind Engineering and Industrial Aerodynamics*, 254, 105886.
- American Society of Civil Engineers. (2022, January). Wind tunnel testing for buildings and other structures. American Society of Civil Engineers.
- American Society of Civil Engineers. (2022). *ASCE-7-2022-Minimum Design Loads and Associated Criteria for Buildings and Other Structures*. Reston, Virginia, USA.
- Bisplinghoff, L., Ashley, H., & Halfman, R. L. (1996). *Fundamentals of Aeroelasticity* (2nd ed.). Dover Publications.
- Bisplinghoff, R. L., Ashley, H., & Halfman, R. L. (2013). *Aeroelasticity*. Courier Corporation.
- Blevins, R. D. (1990). *Flow-induced vibration*, K. P. Company, Ed. 2nd ed.
- Brydges, J. (2019). Simulation of Flow Over Flat Plates for PV Wind Loads Assessment.
- Cárdenas-Rondón, J. A., Ogueta-Gutiérrez, M., Franchini, S., & Manzanares-Bercial, R. (2023). “Statistical analysis of two-dimensional flat solar trackers using aerodynamic derivatives at different heights above ground”. *Journal of Wind Engineering and Industrial Aerodynamics*, 243, 105606. <https://doi.org/10.1016/j.jweia.2023.105606>.
- Cárdenas Rondón, J. A. (2023). *Experimental study of self-excited aeroelastic instability in two-dimensional single-axis flat solar trackers* [Doctoral dissertation, Universidad Politécnica de Madrid].
- Cárdenas-Rondón, J. A., Carbajosa, C., Marín-Coca, S., & Martínez-Cava, A. (2024). Parametric analysis of self-excited aeroelastic instability of an isolated single-axis two-dimensional flat solar tracker. *Results in Engineering*, 24, 103539.
- Chen, J. M., & Fang, Y. C. (1996). “Strouhal numbers of inclined flat plates”. *Journal of wind engineering and industrial aerodynamics*, 61(2-3), 99-112.
- Dallaire, P. O. (2010). *Étude des vibrations éoliennes stationnaires*. Library and Archives Canada Bibliothèque et Archives Canada, Ottawa.

- Dowell, E. H. (2015). *A modern course in aeroelasticity*, 5th Edition, Springer, <https://doi.org/10.1007/978-3-319-09453-3>.
- Enshaei, ., et al. (2023). “Low-Tilt Torsional Instability of Single-Axis Solar Trackers”. *16th International Conference on Wind Engineering*, Florence, Italy.
- ESDU (1970). “Fluid Forces and Moments on Flat Plates”. I. Engineering Sciences Data Unit (ESDU, London).
- Fage, A., & Johansen, F. C. (1927). “On the flow of air over an inclined flat plate of infinite span”. *Proceedings of the Royal Society of London. Series A, Containing Papers of a Mathematical and Physical Character*, 116(773), 170-197.
- Farquharson, F. B. (1954). Aerodynamic stability of suspension bridges. *Univ. of Washington Experiment Station, Bulletin*, 116, PART-I.
- Gifford, J., 2019. What broke at Oakey. URL: <https://www.pv-magazine-australia.com/2019/12/07/long-read-what-broke-at-oakey/>. PV Magazine.
- Ginger, J. D., Bodhinayake, G. G., & Ingham, S. (2019). “Wind loads for designing ground-mounted solar panel arrays”. *Australian Journal of Structural Engineering*, 20(3), 204-218. <https://doi.org/10.1080/13287982.2019.1623001>.
- Holmes, J. D., Allsop, A. C., & Ginger, J. D. (2014). Gust durations, gust factors and gust response factors in wind codes and standards. *Wind and Structures*, 19(3), 339-352.
- Holmes, J. D. and Bekele, S.A. (2021). *Wind Loading of Structures*, 4th Edition, CRC Press, Boca Raton, USA.
- Irwin, P. A. (1998). The role of wind tunnel modelling in the prediction of wind effects on bridges. *Bridge aerodynamics*.
- Irwin, P. A. (2008). Bluff body aerodynamics in wind engineering. *Journal of Wind Engineering and Industrial Aerodynamics*, 96(6-7), 701-712.
- Koekemoer, J. H., Bredell, J. R., Venter, G., & Reinecke, J. (2024). Field measurements of wind load effects in a photovoltaic single-axis tracker mounting rail. *Journal of Wind Engineering and Industrial Aerodynamics*, 253, 105876.
- Kopp, G. A. (2023). Updates to the wind tunnel method for determining design loads in ASCE 49-21. *Wind & structures*, 37(2), 163-178.
- Martínez-García, E., Blanco-Marigorta, E., Gayo, J. P., & Navarro-Manso, A. (2021). “Influence of inertia and aspect ratio on the torsional galloping of single-axis solar trackers”. *Engineering Structures*, 243, 112682. <https://doi.org/10.1016/j.engstruct.2021.112682>.
- Macdonald, J. H., Irwin, P. A., & Fletcher, M. S. (2002). Vortex-induced vibrations of the Second Severn Crossing cable-stayed bridge—full-scale and wind tunnel measurements. *Proceedings of the Institution of Civil Engineers-Structures and Buildings*, 152(2), 123-134.
- Nakamura, Y. (1979). On the aerodynamic mechanism of torsional flutter of bluff structures. *Journal of Sound and Vibration*, 67(2), 163-177.

- Nakamura, Y., & Miota, T. (1975). "Torsional flutter of rectangular prisms". *Journal of the Engineering Mechanics Division*, **101**(2), 125-142.
- Parkinson, G. V., & Smith, J. D. (1964). The square prism as an aeroelastic non-linear oscillator. *The Quarterly Journal of Mechanics and Applied Mathematics*, *17*(2), 225-239.
- Pigolotti, L., Mannini, C., & Bartoli, G. (2017). Experimental study on the flutter-induced motion of two-degree-of-freedom plates. *Journal of Fluids and Structures*, *75*, 77-98.
- Rodríguez-Casado, C., Martínez-García, E., Manzanares-Bercial, R., Ruiz-Moral, J. L., Blanco-Marigorta, E., & Navarro-Manso, A. (2024). "Experimental Benchmark for the 3D wind tunnel testing of torsional aeroelastic instabilities in single-axis solar trackers". *Journal of Wind Engineering and Industrial Aerodynamics*, **253**, 105838. <https://doi.org/10.1016/j.jrineng.2024.103539>.
- Rohr, C., Bourke, A., & Banks, D. (2015, June). "Torsional instability of single-axis solar tracking systems". In *Proceedings of the 14th international conference on wind engineering, Porto Alegre* (pp. 21-26).
- Scanlan, R. H., & Tomko, J. J. (1971). "Airfoil and ridge deck flutter derivatives". *Journal of the engineering mechanics division*, **97**(6), 1717-1737. <https://doi.org/10.1061/JMCEA3.0001526>.
- Simiu, E., & Yeo, D. (2019). *Wind effects on structures: Modern structural design for wind*. John Wiley & Sons.
- Slater, J. E. (1969). *Aeroelastic instability of a structural angle section* (Doctoral dissertation, University of British Columbia).
- Standards Australia. (2021). *Structural design actions. Part 2: Wind Actions*, Sydney, New South Wales, Australia, Australian/New Zealand Standard, AS-NZS 1170.2:2021.
- Strobel, K., & Banks, D. (2014). "Effects of vortex shedding in arrays of long inclined flat plates and ramifications for ground-mounted photovoltaic arrays". *Journal of Wind Engineering and Industrial Aerodynamics*, **133**, 146-149. <https://doi.org/10.1016/j.jweia.2014.06.013>.
- Surry, D. (1982). Consequences of distortions in the flow including mismatching scales and intensities of turbulence. *Wind tunnel modeling for civil engineering applications*, 137-185.
- Taylor, Z. J., Gurka, R., Kopp, G. A., & Liberzon, A. (2010). Long-duration time-resolved PIV to study unsteady aerodynamics. *IEEE Transactions on Instrumentation and Measurement*, *59*(12), 3262-3269.
- Taylor, Z. J., & Browne, M. T. (2020). "Hirid pressure integration and offsetting analysis for multi-row wind loading in an array of single-axis trackers". *Journal of Wind Engineering and Industrial Aerodynamics*, **197**, 104056. <https://doi.org/10.1016/j.jweia.2019.104056>.

- Taylor, Z. J., Feero, M. A., & Browne, M. T. (2023). "Aeroelastic instability mechanisms of single-axis solar trackers". *Journal of Wind Engineering and Industrial Aerodynamics*, **244**, 105626. <https://doi.org/10.1016/j.jweia.2023.105626>.
- Theodorsen, T. (1935). "General Theory of Aerodynamic Instability and the Mechanism of Flutter", 96, National Advisory Committee for Aeronautics, Technical Report.
- Valentín, D., Valero, C., Egusquiza, M., & Presas, A. (2022). "Failure investigation of a solar tracker due to wind-induced torsional galloping". *Engineering Failure Analysis*, **135**, 10613. <https://doi.org/10.1016/j.engfailanal.2022.106137>.
- Wardlaw, R. L. (1994). Flutter and torsional instability. In *Wind-excited vibrations of structures* (pp. 293-319). Vienna: Springer Vienna.
- Warsido, W., Bitsuamlak, G. T., Barata, J., & Chowdhury, A. G. (2014). "Influence of scaling parameters on the wind loading of solar arrays". *Journal of fluids and structures*, **48**, 295-315. <https://doi.org/10.1016/j.jfluidstructs.2014.03.005>.
- Yoshimura, T., & Nakamura, Y. (1980). On the indicial aerodynamic moment responses of bridge deck sections. In *Wind Engineering* (pp. 877-885). Pergamon.
- Young, E., He, X., King, R., & Corbus, D. (2020). A fluid-structure interaction solver for investigating torsional galloping in solar-tracking photovoltaic panel arrays. *Journal of Renewable and Sustainable Energy*, *12*(6).
- Zhang, X., Ma, W., Kang, X., Shao, Q., & Tang, Z. (2023). "Experimental study of the torsional aeroelastic instability of single-axis solar trackers under different turbulence intensities". *Journal of Wind Engineering and Industrial Aerodynamics*, **240**, 105486. <https://doi.org/10.1016/j.jweia.2023.105486>.

APPENDIX A: SOLAR ARRAY MODEL

A.1 Aeroelastic modelling calculations

- **Solar panels**
 - a) Bending stiffness

Figure A.1 shows the top view of the prototype solar panel module. The components of the solar panel considered for the aeroelastic modelling are shown in Figure A.2.

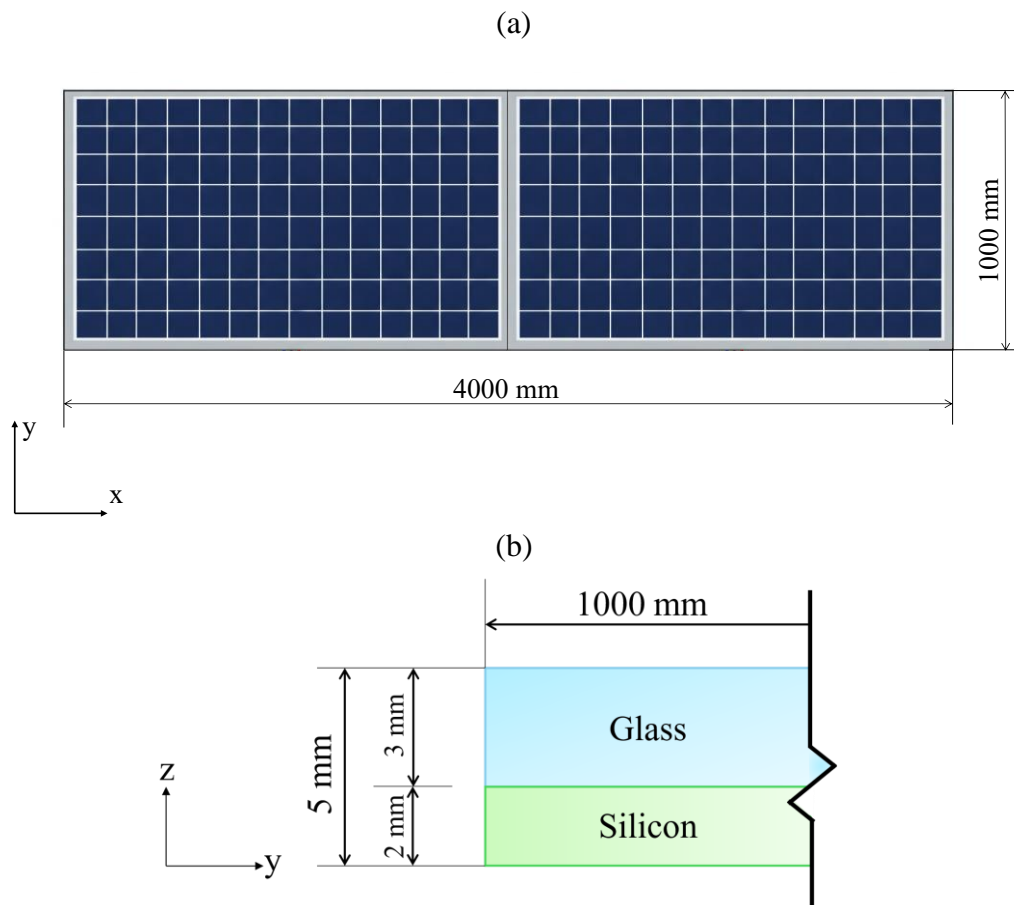
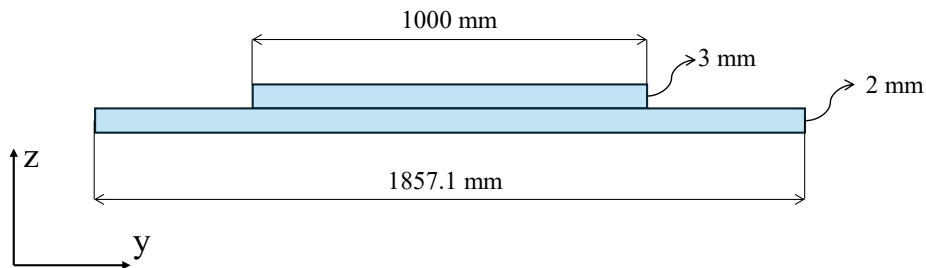


Figure A.1. (a) Prototype solar panel module dimensions, and (b) Schematic diagram of prototype solar panel components

The solar panel is a composite section, therefore turning silicone to glass, the relationship n between Young's moduli is $n = E_{silicon}/E_{glass} = 130/70 = 1.857$.

Then, the transformed section is



The location of the neutral axis \bar{z} can be determined as

$$\bar{z} = \frac{A'_s \times z_s + A_g \times z_g}{A'_s + A_g}$$

Where A'_s is the area of the transformed silicon section, A_g is the area of the glass section.

z_s, z_g the distances from the centroid of the silicon and glass sections to the horizontal respectively.

$$\bar{z} = \frac{3714.2 \text{ mm}^2 \times 1 \text{ mm} + 3000 \text{ mm}^2 \times 3.5 \text{ mm}}{3714.2 \text{ mm}^2 + 3000 \text{ mm}^2} = 2.117 \text{ mm}$$

The second moment of area of the composite section is

$$I_y = \sum \left[\frac{b_i \times (h_i)^3}{12} + A_i \times (d_i)^2 \right]$$

Where d_i are the distances between the centroid of each component and \bar{z} .

$$I_{y-silicon} = \frac{1857.1 \text{ mm} \times (2 \text{ mm})^3}{12} + 3714.2 \text{ mm}^2 \times (1.117 \text{ mm})^2$$

$$= 5872.233 \text{ mm}^4$$

$$I_{y-glass} = \frac{1000 \text{ mm} \times (1 \text{ mm})^3}{12} + 3000 \text{ mm}^2 \times (1.383 \text{ mm})^2 = 7988.067 \text{ mm}^4$$

$$\rightarrow I_y = I_{y-silicon} + I_{y-glass} = 5872.233 \text{ mm}^4 + 7988.067 \text{ mm}^4 = 13860.3 \text{ mm}^4$$

$$I_y = 1.386 \times 10^{-8} \text{ m}^4$$

Therefore, taking $E = 70 \text{ GPa}$,

$$EI = 1.386 \times 10^{-8} \text{ m}^4 \times 70 \text{ GPa} \cong 9.702 \times 10^{-7} \text{ GPa m}^4 = 970.2 \text{ Pa m}^4$$

b) Cauchy Number condition

Using Equation 3.2 gives:

$$\frac{(EI)_m}{(EI)_p} = L_r^4 \times U_r^2 \rightarrow I_m = \frac{L_r^4 \times U_r^2 (EI)_p}{E_m}$$

$$I_m = \frac{\left(\frac{1}{20}\right)^4 \times \left(\frac{1}{2}\right)^2 \times 9.702 \times 10^{-7} \text{ GPa m}^4}{4 \text{ GPa}}$$

$$I_m = 3.789 \times 10^{-13} \text{ m}^4. \text{ (Required second moment of area in model).}$$

$$\text{At the same time, } I_m = \frac{b_m(d_m)^3}{12} \rightarrow \frac{b_m(d_m)^3}{12} = 3.789 \times 10^{-13} \text{ m}^4$$

$$\rightarrow d_m = \sqrt[3]{\frac{12 \times 3.789 \times 10^{-13} \text{ m}^4}{0.05}} = 0.000469 \text{ m} \rightarrow d_m = 0.47 \text{ mm}.$$

c) Mass distribution condition

The mass per unit length in the y-direction is:

$$m_p = \frac{2 \times 52.44 \text{ kg}}{1 \text{ m}} = 104.88 \frac{\text{kg}}{\text{m}}$$

Using Equation 3.4 gives,

$$\frac{m_m}{m_p} = \rho_r \times L_r^2 \rightarrow m_m = m_p \times \rho_r \times L_r^2$$

Then, taking $\rho_m = \rho_p$,

$$m_m = 104.88 \frac{kg}{m} \times 1 \times \left(\frac{1}{20}\right)^2 = 0.262 \frac{kg}{m}. \text{ (Required mass per unit length in the model).}$$

The mass given by the model considering bending stiffness condition is:

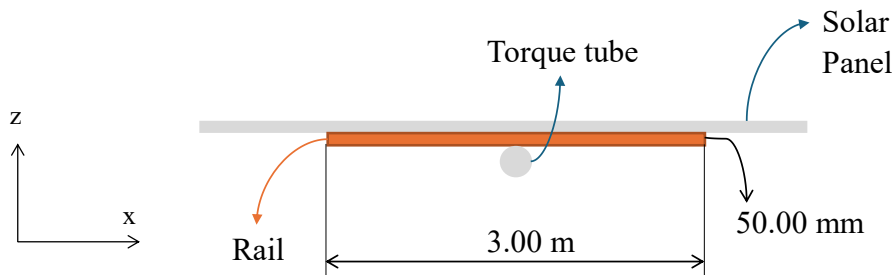
$$m_m = 0.2 m \times 0.00047 m \times 1300 \frac{kg}{m^3} = 0.122 \frac{kg}{m}.$$

→ The additional mass required on the model to comply with the mass distribution condition is:

$$\Delta m_m = 0.262 \frac{kg}{m} - 0.122 \frac{kg}{m} = 0.14 \frac{kg}{m}.$$

- **Rails**

a) Bending stiffness about z-axis



$$I_p = \frac{bd^3}{12} = \frac{3 \times 0.05^3}{12} = 3.125 \times 10^{-5} m^4$$

$$\frac{(EI)_m}{(EI)_p} = L_r^4 \times U_r^2 = \left(\frac{1}{20}\right)^4 \times \left(\frac{1}{2}\right)^2 = 1.562 \times 10^{-6}$$

Adopting $E_p = 70 \text{ GPa}$ (Aluminium alloy), $E_m = 4 \text{ GPa}$ (PLA plastic)

$$I_m = \frac{3.125 \times 10^{-5} m^4 \times 1.562 \times 10^{-6} \times 70}{4} = 8.54 \times 10^{-10} m^4. \text{ (Required second moment of area)}$$

→ Length of the rail in the model $br_m = 0.15 m$,

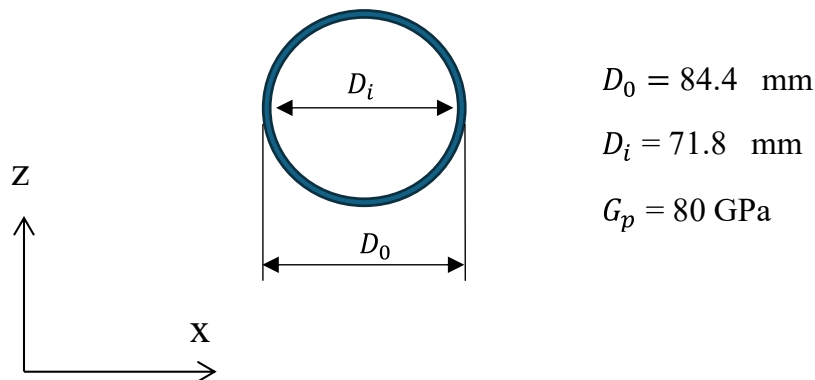
$$I_m = \frac{br_m \times hr_m^3}{12} = \frac{0.15 m \times hr_m^3}{12} = 1.139 \times 10^{-9} m^4$$

→ The height of the model rail is, $hr_m = \sqrt[3]{\frac{8.54 \times 10^{-10} m^4 \times 12}{0.15 m}} = 0.00408 m \cong 4.10 mm$

- **Torque tube**

Prototype torque tubes were selected from tubes used commercially by the industry.

- Models I-a, I-b and I-c



a) **Shear stiffness**

The polar moment of inertia of the prototype torque tube is

$$J_{0p} = \frac{\pi}{32} [D_{0p}^4 - (D_{ip})^4],$$

$$J_{0p} = \frac{\pi}{32} [(84.4 \text{ mm})^4 - (71.8 \text{ mm})^4] = 2.372 \times 10^6 \text{ mm}^4$$

b) Cauchy Number condition

Using Equation 3.3, the Cauchy number for shear stiffness ratio gives,

$$GJ_{0r} = \frac{(GJ_0)_m}{(GJ_0)_p} = L_r^4 U_r^2.$$

$$\text{Solving for } J_{0m} \rightarrow J_{0m} = \frac{L_r^4 U_r^2 \times (GJ_0)_p}{G_m}$$

Applying a diameter relationship for the model $D_{im} = 0.98D_{0m}$, the model outer diameter D_{0m} is

$$D_{0m} = \sqrt[4]{\frac{L_r^4 U_r^2 \times (GJ_0)_p}{G_m} \times \frac{32}{\pi} \times 0.02}$$

$$D_{0m} = \sqrt[4]{\frac{\left(\frac{1}{20}\right)^4 \times \left(\frac{1}{2}\right)^2 \times 80 \text{ GPa} \times 2.372 \times 10^6 \text{ mm}^4}{36 \text{ GPa}} \times \frac{32}{\pi} \times 0.02} \cong 8 \text{ mm}$$

Then, $D_{im} = 0.98D_{0m} = 0.98 \times 8 \text{ mm} = 7.84 \text{ mm}$

c) Mass distribution

The prototype mass per unit length is:

$$m_p = \frac{\pi}{4} \times (D_{0p}^2 - D_{ip}^2) \times l \times \rho_{steel} = \frac{\pi}{4} \times (0.0844^2 - 0.0718^2) \times 1m \times 8000 \frac{\text{kg}}{\text{m}^3}$$

$$m_p \cong 15 \text{ kg/m}$$

Using Equation 3.4 gives,

$$\frac{m_m}{m_p} = \rho_r \times L_r^2 \rightarrow m_m = m_p \times 1 \times L_r^2$$

Then, the required model mass per unit length is

$$m_m = 15 \text{ kg} \times \left(\frac{1}{20}\right)^2 = 0.04 \frac{\text{kg}}{\text{m}}$$

The mass given by the model is

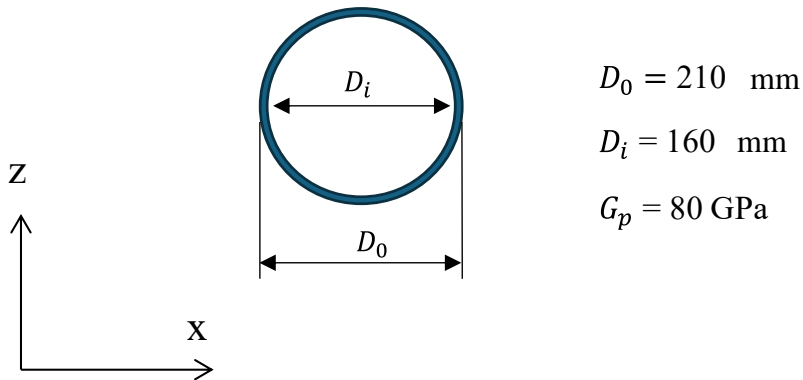
$$m_m = \frac{\pi}{4} [(0.008 \text{ m})^2 - (0.0078 \text{ m})^2] \times 8400 \frac{\text{kg}}{\text{m}^3} \cong 0.02 \frac{\text{kg}}{\text{m}}$$

→ The additional mass required on the model to comply with the mass distribution condition is:

$$\Delta m_m = 0.04 \frac{\text{kg}}{\text{m}} - 0.02 \frac{\text{kg}}{\text{m}} = 0.02 \frac{\text{kg}}{\text{m}}$$

- Models II-a and II-b

a) Torsional stiffness



The polar moment of inertia of the torque tube prototype is

$$J_{0p} = \frac{\pi}{32} [D_p^4 - (D_p - 2t_p)^4],$$

$$J_{0p} = \frac{\pi}{32} [(210 \text{ mm})^4 - (160 \text{ mm})^4] = 1.258 \times 10^8 \text{ mm}^4$$

Using equation 3.3, the Cauchy number for shear condition gives,

$$GJ_{0r} = \frac{(GJ_0)_m}{(GJ_0)_p} = L_r^4 U_r^2.$$

$$\text{Solving for } J_{0m} \rightarrow J_{0m} = \frac{L_r^4 U_r^2 \times (GJ_0)_p}{G_m}$$

Then, the model diameter D_{0m} is

$$D_{0m} = \sqrt[4]{\frac{L_r^4 U_r^2 \times (GJ_0)_p}{G_m} \times \frac{32}{\pi}}$$

$$D_{0m} = \sqrt[4]{\frac{\left(\frac{1}{20}\right)^4 \times \left(\frac{1}{2}\right)^2 \times 80 \text{ GPa} \times 1.258 \times 10^8 \text{ m}^4}{36 \text{ GPa}} \times \frac{32}{\pi}} \cong 8 \text{ mm}$$

The mass per unit length is:

$$\begin{aligned} m_p &= \frac{\pi}{4} \times (D_{0p}^2 - D_{ip}^2) \times l \times \rho_{steel} = \frac{\pi}{4} \times (0.21^2 - 0.16^2) \times 1 \text{ m} \times 8000 \frac{\text{kg}}{\text{m}^3} \\ &= 116 \text{ kg/m} \end{aligned}$$

Using Equation 3.4 gives,

$$\frac{m_m}{m_p} = \rho_r \times L_r^2 \rightarrow m_m = m_p \times 1 \times L_r^2$$

Then, the required model mass per unit length is

$$m_m = 116 \text{ kg} \times \left(\frac{1}{20}\right)^2 \cong 0.30 \frac{\text{kg}}{\text{m}}$$

The mass given by the model is

$$m_m = \frac{\pi}{4} (0.008 \text{ m})^2 \times 8000 \frac{\text{kg}}{\text{m}^3} = 0.40 \frac{\text{kg}}{\text{m}}$$

Figure A.2 shows a diagram with the dimensions of the model solar panels, rails and torque tubes. Figure A.3 shows a photo of the aeroelastic models under construction.

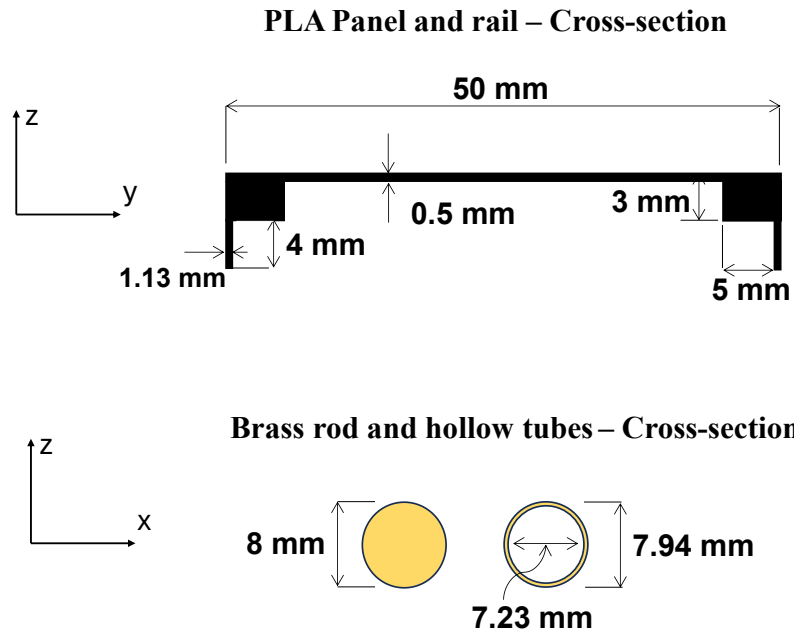


Figure A.2. Diagram of the model panels, rails and torque tubes.
Hollow tube (Models I-a, I-b and I-c), and Rod (Models II-a and II-b)



Figure A.3. Detail of the construction of the aeroelastic models

Taking Model I-c as an example, the total polar mass moment of inertia I_0 about the centre of the torque tube was calculated as follows:

The length of the tube is $l = 1.65 \text{ m}$, brass density is $\rho_{brass} = 8890 \text{ kg/m}^3$, PLA density is $\rho_{PLA} = 1240 \text{ kg/m}^3$. Therefore,

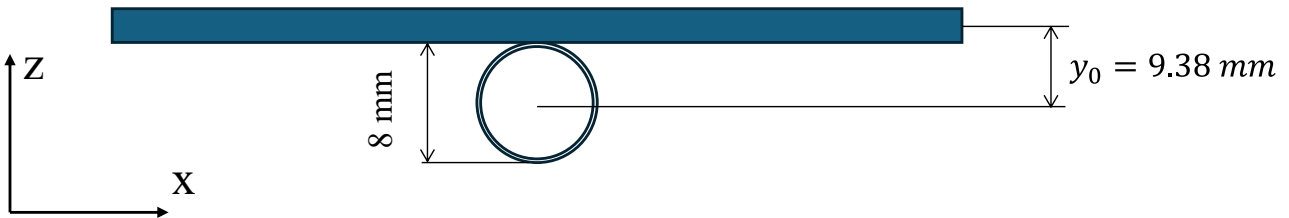
$$\begin{aligned} mass_{tube} &= \rho_{brass} \times \pi \times (r_{om}^2 - r_{im}^2) \times l \\ &= 8890 \times \pi \times (0.004^2 - 0.0035^2) \times 1.65 = 0.104 \text{ kg} \end{aligned}$$

$$mass_{panels} = \rho_{PLA} \times b \times d \times l_{modules} = 1240 \times 0.20 \times 0.0008 \times 1.60 = 0.32 \text{ kg}$$

Considering additional mass due to mass distribution,

$$mass_{panels} = 0.32 \text{ kg} + 0.060 \text{ kg} = 0.38 \text{ kg}$$

The distance of the centre line of the panels to the centre of the tube is shown in the following diagram,



The total polar moment of inertia for Model I-c is:

$$I_0 = I_{0 \text{ tube}} + I_{0 \text{ panels}} + mass_{panels} \times y_0^2$$

$$I_{0 \text{ tube}} = \frac{1}{2} \times 0.104 \times (0.004^2 - 0.0035^2) = 1.95 \times 10^{-7} \text{ kgm}^2$$

$$I_{0 \text{ panels}} = \frac{1}{12} \times 0.38 \times (0.20^2) = 1.26 \times 10^{-3} \text{ kgm}^2$$

→

$$I_0 = 1.95 \times 10^{-7} + 1.26 \times 10^{-3} + 0.38 \text{ kg} \times (0.00938 \text{ m})^2 = 0.0013 \text{ kgm}^2$$

APPENDIX B: MEASURING EQUIPMENT

This Appendix details the instruments mentioned in Section 3 to measure wind speed and wind loading (i.e. aerodynamic moment).

Figure B.1 (a) shows the Turbulent Flow Instrumentation (TFI) Cobra Probe used in this study to record the wind speed in the wind tunnel. The Probe was connected to a data acquisition system (DAQ), which is shown in Figure B.1 (b).

(a)

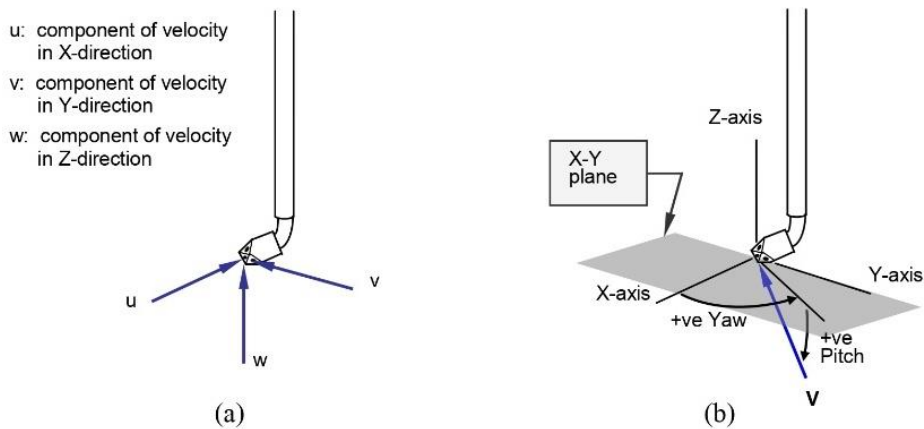


(b)



Figure B.1. Wind speed (a) measurement instrument (Cobra Probe), and (b) data acquisition system (DAQ)

Figure B.2 shows the flow axis system with respect to the Probe head and the equations to determine the wind velocity components using the pitch and yaw angles.



Components

$$|\mathbf{V}| = \sqrt{u^2 + v^2 + w^2}$$

$$u = \bar{u} + u' = |\mathbf{V}| \cdot \cos(\theta) \cdot \cos(\psi)$$

$$v = \bar{v} + v' = |\mathbf{V}| \cdot \cos(\theta) \cdot \sin(\psi)$$

$$w = \bar{w} + w' = |\mathbf{V}| \cdot \sin(\theta)$$

Angles

$$\theta = \sin^{-1} \left(\frac{w}{|\mathbf{V}|} \right)$$

$$\psi = \tan^{-1} \left(\frac{v}{u} \right)$$

Figure B.2. (a) Flow axis system with respect to the Probe head; (b) Positive flow pitch and yaw angles. Extracted from the Turbulent Flow Instrumentation

The data collected was processed by the TFI Device Control software which created a file with the time history of each run, as shown in Figure B.3.

```

Device type : Four-hole Cobra Probe
Device ID : 139

Number of samples : 30,720
Output data rate (Hz) : 250.0
Output block size : 2,048
First sample date : 29-Aug-24
First sample time : 15:36:21.555
Has reference pressure : No

Vel (m/s)      Yaw (°) Pitch (°)
              Pstatic (Pa)
9.431  0.3909  -0.3201  -19.4
8.433  3.667   -6.251   -8.5
7.904  5.144   -8.025   -5.0
7.286  8.292  -11.19   0.0
6.210  6.845   -7.099   -2.2
7.878  1.184   -5.306  -10.4
5.961  2.342  -14.07   -3.0
7.338  3.017   2.319   -10.6
7.234  10.19   3.892   -5.0
5.801  2.349   1.526   -6.8
8.353  6.151   9.694  -15.1
4.789  16.02  -10.63   3.2
8.546  0.2995  -3.913  -14.1
8.105  -6.359  -0.3204 -20.9
9.471  -7.012  2.667   -30.9
9.986  -3.065  -3.828  -24.3

```

Figure B.3. Wind speed time history sample, measured with the TFI Cobra Probe

The moment transducers used in this study are shown in Figure B.4.

(a)

(b)



Figure B.4. Moment (torque) transducers used in this study. (a) *ME Systeme TD70* (Range: 1 Nm), and (b) *ME Systeme TS70* (Range: 5 Nm)

Table B.1 provides general technical details about the moment transducers. This information was extracted from the technical sheets available in the web page of the transducer's manufacturer (ME Systeme).

Table B.1. *ME Systeme TD/TS series* technical data sheet.

Basis Data		Electrical Data	
Type	Bending spring	Input resistance	350 Ohm
Bending moment limit	5 Nm	Tolerance input resistance	10 Ohm
Maximum operating torque	150 %FS	Output resistance	350 Ohm
Breaking torque	400 %FS	Tolerance output resistance	10 Ohm
Axial force limit	100 N	Insulation resistance	5 GOhm
Lateral force limit	100 N	Rated range of excitation voltage f	2.5...5 V
Torque introduction	Pitch circle	Operating range of excitation voltage f	1 ...10 V
Connection Data			
Connection type		4 conductors open	
Name of the connection		STC-31V-4	
Cable length		2 m	
Temperature			
Rated temperature range f		-10... 60 °C	
Operating temperature range f		-10 ... 85 °C	
Storage temperature range f		-10 ... 85 °C	

The moment (torque) transducers were connected to a National Instruments data acquisition system, *NI cDAQ*, shown in Figure B.5. The *NI cDAQ* was operated using LabView to record and monitor measurements.



Figure B.5. National Instruments data acquisition device *NI cDAQ*.

The data collected was saved as a file comprising the time history of each run, as shown in Figure B.6.

```

LabVIEW Measurement
Writer_Version 2
Reader_Version 2
Separator Tab
Decimal_Separator .
Multi_Headings No
X_Columns One
Time_Pref Absolute
Operator CTSLabview
Date 2024/11/27
Time 16:12:26.3058043999996814612
***End_of_Header***

Channels 1
Samples 500
Date 2024/11/27
Time 16:12:26.3058043999996814612
Y_Unit_Label Nm
X_Dimension Time
X0 0.0000000000000000E+0
Delta_X 0.000620
***End_of_Header***
X_Value Torque (Filtered) Comment
0.000000 0.098382
0.000620 0.324829
0.001240 0.418117
0.001860 0.344118
0.002480 0.338649
0.003100 0.367451
0.003720 0.352934
0.004340 0.350418
0.004960 0.355998
0.005580 0.350809
0.006200 0.352068
0.006820 0.358052
0.007440 0.350772
0.008060 0.338580
0.008680 0.334800
0.009300 0.330697
0.009920 0.330572
0.010540 0.342354
0.011160 0.345252

```

Figure B.6. Aerodynamic moment time history sample, measured with the *ME Systeme TS70* moment transducer.

APPENDIX C: SUPPLEMENTARY DATA FOR CHAPTER 4

C.1 Moment coefficients

Table C.1 to Table C.3 provide moment coefficients (i.e. mean, maximum, minimum and the standard deviation) for a range of tilt angles, α , and wind directions, θ , for model I-a and $\bar{U}_h = 6.5 \text{ m/s}, 7.5 \text{ m/s}$, and 8.5 m/s respectively. This data is complementary to that shown in Section 4.1.2.

Table C.1. Mean, maximum, minimum and standard deviation moment coefficient.

Model I-a. $\bar{U}_h = 6.5 \text{ m/s}, k_0 = 11.6 \text{ Nm}$ (model scale)

$C_{\bar{M}}$								
θ	$\alpha = 0^\circ$	$\alpha = 5^\circ$	$\alpha = 10^\circ$	$\alpha = 20^\circ$	$\alpha = 25^\circ$	$\alpha = 30^\circ$	$\alpha = 40^\circ$	$\alpha = 50^\circ$
0°	-0.006	0.143	0.182	0.180	0.121	0.104	0.086	0.059
45°	-0.019	0.060	0.102	0.123	0.114	0.101	0.200	0.047
90°	0.001	-0.010	0.012	0.011	0.001	0.004	-0.003	0.013
135°	0.052	0.108	0.154	0.170	0.170	0.166	0.254	0.062
180°	0.077	0.201	0.236	0.190	0.127	0.118	0.088	0.044
$C_{\bar{M}}$								
θ	$\alpha = 0^\circ$	$\alpha = 5^\circ$	$\alpha = 10^\circ$	$\alpha = 20^\circ$	$\alpha = 25^\circ$	$\alpha = 30^\circ$	$\alpha = 40^\circ$	$\alpha = 50^\circ$
0°	0.331	0.454	0.498	0.462	0.320	0.297	0.232	0.141
45°	0.000	0.270	0.354	0.344	0.326	0.292	0.535	0.128
90°	0.071	0.061	0.091	0.079	0.072	0.088	0.088	0.131
135°	0.276	0.383	0.446	0.428	0.391	0.403	0.685	0.158
180°	0.330	0.569	0.659	0.500	0.372	0.404	0.289	0.155
$C_{\bar{M}}$								
θ	$\alpha = 0^\circ$	$\alpha = 5^\circ$	$\alpha = 10^\circ$	$\alpha = 20^\circ$	$\alpha = 25^\circ$	$\alpha = 30^\circ$	$\alpha = 40^\circ$	$\alpha = 50^\circ$
0°	-0.259	0.007	0.013	0.039	0.009	-0.019	-0.021	-0.017
45°	-0.239	-0.022	-0.039	0.012	0.016	-0.004	-0.018	-0.018
90°	-0.109	-0.051	-0.050	-0.042	-0.034	-0.055	-0.070	-0.071
135°	-0.159	-0.013	-0.005	0.030	0.038	0.008	0.007	-0.015
180°	-0.121	0.001	-0.001	-0.001	-0.017	-0.096	-0.030	-0.034
C_{σ_M}								
θ	$\alpha = 0^\circ$	$\alpha = 5^\circ$	$\alpha = 10^\circ$	$\alpha = 20^\circ$	$\alpha = 25^\circ$	$\alpha = 30^\circ$	$\alpha = 40^\circ$	$\alpha = 50^\circ$
0°	0.041	0.049	0.057	0.046	0.036	0.037	0.028	0.018
45°	0.029	0.037	0.046	0.038	0.033	0.034	0.064	0.015
90°	0.007	0.009	0.013	0.011	0.011	0.013	0.014	0.020
135°	0.027	0.040	0.049	0.043	0.045	0.050	0.088	0.020
180°	0.038	0.069	0.076	0.057	0.047	0.050	0.033	0.021

Table C.2. Mean, maximum, minimum and standard deviation moment coefficient.

Model I-a. $\bar{U}_h = 7.5 \text{ m/s}$, $k_0 = 11.6 \text{ Nm}$ (model scale)

$C_{\bar{M}}$								
θ	$\alpha = 0^\circ$	$\alpha = 5^\circ$	$\alpha = 10^\circ$	$\alpha = 20^\circ$	$\alpha = 25^\circ$	$\alpha = 30^\circ$	$\alpha = 40^\circ$	$\alpha = 50^\circ$
0°	0.026	0.148	0.174	0.162	0.118	0.113	0.089	0.068
45°	-0.005	0.071	0.091	0.135	0.115	0.114	0.127	0.064
90°	-0.002	-0.008	-0.005	0.007	0.005	0.006	0.001	0.004
135°	0.058	0.120	0.138	0.159	0.168	0.157	0.162	0.073
180°	0.091	0.203	0.219	0.170	0.125	0.114	0.080	0.059
$C_{\bar{M}}$								
θ	$\alpha = 0^\circ$	$\alpha = 5^\circ$	$\alpha = 10^\circ$	$\alpha = 20^\circ$	$\alpha = 25^\circ$	$\alpha = 30^\circ$	$\alpha = 40^\circ$	$\alpha = 50^\circ$
0°	0.310	0.408	0.487	0.403	0.331	0.300	0.249	0.196
45°	0.199	0.306	0.325	0.354	0.329	0.295	0.341	0.182
90°	0.071	0.113	0.061	0.064	0.094	0.082	0.071	0.091
135°	0.245	0.407	0.425	0.395	0.432	0.388	0.436	0.204
180°	0.310	0.588	0.577	0.504	0.416	0.327	0.311	0.205
$C_{\bar{M}}$								
θ	$\alpha = 0^\circ$	$\alpha = 5^\circ$	$\alpha = 10^\circ$	$\alpha = 20^\circ$	$\alpha = 25^\circ$	$\alpha = 30^\circ$	$\alpha = 40^\circ$	$\alpha = 50^\circ$
0°	-0.148	0.016	0.024	0.031	0.000	-0.007	-0.031	-0.018
45°	-0.172	-0.013	-0.011	0.023	-0.002	0.012	-0.011	-0.030
90°	-0.075	-0.112	-0.077	-0.037	-0.025	-0.039	-0.061	-0.054
135°	-0.059	0.002	-0.004	0.029	0.014	0.006	0.004	-0.016
180°	-0.047	0.003	-0.005	0.002	-0.014	-0.025	-0.057	-0.016
C_{σ_M}								
θ	$\alpha = 0^\circ$	$\alpha = 5^\circ$	$\alpha = 10^\circ$	$\alpha = 20^\circ$	$\alpha = 25^\circ$	$\alpha = 30^\circ$	$\alpha = 40^\circ$	$\alpha = 50^\circ$
0°	0.042	0.051	0.055	0.040	0.038	0.035	0.032	0.025
45°	0.028	0.040	0.044	0.036	0.038	0.031	0.041	0.023
90°	0.009	0.009	0.009	0.010	0.010	0.011	0.012	0.013
135°	0.031	0.044	0.047	0.044	0.047	0.047	0.056	0.026
180°	0.041	0.071	0.071	0.053	0.050	0.045	0.039	0.027

Table C.3. Mean, maximum, minimum and standard deviation moment coefficient.

Model I-a. $\bar{U}_h = 8.5 \text{ m/s}$, $k_0 = 11.6 \text{ Nm}$ (model scale)

$C_{\bar{M}}$								
θ	$\alpha = 0^\circ$	$\alpha = 5^\circ$	$\alpha = 10^\circ$	$\alpha = 20^\circ$	$\alpha = 25^\circ$	$\alpha = 30^\circ$	$\alpha = 40^\circ$	$\alpha = 50^\circ$
0°	0.034	0.150	0.155	0.139	0.103	0.103	0.091	0.075
45°	-0.004	0.067	0.087	0.110	0.091	0.100	0.081	0.056
90°	0.002	-0.004	0.001	0.005	-0.008	0.010	0.016	0.003
135°	-0.004	0.125	0.141	0.168	0.158	0.158	0.103	0.072
180°	0.034	0.204	0.208	0.162	0.109	0.111	0.086	0.056
$C_{\bar{M}}$								
θ	$\alpha = 0^\circ$	$\alpha = 5^\circ$	$\alpha = 10^\circ$	$\alpha = 20^\circ$	$\alpha = 25^\circ$	$\alpha = 30^\circ$	$\alpha = 40^\circ$	$\alpha = 50^\circ$
0°	0.317	0.448	0.455	0.383	0.363	0.308	0.230	0.200
45°	0.250	0.318	0.351	0.343	0.308	0.315	0.217	0.174
90°	0.113	0.134	0.075	0.096	0.096	0.102	0.110	0.058
135°	0.250	0.472	0.481	0.456	0.409	0.392	0.278	0.201
180°	0.317	0.582	0.604	0.522	0.375	0.337	0.245	0.186
$C_{\bar{M}}$								
θ	$\alpha = 0^\circ$	$\alpha = 5^\circ$	$\alpha = 10^\circ$	$\alpha = 20^\circ$	$\alpha = 25^\circ$	$\alpha = 30^\circ$	$\alpha = 40^\circ$	$\alpha = 50^\circ$
0°	-0.139	-0.001	-0.007	0.001	-0.019	-0.022	-0.011	-0.033
45°	-0.175	-0.042	-0.056	-0.008	-0.016	-0.010	-0.007	-0.030
90°	-0.092	-0.102	-0.055	-0.045	-0.049	-0.045	-0.039	-0.035
135°	-0.175	-0.007	-0.039	0.014	0.005	0.004	0.003	-0.029
180°	-0.139	-0.005	-0.026	-0.008	-0.023	-0.039	-0.024	-0.034
C_{σ_M}								
θ	$\alpha = 0^\circ$	$\alpha = 5^\circ$	$\alpha = 10^\circ$	$\alpha = 20^\circ$	$\alpha = 25^\circ$	$\alpha = 30^\circ$	$\alpha = 40^\circ$	$\alpha = 50^\circ$
0°	0.045	0.053	0.053	0.044	0.046	0.038	0.029	0.026
45°	0.035	0.041	0.044	0.040	0.037	0.034	0.026	0.022
90°	0.012	0.011	0.012	0.011	0.011	0.013	0.013	0.008
135°	0.035	0.052	0.050	0.052	0.048	0.046	0.036	0.027
180°	0.045	0.077	0.072	0.062	0.050	0.044	0.032	0.028

Figure C.1 shows the variation of the mean moment coefficient $C_{\bar{M}}$ with tilt angle, α , for several wind directions, θ , for Model I-b. This data is complementary to that shown in Section 4.1.2.

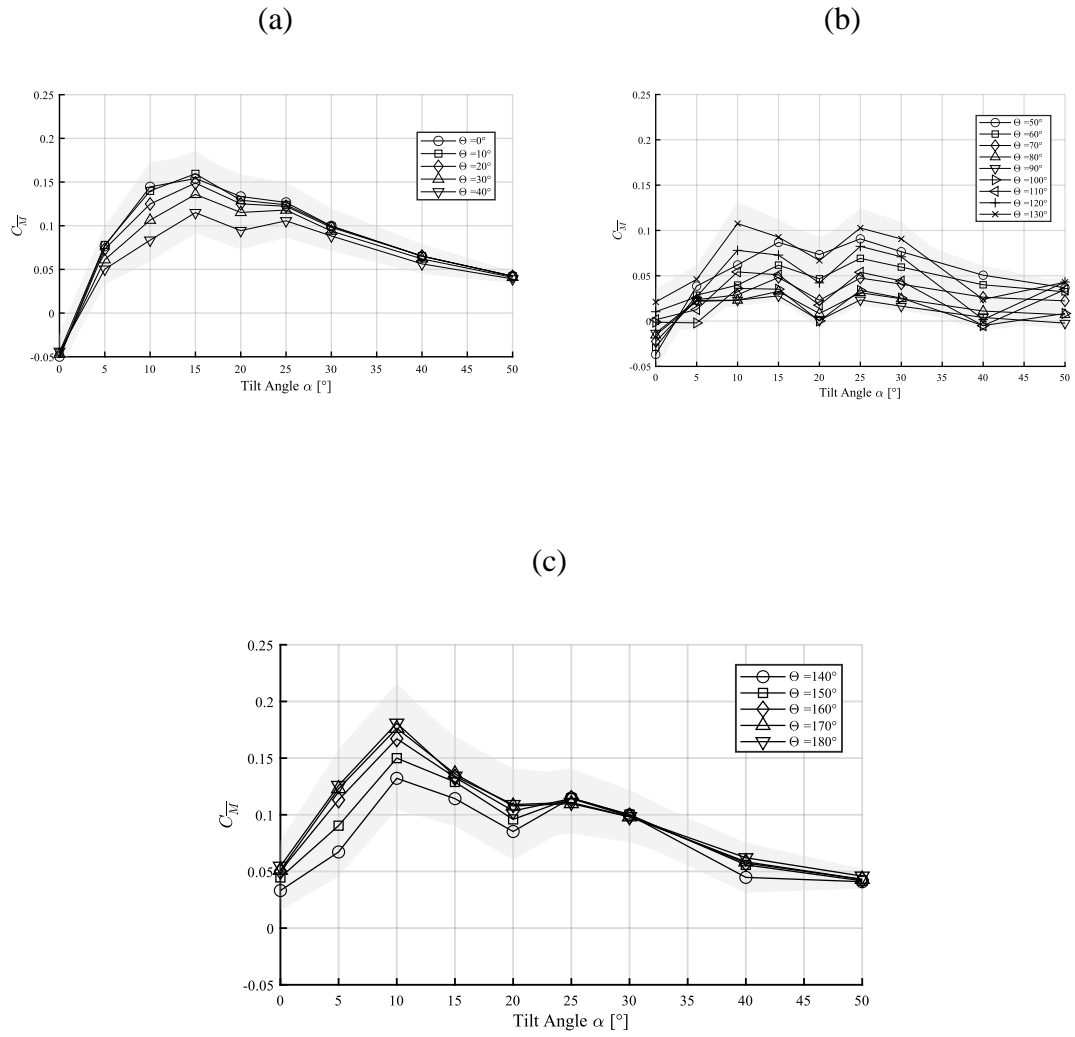


Figure C.1. Mean moment coefficient $C_{\bar{M}}$ vs tilt angle α , for (a) $0^\circ < \theta < 40^\circ$, (b) $50^\circ < \theta < 130^\circ$, and (c) $140^\circ < \theta < 180^\circ$. Uncertainty shown as a grey shade. Model I-b. $\bar{U}_h = 6.5 \text{ m/s}$ (model scale)

Table C.4 provides moment coefficients for a range of tilt angles, α , and wind directions, θ , for model I-b and $\bar{U}_h = 6.5 \text{ m/s}$. This data is complementary to that shown in Section 4.1.2.

Table C.4. Maximum and minimum moment coefficients. Model I-b. $\bar{U}_h = 6.5 \text{ m/s}$

$k_0 = 7.9 \text{ Nm (model scale)}$

$C_{\bar{M}}$									
θ	$\alpha = 0^\circ$	$\alpha = 5^\circ$	$\alpha = 10^\circ$	$\alpha = 15^\circ$	$\alpha = 20^\circ$	$\alpha = 25^\circ$	$\alpha = 30^\circ$	$\alpha = 40^\circ$	$\alpha = 50^\circ$
0°	0.06	0.21	0.31	0.30	0.27	0.25	0.20	0.15	0.08
10°	0.05	0.21	0.27	0.30	0.24	0.25	0.20	0.14	0.10
20°	0.05	0.22	0.24	0.30	0.26	0.25	0.20	0.14	0.09
30°	0.05	0.19	0.25	0.27	0.24	0.24	0.20	0.13	0.08
40°	0.04	0.16	0.22	0.25	0.21	0.21	0.18	0.12	0.07
50°	0.04	0.14	0.18	0.21	0.19	0.19	0.17	0.11	0.06
60°	0.03	0.10	0.12	0.15	0.15	0.15	0.15	0.10	0.06
70°	0.03	0.08	0.10	0.12	0.10	0.12	0.11	0.08	0.05
80°	0.02	0.06	0.07	0.09	0.06	0.09	0.08	0.05	0.05
90°	0.01	0.06	0.06	0.06	0.03	0.06	0.05	0.03	0.03
100°	0.04	0.05	0.10	0.09	0.06	0.10	0.09	0.02	0.05
110°	0.06	0.08	0.13	0.12	0.11	0.15	0.11	0.03	0.06
120°	0.08	0.15	0.20	0.18	0.15	0.20	0.16	0.05	0.08
130°	0.10	0.18	0.25	0.24	0.20	0.23	0.22	0.09	0.08
140°	0.12	0.21	0.31	0.27	0.21	0.25	0.21	0.12	0.08
150°	0.15	0.25	0.30	0.32	0.26	0.25	0.23	0.13	0.08
160°	0.16	0.29	0.36	0.31	0.29	0.26	0.22	0.14	0.09
170°	0.16	0.29	0.40	0.33	0.28	0.26	0.24	0.13	0.08
180°	0.17	0.30	0.37	0.30	0.30	0.26	0.23	0.13	0.08
$C_{\bar{M}}$									
θ	$\alpha = 0^\circ$	$\alpha = 5^\circ$	$\alpha = 10^\circ$	$\alpha = 15^\circ$	$\alpha = 20^\circ$	$\alpha = 25^\circ$	$\alpha = 30^\circ$	$\alpha = 40^\circ$	$\alpha = 50^\circ$
0°	-0.15	0.05	0.01	-0.01	0.00	0.04	0.04	0.02	0.07
10°	-0.15	0.05	0.01	-0.02	0.00	0.05	0.04	0.02	0.07
20°	-0.16	0.04	0.01	0.00	0.00	0.04	0.03	0.03	0.06
30°	-0.14	0.03	0.02	0.00	-0.02	0.03	0.04	0.02	0.06
40°	-0.14	0.02	0.00	-0.01	-0.02	0.00	0.03	0.03	0.05
50°	-0.12	0.01	0.01	0.00	-0.04	0.00	0.03	0.02	0.04
60°	-0.11	-0.01	0.00	-0.01	-0.04	-0.01	0.01	0.02	0.01
70°	-0.08	-0.02	-0.01	-0.02	-0.05	-0.01	0.00	0.00	0.01
80°	-0.06	-0.02	-0.02	-0.02	-0.02	-0.01	0.00	0.00	0.01
90°	-0.04	-0.02	-0.02	-0.04	-0.01	0.00	0.00	-0.01	0.00
100°	-0.08	-0.03	-0.03	-0.02	-0.05	0.00	0.00	-0.01	0.00
110°	-0.04	-0.02	-0.03	0.00	-0.04	0.01	0.01	0.00	0.01
120°	-0.06	-0.01	-0.03	-0.02	-0.06	0.01	0.02	0.02	0.02
130°	-0.07	0.00	-0.01	-0.01	-0.05	0.02	0.02	0.02	0.03
140°	-0.06	0.00	0.00	-0.02	-0.02	0.02	0.04	0.02	0.05
150°	-0.06	-0.01	0.00	-0.01	0.01	0.04	0.02	0.01	0.05
160°	-0.04	-0.01	0.00	0.00	0.02	0.05	0.01	0.02	0.05
170°	-0.05	0.00	0.00	0.00	0.03	0.06	-0.01	0.00	0.03
180°	-0.05	-0.02	0.00	0.01	0.03	0.06	0.00	0.02	0.03

Figure C.2. shows the variation of the mean moment coefficient $C_{\bar{M}}$ with tilt angle, α , for several wind directions, θ , for Model I-b. This data is complementary to that shown in Section 4.1.2.

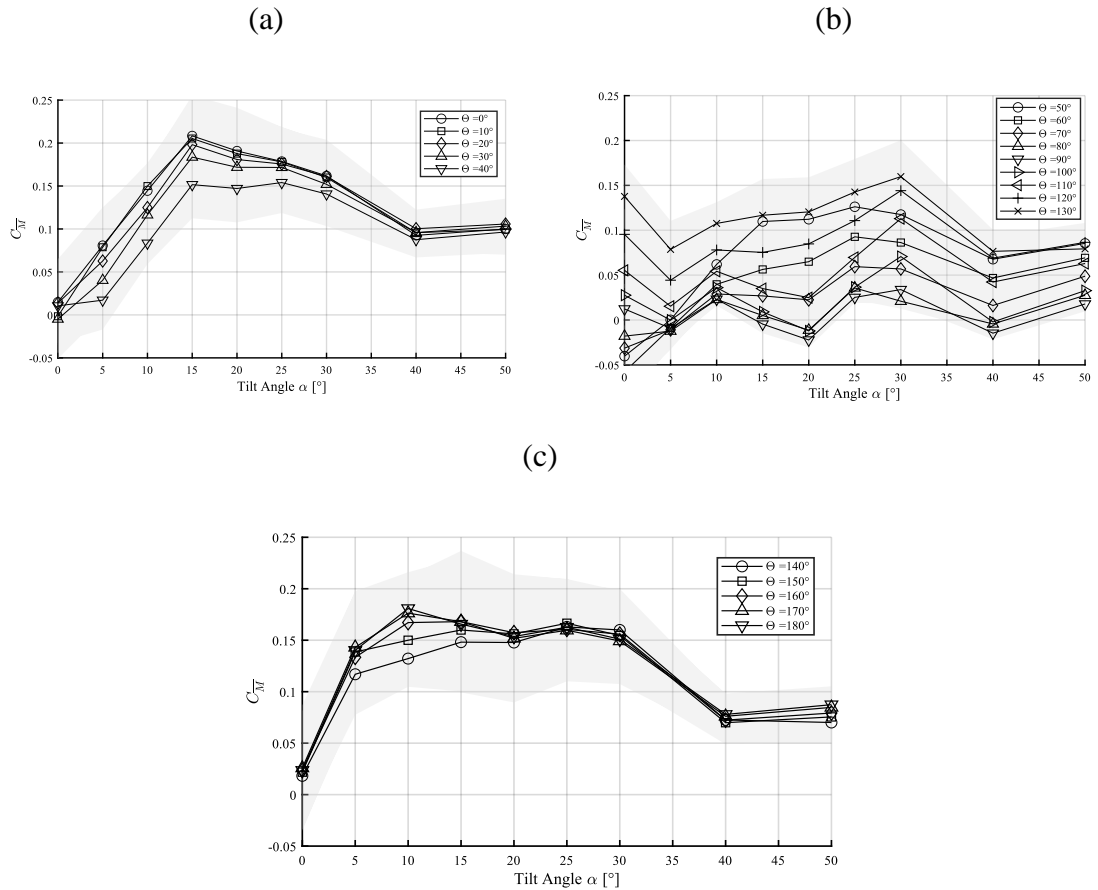


Figure C.2. Mean moment coefficient $C_{\bar{M}}$ vs tilt angle α , for (a) $0^\circ < \theta < 40^\circ$, (b) $50^\circ < \theta < 130^\circ$, and (c) $140^\circ < \theta < 180^\circ$. Uncertainty shown as a grey shade. Model I-b. $\bar{U}_h = 7.5 \text{ m/s}$ (model scale)

Table C.5 provides moment coefficients (i.e. maximum and minimum) for a range of tilt angles, α , and wind directions, θ , for model I-b and $\bar{U}_h = 7.5 \text{ m/s}$. This data is complementary to that shown in Section 4.1.2.

Table C.5. Maximum and minimum moment coefficients. Model I-b. $\bar{U}_h = 7.5 \text{ m/s}$

$k_0 = 7.9 \text{ Nm (model scale)}$

$C_{\bar{M}}$									
θ	$\alpha = 0^\circ$	$\alpha = 5^\circ$	$\alpha = 10^\circ$	$\alpha = 15^\circ$	$\alpha = 20^\circ$	$\alpha = 25^\circ$	$\alpha = 30^\circ$	$\alpha = 40^\circ$	$\alpha = 50^\circ$
0°	0.47	0.32	0.31	0.51	0.54	0.41	0.39	0.21	0.23
10°	0.45	0.38	0.27	0.46	0.49	0.44	0.39	0.21	0.23
20°	0.45	0.27	0.24	0.48	0.51	0.40	0.35	0.23	0.22
30°	0.41	0.28	0.25	0.43	0.47	0.38	0.34	0.21	0.25
40°	0.38	0.19	0.22	0.38	0.37	0.43	0.34	0.19	0.22
50°	0.13	0.19	0.18	0.32	0.33	0.30	0.32	0.18	0.19
60°	0.02	0.13	0.12	0.22	0.24	0.25	0.23	0.14	0.17
70°	0.02	0.11	0.10	0.17	0.15	0.24	0.18	0.13	0.13
80°	0.02	0.06	0.07	0.09	0.11	0.12	0.09	0.08	0.10
90°	0.06	0.05	0.06	0.05	0.02	0.08	0.15	0.02	0.07
100°	0.14	0.09	0.10	0.10	0.07	0.15	0.22	0.09	0.11
110°	0.22	0.15	0.13	0.22	0.17	0.21	0.33	0.17	0.17
120°	0.29	0.21	0.20	0.28	0.27	0.31	0.34	0.19	0.21
130°	0.39	0.26	0.25	0.41	0.38	0.33	0.37	0.20	0.17
140°	0.44	0.34	0.31	0.44	0.43	0.42	0.40	0.19	0.18
150°	0.56	0.45	0.30	0.50	0.49	0.40	0.42	0.18	0.18
160°	0.58	0.49	0.36	0.56	0.50	0.43	0.45	0.19	0.18
170°	0.60	0.51	0.40	0.78	0.83	0.55	0.44	0.20	0.18
180°	0.58	0.56	0.37	0.64	0.83	0.43	0.39	0.18	0.18
$C_{\bar{M}}$									
θ	$\alpha = 0^\circ$	$\alpha = 5^\circ$	$\alpha = 10^\circ$	$\alpha = 15^\circ$	$\alpha = 20^\circ$	$\alpha = 25^\circ$	$\alpha = 30^\circ$	$\alpha = 40^\circ$	$\alpha = 50^\circ$
0°	-0.02	-0.08	0.04	0.03	-0.01	0.01	0.01	0.01	-0.01
10°	0.03	-0.07	0.05	0.03	-0.02	0.03	0.01	0.00	-0.03
20°	0.04	-0.08	0.04	0.05	-0.01	0.02	0.01	0.01	-0.01
30°	0.03	-0.10	0.03	0.04	0.00	0.03	0.02	0.01	0.00
40°	-0.01	-0.12	0.00	0.04	0.00	0.03	0.01	0.01	0.00
50°	-0.28	-0.14	0.00	0.01	-0.01	0.01	0.01	-0.01	0.00
60°	-0.24	-0.11	-0.01	-0.02	-0.02	0.01	0.00	-0.02	0.00
70°	-0.17	-0.11	-0.01	-0.05	-0.04	0.00	-0.01	-0.03	-0.01
80°	-0.11	-0.10	-0.01	-0.05	-0.05	0.00	-0.02	-0.04	-0.02
90°	-0.03	-0.07	0.00	-0.05	-0.05	-0.01	-0.01	-0.06	-0.02
100°	-0.02	-0.07	0.00	-0.06	-0.05	-0.01	0.00	-0.03	-0.01
110°	-0.02	-0.08	0.01	-0.06	-0.04	-0.01	-0.01	-0.01	0.01
120°	0.00	-0.07	0.01	-0.01	-0.02	0.01	0.01	-0.01	0.00
130°	0.01	-0.07	0.02	0.01	-0.03	0.01	-0.01	-0.01	-0.02
140°	0.02	-0.07	0.02	-0.01	-0.03	0.01	0.00	0.00	-0.02
150°	0.04	-0.03	0.04	-0.05	-0.04	0.01	-0.05	0.00	0.00
160°	0.05	0.00	0.05	-0.11	-0.04	-0.01	-0.04	0.00	0.00
170°	0.06	0.01	0.06	-0.12	-0.10	-0.07	-0.01	0.00	0.01
180°	0.03	0.00	0.06	-0.07	-0.08	-0.02	0.00	0.00	0.01

Figure C.3 shows the variation of the mean moment coefficient $C_{\overline{M}}$ with tilt angle, α , for several wind directions, θ , for Model I-b.

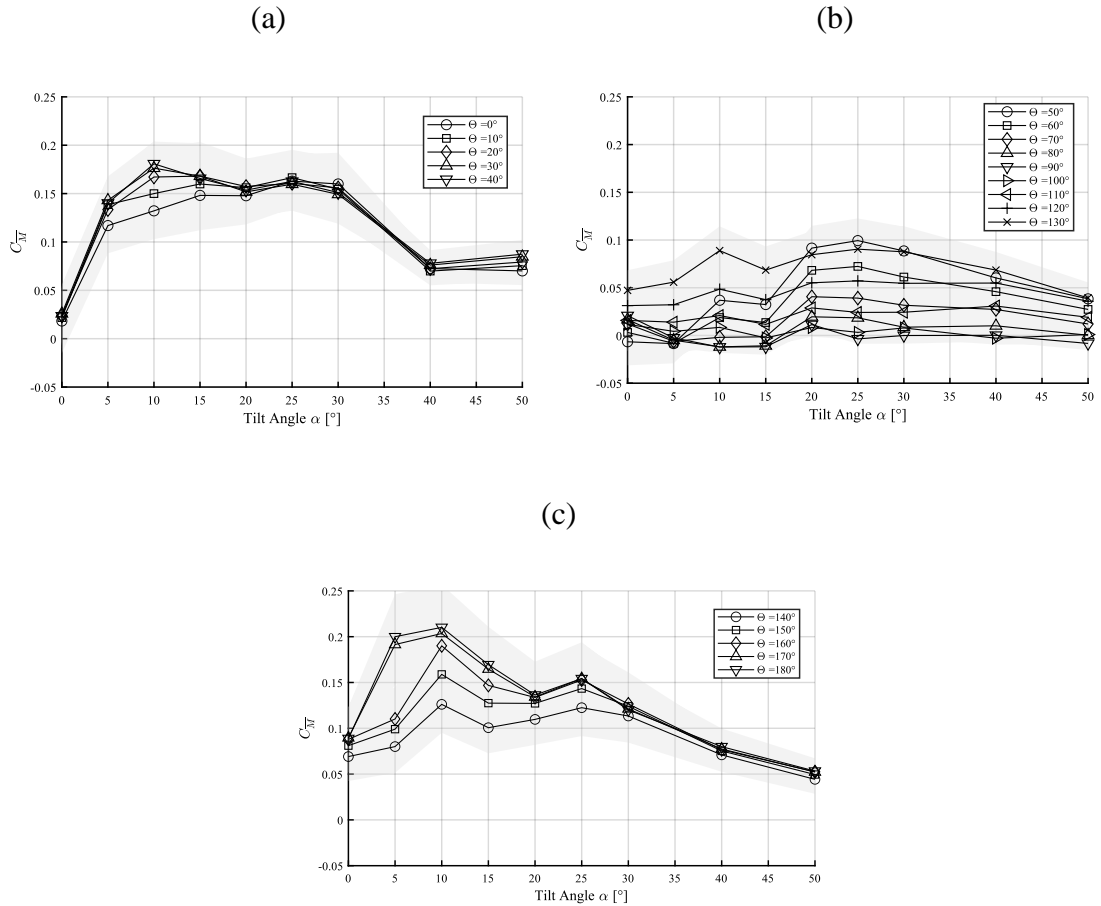


Figure C.3. Mean moment coefficient $C_{\overline{M}}$ vs tilt angle α , for (a) $0^\circ < \theta < 40^\circ$, (b) $50^\circ < \theta < 130^\circ$, and (c) $140^\circ < \theta < 180^\circ$. Uncertainty shown as a grey shade. Model I-c. $\overline{U}_h =$

$$5.5 \text{ m/s (model scale)}$$

Table C.6 provides moment coefficients (i.e. maximum and minimum) for a range of tilt angles, α , and wind directions, θ , for model I-c and $\overline{U}_h = 5.5 \text{ m/s}$. This data is complementary to that shown in Section 4.1.2.

Table C.6. Maximum and minimum moment coefficients. Model I-c. $\bar{U}_h = 5.5 \text{ m/s}$

$k_0 = 6.0 \text{ Nm (model scale)}$

$C_{\bar{M}}$									
θ	$\alpha = 0^\circ$	$\alpha = 5^\circ$	$\alpha = 10^\circ$	$\alpha = 15^\circ$	$\alpha = 20^\circ$	$\alpha = 25^\circ$	$\alpha = 30^\circ$	$\alpha = 40^\circ$	$\alpha = 50^\circ$
0°	0.13	0.15	0.30	0.29	0.31	0.33	0.31	0.15	0.11
10°	0.14	0.14	0.31	0.29	0.30	0.34	0.31	0.15	0.12
20°	0.13	0.14	0.29	0.26	0.30	0.33	0.32	0.15	0.12
30°	0.13	0.13	0.27	0.26	0.28	0.30	0.28	0.15	0.13
40°	0.11	0.11	0.21	0.20	0.25	0.27	0.25	0.14	0.11
50°	0.12	0.10	0.14	0.14	0.21	0.22	0.21	0.13	0.11
60°	0.09	0.09	0.11	0.12	0.17	0.19	0.17	0.11	0.09
70°	0.07	0.06	0.06	0.08	0.14	0.12	0.13	0.09	0.07
80°	0.05	0.03	0.02	0.04	0.07	0.08	0.08	0.06	0.05
90°	0.06	0.03	0.02	0.02	0.05	0.03	0.04	0.04	0.03
100°	0.06	0.05	0.06	0.05	0.07	0.06	0.08	0.04	0.06
110°	0.08	0.09	0.09	0.08	0.12	0.12	0.12	0.11	0.08
120°	0.11	0.13	0.16	0.15	0.16	0.18	0.18	0.15	0.11
130°	0.15	0.17	0.24	0.25	0.22	0.25	0.24	0.16	0.11
140°	0.21	0.22	0.30	0.25	0.27	0.29	0.27	0.17	0.12
150°	0.21	0.24	0.37	0.31	0.29	0.33	0.28	0.16	0.12
160°	0.24	0.26	0.39	0.38	0.30	0.37	0.32	0.17	0.12
170°	0.24	0.41	0.41	0.36	0.34	0.37	0.30	0.18	0.12
180°	0.24	0.42	0.44	0.35	0.32	0.40	0.31	0.17	0.12
$C_{\bar{M}}$									
θ	$\alpha = 0^\circ$	$\alpha = 5^\circ$	$\alpha = 10^\circ$	$\alpha = 15^\circ$	$\alpha = 20^\circ$	$\alpha = 25^\circ$	$\alpha = 30^\circ$	$\alpha = 40^\circ$	$\alpha = 50^\circ$
0°	-0.16	-0.08	0.05	0.02	0.05	0.02	0.04	0.02	0.00
10°	-0.15	-0.08	0.05	0.01	0.04	0.02	0.04	0.02	-0.01
20°	-0.15	-0.09	0.04	0.00	0.04	0.02	0.02	0.02	-0.01
30°	-0.16	-0.09	0.03	-0.01	0.04	0.01	0.02	0.02	-0.01
40°	-0.15	-0.11	0.00	-0.03	0.03	0.01	0.01	0.01	-0.01
50°	-0.13	-0.09	-0.02	-0.05	0.01	0.01	0.00	0.01	-0.02
60°	-0.10	-0.09	-0.03	-0.05	0.01	0.01	-0.02	0.00	-0.03
70°	-0.07	-0.07	-0.04	-0.05	0.00	0.00	-0.03	-0.01	-0.04
80°	-0.04	-0.05	-0.04	-0.05	-0.01	-0.01	-0.03	-0.03	-0.04
90°	-0.02	-0.04	-0.04	-0.05	-0.01	-0.02	-0.04	-0.03	-0.04
100°	-0.02	-0.03	-0.02	-0.04	-0.03	-0.02	-0.03	-0.03	-0.06
110°	-0.03	-0.03	-0.02	-0.04	-0.02	-0.02	-0.03	-0.01	-0.03
120°	-0.05	-0.04	-0.01	-0.03	-0.02	-0.01	-0.02	-0.01	-0.03
130°	-0.05	-0.04	0.01	-0.01	0.00	0.00	-0.01	-0.01	-0.03
140°	-0.06	-0.03	0.02	-0.02	0.01	0.01	0.01	0.00	-0.02
150°	-0.05	-0.02	0.04	0.02	0.01	0.01	0.01	0.00	-0.01
160°	-0.07	-0.01	0.05	0.02	0.02	0.01	-0.01	0.01	0.00
170°	-0.05	0.04	0.05	0.04	0.01	0.01	-0.03	0.00	-0.01
180°	-0.07	0.04	0.06	0.04	0.01	0.02	-0.01	0.00	-0.01

Figure C.4 shows the variation of the mean moment coefficient $C_{\bar{M}}$ with tilt angle, α , for several wind directions, θ , for Model I-c.

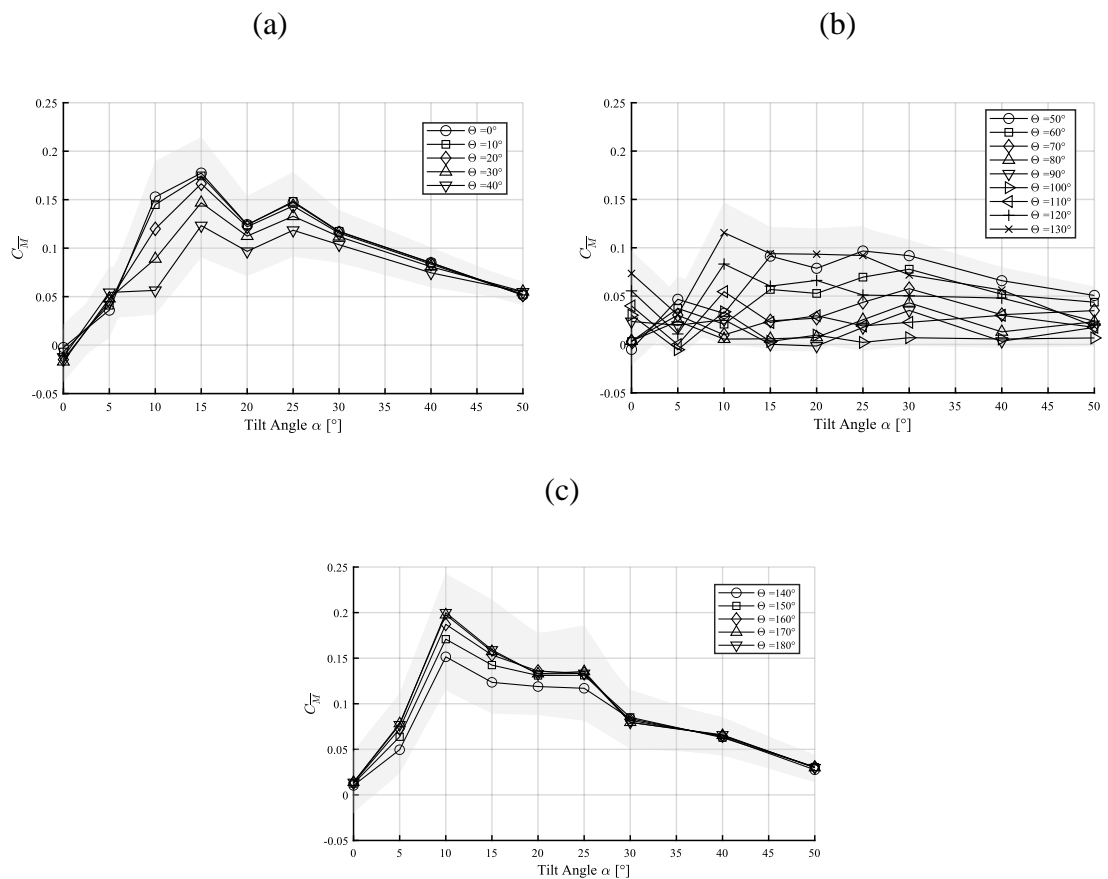


Figure C.4. Mean moment coefficient $C_{\bar{M}}$ vs tilt angle α , for (a) $0^\circ < \theta < 40^\circ$, (b) $50^\circ < \theta < 130^\circ$, and (c) $140^\circ < \theta < 180^\circ$. Uncertainty shown as a grey shade. Model I-c. $\bar{U}_h = 6.5 \text{ m/s}$ (model scale)

Table C.7 provides moment coefficients (i.e. maximum and minimum) for a range of tilt angles, α , and wind directions, θ , for model I-c and $\bar{U}_h = 6.5 \text{ m/s}$. This data is complementary to that shown in Section 4.1.2.

Table C.7. Maximum and minimum moment coefficients. Model I-c. $\bar{U}_h = 6.5 \text{ m/s}$

$k_0 = 6.0 \text{ Nm (model scale)}$

$C_{\bar{M}}$									
θ	$\alpha = 0^\circ$	$\alpha = 5^\circ$	$\alpha = 10^\circ$	$\alpha = 15^\circ$	$\alpha = 20^\circ$	$\alpha = 25^\circ$	$\alpha = 30^\circ$	$\alpha = 40^\circ$	$\alpha = 50^\circ$
0°	0.11	0.17	0.33	0.37	0.31	0.29	0.23	0.17	0.10
10°	0.11	0.17	0.30	0.35	0.28	0.30	0.23	0.16	0.10
20°	0.09	0.17	0.28	0.36	0.29	0.29	0.22	0.16	0.10
30°	0.07	0.20	0.23	0.32	0.27	0.27	0.23	0.16	0.10
40°	0.08	0.19	0.19	0.30	0.23	0.25	0.21	0.15	0.11
50°	0.07	0.16	0.14	0.26	0.19	0.22	0.18	0.14	0.10
60°	0.06	0.14	0.10	0.19	0.16	0.17	0.16	0.12	0.09
70°	0.05	0.11	0.06	0.11	0.12	0.12	0.12	0.09	0.08
80°	0.03	0.08	0.04	0.07	0.07	0.08	0.09	0.07	0.06
90°	0.06	0.06	0.07	0.04	0.03	0.05	0.07	0.04	0.05
100°	0.09	0.04	0.10	0.07	0.08	0.05	0.06	0.07	0.06
110°	0.12	0.08	0.17	0.12	0.14	0.11	0.11	0.11	0.08
120°	0.17	0.11	0.26	0.18	0.19	0.19	0.17	0.14	0.09
130°	0.21	0.14	0.27	0.24	0.25	0.27	0.21	0.15	0.08
140°	0.26	0.17	0.37	0.30	0.29	0.31	0.23	0.15	0.09
150°	0.28	0.20	0.40	0.37	0.36	0.32	0.22	0.15	0.10
160°	0.29	0.22	0.38	0.43	0.37	0.37	0.21	0.14	0.09
170°	0.31	0.22	0.42	0.45	0.40	0.39	0.20	0.15	0.09
180°	0.30	0.21	0.43	0.43	0.37	0.41	0.20	0.16	0.09
$C_{\bar{M}}$									
θ	$\alpha = 0^\circ$	$\alpha = 5^\circ$	$\alpha = 10^\circ$	$\alpha = 15^\circ$	$\alpha = 20^\circ$	$\alpha = 25^\circ$	$\alpha = 30^\circ$	$\alpha = 40^\circ$	$\alpha = 50^\circ$
0°	-0.11	-0.11	0.04	0.04	0.02	0.04	0.04	0.03	0.01
10°	-0.11	-0.09	0.04	0.04	0.01	0.04	0.05	0.02	0.01
20°	-0.12	-0.09	0.01	0.04	0.02	0.04	0.05	0.02	0.01
30°	-0.11	-0.09	0.00	0.02	0.02	0.04	0.05	0.01	0.01
40°	-0.10	-0.07	-0.02	0.00	0.02	0.03	0.05	0.02	0.01
50°	-0.10	-0.06	-0.03	-0.01	0.01	0.02	0.04	0.01	0.01
60°	-0.07	-0.05	-0.03	-0.01	0.00	0.02	0.04	0.00	0.00
70°	-0.05	-0.04	-0.03	-0.02	-0.02	0.00	0.02	-0.01	0.00
80°	-0.03	-0.02	-0.02	-0.03	-0.03	0.00	0.02	-0.02	-0.01
90°	0.00	-0.02	0.00	-0.03	-0.02	0.00	0.01	-0.02	-0.01
100°	-0.01	-0.05	0.00	-0.03	-0.02	-0.03	-0.02	-0.03	-0.02
110°	-0.02	-0.05	0.00	-0.03	-0.02	-0.03	-0.02	-0.02	-0.03
120°	-0.02	-0.08	0.01	-0.02	-0.02	-0.03	-0.01	-0.03	-0.04
130°	-0.02	-0.07	0.02	-0.01	0.00	-0.02	-0.01	-0.03	-0.04
140°	-0.01	-0.06	0.03	-0.01	0.01	0.00	-0.01	-0.01	-0.02
150°	0.01	-0.06	0.04	-0.02	-0.02	-0.02	-0.01	-0.01	-0.03
160°	0.00	-0.07	0.05	-0.04	-0.03	-0.03	-0.01	-0.01	-0.03
170°	0.01	-0.06	0.06	-0.03	-0.07	-0.04	-0.01	-0.01	-0.02
180°	0.03	-0.05	0.06	-0.05	-0.05	-0.07	-0.01	-0.01	-0.02

Table C.8 provides moment coefficients (i.e. mean, maximum and minimum) for a range of tilt angles, α , and wind directions, θ , for model II-b and $\bar{U}_h = 7.5 \text{ m/s}$. This data is complementary to that shown in Section 4.1.2.

Table C.8. Mean, maximum, minimum moment coefficient and standard deviation.

Model II-b. $\bar{U}_h = 7.5 \text{ m/s}$, $k_0 = 8.8 \text{ Nm}$ (model scale)

$C_{\bar{M}}$								
θ	$\alpha = 0^\circ$	$\alpha = 5^\circ$	$\alpha = 10^\circ$	$\alpha = 20^\circ$	$\alpha = 25^\circ$	$\alpha = 30^\circ$	$\alpha = 40^\circ$	$\alpha = 50^\circ$
0°	-0.010	0.216	0.202	0.174	0.140	0.120	0.110	0.077
40°	-0.007	0.141	0.140	0.132	0.112	0.103	0.091	0.074
90°	-0.001	0.006	-0.001	-0.001	-0.007	0.000	0.005	0.008
140°	0.008	0.151	0.151	0.146	0.119	0.103	0.079	0.038
180°	0.001	0.212	0.186	0.157	0.123	0.105	0.088	0.046
$C_{\bar{M}}$								
θ	$\alpha = 0^\circ$	$\alpha = 5^\circ$	$\alpha = 10^\circ$	$\alpha = 20^\circ$	$\alpha = 25^\circ$	$\alpha = 30^\circ$	$\alpha = 40^\circ$	$\alpha = 50^\circ$
0°	0.247	0.432	0.431	0.374	0.304	0.250	0.188	0.148
40°	0.139	0.313	0.309	0.281	0.260	0.211	0.176	0.147
90°	0.024	0.050	0.055	0.048	0.041	0.053	0.060	0.062
140°	0.183	0.412	0.387	0.343	0.313	0.254	0.189	0.117
180°	0.207	0.645	0.619	0.585	0.305	0.236	0.171	0.119
$C_{\bar{M}}$								
θ	$\alpha = 0^\circ$	$\alpha = 5^\circ$	$\alpha = 10^\circ$	$\alpha = 20^\circ$	$\alpha = 25^\circ$	$\alpha = 30^\circ$	$\alpha = 40^\circ$	$\alpha = 50^\circ$
0°	-0.154	0.059	0.027	0.035	0.023	0.014	0.035	0.002
40°	-0.143	0.036	0.016	0.032	0.022	0.015	0.023	0.005
90°	-0.058	-0.026	-0.033	-0.035	-0.036	-0.032	-0.030	-0.029
140°	-0.166	-0.006	-0.015	0.000	-0.020	-0.008	0.000	-0.040
180°	-0.169	-0.021	-0.108	-0.083	-0.043	-0.007	0.012	-0.010
C_{σ_M}								
θ	$\alpha = 0^\circ$	$\alpha = 5^\circ$	$\alpha = 10^\circ$	$\alpha = 20^\circ$	$\alpha = 25^\circ$	$\alpha = 30^\circ$	$\alpha = 40^\circ$	$\alpha = 50^\circ$
0°	0.035	0.042	0.044	0.035	0.030	0.022	0.017	0.017
40°	0.031	0.034	0.035	0.029	0.024	0.020	0.016	0.016
90°	0.006	0.006	0.008	0.008	0.007	0.007	0.008	0.008
140°	0.034	0.044	0.045	0.039	0.035	0.029	0.022	0.017
180°	0.046	0.065	0.071	0.060	0.040	0.027	0.020	0.015

C.2 Calculation of the critical wind speed

The critical wind speed for torsional galloping was calculated using Equation 2.4. The structural damping c_0 was extracted from Table 3.2. The variation $(\partial C_M/\partial\alpha)$ was calculated as the ratio between the difference between mean moment coefficients of consecutive tilt angles (Section 4.1.2), and the difference of consecutive tilt angles in radians. For instance: $(\partial C_M/\partial\alpha)_{10^\circ} = (C_{M_{10^\circ}} - C_{M_{5^\circ}})/((10^\circ - 5^\circ) \times (\pi/180^\circ))$. Given that the variations $(\partial C_M/\partial\alpha)$ correspond to the stable condition, to approximate the critical wind speed using Blevin's theory, the $(\partial C_M/\partial\alpha)$ were incremented (i.e. 100%) and taken as negative (i.e. Blevins' condition for instability: $(\partial C_M/\partial\alpha) < 0$) and then applied in Equation 2.4. The incremented values of $(\partial C_M/\partial\alpha)$ and the critical wind speeds obtained for Models I-a, I-b, I-c, II-a and II-b are shown in Table B.9. It should be noted that Blevin's theory equations is most accurate for $\alpha \approx 0^\circ$. Therefore, it should be expected that as the tilt angle increases, the critical wind speed approximation is less accurate/valid.

Table C.9. Theoretical critical wind speeds obtained with Blevins' theory

Model	Tilt angle α [°]	$(\partial C_M / \partial \alpha)$		U_{cr} (Blevins) [m/s]	
		$\theta = 0^\circ$	$\theta = 180^\circ$	$\theta = 0^\circ$	$\theta = 180^\circ$
I-a	0	-3.90		10.1	
	5	-2.65	-3.90	14.8	10.1
	10	-0.12	-0.07	326.8	560.2
	20	-0.18	-0.53	217.9	74
I-b	0	-2.36		11.3	
	5	-1.5	-1.6	17.8	16.7
	10	-0.84	-1.6	31.7	16.7
	20	-0.21	-0.46	127	58
I-c	0	-2.40		12.6	
	5	-2.40	-2.40	12.6	18.9
	10	-2.40	-1.6	12.6	18.9
	20	-0.69	-0.46	13.9	43.9
II-a	0	-2.03		19.3	
	5	-1.61	-3.29	24.4	11.9
	10	-0.70	-0.33	56	118.8
	20	-0.89	-0.03	44.1	1307.2
II-b	0	-5.18		8.8	
	5	-5.2	-4.83	8.8	9.4
	10	-0.32	-0.62	142	73.3
	20	-0.33	-0.33	137.7	137.7

Figure C.5 shows examples of the critical wind speed determined with the methodology explained in Section 3.6.2. for models I-b, I-c and II-b.

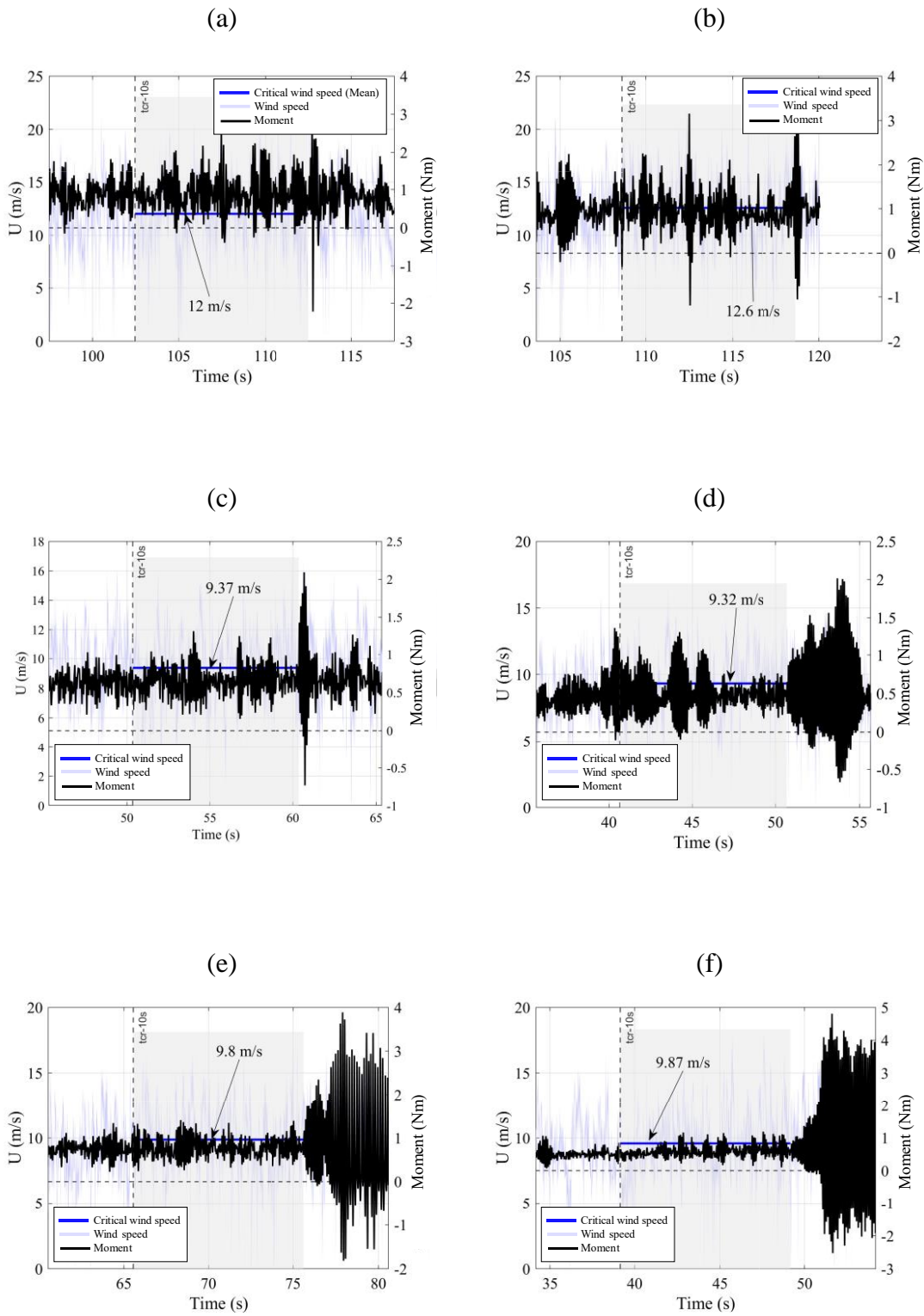


Figure C.5. Wind speed and Moment vs time. Critical wind speed indicated for (a) $\alpha = 10^\circ$, (b) $\alpha = 20^\circ$; $\theta = 0^\circ$ - Model I-b; (c) $\alpha = 5^\circ$, (d) $\alpha = 20^\circ$; $\theta = 0^\circ$ - Model I-c; (e) $\alpha = 5^\circ$ (d) $\alpha = 20^\circ$; $\theta = 0^\circ$ - Model II-b

The experimental variation ($\partial C_M/\partial\alpha$) during instability was calculated using Equation 2.4, solving for ($\partial C_M/\partial\alpha$). Therefore,

$$\left(\frac{\partial C_M}{\partial\alpha}\right) = -\frac{8c_0}{U_{cr}\rho b^3 l}$$

Table C.10 shows the variation ($\partial C_M/\partial\alpha$) during instability for models I-b, I-c and II-b respectively.

Table C.10. Experimental variation ($\partial C_M/\partial\alpha$) for the critical condition

Model	Tilt angle α (°)	Wind direction θ (°)	Experimental U_{cr} (m/s)	Experimental ($\partial C_M/\partial\alpha$)	
I-b	0°	0°	14	-2.29	
	5°	0°	12	-2.67	
		180°	11.2	-2.86	
	10°	0°	12.6	-2.56	
		180°	10.8	-2.88	
	15°	0°	10.7	-2.91	
		180°	9.9	-3.14	
	20°	0°	11.2	-2.86	
		180°	9.4	-3.33	
	25°	0°	10.6	-2.91	
		180°	11.3	-2.76	
	I-c	0°	0°	12.4	-3.37
		5°	0°	9.7	-3.56
			180°	8.4	-4.12
10°		0°	10	-3.45	
		180°	9.1	-3.79	
15°		0°	9	-3.92	
		180°	8.8	-3.93	
20°		0°	9.2	-3.75	
		180°	8.6	-4.02	
25°		0°	11.5	-3.00	
II-b		0°	0°	13.8	-3.95
		5°	0°	9.8	-5.58
			180°	8.2	-6.64
		10°	0°	10.9	-5.01
	180°		9.3	-5.88	
	20°	0°	9.9	-5.53	
		180°	9.1	-6.01	

C.3 Moment and wind spectra before and after torsional galloping

Figure C.6 shows the variation of the moment frequency variation before and after instability onset for Model I-b and II-b.

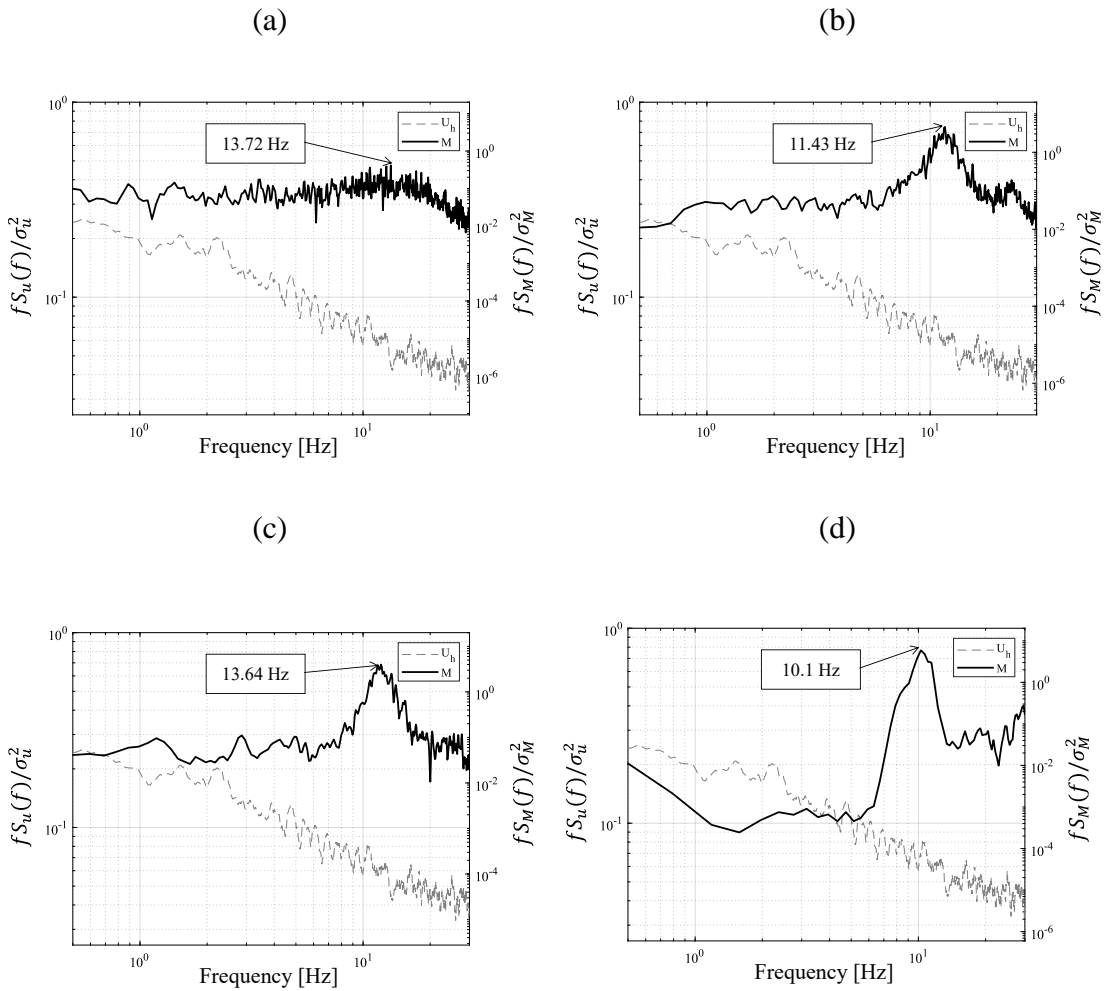


Figure C.6. Power spectral density of the wind speed and moment (a) before torsional galloping, and (b) during torsional galloping. Model I-b, $\alpha = 10^\circ$, and $\theta = 0^\circ$. Idem Model II-b, before (c) and after (d) instability, $\alpha = 20^\circ$ and $\theta = 0^\circ$

C.4 Effective damping and stiffness (Model I-b and Model II-b)

Figure C.7 and Figure C.8 show the variation of effective damping and effective stiffness with the critical wind speed for models I-b and II-b. These results are related to the discussion of Section 4.3.

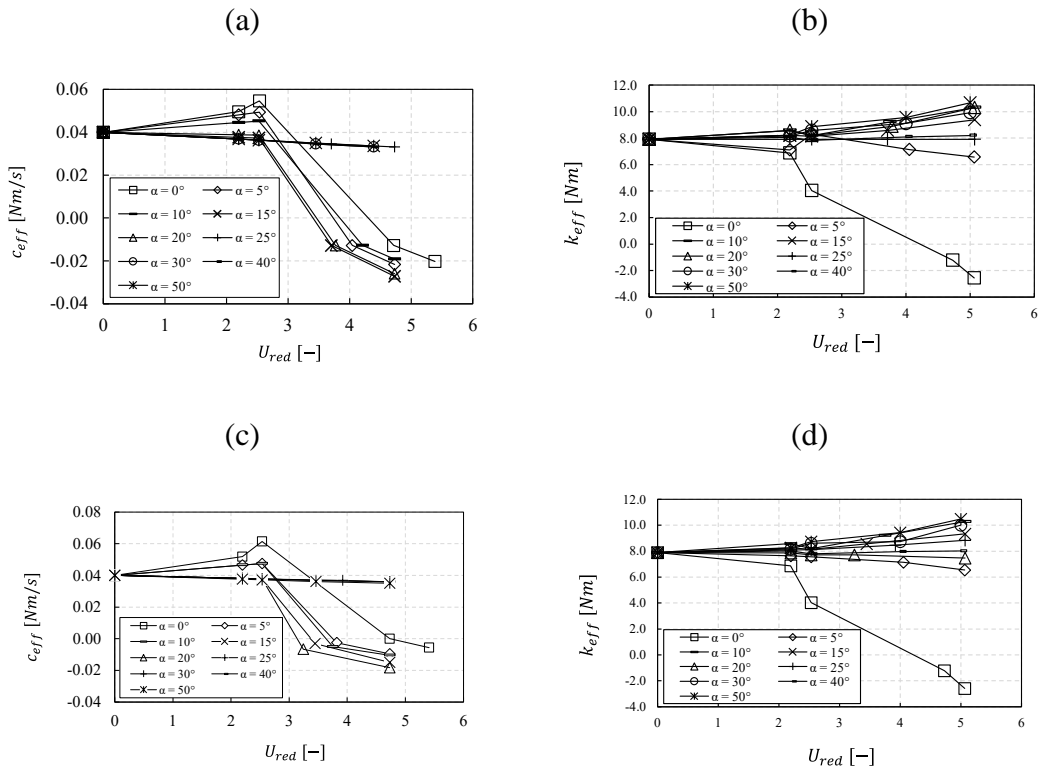


Figure C.7. (a), (c) Effective damping vs reduced wind speed and, (b) (d) effective stiffness vs reduced wind speed, for $\theta = 0^\circ$ (a) - (c) and for $\theta = 180^\circ$ (b) - (d).

Model I-b

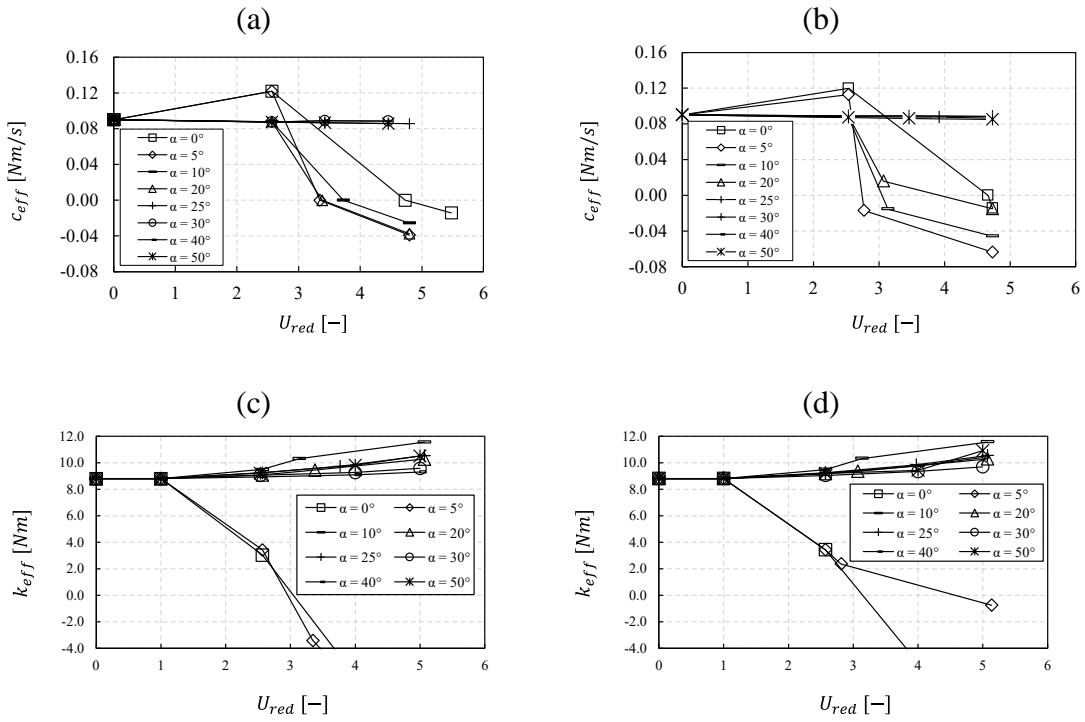


Figure C.8. (a), (c) Effective damping vs reduced wind speed and, (b) (d) effective stiffness vs reduced wind speed, for $\theta = 0^\circ$ (a) - (c) and for $\theta = 180^\circ$ (b) - (d). Model

II-b

C.5 Aerodynamic derivatives (Model I-b and Model II-b)

Figure C.11 and Figure C.12 show the quasi-steady aerodynamic derivative A_2^* and A_3^* as function of U_{red} , for Model I-b and II-b, for $\theta = 0^\circ$, respectively. These results relate to the discussion in Section 4.4, on the variation of the aerodynamic derivatives A_2^* and A_3^* with the reduced wind speed U_{red} .

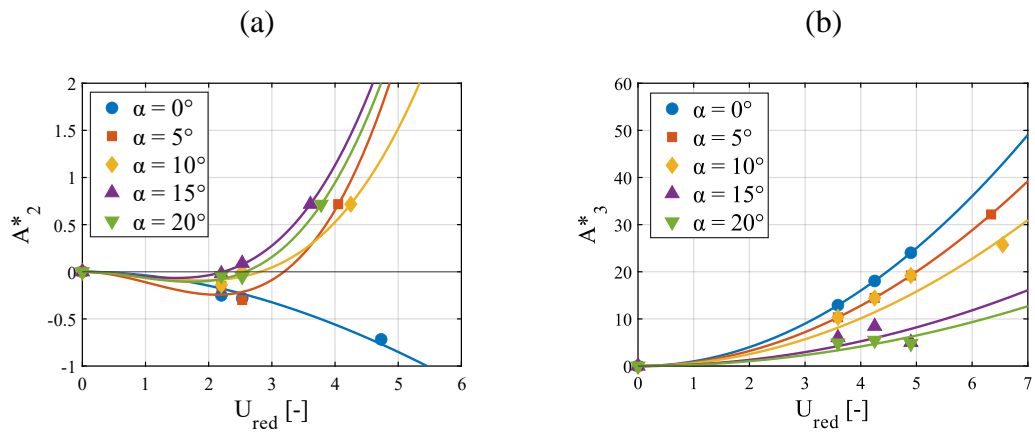


Figure C.9. (a) Aerodynamic derivative A_2^* vs reduced wind speed U_{red} , and (b) Aerodynamic derivative A_3^* vs reduced wind speed U_{red} , for $\theta = 0^\circ$. Model I-b

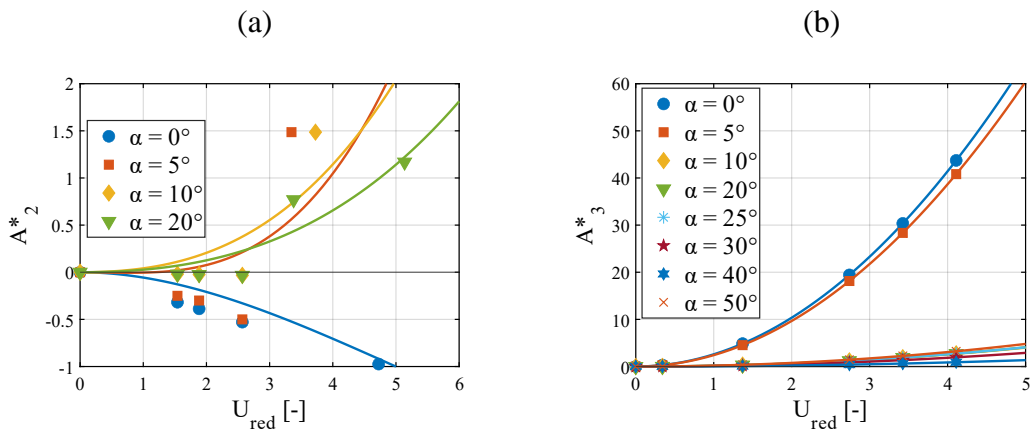


Figure C.10. (a) Aerodynamic derivative A_2^* vs reduced wind speed U_{red} , and (b) Aerodynamic derivative A_3^* vs reduced wind speed U_{red} , for $\theta = 0^\circ$. Model II-b